Distribution Agreement

In presenting this thesis or dissertation as a partial fulfillment of the requirements for an advanced degree from Emory University, I hereby grant to Emory University and its agents the non-exclusive license to archive, make accessible, and display my thesis or dissertation in whole or in part in all forms of media, now or hereafter known, including display on the world wide web. I understand that I may select some access restrictions as part of the online submission of this thesis or dissertation. I retain all ownership rights to the copyright of the thesis or dissertation. I also retain the right to use in future works (such as articles or books) all or part of this thesis or dissertation.

Signature:

_____ _____

W. Seth Childers Date

Amyloid: Merging the Properties of Membranes and Enzymes

By

W. Seth Childers
Doctor of Philosophy

Chemistry

_____

Dr. David G. Lynn
Advisor

_____

Dr. Dale E. Edmondson
Committee Member

_____

Dr. Stefan Lutz
Committee Member

Accepted:

_____

Lisa A. Tedesco, Ph.D. Dean of the James T. Laney School of Graduate Studies

_____ Date

Amyloid: Merging the Properties of Membranes and Enzymes

By

W. Seth Childers
B. ChE. Georgia Institute of Technology, 1999

Advisor: David G. Lynn, PhD.

An abstract of
A dissertation submitted to the Faculty of the
James T. Laney School of Graduate Studies of Emory University
in partial fulfillment of the requirements for the degree of
Doctor of Philosophy
in Chemistry
2010

Abstract

Amyloid: Merging the Properties of Membranes and Enzymes
By W. Seth Childers

Since the first observation of amyloid deposits more than 150 years ago, amyloid fibers have played a critical yet uncertain role in neurodegenerative disease. At the core of this uncertainty are the cross-β variations proposed to lead to distinct amyloid polymorphs that underpin different phenotypes. Yet it is unclear how peptide sequence directs polymorphism and functional differences. Here I have used the critical nucleating core of the Alzheimer's Disease peptide, Aβ(16-22), as a model to address the molecular origins of amyloid polymorphism and understand core properties that lead to amyloid's diverse functions. Solid-state NMR and diffraction studies revealed that simple amino acid changes direct structural polymorphs by modulating both β-strand and β-sheet pleat registry. Interestingly, these short peptides form hollow nanotubes in which peptides interact via termini interactions to form a peptide bilayer wall. Like membranes, these amyloid assemblies have diverse conditionally dependent phases including fibers, nanotubes, oligomers, twisted and helical ribbons, and lamellar bundles of nanotubes. The cross-β assemblies bind small molecules (e.g. congo red) and precisely template them into organized molecular arrays providing the spectroscopic origins of congo red's apple-green birefringence. I further demonstrated that these lysine-rich amyloid assemblies serve as retro-aldolase catalysts. Taken together, I argue that physical properties of amyloids can best be seen as merging the long-range order of membranes with the catalytic features of enzymes and that simple amyloid structures could provide an early prebiotic catalyst leading to the emergence of complex chemical systems.

Amyloid: Merging the Properties of Membranes and Enzymes

By

W. Seth Childers
B. ChE. Georgia Institute of Technology, 1999

Advisor: David G. Lynn, PhD.

A dissertation submitted to the Faculty of the
James T. Laney School of Graduate Studies of Emory University
in partial fulfillment of the requirements for the degree of
Doctor of Philosophy
in Chemistry
2010

Acknowledgements

I began my graduate studies in bimolecular chemistry with background of a process chemical engineer who had never taken a college class in biochemistry or biology. I remember applying to graduate school and leaving engineering was an uneasy choice, however one of my first experiences was visitation weekend at Emory's Chemistry Department. During my visit, I met Drew Palmer, Justin Maresh and David Lynn and was impressed by the way they discussed with passion and excitement for hours about their scientific discoveries. At that moment I realized that scientific research is definitely what I wanted to do and eventually came to Emory for graduate studies.

After joining graduate school I had a steep learning curve, and would like to thank Prof. Stefan Lutz, as his course challenged me in a way that I learned biochemistry's jargon and became comfortable reading and critiquing the primary literature. As well, I thank Prof. Dale Edmondson for introducing me to a variety of spectroscopic techniques in his biophysical chemical course that helped me answer questions throughout my research. I'm not sure I could have made it through all the course work without several friendships with Betul Kacar, Yue Liu, Yi-Han Lin, and Kitty Liu. We spent many late nights doing homework, studying for test and cumulative exams, practicing for yearly research talks, and dealing with the everyday stressed of a graduate student together. Having great friends like Betul, Yue, Yi-Han, and Kitty that joined me on my journey through graduate school made it a special experience. I would also like to thank Drew Palmer, Anil Mehta, and Steven Dublin for many interesting conversations about science over lunch and coffee. These conversations helped me develop my own ideas towards my dissertation and explore the type of research I would like to do in the future.

I was very fortunate to follow the footsteps and learn from Kun Lu, Jijun Dong, Peng Liu, and Rong Ni. Their research discoveries created fascinating questions and ideas and

provided the unique foundation for my own graduate studies. I am very appreciative of all the knowledge and skills they passed on to me. I would also like to further thank Rong Ni, as we worked together for many years together on the amyloid project. I learned a great deal from many hours of brainstorming together that helped each of us design better experiments and understand unexpected results. Throughout my graduate student career I was very fortunate to have a daily group meeting with Anil (i.e. afternoon coffee break) where I developed many of my final experiments and refined interpretation my experimental results. As I leave the lab I'm very anxious to learn what new discoveries Savannah, Tolu, Erin, and Chenrui will reveal.

To explore questions within this dissertation I needed to learn skills for many biophysical techniques. I would like to thank Robert Apkarian for taking the time to teach me the connections between theory and practice Electron Microscopy. As well, Jeanette Taylor for giving me initial training in electron diffraction, and patiently allowing me to learn how to optimize the microscope for electron diffraction collection. I was also fortunate to learn solid-state NMR techniques from one of the best in the field, Anil Mehta. I'm very grateful to Anil for taking the time to answer all my questions about NMR, and for teaching me how to apply NMR techniques to answer structural questions.

I would like to thank my advisor Prof. David Lynn. His enthusiasm, patience, kindness, passion and curiosity provided ideal environment to develop as a scientist. It was always very exciting to share my research with David, and brainstorm together to come up with new experiments. Perhaps most exciting was our collaboration working on amyloid catalysis with Thinh Bui. I'm very grateful that David synthesized the Methodol compound, giving me the chance to study amyloid's unique catalytic abilities during my final weeks of graduate school. This collaboration made it very exciting to share and learn about amyloid as a catalyst. Furthermore, I am very appreciative of David for giving me many opportunities to learn new ways of teaching and communicating science to society. In the future I hope to be able to

connect research, teaching, and out-reach in a way that David Lynn has set as an example. Finally, I would like to thank my family, Kitty, Mom, Dad, and Kitty's parents for all the love and support they provided during my graduate studies.

Table of Contents

List of Figures

Chapter 1 Figures

Chapter 2 Figures

Chapter 3 Figures

Chapter 4 Figures

Chapter 5 Figures

Chapter 6 Figures

Chapter 7 Figures

Chapter 8 Figures

Chapter 1 : Amyloid - An Enigmatic Peptide Assembly

While amyloid has been commonly associated with more than twenty neurodegenerative diseases[1], numerous examples have indicated that all polypeptides under the appropriate conditions may form amyloid[2,3,4]. Several examples of Nature exploiting amyloid's conformational configuration, material properties, and repetitive nature have emerged. For example, a variety of fungal organisms have exploited amyloid aggregates as heritable elements that direct phenotypes[5] by encoding information within amyloid conformation. Similarly, Het-s amyloid acts as an apparent mediator of self/non-self recognition to prevent incompatible fusions of fungal strains[6]. Amyloid's material properties have also been exploited by *Austrofundulus Limnaeus* for the construction of protective egg envelope for developing embryos[7] and barnacles use amyloid as a major adhesive component[8]. Furthermore, bacteria exploit amyloid as the structural foundation for their interconnecting biofilm that promotes quorum phenotypes such as virulence[9,10]. Humans are no exception, as Pmel17 amyloid fibers appear to play a role in directing the polymerization of the skin pigment polymer melanin[11,12]. With the profound impact amyloid has on biology ranging from neurodegenerative disease to diverse beneficial functions it has become increasingly important to dissect amyloid's structure-function relationship to delineate the fine line between toxic, benign, and functional forms of amyloid.

Amyloid: An Historic Structural Challenge

In 1855, Virchow[13] coined the term amyloid to describe unusual deposits observed in the cerebral corpora amylacea[14]. Virchow studied these complex deposits by staining them with iodine and observed a pale blue stained material turn violet upon addition of sulfuric acid. Such observations were consistent with cellulose or starch, and the name amyloid was assigned[13]. Since then it has been shown that the major component of amyloid plaques is

actually fibrous β-sheet rich proteins[14,15], and positive iodine stain may be attributed to proteoglycans bound to amyloid[16,17]. Methods to identify suspect deposits as amyloid were advanced by Divry and Florkin[18] who developed an amyloid staining protocol using the textile dye congo red (CR). An example of CR staining of amyloid plaques associated with three neurodegenerative disease is shown in Figure 1-1.When CR stained plaques are viewed using linearly polarized light, a pink stain is observed within the plaque structure. Amyloid's unique fingerprint is revealed when the sample is placed between crossed polarizers and an apple-green birefringence is observed indicating the CR molecules have been highly organized by an amyloid deposit[18,19,20,21,22]. Since then, other dyes such as thioflavine T[23] has been developed as a fluorescence assay that has enabled high throughput screens of amyloid aggregation. These early structural diagnostic tools still serve[24] as the primary diagnostic assays of amyloid assemblies.

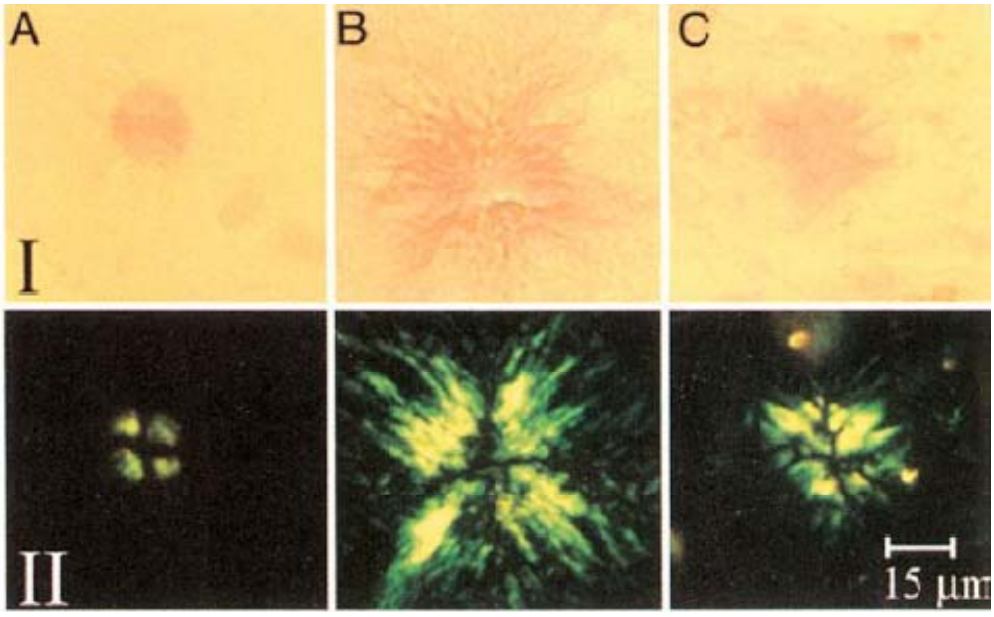

Figure 1-1 : Amyloid plaques from three diseases stained with the histochemical dye CR: AD (A), GSS (B), and DS (C). I : amyloid in linearly polarized light; II, amyloid samples between crossed polarizers displaying apple-green birefringence[25].

The structural organization of these protein aggregates was later revealed by x-ray fiber diffraction studies.[26,27] Studies of aligned synthetic amyloid peptide revealed a distinct

diffraction pattern characterized by orthogonal d-spacings at 4.6-4.8Å and ~10Å (Figure 1-2). These d-spacings were assigned to a periodic grid-like arrangement of hydrogen bonded β-strands separated by 4.7Å forming long β-sheets that run parallel to the fiber axis. Individual β-sheets laminated together through side-chain stacking separated by ~10Å[26,27] form the ~5 nm fiber diameter. This orthogonal grid-like arrangement of peptides is known as the cross-β structure[26,27] and is a common structural feature of all amyloid. Diffraction methods have since been optimized to yield additional information about variations in cross-β folds for amyloid structures[28,29,30,31,32]. Given anisotropic growth of amyloid assemblies as micron long 5nm diameter fibers, cross-β assemblies have been commonly referred to as "one-dimensional"[33] or "linear" crystallization[6].

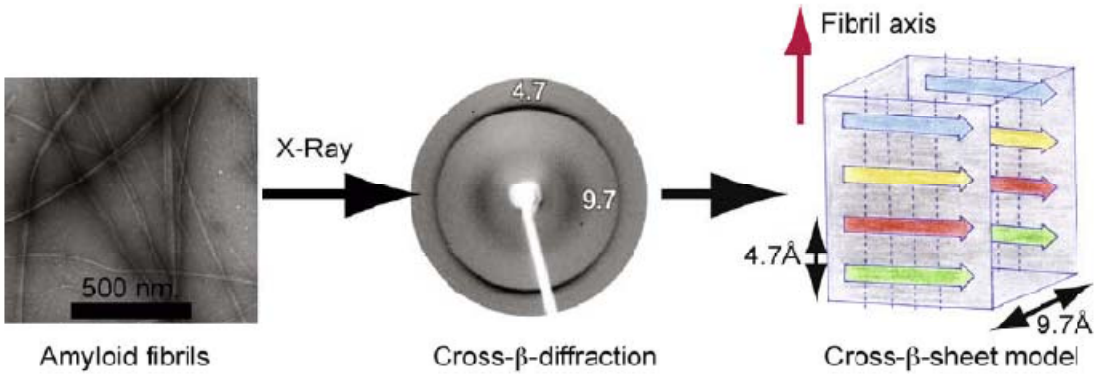

Figure 1-2 : Amyloid as peptides organized as a cross-β structure[34]. From left to right: a typical TEM image of amyloid fibers, x-ray diffraction of aligned fibers. The periodic cross-β peptide arrangements that give rise to the observed cross-β diffraction. Reprinted from Maji SK, Wang L, Greenwald J, Riek R (2009) Structure-activity relationship of amyloid fibrils. FEBS letters 583: 2610-2617 with permission from Elsevier.

While diffraction revealed the periodic organization of peptides with respect to the fiber axis, organization within β-sheets was unclear as individual β-strands could organize parallel or anti-parallel. Furthermore, these paracrystalline assemblies were unsuitable for traditional

analysis by solution state NMR or x-ray crystallography and methods using solid-state NMR became a focus to study these assemblies. Methods were developed so β-sheet configurations could be determined by placing ^{13}C isotopes in the carbonyls of the peptide backbone to enable measurements of ^{13}C-^{13}C dipolar couplings via DRAWS (Dipolar recoupling with a windowless sequence) [35,36,37]. Typically, dipolar couplings corresponding to ^{13}C-^{13}C distances of ~6Å can be detected. Lynn and co-workers exploited the fact that ^{13}C-^{13}C distances of isotopically labeled backbone carbonyls would be dependent upon β-sheet registry. Indeed, using solid-state NMR DRAWS interstrand peptide distances measurements (Figure 1-3) were made between carbonyls on adjacent peptide chains that directly constrained the Aβ(10-35) peptides to be in a parallel β-sheet arrangement[36,38]. Solid-state NMR methods have now provided the necessary constraints to understand the intermolecular peptide arrangements within diverse cross-β assemblies.

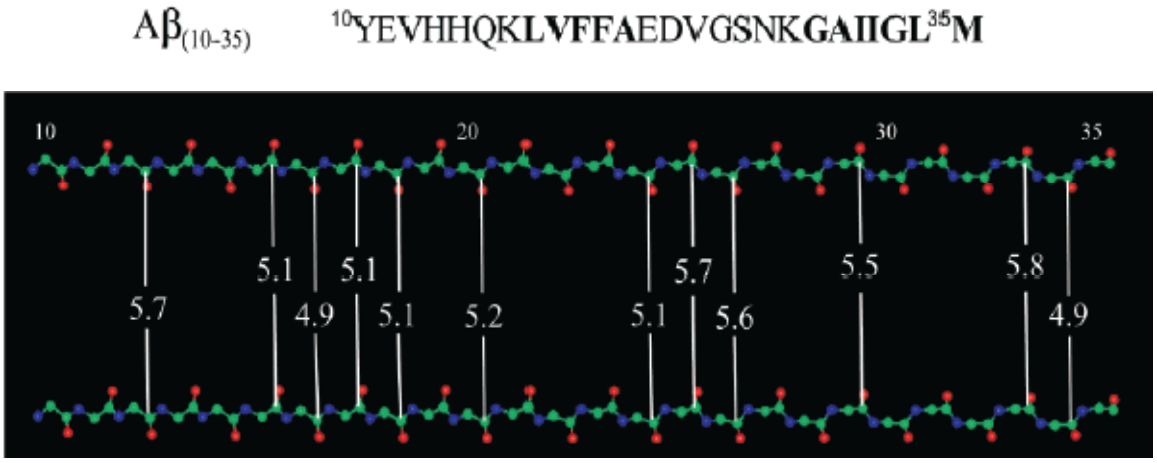

Figure 1-3 : Summary of the inter peptide ^{13}C carbonyl contacts observed for A*β*(10-35) by solid-state NMR. Inter peptide distances were measured using DRAWS at positions V12, Q15-V18, F20, V24-G26, G29, G33, and L34 ^{13}C carbonyls[37,38].

A combination of diffraction[26,27,30,32], and solid-state NMR[36,37,39] approaches have independently revealed the common cross-β core of all amyloid assemblies. However,

knowledge of a shared cross-β motif has not explained the radically different biological functions that have been observed across peptide sequences. The most significant amyloid structural challenge remains how primary sequence directs structural and morphological variations within cross-β assemblies, and whether any functional significance can be attributed to these structural variations. Despite structural knowledge of the common cross-β spine,[26,27,29,30,31,32,37] it remains unclear how historically used histochemical dyes[18] identify the cross-β structure. Establishing structural connections between histochemical dyes and the cross-β structure variation may enable improved Alzheimer's disease diagnostics, distinguish amyloid structural variations and help reveal amyloid's functional significance.

Connecting Observed Morphological Variation with Cross-β Tertiary Structure

Variations within amyloid assemblies morphology appear to be impacted by both sequence and assembly conditions[40,41]. For example, morphological variations from highly twisted to more rigid assemblies have been observed as the result of different agitation conditions,[39,42,43] and both left-handed and right-handed twisted morphologies have been observed[44,45]. The connections between such subtle morphological variations and atomic level peptide organization are not well defined. A more surprising observation has been two radically different amyloid morphologies: spherical oligomers[46] and hollow nanotubes[47]. Substantial experimental evidence has now suggested that amyloid oligomers may be the most neurotoxic amyloid species[48,49,50]. An illustration of this morphological difference is seen in cryo-etch high resolution scanning electron microcopy (HR-SEM) imaging of oligomers and fibers formed from Aβ(13-21) and this drastic morphological variation is present even though each structure is composed of the same peptide (Figure 1-4).

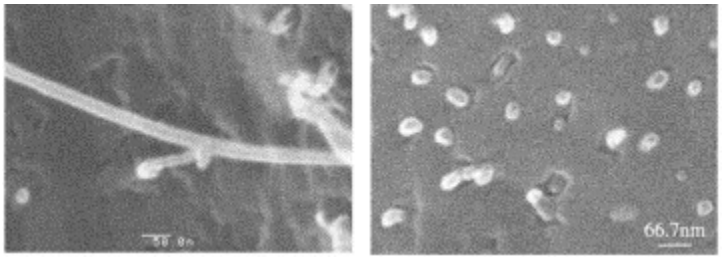

Figure 1-4 : Cryo-etch HR-SEM of 3 mM Aβ(13-21), dissolved in distilled water and titrated to pH 5.6 and allowed to incubate for 3-days. Both smooth fibrils with a 20 nm diameter (left) and spherical particles 10–20 nm (right) were observed[46].

Despite the apparent toxicity of oligomer structures[48,49,50], the internal peptide organization within oligomers is not well defined. These spherical oligomers (Figure 1-4) could be highly structured and accommodate the cross-β structure or they could be more fluid similar to a lipid micelle. A second radically different amyloid morphology are hollow nanotubes with a diameter nearly 10-fold greater than the fibers[47]. The hollow nanotube morphology, in some ways similar to carbon nanotubes, may provide a peptide based scaffold for nanotechnology development[47,51]. Figure 1-5 proposed that the morphological change from fibers to hollow nanotubes may be the result of extended β-sheet lamination. While amyloid fibers are composed of 5-6 laminated β-sheets, the structural model proposes that nanotubes are made up of a coiled 130 laminate β-sheet structure. While provocative, sparse spectroscopic data exists to support this model and mechanistically it remains less clear how β-sheets can undergo extended lamination.

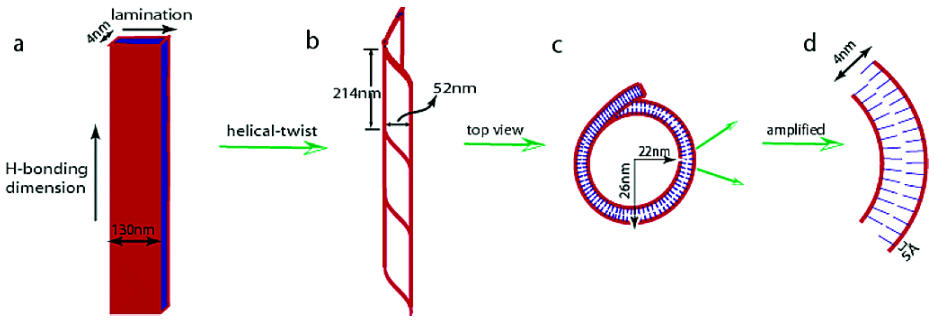

Figure 1-5 : First generation model for amyloid hollow amyloid nanotubes (a) A flat rectangular bilayer, 130 nm wide × 4 nm thick. The 4 nm thickness is made up of the extended peptide chain. Long h-bonded β-sheets make up the long length and extended β-sheets lamination results in a 130 nm width. (b) The coiled tubular sheet with an outer diameter of 52 nm and an outer helical pitch of 214 nm. (c) Top view of the 44 nm internal cavity. (d) Amplified view of the 4 nm wall made up of two peptide chains[47].

Overall, the proposed structural models raise numerous questions about the distinct molecular level origins of morphological selection of twisted fibers, hollow nanotubes, and oligomers. Understanding the inter-relationship and physical properties of these radically different morphologies is a significant hurdle in amyloid structural characterization. However, these short peptides present an ideal model system to understand how to build complex structural morphologies from the bottom up.

The Next Amyloid Structural Challenge: Strain Diversity

While it has been postulated that all polypeptides under appropriate conditions can form amyloid structures[4,52], the polypeptide sequence alone can direct diverse amyloid forms or "strains". The assignment of amyloid structural variation as "strains" has emerged in the context of yeast prions[5,6,53,54]. These β-sheet rich aggregates function as heritable elements that control stable phenotypes by passing information from mother to daughter cells via distinct amyloid conformations[55]. In yeast cell division, amyloid-like aggregates are broken up into smaller fragments passed on to daughter cells (Figure 1-6). The small fragments then catalyze the conversion of soluble prion forms into aggregated forms[55]. It appears that distinct phenotypes are encoded at the level of amyloid conformation, with each conformation or "strain" yielding distinct phenotypes. Yeast in fact utilize prions to control a wide array of functions[5]. In contrast to modern genomes where simple rules of DNA base pairing underlie the genetic code,

the structural nature in which prions encode information is poorly understood and must be understood if it is to be predictable and productably used.

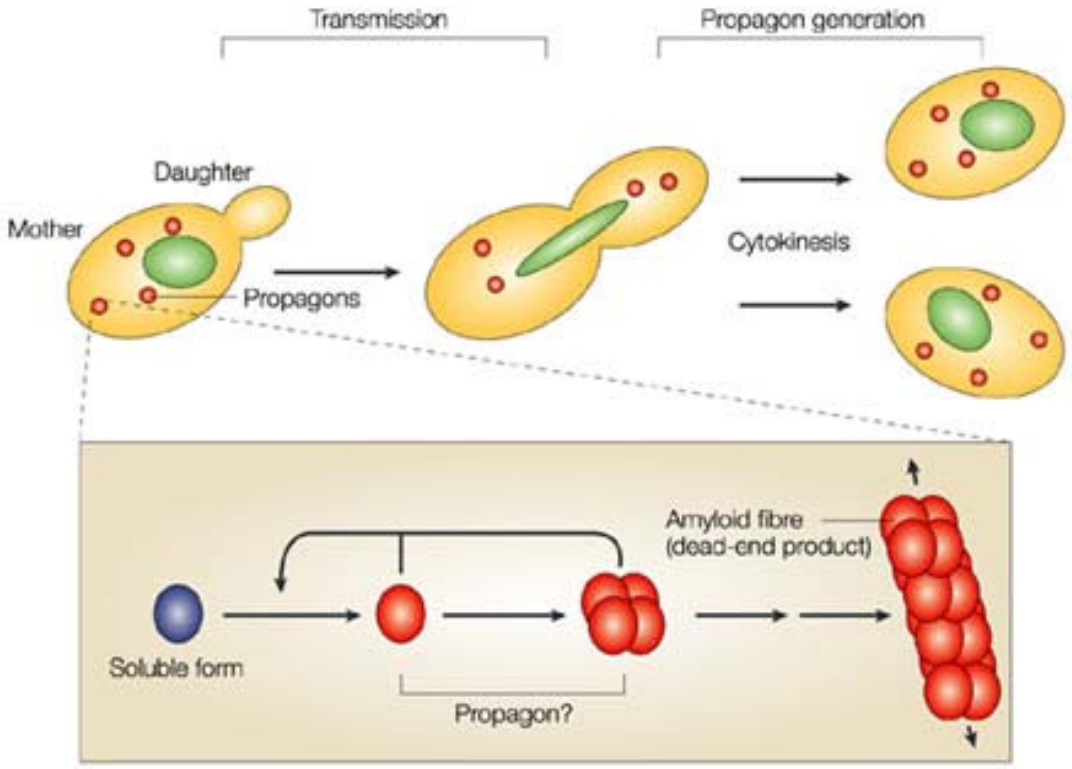

Figure 1-6 : Model for prion replication in which an early protein aggregate called a 'propagon' that seeds the conversion of soluble prions (blue spheres) into aggregated amyloid structures (red spheres). During cell division, prions are broken up into smaller fragments and transmitted to the daughter cell to ensure continued propagation of the [PSI^{+}] phenotype[55]. Reprinted from Tuite MF, Cox BS (2003) Propagation of yeast prions. Nat Rev Mol Cell Biol 4: 878-890 with permission from Elsevier.

The Molecular Origins of Prions Species Barriers and Self Recognition Elements

As illustrated in Figure 1-7, within a given type of family of prions a wide array of aggregated amyloid conformations are possible. Each prion sequence contains a unique, even

subtly different, peptide conformation that propagates, as illustrated by species A, B, and C in Figure 1-7. Some species (e.g. species A and B in Figure 1-7) share common cross-β folds, while others (e.g. species A and C in Figure 1-7) are incompatible, resulting in an apparent species barrier. In one illustrative example, a species barrier was identified between closely related yeast species and it was determined that a single amino acid substitution created the apparent barrier[56,57]. It remains puzzling how a single amino acid substitution can define the accessible amyloid conformation of a given sequence and why certain amyloid conformations are incompatible, defining the observed species barrier.

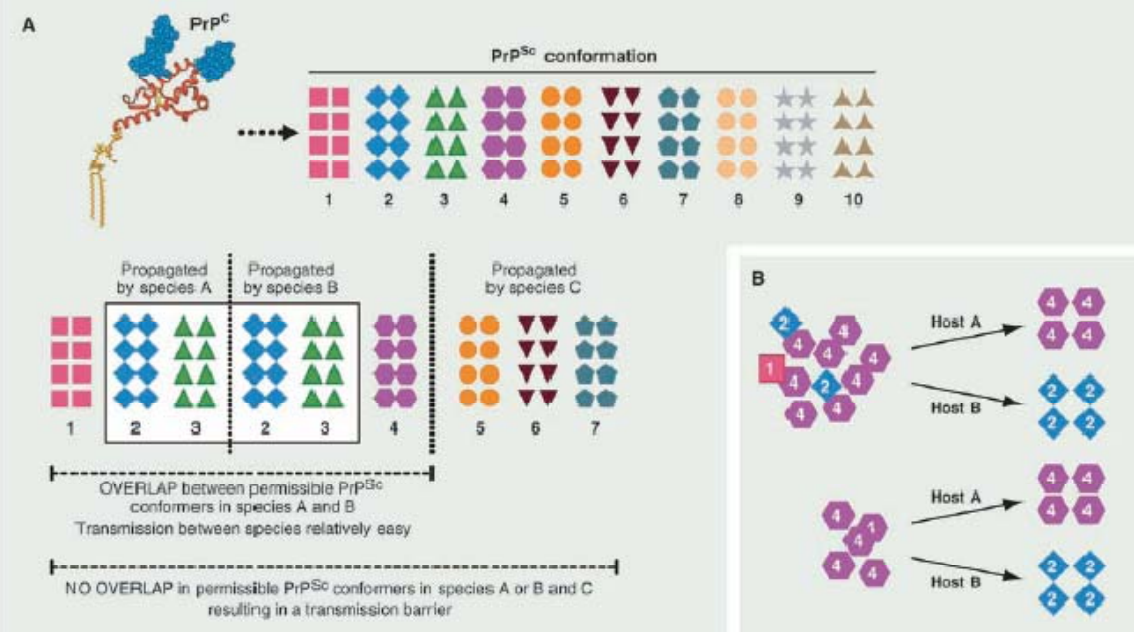

Figure 1-7 : Concept of Prion Strains and Species Barriers. A wide range of mammalian PrPSc amyloid configurations are possible, however only a subset are compatible with a given PrP polypeptide sequence. Three species A/B/C are considered and where there is overlap in possible amyloid conformation for two peptide sequences transmission is possible, however if there is no amyloid conformation overlap between peptide sequences, then a species barrier has been created[58]. From Collinge J, Clarke AR (2007) A general model of prion strains and their pathogenicity. Science 318: 930-936. Reprinted with permission from AAAS.

It has been widely speculated that prion propagation is a highly sequence-specific process, and this property has been exploited by fungi for self/non-self recognition in the regulation of cellular events[6]. For example, *P. anserina* uses subtly different Het-s/Het-S prion sequences that differ by a mere 2 amino acids[59] to prevent fusions of fungal strains with different genomes[5,6,60]. Individual colonies undergo trial fusions at several loci where pure prion assemblies and co-assemblies are possible (Figure 1-8). As the soluble [Het-s*] is converted to an amyloid-rich prion state [Het-s], the prion form facilitates programmed cell death for incompatible fusions (Figure 1-8).

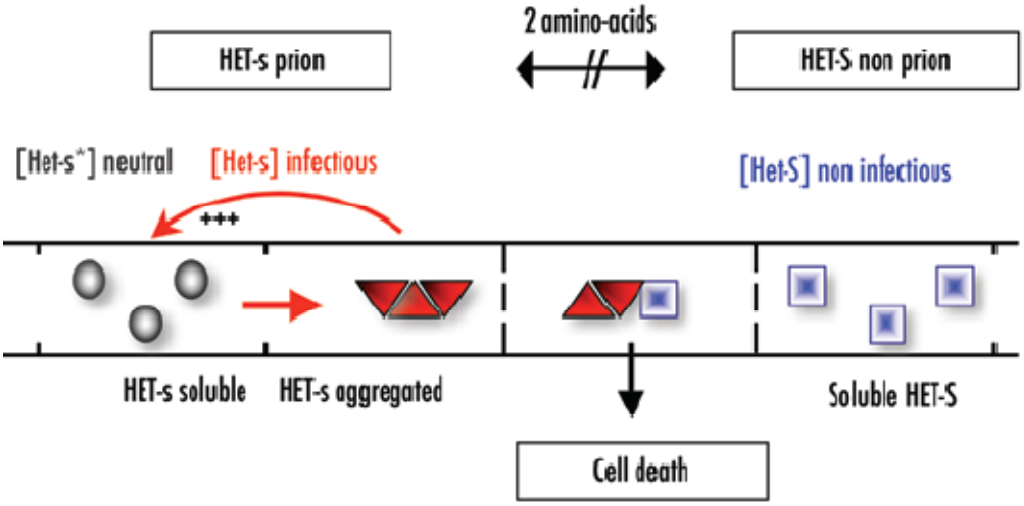

Figure 1-8 : Prevention of fusion of fungal strains carrying different genomes in P. anserina. The two prion alleles differ by 2 amino acids that upon co-assembly facilitate programmed cell death[61]. From Maddelein ML (2007) Infectious Fold and Amyloid Propagation in Podospora anserina. Prion 1: 44-47.

Extensive solid-state NMR efforts have now revealed the cross-β structure of Het-s, however the impact of co-assembly has presented new structural characterization challenges in heterogeneity and molecular complexity within aggregates. Resolving this structural hurdle will reveal how allele co-assembly impacts the structure and how this conformational information is translated into programmed cell death.

Extension of the Strain Concept to Neurodegenerative Amyloid

Increasingly, the prion strain concept has been applied to the observed structural polymorphism in neurodegenerative associated amyloid[62]. Several examples have shown that by modulating in vitro assembly conditions of Aβ(1-40) it is possible to assemble a range of polymorphs or "strains"[62]. Such observations suggest that certain strains are the source of toxicity while others are benign deposits[63]. The amyloid's paracrystallinity with collective molecular weights in the megadalton range have made them unsuitable for traditional structural analysis using x-ray crystallography or solution-state NMR. However, solid-state NMR was used to initially reveal Aβ(10-35) assembled into cross-β structure composed of parallel β-sheets[38,64]. And more recently solid-state NMR methods have been applied towards solving the structure of Aβ(1-40) under agitated conditions[65]. A key to building the proposed model was observation of dipolar couplings between residues D23 and K28, which are consistent with the two residues forming a salt bridge to yield the resulting fold[65]. Despite these structural characterization efforts, the tertiary structural features that define a toxic polymorph remain unclear. Systematic studies of how subtle changes in primary sequence impact the local cross-β arrangements are needed.

The Dramatic Impact of Amyloid Co-Assembly in Neurodegenerative Disease

As observed with prions, emerging evidence now suggests that co-assemblies may result in unique amyloid forms and may also play a role in neurodegenerative disease. The complex cellular cytosol of mammalian tissues is presented to several polypeptides with amyloid propensity. Post-mortem examination of neocortical sections from Alzheimer's disease brain tissues stained with anti-bodies for Aβ(1-40) and Aβ(1-42) reveal micro heterogeneity in the amyloid deposit distribution[66]. Antibody staining reveals Aβ(1-42) is distributed throughout the nervous tissue in diffuse parenchymal deposits as well as within blood vessels. Interestingly, Aβ(1-40) and Aβ(1-42) are co-deposited within blood vessels, while diffuse parenchymal

deposits appear to be enriched in Aβ(1-42). From these histochemical investigations it appears that both pure assembly and mixed assembly may occur within complex tissue environments[66].

The relevance of pure versus mixed assembly was illuminated by a case where homozygous carriers of an Aβ(1-42) A2V mutant are susceptible to familial Alzheimer 's disease, however heterozygous carriers were unaffected[67]. In vitro studies have indicated that both Aβ(1-42) and Aβ(1-42) A2V have the capacity to form amyloid structures, however equimolar peptide mixtures appear incapable of forming amyloid assemblies under the conditions studied (Figure 1-9). And further, cell viability is dependent on whether peptide assemblies are pure or presented as mixtures[67]. In this scenario a single residue change from alanine to valine impacted the ability of the two peptides to co-assemble with a dramatic impact on cell viability. The molecular recognition events that lead to the inability to co-assemble remain puzzling. Indeed, with these two examples amongst numerous others it is clear that the compatibility of amyloid peptide to co-assemble may well play a significant role in the pathology of neurodegenerative diseases.

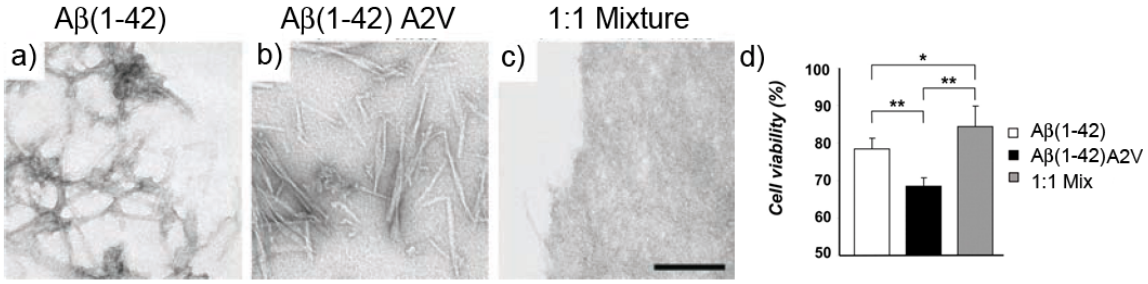

Figure 1-9 : Electron micrographs of negatively stained aggregates from the self-assembly of a) Aβ(1-42), (b) Aβ(1-42) A2V, and an (c) Equimolar mixture of Aβ(1-42) and Aβ(1-42) A2V, and (d) cell viability comparing pure assemblies of Aβ(1-42) and Aβ(1-42) A2V to the equimolar co-assembly[67]. From Di Fede G, Catania M, Morbin M, Rossi G, Suardi S, et al. (2009) A Recessive Mutation in the APP Gene with Dominant-Negative Effect on Amyloidogenesis. Science 323: 1473-1477. Reprinted with permission from AAAS.

The Intertwined Nature of Amyloid Dyes and Strain Architecture

One promising approach to identifying toxic strains is through use of molecular dyes that specifically bind toxic strains over non-toxic strains. Two commonly used histochemical stains appear to bind all amyloid regardless of primary sequence: thioflavine T[23] and congo red[68,69,70]. Certain congo red derivatives[71] and more recently the thioflavine T derivative Pittsburgh Compound B (PIB) appear to have strain specificity[72]. An intriguing study investigated why humans and non-human primates accumulate amyloid-rich senile plaques composed of Aβ with the same exact sequence, yet aged non-human primates have not been observed with AD pathology[72]. In this study PIB was found to selectively bind to the temporal and occipital cortical homogenates from Alzheimer's disease (AD) tissue, but binding was low in non-demented cortical homogenates as well as those from non-human primates (Figure 1-10)[72]. From this study it appears the tertiary features that classify an amyloid strain as toxic can be identified through use of a small molecule. However, no single amyloid binding site has been definitively characterized. Furthermore, the assignment of binding site types unique to toxic or functional amyloid conformational strains is far from being known.

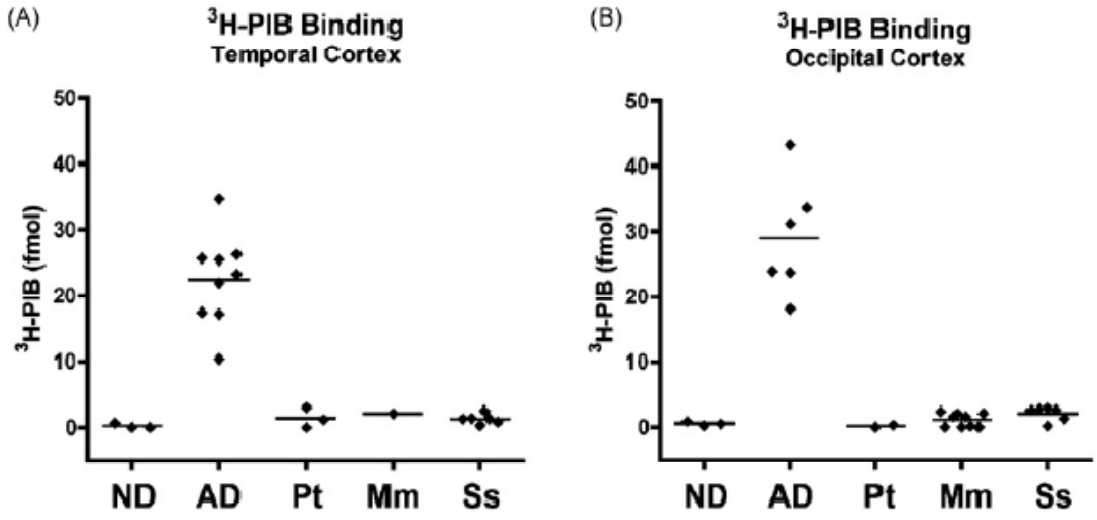

Figure 1-10 : Quantification of ^{3}H-PIB binding in cortical homogenates from aged humans compared with nonhuman primates[72]. Despite comparable mean levels of insoluble Aβ amyloid, ^{3}H-PIB (1 nM) binding is low to undetectable in aged nonhuman primate temporal (A) and occipital (B) cortices compared to the same regions from humans with Alzheimer's disease. ND: nondemented human; AD: Alzheimer's disease; Pt: *Pan troglodytes* (chimpanzee); Mm: *Macaca mulatta* (rhesus macaque); Ss: *Saimiri sciureus* (squirrel monkey). Bars = mean[72]. Reprinted from Rosen RF, Walker LC, LeVine Iii H PIB binding in aged primate brain: Enrichment of high-affinity sites in humans with Alzheimer's disease. Neurobiology of aging In Press, with permission from Elsevier.

Mounting Unanswered Questions about a Common Protein Fold

Since its first identification more than 150 years ago[13], amyloid has presented itself as a most enigmatic material. Structural characterization efforts[26,27,30,32,64,65,73], even though challenged by paracrystallinity, have yielded a common cross-β spine (Figure 1-2) shared by all amyloid structures. Despite this commonality, diverse morphologies[39],[40,48,49,50,74] and internal peptide structural variations exist. It appears that these subtle structural variations may indeed create a rich tapestry of beneficial functions as well as modulating the degree of neurotoxicity. Progress towards full tertiary structural models of amyloids composed of long peptides has been slow with only a few currently reported[64,65,73]. To understand how peptide primary sequence can create amyloid structural variation, short amyloid forming peptides may be used to learn the rules of amyloid assembly. The nucleating core of the Alzheimer 's disease peptide, KLVFFAE or Aβ(16-22), has been heavily studied using an array of biophysical techniques[47,75,76,77]. This short peptide maintains the advantage of solubility and relative ease of synthesis and purification with respect to longer biologically relevant peptides. In this dissertation, I will use Aβ(16-22), as a model system to systematically explore how amyloid

sequence and assembly conditions encode structural and morphological variation and how small molecules bind and interact with the resulting structures.

References

1. Walker LC, LeVine H, Mattson MP, Jucker M (2006) Inducible proteopathies. Trends in Neurosciences 29: 438-443.

2. Chiti F, Webster P, Taddei N, Clark A, Stefani M, et al. Designing conditions for in vitro formation of amyloid protofilaments and fibrils; 1998 Nov 08-09; Irvine, California. Natl Acad Sciences. pp. 3590-3594.

3. Guijarro JI, Sunde M, Jones JA, Campbell ID, Dobson CM (1998) Amyloid fibril formation by an SH3 domain. Proceedings of the National Academy of Sciences of the United States of America 95: 4224-4228.

4. Dobson CM (1999) Protein misfolding, evolution and disease. Trends Biochem Sci 24: 329-332.

5. Tessier PM, Lindquist S (2009) Unraveling infectious structures, strain variants and species barriers for the yeast prion PSI+. Nature Structural & Molecular Biology 16: 598-605.

6. Inge-Vechtomov SG, Zhouravleva GA, Chernoff YO (2007) Biological Roles of Prion Domains. Prion 1: 228-235.

7. Iconomidou VA, Hamodrakas SJ (2008) Natural protective amyloids. Current Protein & Peptide Science 9: 291-309.

8. Barlow DE, Dickinson GH, Orihuela B, Kulp JL, Rittschof D, et al. (2010) Characterization of the Adhesive Plaque of the Barnacle Balanus amphitrite: Amyloid-Like Nanofibrils Are a Major Component. Langmuir 26: 6549-6556.

9. Hammer ND, Schmidt JC, Chapman MR (2007) The curli nucleator protein, CsgB, contains an amyloidogenic domain that directs CsgA polymerization. Proc Natl Acad Sci U S A 104: 12494-12499.

10. Romero D, Aguilar C, Losick R, Kolter R (2010) Amyloid fibers provide structural integrity to Bacillus subtilis biofilms. Proceedings of the National Academy of Sciences of the United States of America 107: 2230-2234.

11. Fowler DM, Koulov AV, Alory-Jost C, Marks MS, Balch WE, et al. (2006) Functional Amyloid Formation within Mammalian Tissue. PLoS Biology 4: e6.

12. Fowler DM, Koulov AV, Balch WE, Kelly JW (2007) Functional amyloid - from bacteria to humans. Trends in Biochemical Sciences 32: 217-224.

13. Virchow R (1855) Zur Cellulose-Fruge. Virchows Arch 8: 140-144.

14. Sipe JD, Cohen AS (2000) Review: History of the Amyloid Fibril. Journal of Structural Biology 130: 88-98.

15. Masters CL, Simms G, Weinman NA, Multhaup G, McDonald BL, et al. (1985) Amyloid Plaque Core Protein in Alzheimer's Disease and Down Syndrome. Proceedings of the National Academy of Sciences of the United States of America 82: 4245-4249.

16. Sandwall E, O'Callaghan P, Zhang X, Lindahl U, Lannfelt L, et al. (2010) Heparan sulfate mediates amyloid-beta internalization and cytotoxicity. Glycobiology 20: 533-541.

17. Madine J, Clayton JC, Yates EA, Middleton DA (2009) Exploiting a C-13-labelled heparin analogue for in situ solid-state NMR investigations of peptide-glycan interactions within amyloid fibrils. Organic & Biomolecular Chemistry 7: 2414-2420.

18. Divry P FM (1927) The optic properties of amyloid. Omptes rendus des seances de la societie de biologie et de ses filiales 97: 1808-1810.

19. Puchtler H, Sweat F, Levine M (1962) On the Binding of Congo Red to Amyloid. J Histochem Cytochem 10: 355-364.

20. Wolman M, Bubis JJ (1965) Cause of Green Polarization Color of Amyloid Stained with Congo Red Histochemie 4: 351-&.

21. Benditt EP, Eriksen N, Berglund C (1970) Congo Red Dichroism with Dispersed Amyloid Fibrils, an Extrinsic Cotton Effect. Proc Natl Acad Sci U S A 66: 1044-1051.

22. Glenner GG, Page DL, Eanes ED (1972) The relationship of the properties of Congo Red-stained amyloid fibriles and the β-conformation. J Histochem Cytochem 20: 821-826.

23. Levine H (1993) Thioflavine T interactions with synthetic Alzheimers Disease beta-amyloid peptides - detection of amyloid aggregation in solution. . Protein Science 2: 404-410.

24. Nilsson MR (2004) Techniques to study amyloid fibril formation in vitro. Methods 34: 151-160.

25. Jin L-W, Claborn KA, Kurimoto M, Geday MA, Maezawa I, et al. (2003) Imaging linear birefringence and dichroism in cerebral amyloid pathologies. Proc Natl Acad Sci U S A 100: 15294-15298.

26. Eanes ED, Glenner GG (1968) X-ray diffraction studies on amyloid filaments. J Histochem Cytochem 16: 673-677.

27. Geddes AJ, Parker KD, Atkins EDT, Beighton E (1968) "Cross-β" Conformation in Proteins. J Mol Biol 32: 343-358.

28. Serpell LC (2000) Alzheimer's amyloid fibrils: structure and assembly. Biochimica Et Biophysica Acta-Molecular Basis of Disease 1502: 16-30.

29. Sikorski P, Atkins ED, Serpell LC (2003) Structure and texture of fibrous crystals formed by Alzheimer's Aβ(11-25) peptide fragment. Structure 11: 915-926.

30. Makin OS, Atkins E, Sikorski P, Johansson J, Serpell LC (2005) Molecular basis for amyloid fibril formation and stability. Proc Natl Acad Sci 102: 315-320.

31. Nelson R, Sawaya MR, Balbirnie M, Madsen AO, Riekel C, et al. (2005) Structure of the cross-β spine of amyloid-like fibrils. Nature 435: 773-778.

32. Sawaya MR, Sambashivan S, Nelson R, Ivanova MI, Sievers SA, et al. (2007) Atomic structures of amyloid cross-β spines reveal varied steric zippers. Nature 447: 453-457.

33. Jarrett JT, Lansbury PT (1993) Seeding "one-dimensional crystallization" of amyloid: a pathogenic mechanism in Alzheimer's disease and scrapie? Cell 73: 1055-1058.

34. Maji SK, Wang L, Greenwald J, Riek R (2009) Structure-activity relationship of amyloid fibrils. FEBS letters 583: 2610-2617.

35. Gregory DM, Benzinger TL, Burkoth TS, Miller-Auer H, Lynn DG, et al. (1998) Dipolar recoupling NMR of biomolecular self-assemblies: determining inter- and intrastrand distances in fibrilized Alzheimer's β-amyloid peptide. Solid State Nucl Magn Reson 13: 149-166.

36. Benzinger TLS, Gregory DM, Burkoth TS, Miller-Auer H, Lynn DG, et al. (1998) Propagating structure of Alzheimer's β -amyloid(10-35) is parallel beta -sheet with residues in exact register. Proc Natl Acad Sci U S A 95: 13407-13412.

37. Benzinger TL, Gregory DM, Burkoth TS, Miller-Auer H, Lynn DG, et al. (2000) Two-Dimensional Structure of β-Amyloid(10-35) Fibrils. Biochemistry 39: 3491-3499.

38. Burkoth TS, Benzinger TLS, Urban V, Morgan DM, Gregory DM, et al. (2000) Structure of the beta-Amyloid (10-35) Fibril. J Am Chem Soc 122: 7883-7889.

39. Petkova AT, Leapman RD, Guo Z, Yau WM, Mattson MP, et al. (2005) Self-Propagating, Molecular-Level polymorphism in Alzheimer's β-Amyloid Fibrils. Science 307: 262-265.

40. Dong J, Shokes JE, Scott RA, Lynn DG (2006) Modulating amyloid self-assembly and fibril morphology with Zn(II). J Am Chem Soc 128: 3540-3542.

41. Morgan DM, Dong JJ, Jacob J, Lu K, Apkarian RP, et al. (2002) Metal switch for amyloid formation: Insight into the structure of the nucleus. Journal of the American Chemical Society 124: 12644-12645.

42. Petkova AT, Ishii Y, Balbach JJ, Antzutkin ON, Leapman RD, et al. (2002) A structural model for Alzheimer's β-amyloid fibrils based on experimental constraints from solid state NMR. Proc Natl Acad Sci 99: 16742-16747.

43. Paparcone R, Sanchez J, Buehler MJ (2010) Comparative Study of Polymorphous Alzheimer's A beta(1-40) Amyloid Nanofibrils and Microfibers. Journal of Computational and Theoretical Nanoscience 7: 1279-1286.

44. Rubin N, Perugia E, Goldschmidt M, Fridkin M, Addadi L (2008) Chirality of amyloid suprastructures. Journal of the American Chemical Society 130: 4602-4607.

45. Rubin N, Perugia E, Wolf SG, Klein E, Fridkin M, et al. (2010) Relation between Serum Amyloid A Truncated Peptides and Their Suprastructure Chirality. Journal of the American Chemical Society 132: 4242-4248.

46. Dong JJ, Apkarian RP, Lynn DG (2005) Imaging amyloid beta peptide oligomeric particles in solution. Bioorganic & Medicinal Chemistry 13: 5213-5217.

47. Lu K, Jacob J, Thiyagarajan P, Conticello VP, Lynn DG (2003) Exploiting amyloid fibril lamination for nanotube self-assembly. J Am Chem Soc 125: 6391-6393.

48. Lambert MP, Barlow AK, Chromy BA, Edwards C, Freed R, et al. (1998) Diffusible, nonfibrillar ligands derived from A beta(1-42) are potent central nervous system neurotoxins. Proceedings of the National Academy of Sciences of the United States of America 95: 6448-6453.

49. Glabe CG, Kayed R (2006) Common structure and toxic function of amyloid oligomers implies a common mechanism of pathogenesis. Neurology 66: S74-S78.

50. Kayed R, Head E, Thompson JL, McIntire TM, Milton SC, et al. (2003) Common structure of soluble amyloid oligomers implies common mechanism of pathogenesis. Science 300: 486-489.

51. Lu K (2005) Discovery of Diverse Peptide Nanotube Architecture from the Self-assembly of Designed Amyloid-β Cassettes. Atlanta: Emory University. 257 p.

52. Guijarro JIa, Sunde M, Jones JA, Campbell ID, Dobson CM (1998) Amyloid fibril formation by an SH3 domain. Proceedings of the National Academy of Sciences of the United States of America 95: 4224-4228.

53. Serio TR, Cashikar AG, Kowal AS, Sawicki GJ, Moslehi JJ, et al. (2000) Nucleated conformational conversion and the replication of conformational information by a prion determinant. Science 289: 1317-1321.

54. Wickner RB, Edskes HK, Roberts BT, Baxa U, Pierce MM, et al. (2004) Prions: proteins as genes and infectious entities. Genes & Development 18: 470-485.

55. Tuite MF, Cox BS (2003) Propagation of yeast prions. Nat Rev Mol Cell Biol 4: 878-890.

56. Chen BX, Newnam GP, Chernoff YO (2007) Prion species barrier between the closely related yeast proteins is detected despite coaggregation. Proceedings of the National Academy of Sciences of the United States of America 104: 2791-2796.

57. Chen BX, Bruce KL, Newnam GP, Gyoneva S, Romanyuk AV, et al. (2010) Genetic and epigenetic control of the efficiency and fidelity of cross-species prion transmission. Molecular Microbiology 76: 1483-1499.

58. Collinge J, Clarke AR (2007) A general model of prion strains and their pathogenicity. Science 318: 930-936.

59. Deleu C, Clave C, Begueret J (1993) A single amino-acid difference is sufficient to elicit vegative incompatibility in fungus podospora-anserina Genetics 135: 45-52.

60. Coustou V, Deleu C, Saupe S, Begueret J (1997) The protein product of the het-s heterokaryon incompatibility gene of the fungus Podospora anserina behaves as a prion analog. Proceedings of the National Academy of Sciences of the United States of America 94: 9773-9778.

61. Maddelein ML (2007) Infectious Fold and Amyloid Propagation in Podospora anserina. Prion 1: 44-47.

62. LeVine H, Walker LC (2010) Molecular polymorphism of A beta in Alzheimer's disease. Neurobiology of aging 31: 542-548.

63. Dong J, Canfield JM, Mehta AK, Shokes JE, Tian B, et al. (2007) Engineering metal ion coordination to regulate amyloid fibril assembly and toxicity. Proc Natl Acad Sci 104: 13313-13318.

64. Benzinger TL, Gregory DM, Burkoth TS, Miller-Auer H, Lynn DG, et al. (1998) Propagating structure of Alzheimer's β-amyloid(10-35) is parallel β-sheet with residues in exact register. Proc Natl Acad Sci 95: 13407-13412.

65. Petkova AT, Yau WM, Tycko R (2006) Experimental Constraints on Quaternary Structure in Alzheimer's Beta-Amyloid Fibrils. Biochemistry 45: 498-512.

66. Walker LC, Rosen RF, Levine H (2008) Diversity of A beta deposits in the aged brain: a window on molecular heterogeneity? Romanian Journal of Morphology and Embryology 49: 5-11.

67. Di Fede G, Catania M, Morbin M, Rossi G, Suardi S, et al. (2009) A Recessive Mutation in the APP Gene with Dominant-Negative Effect on Amyloidogenesis. Science 323: 1473-1477.

68. Howie AJ, Brewer DB (2009) Optical properties of amyloid stained by Congo red: History and mechanisms. Micron 40: 285-301.

69. Kaminksy W, Jin LW, Powell S, Maezawa I, Claborn K, et al. (2006) Polarimetric imaging of amyloid. Micron 37: 324-338.

70. Kurimoto M, Mueller B, Kaminsky W, Kahr B, Jin L-W (2002) Dyeing Crystals to Dyeing Tissues: Congo Red in Anisotropic Media. Mol Cryst Liq Cryst 389: 1.

71. Ashburn TTH, H.; McGuiness, B.F.; Landsbury, P.T. (1996) Amyloid probes based on Congo Red distinguish between fibrils compromising different peptides. Chemistry and Biology 3: 351-358.

72. Rosen RF, Walker LC, LeVine Iii H PIB binding in aged primate brain: Enrichment of high-affinity sites in humans with Alzheimer's disease. Neurobiology of aging In Press, Corrected Proof.

73. Wasmer C, Lange A, Van Melckebeke H, Siemer AB, Riek R, et al. (2008) Amyloid Fibrils of the HET-s(218-289) Prion Form a β Solenoid with a Triangular Hydrophobic Core. Science 319: 1523-1526.

74. Castelletto V, Hamley IW, Harris PJF, Olsson U, Spencer N (2009) Influence of the Solvent on the Self-Assembly of a Modified Amyloid Beta Peptide Fragment. I. Morphological Investigation. Journal of Physical Chemistry B 113: 9978-9987.

75. Balbach JJ, Ishii Y, Antzutkin ON, Leapman RD, Rizzo NW, et al. (2000) Amyloid Fibril Formation by Aβ16-22, a Seven-Residue Fragment of the Alzheimer's β-Amyloid Peptide, and Structural Characterization by Solid State NMR. Biochemistry 39: 13748-13759.

76. Klimov DK, Thirumalai D (2003) Dissecting the assembly of A beta(16-22) amyloid peptides into antiparallel beta sheets. Structure 11: 295-307.

77. Petty SA, Decatur SM (2005) Experimental evidence for the reorganization of beta-strands within aggregates of the a beta(16-22) peptide. Journal of the American Chemical Society 127: 13488-13489.

Chapter 2 : Molecular Origins of Cross-β Strains[1]

Amyloid assemblies are known as β-sheet rich unbranched fibers and are associated many neurodegenerative diseases[1]. Although amyloid structures of the same sequence can appear nearly identical via microscopy, atomic-level variations seem to explain the distinct "strains" that modulate cellular toxicity[2,3]. Even at the level of histological examination, amyloid plaques of Alzheimer's patient and primates that contain the same Aβ peptide show very different structures and corresponding phenotypes[4,5].

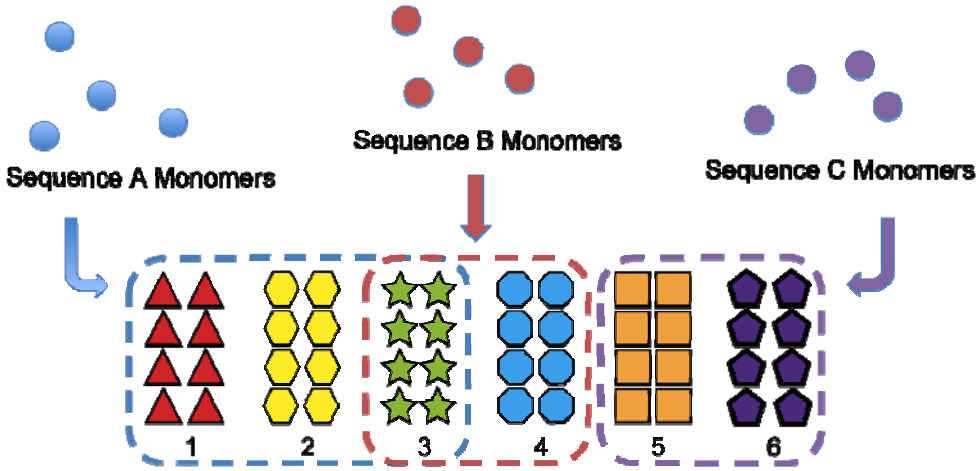

Figure 2-1: Concept of prion strain: a wide range of distinct prion aggregated conformations across prion sequences. Each self-assembled strain numbered 1-6 is made up of unique conformations represented by different colored symbols. Sequence A and B share some common aggregated conformations, while Sequence A/B share no similarities with C resulting in a species barrier.

[1] Results published as Mehta AK, Lu K, Childers WS, Liang Y, Dublin SN, et al. (2008) Facial Symmetry in Protein Self-Assembly. J Am Chem Soc 130: 9829-9835.

Prions also show a wide range of amyloid rich protein-only strains where toxicity is rooted in subtle conformational variations as illustrated in Figure 2-1[6]. It remains to be determined whether structural differences in cross-β structure can account for these strains and how such differences may impact the observed phenotypes.

Progresses towards solving amyloid structures have been slow due to paracrystallinity, insolubility, and most notably, morphological inhomogeniety. The nucleating core of the Aβ peptide of Alzheimer's disease, Aβ(16-22) or KLVFFAE, displays a pH dependent morphology; forming twisted 5 nm diameter fibers at neutral conditions and hollow 52 nm diameter nanotubes under acidic conditions (Figure 2-2). Assembly in 40% acetonitrile not only improved the solubility of the peptide but increased the homogeneity of both the fiber and nanotube soluble assemblies[7]. These radically different morphologies presented an opportunity to define the structural differences that underlie amyloid strain variations.

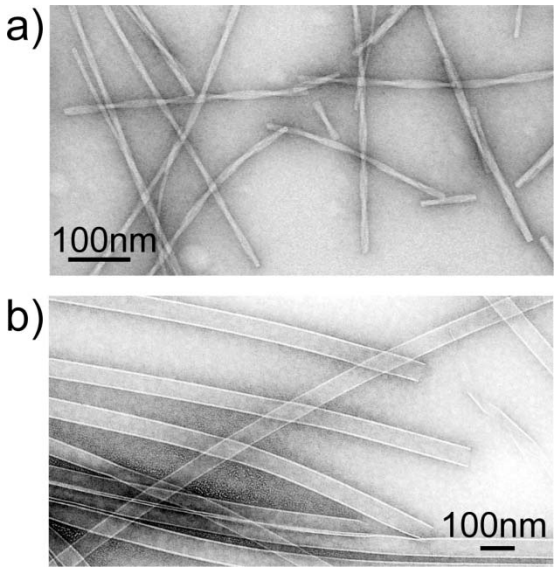

Figure 2-2: Uranyl acetate negatively stained TEM image of pH dependent morphology of KLVFFAE in 40% acetonitrile at (a) neutral conditions and (b) acidic conditions - 0.1% TFA.

The difference between fibers and nanotubes was initially proposed to result from an extended degree of β-sheet lamination[7,8]. The 5nm diameter amyloid fibers are composed of only 5-6 laminated β-sheets, while the 52 nm diameter nanotube required more than 100 laminated β-sheets[7,8]. This chapter will develop atomic-level models for both structures and from these structures propose the driving forces for their formation.

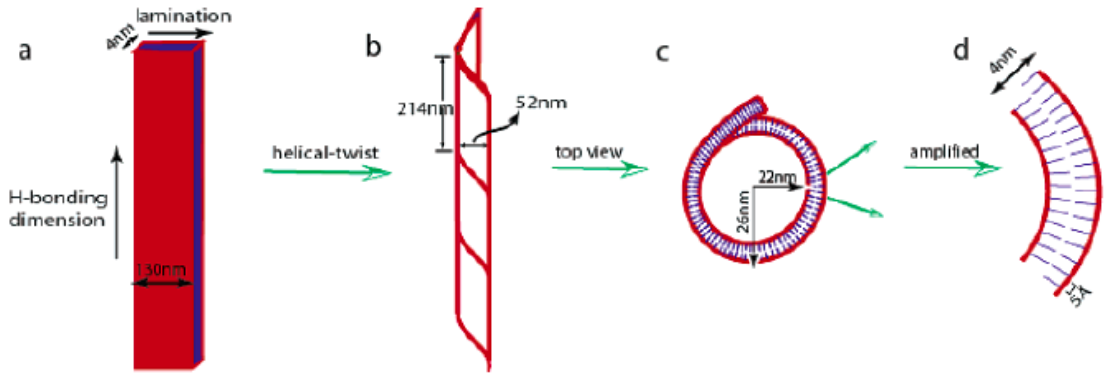

Figure 2-3: Proposed nanotubes bilayer model for the short amyloid peptide KLVFFAE. (a) A flat rectangular bilayer, 130 nm wide x 4 nm thick. (b) The coiled tubular fibril with an outer diameter of 52 nm and an outer helical pitch of 214 nm. (c) Top view of the 44-nm internal cavity. (d) Amplified view of the wall with a thickness of 4 nm and the distance between each parallel β-strand being the backbone H-bond distance of 5 Å.

Methods

FMOC Protection of Isotopically Labeled Amino Acids

Isotopically labeled amino acids were obtained from Cambridge Isotope Laboratories. Prior to use in solid-phase peptide synthesis Isotopically enriched amino acids (Ala, Val, Leu, Phe, Ile, or Gly) were FMOC protected as described previously[9]. Briefly, 2.25 mmol of Isotopically labeled amino acid in 10% (w/v) Na_2CO_3 was added dropwise to a solution of 2.5

mmol Fmoc-O-succinimide in 5 mL of dioxane. The reaction was continuously stirred for 24 hours at room temperature, and reaction completion was monitored by TLC using 10:1 toluene:acetic acid as an eluting solvent (ninhydrin staining was used to monitor amino acid that was not FMOC protected). If reaction was incomplete an additional 0.88 mmol of Fmoc-O-succinimide in 2 mL dioxane was added and allowed to react for an additional 24 hrs at room temperature.

After reaction completion, the reaction mixture was diluted with 30 mL of water and impurities were extracted 3 times with diethyl ether. The water layer containing FMOC labeled amino acids was titrated to pH 2 using HCl, then the FMOC labeled amino acid was extracted 3 times using ethyl acetate. The ethyl acetate washes were collected and washed twice with 1N HCl, then once with distilled water. Anhydrous $MgSO_4$ was added to dry the ethyl acetate layers for 60 minutes. Filtered Ethyl acetate solutions were then rotovaped to remove ethyl acetate and dried in a dessicator overnight[9].

Microwave Assisted Solid-Phase Peptide Synthesis

Peptides were synthesized on a Liberty CEM Microwave Automated Peptide Synthesizer (NC, USA) utilizing a FMOC-Rink Amide MBHA Resin (AnaSpec, CA, USA). All FMOC protected amino acids were purchased from Anaspec, and remaining chemicals from Sigma-Aldrich. Each peptide synthesis was performed at 0.1 mmol using a 30 mL reaction vessel at a scale of 0.1mmol. FMOC-Rink Amide MBHA Resin was initially swollen using ~7 mL dimethylformamide for 15 minutes. FMOC deprotection was achieved by addition of 20% piperdine 0.1M N-Hydroxybenzotriazole (HOBt) in dimethylformamide with microwave power set to maintain temperature between 45-55°C for 180 sec, followed by 3X flushing with dimethylformamide. Each coupling step was performed using 0.1M FMOC protected amino acid, and activated with 0.1 M 2 - (1H - Benzotriazole - 1 - yl) - 1,1,3,3 - tetramethyluronium hexafluorophosphate (HBTU), and 0.2M N,N –Diisopropylethylamine (DIEA) in DMF. Coupling

temperatures were maintained between 75-82°C by optimizing microwave power for 300 sec. After coupling, the resin was rinsed with three aliquots of dimethylformamide. At the end of coupling steps, 20% acetic anhydride in dimethylformamide was added to acetylate the N-terminus of the peptides. The capping reaction was allowed to proceed for 3 hours at room temperature. Resin was filtered and washed with dichloromethane and allowed to air dry. Peptides were cleaved from the resin using trifluoroacetic acid/thioanisole/1,2-ethanedithiol/anisole (90: 5 : 3 : 2, v/v/v/v) at room temperature for 3 hrs. The cleaved peptide-TFA solution was filtered, and precipitated by dropwise addition of cold (-20°C) diethyl ether. Precipitated product was centrifuged at 3000 rpm for 3 min, and the pellet was subjected to 3 additional rounds of washing with cold diethyl ether. Precipitated product was desiccated overnight.

Dried peptides were dissolved in minimal volume of 40% acetonitrile + 0.1% trifluoroacetic acid and purified by RP-HPLC using a C18-reverse phase column with an acetonitrile-water gradient. Samples eluted from HPLC (10μL) were mixed with 2,5-dihydroxybenzoic acid matrix (10 μL), 3x2 μL drops were placed on individual spots of MALDI plate and allow to dry in dessicator, and MALDI subsequently confirmed the molecular weight of each peptide used.

Peptides (1.3 mM) were dissolved in 4:6 CH_3CN/H_2O with 0.1% TFA for nanotube assemblies. Dissolution was assisted by ~2 minutes of continuous vortexing, followed by ~15 minutes of sonication until solution became clear. For fibril assemblies after peptides were dissolved in 4:6 CH_3CN/H_2O, solution was slowly titrated by drop-wise addition of 200 mM NaOH until solution became viscous (pH 6 as measured by pH paper). Peptides were allowed to assemble for approximately 2 weeks at 4 °C until mature as monitored by CD β-sheet signature (Figure 2-8) and homogenous population of hollow tubes visualized by TEM (Figure 2-2).

Solid-State NMR REDOR

To prepare matured samples for solid-state NMR experiments, sodium sulfate was added to each assembly to a final concentration of 9 mM to induce lateral bundling of nanotubes[10]. Previously, sulfate bundling of nanotubes has been shown to protect assemblies from freezing and lyophilization[11].

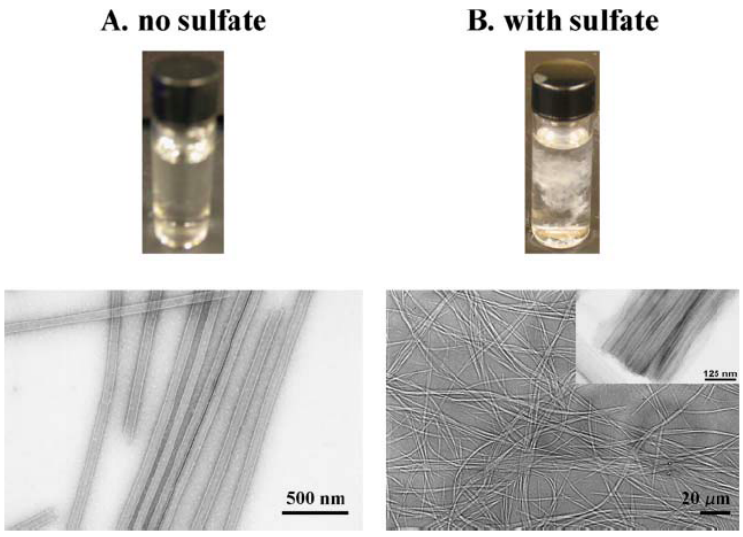

Figure 2-4: Axial alignment of 2.6mM KLVFFAE nanotubes in 40% acetonitrile with 0.1% TFA (A) into lamellar bundles using sodium sulfate (B). Upon addition of sodium sulfate nanotube bundle with an average width of 1 um as indicated in the optical micrograph. TEM inset shows an individual bundle composed of aligned KLVFFAE nanotubes.

Each NMR sample (25-100 mg) was packed into a 4 mm solid-state NMR rotor and centered using boron nitride spacers. NMR spectra were collected with a Bruker (Billerica, MA) Avance 600 spectrometer using a 4mm HCN BioSolids magic-angle spinning (MAS) probe. MAS frequency was actively controlled at 10,000 ± 2 Hz with cooling and spinning air exit temperature maintained below -1 °C to ensure MAS and (radio-frequency) RF heating did not denature the samples. ^{13}C (150.8 MHz) CP-MAS spectra before and after REDOR experiments

confirmed that the samples did not change during the experiment.

The pulse sequence for $^{13}C\{^{15}N\}$ rotational-echo double-resonance (REDOR) consists of two parts, an S sequence, shown in Figure 2-5, and the REDOR S_0 sequence which is identical but does not contain any ^{15}N dephasing pulses. The dipolar Hamiltonian describing the through-space interaction between two heteronuclear spin-½ nuclei has a spin term (I_zS_z) and an orientation dependent term which is proportional to $3\cos^2\theta-1$, where θ is the angle between the I-S dipolar vector and the applied external magnetic field (B_0), and is inversely proportional to r^3 (distance between the spins cubed). When the sample is rotated at the magic-angle with respect to B_0, the dipolar Hamiltonian becomes time dependent and the orientation dependent term is averaged to zero (i.e. the integral over all-space of $3\cos^2\theta-1$ is zero) removing the effects of I-S dipolar coupling. Applying pulses to the dephasing ^{15}N spins interferes with the averaging due to spinning and reintroduces the dipolar coupling which is observed in the REDOR S spectrum, where the signal decays according to T_2 (spin-spin relaxation) and the heteronuclear dipolar coupling. Maximum dephasing occurs when the spacing between π pulses is equal to ½ of the rotor cycle. The sequence without and ^{15}N dephasing π pulses gives the REDOR S_0 spectra, where the magnetization decays according to only T_2. The difference between the REDOR S and S_0 signal (ΔS) is directly proportional to the dipolar coupling, hence the distance between the two spins.

Either xy8 $^{13}C\{^{15}N\}$-REDOR pulse sequence with the dephasing ^{15}N pulses centered at Tr/2 and refocusing pulses centered at Tr or single-pulse $^{13}C\{^{15}N\}$-REDOR pulse sequence[12] with EXORCYCLE phase cycling[13] of the single-observe 4 μs ^{13}C (150.8 MHz) π pulse was used to minimize re-introduction of ^{13}C-^{13}C homonuclear dipolar coupling[14]. To compensate for pulse imperfections 8 μs ^{15}N REDOR rotor synchronized dephasing π pulses were *xy*8 phase cycled[15]. The initial ^{1}H 90° pulse was 1.9 μs, ^{1}H CP RF fields were ramped from 50 to 70 kHz and the ^{13}C CP RF field was kept constant at 50kHz. 128 kHz Spinal64[16] ^{1}H (600.3 MHz)

decoupling was applied during REDOR evolution and acquisition. SPINAL64 pulse widths and ^{1}H decoupling resonance frequency were optimized by comparing the peak heights of the CH and CH_2 resonances of fumaric acid monoethyl ester.

Prior to running all REDOR samples the following parameters were optimized to maximize signal-to-noise: ^{1}H, ^{13}C, ^{15}N and/or ^{19}F RF fields, ^{1}H-^{13}C cross-polarization contact time and recycle delay time – which was set to 5 times the ^{1}H T_1. The ^{1}H RF fields were measured by optimizing the first pulse of the standard ^{13}C CP-ECHO sequence. According to Anil, RF homogeneity will affect the effective pulse width when a train of pulses is applied. Therefore, to determine proper pulse width for ^{13}C 180° pulses the power level was arrayed in REDOR S_0 pulse sequence at long REDOR evolution times (>50 ms typically corresponding to ~500 ^{13}C π pulses) and choosing the pulse width that corresponded to the maximum signal intensity. Similarly, ^{15}N 180° pulses were determined by arraying the ^{15}N power level using the REDOR S experiment at REDOR evolution times corresponding to a $\Delta S/S_0$ between 0.3 and 0.5.

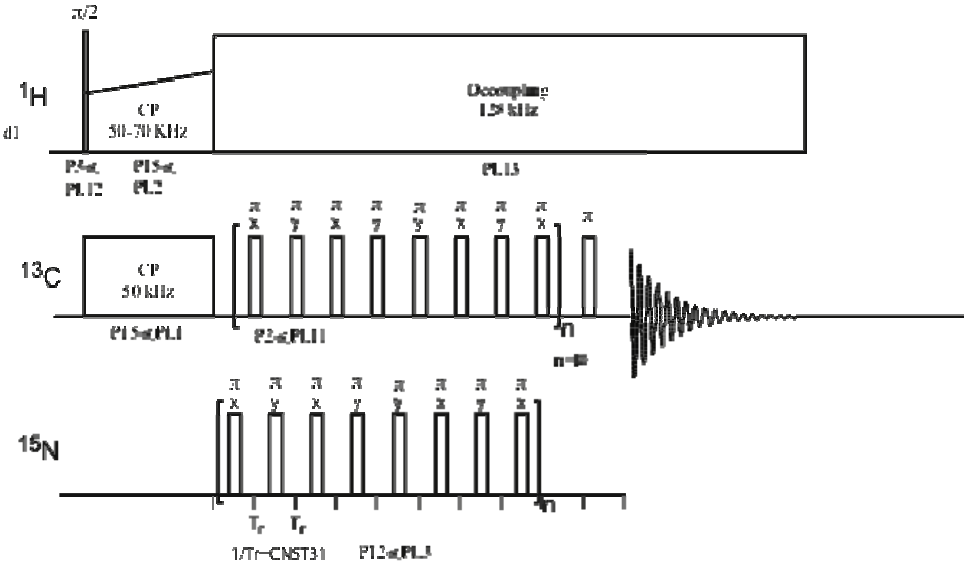

Figure 2-5: $^{13}C\{^{15}N\}$ REDOR pulse sequence for the S experiment. Bruker power levels (PLX) and pulse widths (PX) are given for each pulse.

REDOR data points are the integrated sum of center- and sideband peaks. Error bars were calculated using the noise of each spectrum as the maximum peak height deviation. To normalize for the decay due to T_2, individual REDOR curves are plotted as $\Delta S/S_0$. The steeper the slope of the REDOR dephasing curves the shorter the distance (hence stronger the dipolar coupling) between the two spins. The functional form of the REDOR curves for an isolated heteronuclear spin-pair are identical and can be overlaid on top of each other by simply scaling the x-axis, which makes fitting the REDOR data straight forward. As an example simulated REDOR curves in Figure 2-6 of a 2.5Å (black line) ^{13}C-^{15}N distance displays a steeper slope than a 3.5Å distance (red line).

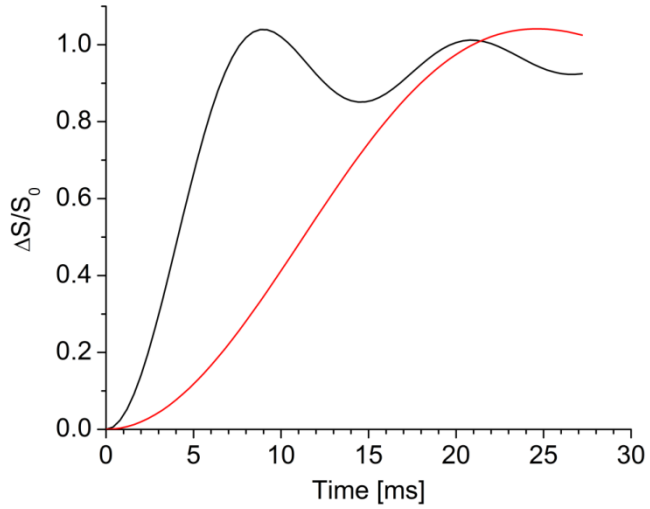

Figure 2-6: Ideal $^{13}C\{^{15}N\}$ REDOR curves for a ^{13}C -^{15}N distance of 2.5Å (black line) and 3.5Å (red line).

By plotting REDOR as $\Delta S/S_0$, the plateau (max dephasing) is directly related to the number of spins that are coupled. If only half of the observe spins (in this case ^{13}C) are coupled to a

dephasing spin (in this case ^{15}N), the REDOR curve will only go to ½ the value observed when all the spins are coupled as illustrated in Figure 2-7.

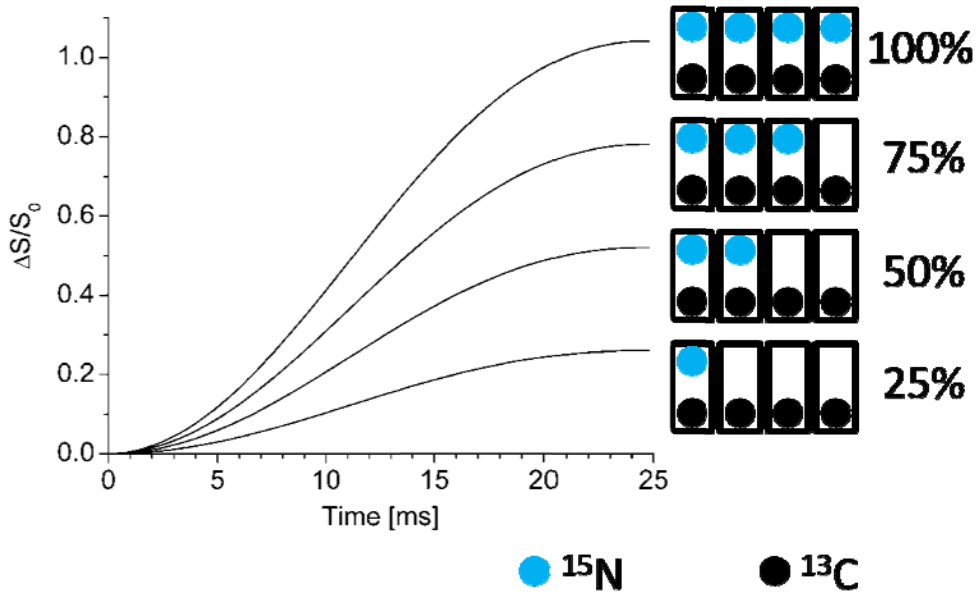

Figure 2-7: Ideal $^{13}C\{^{15}N\}$REDOR curves that vary the percent of ^{13}C near an ^{15}N from 25% to 100%.

A ^{13}C-CP-Echo spectrum was run before and after each REDOR collection to ensure that the sample had not degraded. The ideal scaling factor was determined on $^{13}C\{^{15}N\}$REDOR spectra of [1-^{13}C,^{15}N]alanine diluted 10:1 with natural abundance alanine. To test that spectrometer performance had not degraded over the course the experiment, a $^{13}C\{^{15}N\}$REDOR curve was run before and after ever unknown. If the scaling factor changed by more than 1%, or ^{13}C T_2 decreased by more than 17%, this indicated an issue with either probe or spectrometer performance and the data on the unknown was thrown out.

Circular Dichroism

Samples (15-70 µl) were placed into a quartz cuvette with a 0.1 mm path length (Starna Cells). Each spectra was obtained by scanning wavelength from 300 nm to 185 nm at a scanning rate of 100 nm/min with a resolution of 0.2 nm using Jasco J-810

spectropolarimeter. For each CD run temperature was controlled at 22°C, unless otherwise stated. Prior to recording the presented final wavelength scan CD at 215 nm was recorded for approximately 15-minute period to ensure sample had stabilized at the CD measurement conditions. Three successive wavelength scans were averaged for each sample. Buffer control spectra were averaged and subtracted from the sample spectra. The ellipticity ($[\theta]_{obs}$ mdeg) was converted to mean residue ellipticity ([θ], deg·cm^2·dmol^{-1}) with the equation $[\theta]=[\theta]_{obs}/(10\times n\times C\times l)$, in which, n is the number of peptide bonds, C is the concentration (mol/L) and l is the path length of the cell (cm).

FT-IR Spectroscopy

IR spectra were collected on a Nicolet MAGNA-IR 560 Spectrometer E. S. P. instrument operated at 2 cm^{-1} resolution and 100 scans were averaged to obtain a spectrum. Pellets of peptide nanotube solutions were lyophilized and mixed with KBr. For each sample, KBr was subtracted from the sample measurement.

Electron Diffraction

Samples for diffraction were prepared by placing mature amyloid assemblies on a TEM grid with a peptide concentration of 0.2-2 mM. Each sample was allowed to incubate on the grid for 1 minute, then wicked away with filter paper at one location to preferentially orient assemblies. The organization of amyloid assemblies is variable within each grid. Survey of the entire grid was required to obtain suitable diffraction patterns. Diffraction patterns were recorded using a Philips 410 EM transmission electron microscope in diffraction mode at a camera length setting of 1 m. *d*-spacing was calculated with $d = \lambda L/R$, where R is the distance (mm) from the central bright spot to the arc of interest, L is the camera length (distance in mm between specimen and photographic film), and λ is the electron wavelength (80 kV = 4.2 pm). Camera length was calibrated using an aluminum polycrystalline standard (Electron Microscopy Sciences, Hartfield,

PA) for short distances. Extrapolation of this calibration to longer distances (>4Å) was compared with KLVFFAE nanotube and fiber x-ray powder diffraction data.

Molecular Dynamics

Initial peptide registry for MD simulations were set based on $^{13}C\{^{15}N\}$ REDOR data for both the tubes and the fibers. A total of five sheets, each consisting of five peptides, were stacked on top of each other in various conformations. Unrestrained MD was carried out with the GROMACS 3.2 software package[17,18] at 300 K and 1 bar in an octahedral box of SPC water[19] with periodic boundary conditions using the all-atom OPLS-AA force field[20]. Bond distances were constrained with the LINCS algorithm[21], and an integration time step of 2 fs was employed. Electrostatic interactions were calculated with a 1.2 Å Ewald particle mesh algorithm[22] grid spacing, a spline interpolation of 1.2 Å, and a 9 Å cutoff. Solute and solvent were separately coupled[23] to a thermostat and barostat with time constants of 0.1 and 0.5 ps, respectively. Final models were generated by 50 steps of steepest-descent *in vacuo* energy minimization of the average over the 800 ps MD evolution.

Results

Secondary Structure Analysis

To investigate the conformational differences between amyloid peptide building blocks that construct fibers at neutral conditions and hollow nanotubes at acidic conditions, circular dichroism (CD) and Fourier transform infrared spectroscopes (FT-IR) were used to compare secondary structure. CD of the 1.3 mM KLVFFAE fiber solution displayed a minimum at 198 nm and a shoulder at 212 nm (Figure 2-8a – black line), indicating a potential mixture of random coil and β-sheet conformations.

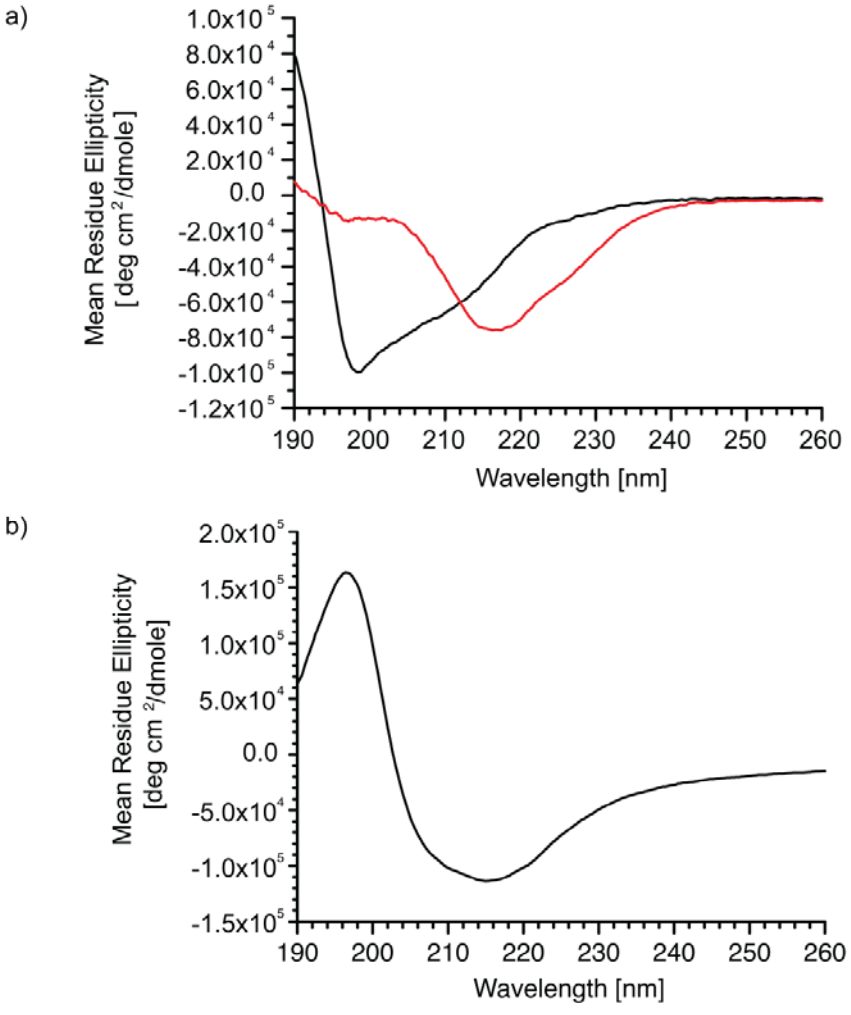

Figure 2-8: CD spectra of 1.3 mM CH_3CO-KLVFFAE-NH_2 assemblies in 40% acetonitrile at (a) neutral fiber forming conditions, and (b) acidic nanotube forming conditions. The CD for fiber assemblies (a) before (black) and after (red) centrifuging the solution. The observed difference can be assigned to removal of unassembled random coil peptide.

To better understand the weak signature in the fiber assembly, the sample was pelleted at 13,600 rpm collected and resuspended in 40% acetonitrile. CD analysis of this pellet displayed a strong negative Cotton effect at 218 nm (Figure 2-2a – red line) consistent with β-sheet secondary structure. CD spectra of the nanotube solution displayed a much clearer minimum at 215 nm without enrichment by centrifugation.

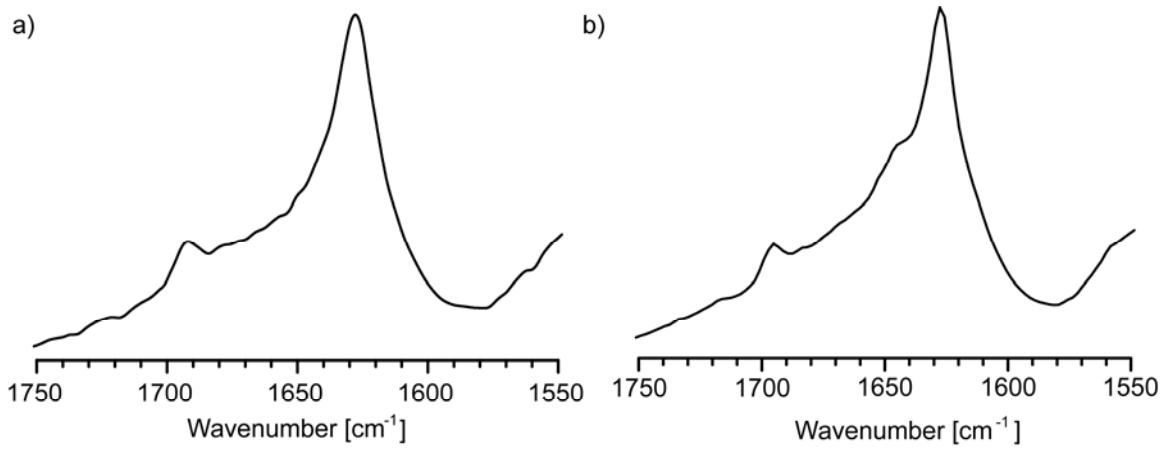

Figure 2-9: FT-IR spectra of 1.3 mM CH_3CO-KLVFFAE-NH_2 assemblies in 40% acetonitrile at (a) neutral (fibers) and (b) acidic conditions (nanotubes).

FT-IR amide I stretch vibrations of both fiber and nanotubes assemblies have a maximum absorption at 1628 cm^{-1}, a frequency commonly associated with β-sheet secondary structure[24]. The peptide nanotubes also have a weak shoulder at 1648 cm^{-1}, consistent with disordered or random-coil peptide conformation[24]. Intriguingly, both fiber and nanotube assemblies also contain a shoulder at 1695 cm^{-1} which has been correlated with anti-parallel β-sheet structure[25]. This evidence was inconsistent with the previously proposed parallel β-sheet bilayer model[7] and instead suggests both fiber and nanotube assemblies are composed of anti-parallel arranged peptides within β-sheets.

β-sheet Registry Determination by Solid-State NMR

Solid-state NMR techniques that exploit distance dependent dipolar couplings to measure intermolecular distances have been used to distinguish β-sheet registries[26,27,28]. Of these, Dipolar Recoupling with a Windowless Sequence (DRAWS)[27,29] measures homonuclear dipolar coupling and rotational-echo double-resonance (REDOR)[30,31] measures heteronuclear dipolar coupling.

The peptide was prepared via solid-phase peptide synthesis, purified via reverse-phase HPLC, and allowed to assemble at 1.3 mM peptide concentration in 40% acetonitrile for 1 week. Prior to NMR structural studies, each sample was analyzed for β-sheet secondary structure by CD and morphology by TEM. Nanotube assemblies were protected from freezing and lyophilization by bundling upon addition of sodium sulfate to a final concentration of 9 mM. Indeed the chemical shift of the ^{13}C enriched carbons was shifted upfield of the random-coil (175 ppm)[32] and consistent with the amide CO being in a β-sheet conformation (Figure 2-10)[32]. Each carbonyl resonance displays a different bredth, and KLVFFAE fibers display 2 distinct ^{13}C leucine -17 carbonyl chemical shifts. The CO chemical shift appears to be sensitive to hydration and this may cause the two distinct chemical shifts, however further experiments and

computations are needed to understand the chemical shift. Nevertheless, each ^{13}CO chemical shift is consistent with β-sheet secondary structure[32].

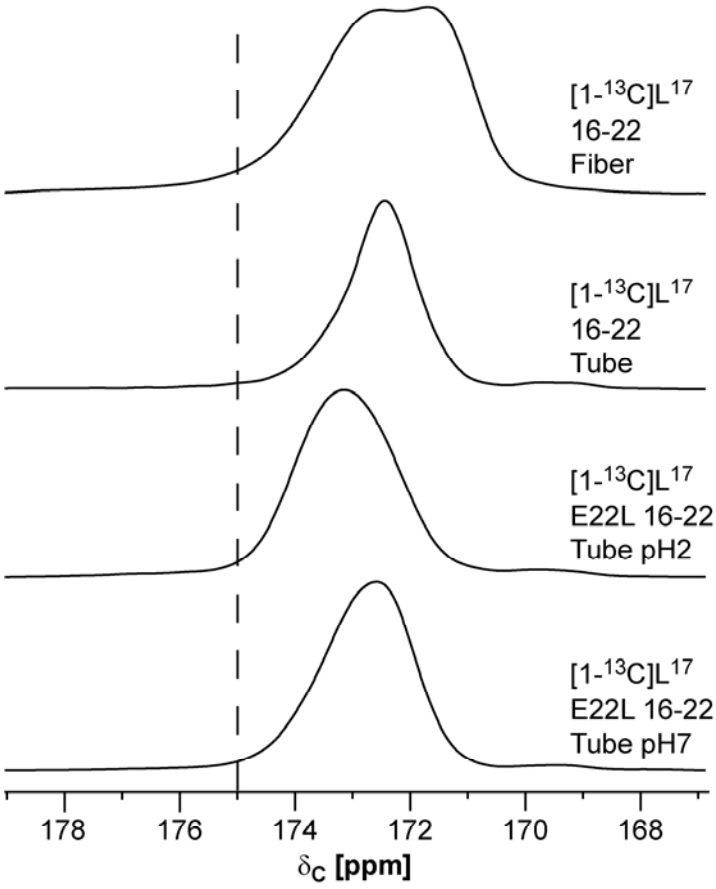

Figure 2-10: ^{13}C chemical shift of [1-^{13}C]L17 Aβ(16-22) peptides assembled as fibers or nanotubes consistent with peptides in a β-sheet conformation. The dashed line indicates the leucine carbonyl chemical shift for random coil. α-Helix carbonyls have chemical shifts downfield of random coil and β-sheet carbonyls are up-field of random coil.

Given that FT-IR spectra suggested that nanotube assemblies were arranged as anti-parallel β-sheets, an isotope labeling scheme was designed that incorporated a ^{13}C into a carbonyl that should be directly hydrogen bonded to an ^{15}N labeled backbone amide if the KLVFFAE peptides formed anti-parallel β-sheets[33]. Specifically, ^{13}C isotopes were incorporated into the

carbonyl of L17 and ^{15}N isotopes were incorporated into A21's backbone amide (Figure 2-11). This labeling strategy distinguishes between different β-sheet registries, as shown by simulated fits in Figure 2-11e. At the same time, if the peptide adopts a parallel registry, then the ^{13}C L17 intermolecular distance should be 4.7 Å.

$^{13}C\{^{15}N\}$REDOR dephasing for CH_3CO-K[1-^{13}C]LVFF[^{15}N]AE-NH_2 fiber assemblies (hollow circle - Figure 2-11) fit to an anti-parallel peptide arrangement, consistent with previous assemblies in phosphate buffered water[34]. In contrast, REDOR dephasing data points for CH_3CO-K[1-^{13}C]LVFF[^{15}N]AE-NH_2 nanotube assemblies are consistent with a longer distance. To obtain a longer ^{13}C-^{15}N distance peptides were shifted out of registry by one residue in the N-terminus and C-terminus directions. Indeed, anti-parallel arrangements (2) that are out-of-register (Figure 2-11b or d) fit the observed REDOR dephasing for nanotube assemblies.

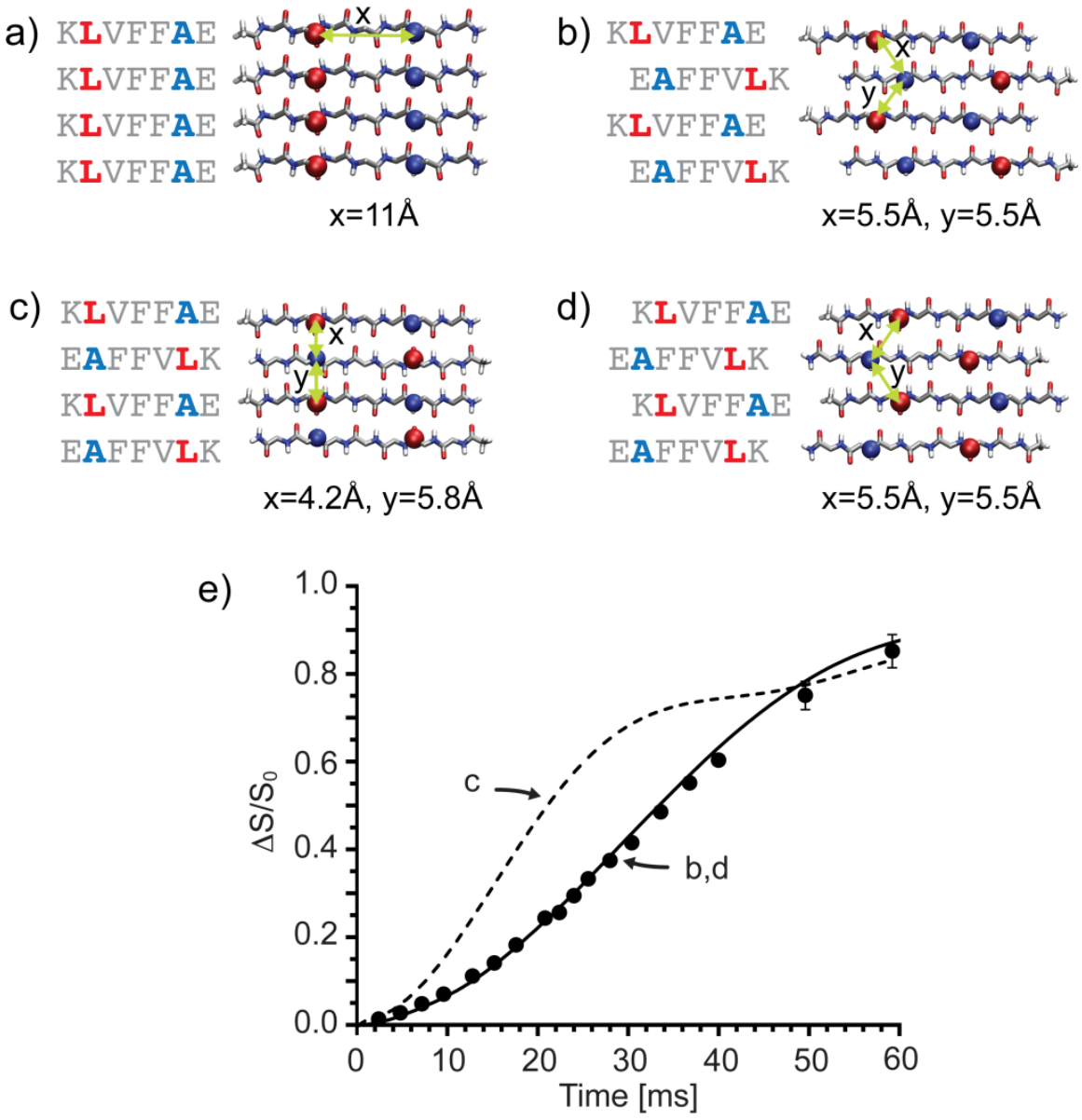

Figure 2-11: Design of CH_3CO-K[1-^{13}C]LVFF[^{15}N]AE-NH_2 isotope labeling scheme to distinguish different β-sheet registries (a,b,c,d) of KLVFFAE nanotubes assembled in 40% acetonitrile 0.1% TFA. ^{13}C{^{15}N}REDOR dephasing (e) with simulated fits for anti-parallel (b) (dashed line) and anti-parallel out-of-register organization (c and d) (solid line). Simulated REDOR curves for the longer intramolecular [1-^{13}C] to [^{15}N] parallel registry is too long (11Å) to exhibit any significant dephasing over 60 ms. (a,b,c,d) Isotope labels are represented as red spheres (^{13}C) and blue spheres (^{15}N).

Using a strategy similar to the L17-A21 isotope labeling scheme, ^{13}C incorporated into V18 CO and ^{15}N into A21 to test if the residues are directly hydrogen bonded as in anti-parallel in-register β-sheets (Figure 2-12b). Again the $^{13}C\{^{15}N\}$REDOR dephasing is consistent with out-of-register β-sheets either with K16 not hydrogen bonded to the remainder of the peptide (Figure 2-12c), or the C-terminal E22 not hydrogen bonded (Figure 2-12d).

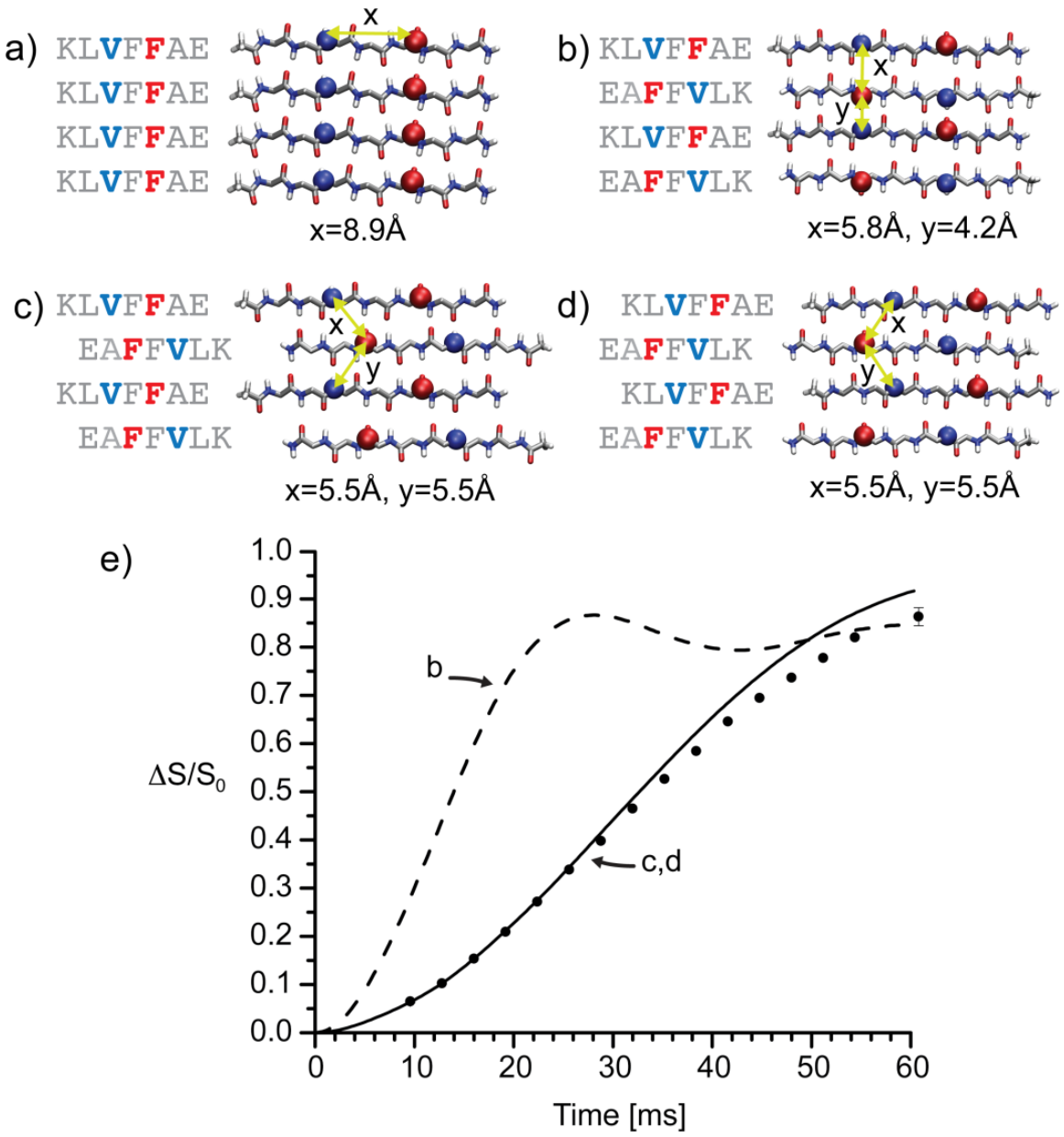

Figure 2-12: Design of KL[1-^{13}C]VF[^{15}N]FAE labeling scheme to distinguish between different β-sheet registries (a,b,c,d) of KLVFFAE nanotubes assembled in 40% acetonitrile 0.1% TFA. ^{13}C{^{15}N} REDOR dephasing with simulated fits for anti-parallel registry as a dashed line (b) and anti-parallel out-of-register organization as solid black line (c and d). Simulated REDOR curves for longer parallel registry [1-^{13}C] to [^{15}N] distance is too long (9Å) to exhibit any significant dephasing over 60 ms. Isotope labels are represented as red spheres (^{13}C) and blue spheres (^{15}N).

To distinguish between the N-terminal out-of-register and C-terminal out-of-register β-sheet configurations, the V18 backbone carbonyl was enriched with ^{13}C and ^{15}N was incorporated as A21's backbone amine. If the K16 residue is out-of-register, V18 and A21 will be hydrogen bonded, while if E22 is out-of-register the ^{13}C -^{15}N distance will be ~8.2Å (Figure 2-13) and the resulting ^{13}C-^{15}N dipolar couplings would be too weak to be observed by ^{13}C{^{15}N}REDOR. This REDOR experiment found dephasing data points fit nicely to H-bonded V18 and A21 residues, establishing an out-of-register β-sheet registry (Figure 2-13a) inconsistent with other β-sheet registries. The previous three REDOR experiments reveal a critical difference in the organization of KLVFFAE fibers as in-register β-sheets and KLVFFAE nanotubes as out-of-register β sheets[33].

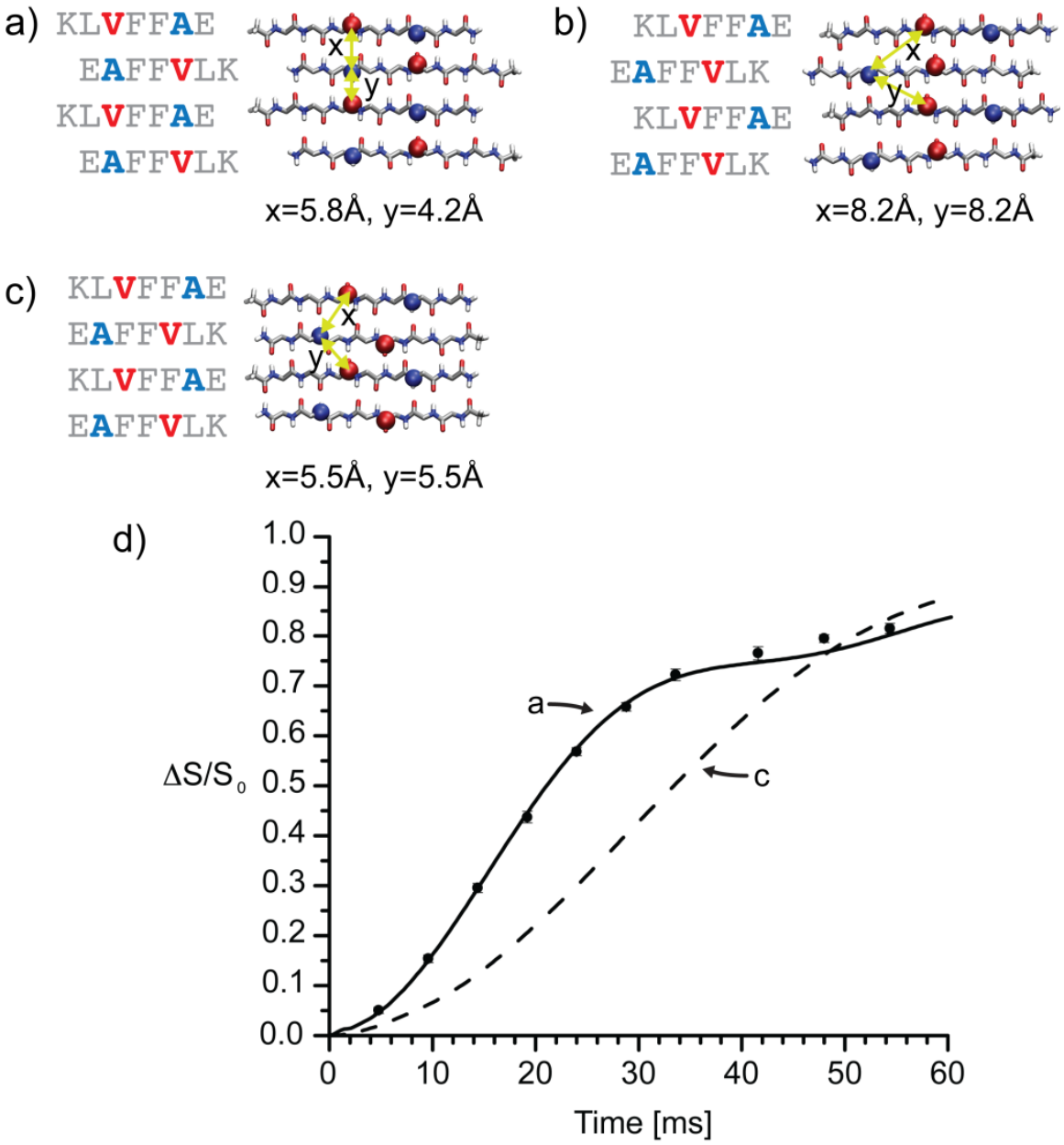

Figure 2-13: Design of KL[1-^{13}C]VFF[^{15}N]AE isotope labeling scheme to distinguish between different anti-parallel β-sheet registries (a,b,c) of KLVFFAE nanotubes in 40% acetonitrile 0.1% TFA. ^{13}C{^{15}N}REDOR dephasing with simulated fits for anti-parallel registry (b) as a solid line and theoretical curves for anti-parallel out-of-register organization (a and b) as dashed black line. Simulated fit for longer anti-parallel C-terminal out-of-registry [1-^{13}C] to [^{15}N] distance is too

long (8.2Å) to exhibit any significant dephasing over 60 ms. Isotope labels are represented as red spheres (^{13}C) and blue spheres (^{15}N).

Solid-State NMR Distance Measurements to Probe the Extended Peptide Backbone

Previous isotope edited IR data[33] for KLVFFAE nanotubes was consistent with both the anti-parallel out-of register β-sheets as well as a β-turn between residues F19 and A21. To test if the β-sheets are fully extended, labeling strategies with a ^{13}C backbone carbonyl in residue *i* and a ^{15}N amide nitrogen on the *i+2* residue can distinguish between extended β-sheet (4.5Å distance), α-helix (3.3Å distance) and β-turn (3.8Å distance) as shown in Figure 2-14.

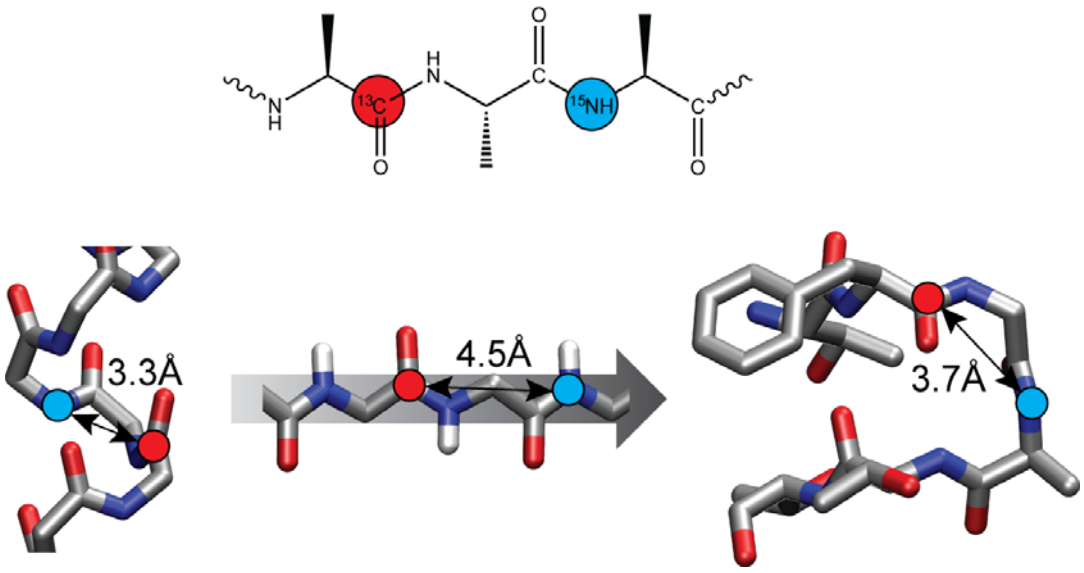

Figure 2-14: Typical distances between the CO carbon of the ith residue to the NH nitrogen of the i+2 residue in a helix, β-sheet and type II β-turn.

The isotope labeled peptide was allowed to assemble under acidic conditions in 40% acetonitrile for two weeks. CD and TEM analysis confirmed assemblies matured into nanotubes. Sodium sulfate was added to a final concentration of 9mM to bundle nanotubes[10], then sample was pelleted at 3000 rpm for 20 minutes at 4°C, frozen with liquid nitrogen and lyophilized. $^{13}C\{^{15}N\}$REDOR measurements on KLV[1-^{13}C]FF[^{15}N]AE-NH_2 (Figure 2-15) indicate ^{13}C-^{15}N distances of 4.4 Å further supporting an extended β-sheet conformation. Specifically, BS-REDOR analysis indicates a 4.4±0.2Å distance and a fractional contribution at 2.5±0.2Å due to dephasing of natural abundance ^{13}C and ^{15}N. As a comparison the dashed line in Figure 2 displays the expected dephasing curve for a type II β-turn.

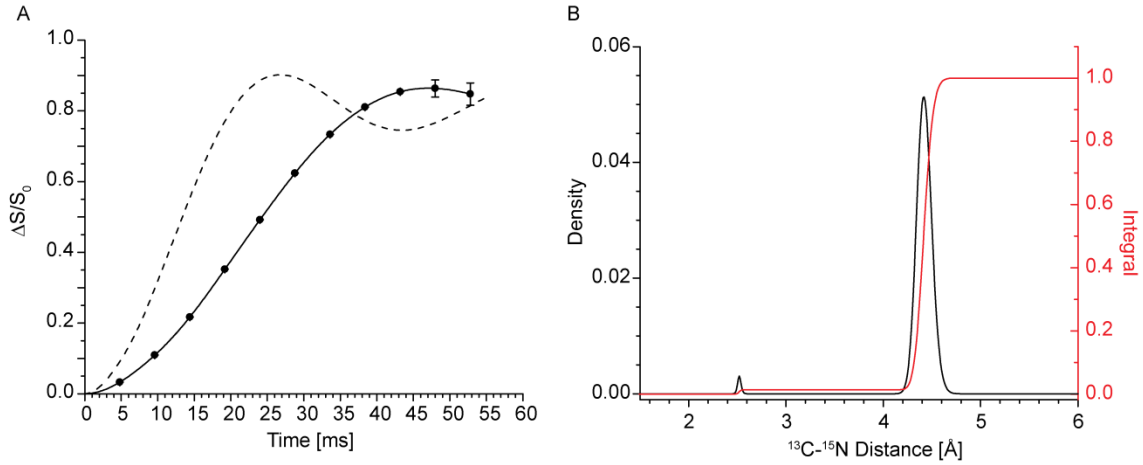

Figure 2-15: $^{13}C\{^{15}N\}$ REDOR dephasing of CH_3CO-KLV[1-^{13}C]FF[^{15}N]AE-NH_2 and (b) BS-REDOR analysis of distance distribution, indicating that KLVFFAE β-sheet peptides are linear.

Shown in Figure 2-16 are the structural models for β-sheet registry based upon the NMR constraints. The key difference is under neutral conditions the peptide forms in-register anti-parallel β-sheets, while under acidic conditions the peptide forms out-of-register β-sheets. To

construct a three-dimensional structural model, the arrangement of the β-sheet face lamination must be considered.

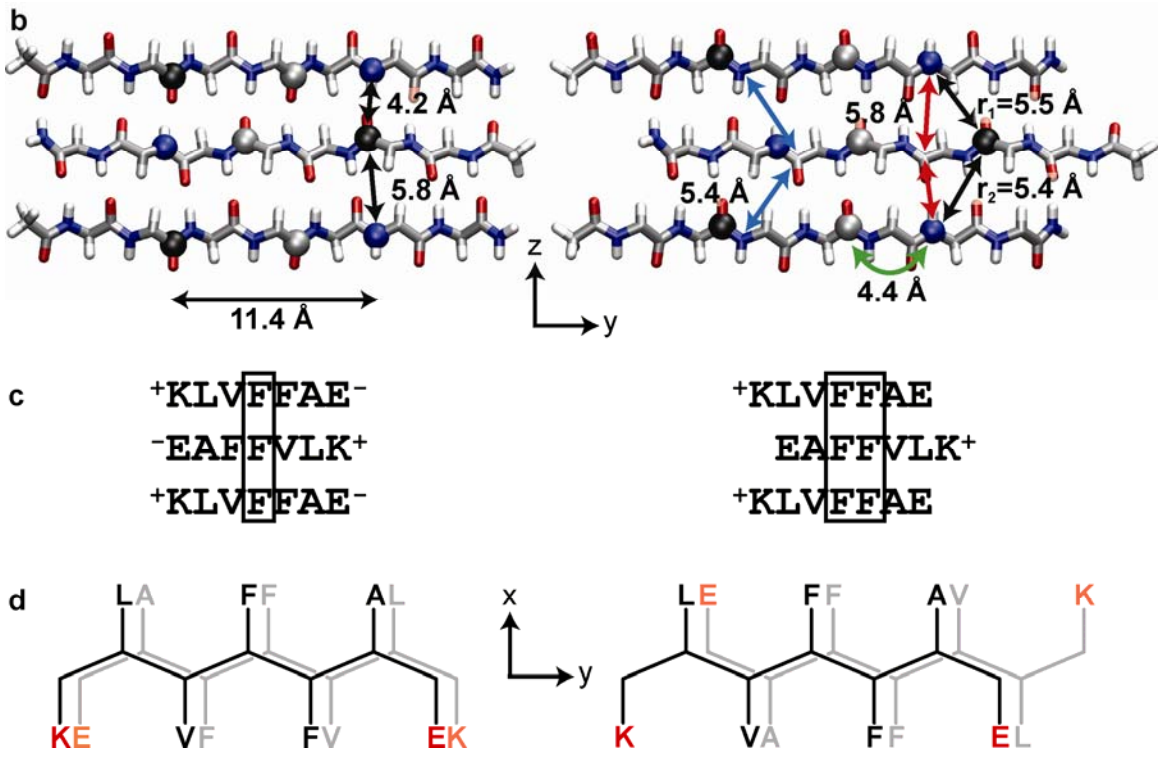

Figure 2-16: Structural models of (*Left*) KLVFFAE fibers (neutral pH) and (*Right*) nanotubes (acidic pH) based off NMR constraints. Backbone hydrogen bonding is oriented along the z axis, β-sheet lamination is along the x-axis, and β-strand axis runs parallel to the y-axis. Black spheres are L17 ^{13}CO, gray spheres are F19 ^{13}CO carbons, and blue spheres are A21 nitrogens. Also shown for tubes is [1-^{13}C]F19-[^{15}N]A21 intramolecular distance of 4.4±0.1Å. (d) A schematic diagram showing β-sheet side-chain surface asymmetry for fibers (left) and symmetry for nanotubes (right). The front peptide is colored black, non-polar residues are colored black/gray and polar residues colored red.

Probes of β-sheet Lamination

The classic cross- β pattern of amyloid is apparent in the x-ray diffraction of both KLVFFAE fibers and nanotubes (Figure 2-17). Both fibers and nanotubes contained a d-spacing corresponding to hydrogen bonded β-sheets (4.7±0.2Å) and d-spacing corresponding to the peptide repeats between laminated β-sheets was 9.9±0.5Å and 9.9±1.0Å for nanotubes and fibers, respectively (Figure 2-17). The apparent differences in line-width of the laminate d-spacings could be attributed to heterogeneity or to a shorter crystallite axis in the lamination direction[35].

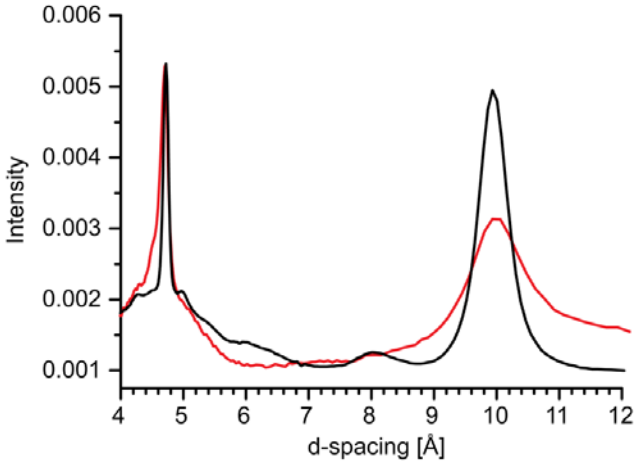

Figure 2-17: X-ray powder diffraction (XRD) patterns of Aβ(16-22) fibers (red) and nanotube (black) lyophilized powders.

These X-ray powder diffraction data can be used as a constraint to evaluate different laminate packing modes. KLVFFAE anti-parallel β-sheets have the potential to stack on top of one another in a variety of different ways (Figure 2-18). In devising these four models, two parameters were varied: (1) how the β-sheet faces interact (top or bottom) and (2) laminating with

termini in the same or opposite directions (parallel or anti-parallel). To evaluate these models, unconstrained MD simulations on solvated models of five laminated β-sheets composed of five hydrogen-bonded peptides were constructed for each orientation (Figure 2-18).

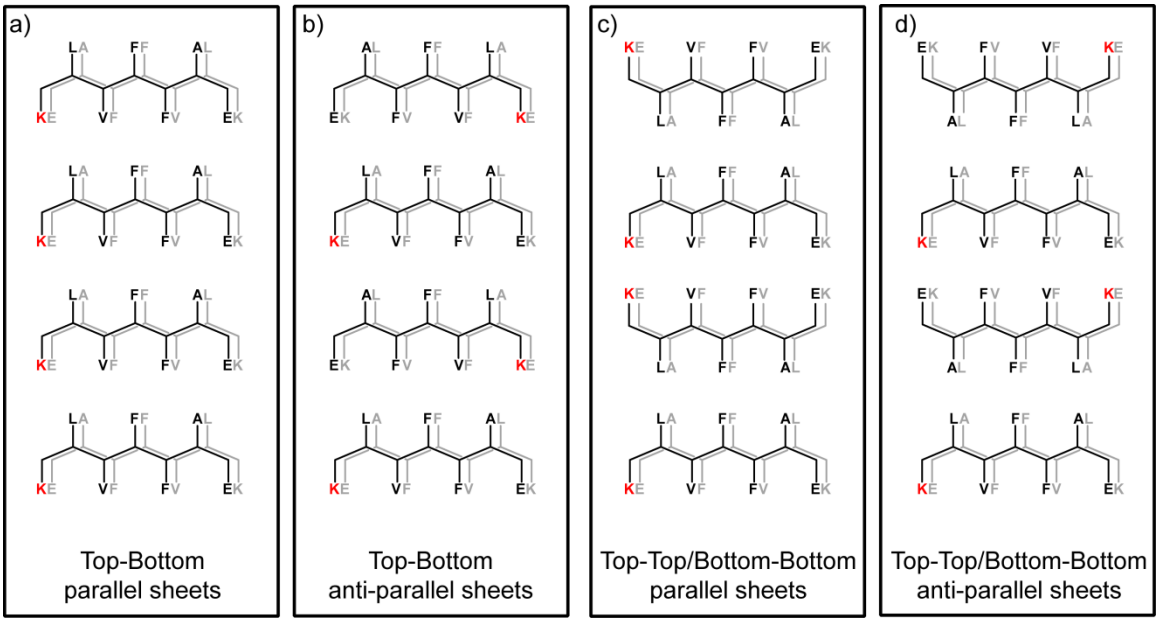

Figure 2-18: Starting orientations used in Aβ(16-22) fiber MD simulations. Each diagram shows 2 anti-parallel sheets laminated in different configurations. In (**a)** and **(c)** the peptides in adjacent β-sheets are parallel. In **(B)** and **(D)** the peptides in adjacent sheets are anti-parallel. Flipping one β-sheet over as shown in **(C)** and **(D)** creates both top-top stacking and bottom-bottom stacking. Only MD simulations starting with the orientation in **(A)** result in β-sheet distances consistent with the X-ray powder diffraction data shown in Figure 2-17.

Except to define the H-bonded β-sheet peptide registry, no additional experimental NMR or X-ray restraints were used during the MD simulations. Short (~1 ns), unrestrained MD with the OPLS-AA (all atom) force-field at 300 K in an octahedral box of ~9000 SPC water molecules was used to explore the energy landscape for local minima. Only peptides from the central 3 X 3 core were analyzed to minimize artifacts arising from edge effects.

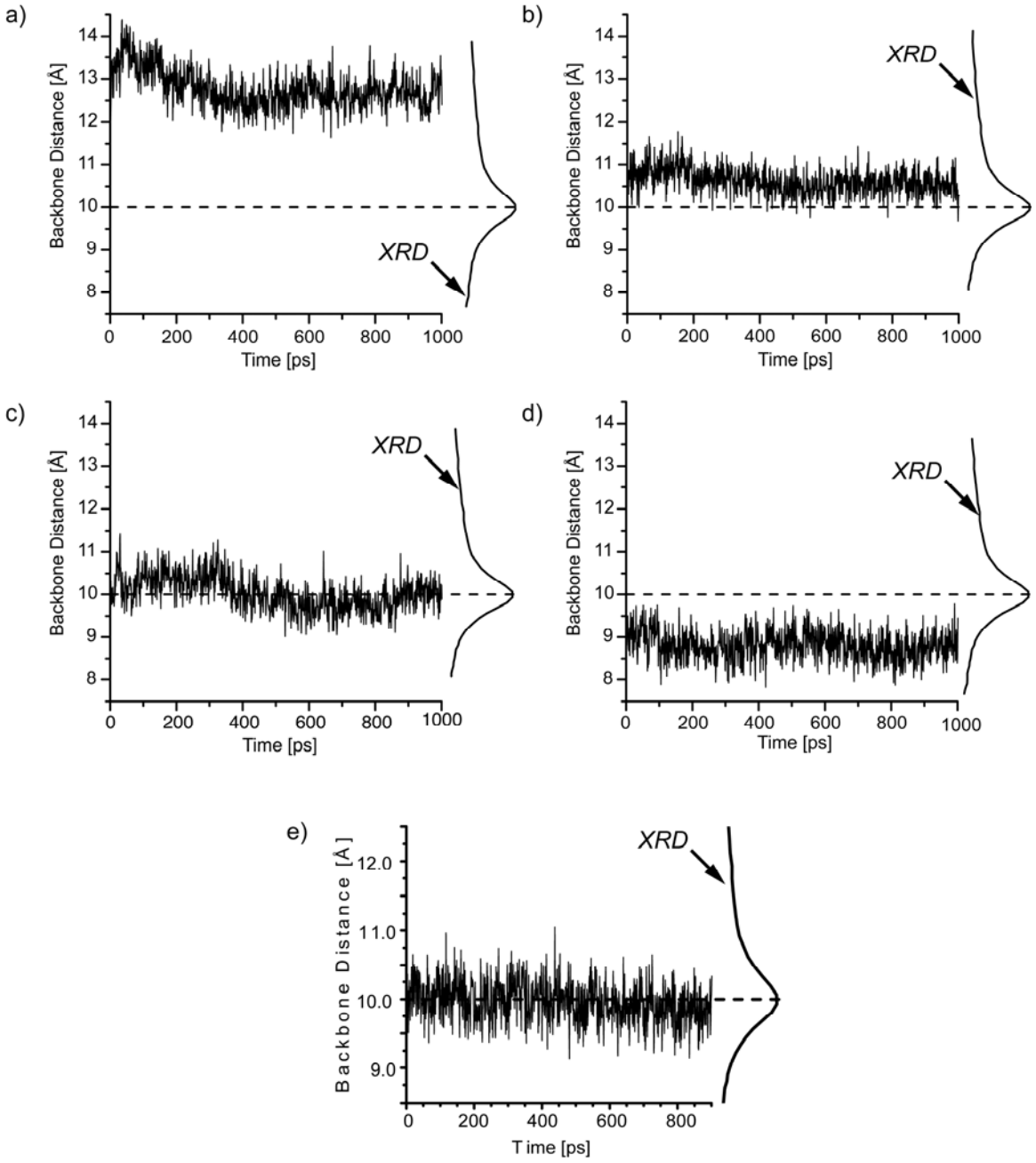

Figure 2-19: Molecular Dynamics results for Aβ(16-22) in-register anti-parallel β-sheet fibers for (a) top-top parallel sheets, (b) bottom-bottom parallel sheets, (c) top-top anti-parallel sheets, (d) bottom-bottom anti-parallel sheets, and (e) top-bottom anti-parallel sheets.

A single fiber model was identified from various MD conformational trajectories consistent with the diffraction β-sheet lamination distance of 9.9 Å (Figure 2-19). The peptides in adjacent sheets are parallel, resulting in the polar and nonpolar β-sheet faces interacting with each other (Figure 2-16). As shown in Figure 2-20, the MD model reveals that charge stabilization exists between residues K and E along each individual fiber β-sheet face. This model suggests that the 50 Å diameter fiber in has a amphiphilic and nonpolar face, which may lead to the formation of the twisted fiber dimmers shown in TEM micrographs (Figure 2-2).

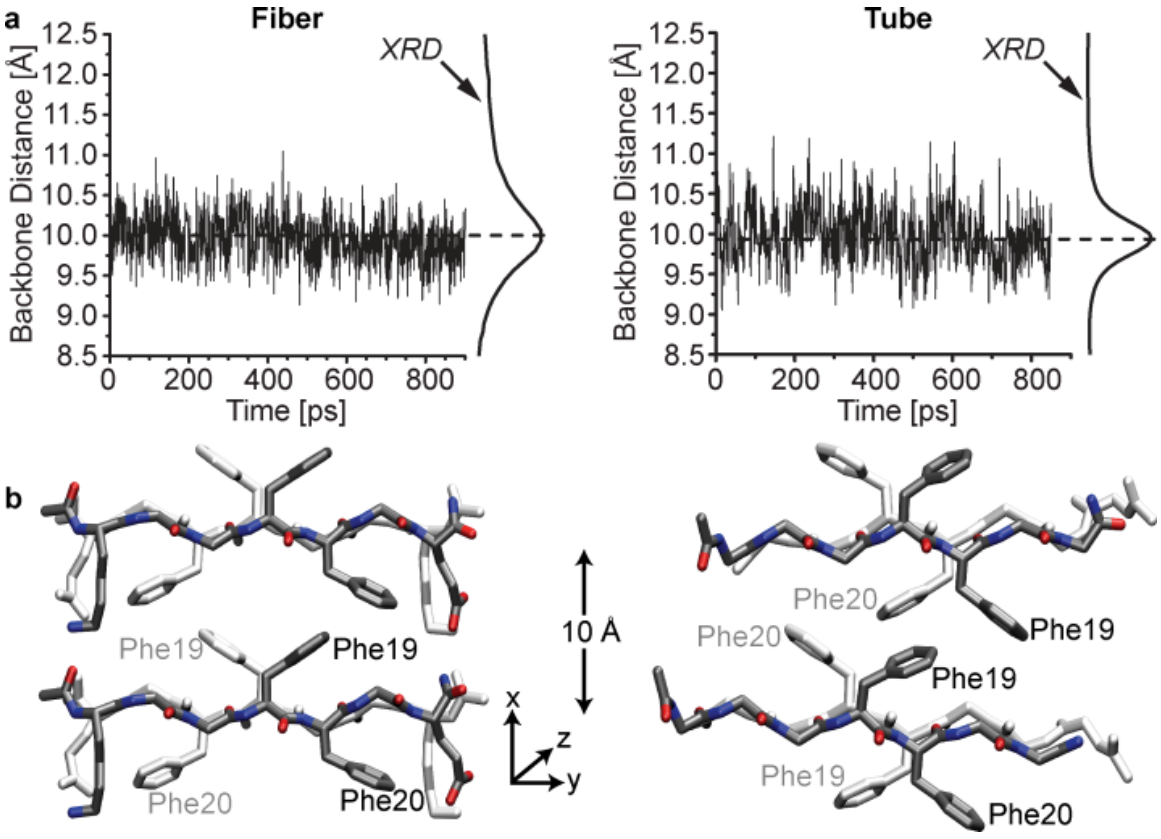

Figure 2-20: Molecular Dynamics results of KLVFFAE for in-register anti-parallel β-sheet fibers (Left) and out-of-register anti-parallel β-sheet nanotubes (right). (a) MD sheet-sheet distances compared with x-ray powder diffraction, (b) corresponding models of two hydrogen-bonded peptides laminated on top of one another. Peptides closest to view are colored gray, farthest from view colored white.

In the nanotube out-of-register anti-parallel configuration, the β-sheet faces are symmetric and multiple sheet stacking arrangements in the MD simulations are consistent with the x-ray fiber diffraction distance. To examine the chemical topology of the interacting β-sheet faces for each registry a lipophillic potential surface was constructed.

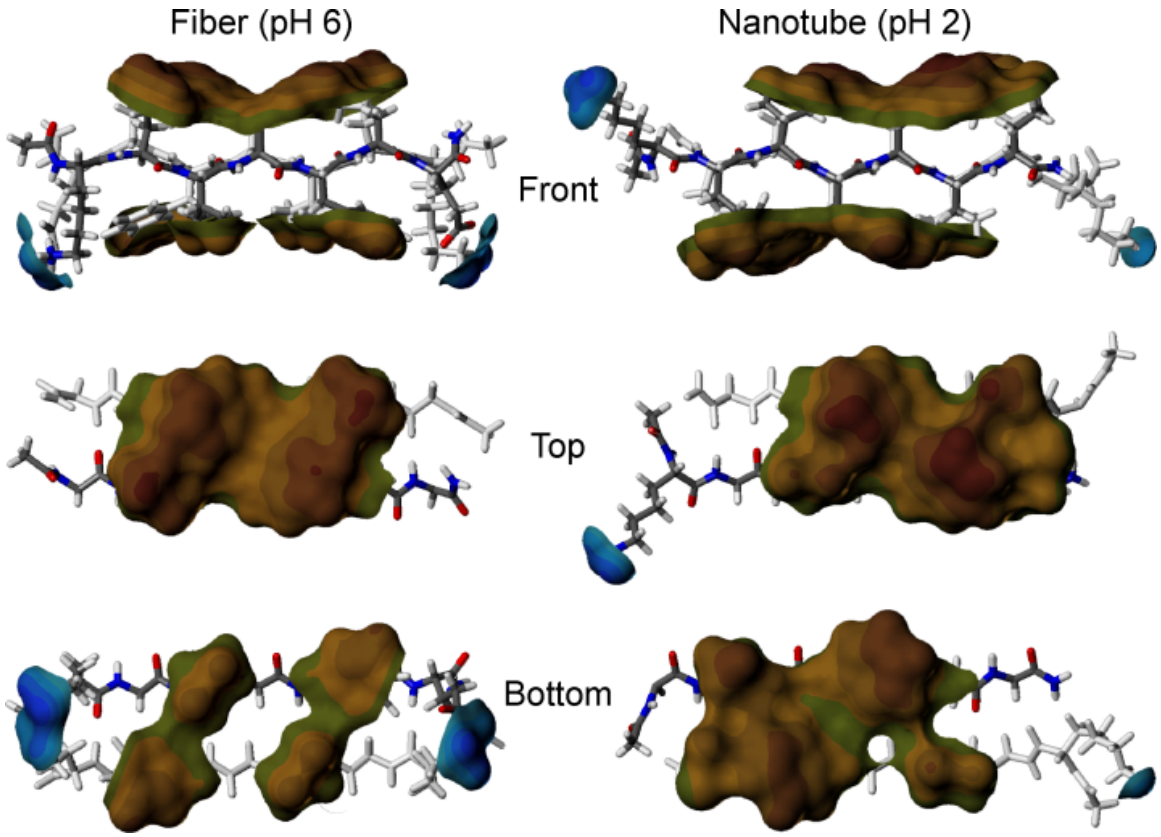

Figure 2-21: Lipophilic potential surface for anti-parallel β-sheets at neutral conditions, compared with out-of register anti-parallel β-sheets at acidic conditions. Colors indicate lipophillic (brown), hydrophillic (blue), and neutral (green).

In Figure 2-21 the calculated solvent accessible surface for hydrogen bonded anti-parallel (fibers) and out-of-register anti-parallel (nanotubes) dimers is displayed as a lipophillic surface.

KLVFFAE fibers contain two distinct surfaces: a large hydrophobic surface and a surface that contains a small hydrophobic stretch flanked by the hydrophilic lysines and glutamates at the termini ends. In contrast, each out-of-register anti-parallel β-sheet surface of the nanotubes forms similar larger hydrophobic surfaces and the N-terminal lysine residue appears to extend into solution.

MD simulations suggest aromatic stacking within the Phe-Phe core (Figure 2-20) that includes edge-to face interactions between F19/F20 in the fibers and F19/F19 and F20/F20 packing in the tubes. In addition, nanotubes have a third Phe-Phe offset stacking interaction between adjacent strands from different sheets (e.g., between white and gray F19's in Figure 6b, right). These unique aromatic packing arrangements within the nanotube models may contribute to the extended lamination. Indeed, a similar Phe zipper has been observed to stabilize β-sheet lamination in fibrous nanocrystals of KFFEAAAKKFFE[36]. To test the importance of this FF dyad in Aβ(16-22) nanotube assembly, these residues were substituted with YY, WW, and II dyads. Under identical assembly conditions, only KLVIIAE assembled into fibers, but appeared unable to form nanotubes.

Cross-Strand Pairing Dictates Peptide Registry

In the arguments developed thus far, the molecular level determinant of the registry switch seen in the fiber to nanotube transition is correlated with the protonation state of E22. The existing structural model suggests that the negatively charged E22 forms a salt bridge with K16, and that K-E cross-strand pairing directs KLVFFAE into anti-parallel β-sheet configuration. To test the importance of K-E cross-strand pairing, E22 was mutated to the non-polar leucine, and assembled at both acidic and neutral pH conditions in 40% acetonitrile. Indeed, independent of, KLVFFAL forms hollow nanotubes (Figure 2-22).

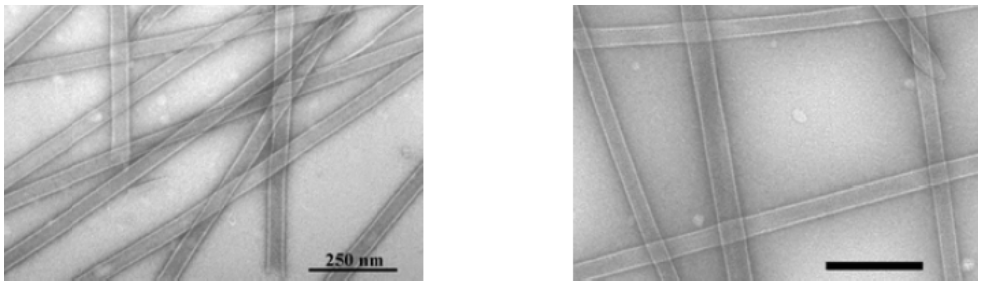

Figure 2-22: TEM micrograph of Aβ(16-22) E22L, KLVFFAL, nanotubes assembled at acidic (left) and neutral (right) conditions.

$^{13}C\{^{15}N\}$ REDOR experiments exploring the CH_3CO-K[1-^{13}C]LVFF[^{15}N]AL-NH_2 isotope enriched peptide established that both acidic and neutral assemblies have nearly identical dephasing profiles, establishing the common anti-parallel out-of-register assembly.

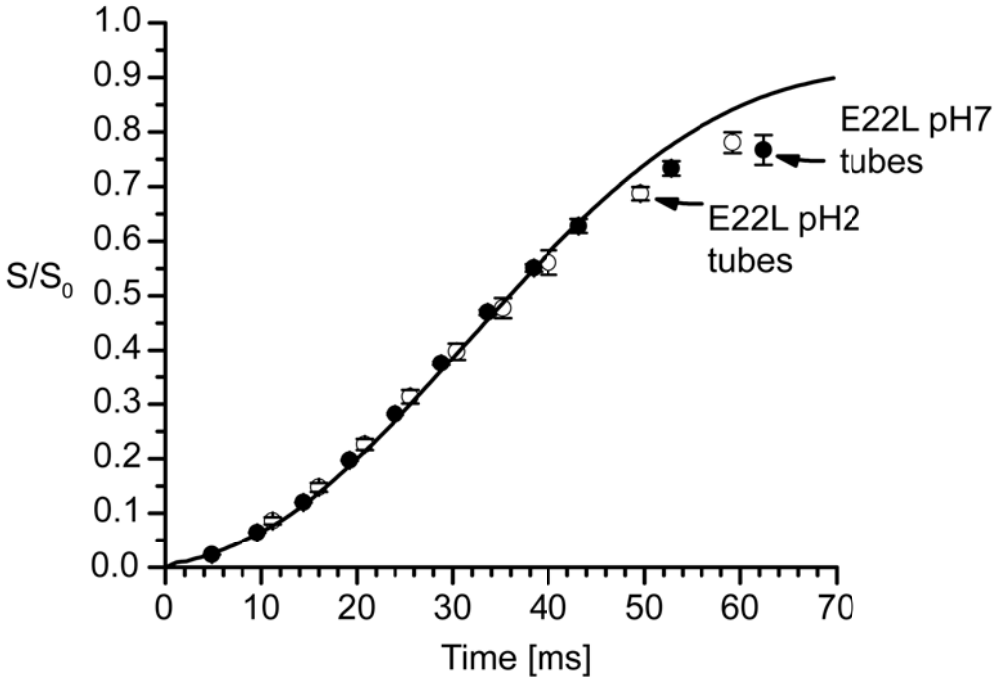

Figure 2-23: $^{13}C\{^{15}N\}$REDOR of CH_3CO-K[1-^{13}C]LVFF[^{15}N]AL-NH_2 nanotube assembly at pH 2 and pH 7 consistent with out-of-register anti-parallel β-sheets. This is the identical registry observed for KLVFFAE nanotubes at acidic pH.

In the absence of K-E salt bridge, the bulky valine packs optimally against A21 as opposed to the bulkier phenylalanine-20, consistent with protein folding cross-strand pairing preferences for β-branched residues (Val, Ile). This packing directs the peptide to form out-of-register anti-parallel β-sheets and this argument has been extended with further mutational analysis[37]. Taken together, the data on KLVFFAE and KLVFFAL self-assembly suggests that the preference of V-A over V-F packing directs out-of-register β-sheets and results in extended lamination leading to nanotubes. In contrast, a salt-bridge between K16 and E22 overrides the V-A cross-strand preference and directs in-register anti-parallel β-sheets resulting in twisted fibers.

The cross-strand pairing arguments suggested the self-assembly of Aβ(16-23) (KLVFFAED), containing an additional negatively charged aspartic acid to the C-terminus, would introduce a competing cross-strand salt-bridge (Figure 2-24). However, V18-A21 cross-strand pairing should direct salt bridge formation between K16-D23. If a K16-D23 salt bridge forms, then F19/F20 would be organized in the same configuration (Figure 2-24) that directs extended lamination within nanotubes.

Figure 2-24: Potential registries of Aβ(16-23). Favorable cross-strand pairings for each registry are highlighted.

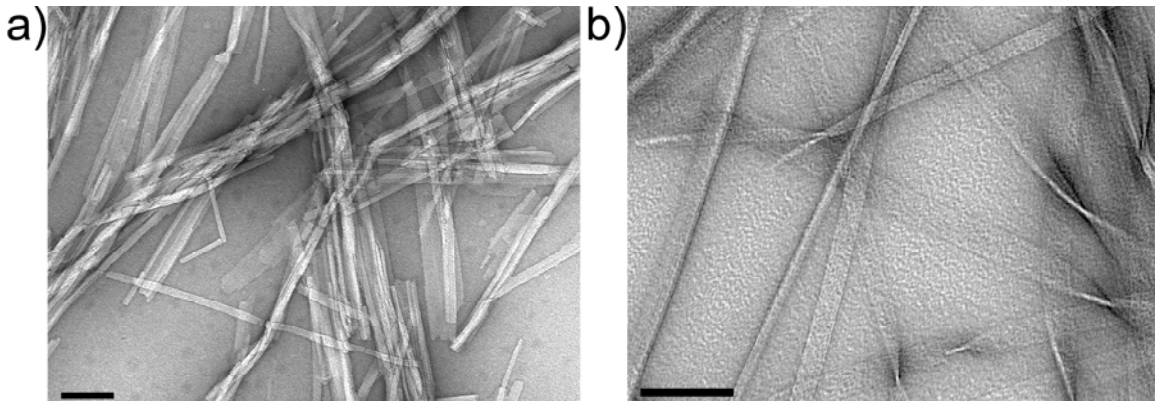

Figure 2-25: TEM micrographs of uranyl acetate negatively stained 1.3 mM KLVFFAED assembled in 40% acetonitrile pH 6 (scale bar = 200 nm) (a), and titrated to pH 2 (b) to debundle sheets (scale bar = 100 nm).

KLVFFAED peptide was assembled at 1.3 mM in 40% acetonitrile under neutral conditions for a 1-week period. As seen in Figure 2-25, the addition of D23 results in assembly into sheets that stick together, as opposed to expected nanotube formation. Previous work with KLVFFAE nanotubes at acidic conditions indicated that shielding the lysine rich positively charged tube surface with divalent ions would induce bundling of nanotubes[10]. Therefore the observed aggregation of KLVFFAED may be the result of the surface being neutralized by having both positive and negatively charged residues. To test this idea, the pH of preformed KLVFFAED bundles was titrated to pH 2 to protonate the glutamic acid and immediately added to TEM grids. In Figure 2-25b the sheets appear to debundle revealing individual sheets with widths ranging from 15-50 nm. While not forming nanotube assemblies, the width of KLVFFAED sheets indicate as many as 50 β-sheets laminate together to form the cross-β sheet assemblies.

These extended laminated structures indicate that the FF dyad may be properly aligned to promote extended sheet stacking, consistent with K16 forming a salt bridge with D23. To test this hypothesis, KL[1-^{13}C]VFF[^{15}N]AED was prepared for REDOR analysis. Fits of ^{13}C{^{15}N}REDOR data indicated that V18 carbonyl is hydrogen bonded to A21's amide with a ^{13}C-^{15}N distance of 4.2 Å. Therefore, V18-A21 cross-strand pairing directs K16 to form a salt bridge with D23 resulting in in-register anti-parallel β-sheets (Figure 2-24 – right).

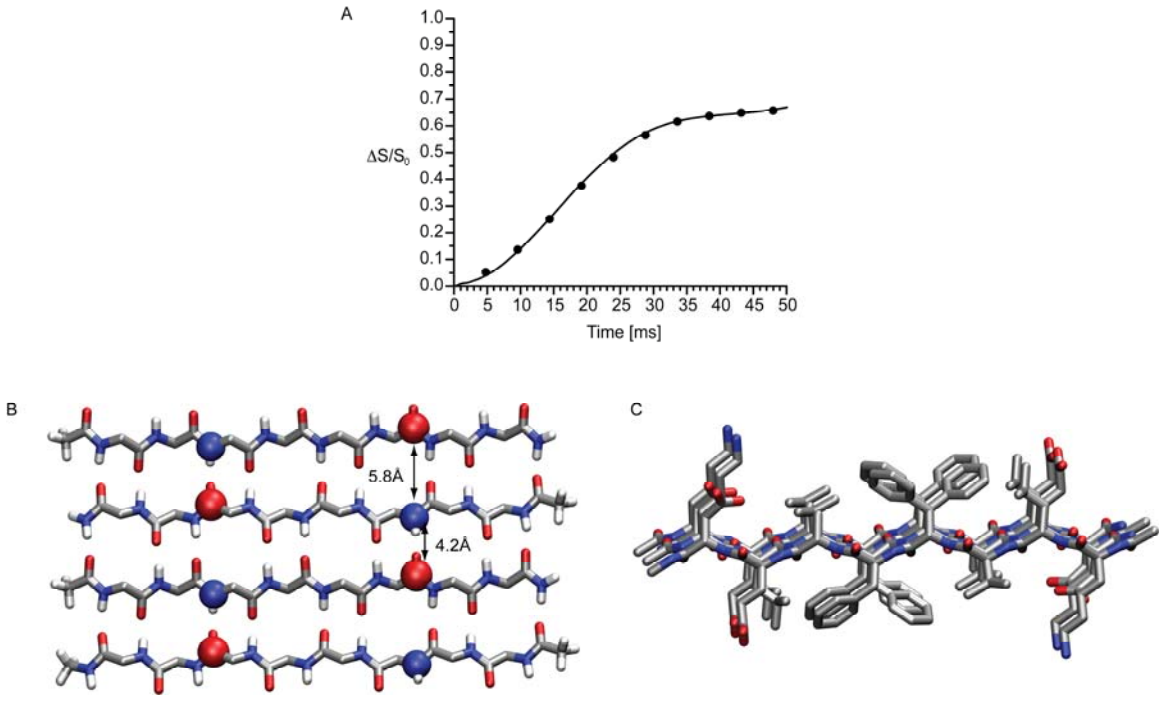

Figure 2-26: ^{13}C{^{15}N} REDOR of 1.3 mM K[1-^{13}C]LVFF[^{15}N]AED bundled sheets assembled in 40% acetonitrile neutral conditions consistent with anti-parallel in-register β-sheets. The solid line is the calculated ^{13}C{^{15}N} REDOR curve for H-bonded L17 to A21 with r1=4.2Å, r2=5.8Å and a N-C-N angle of 156°. The REDOR curve was scaled by 85% indicating that 15% of the sample does not dephase. The chemical shift of the non-dephasing ^{13}C is consistent with being in a random coil conformation.

Orientation of β-sheets

A combination of solid-state NMR, powder x-ray diffraction, and molecular dynamics revealed unique unit cells for fiber and nanotube assemblies. To construct a full 3D model of nanotube and fiber assemblies knowledge of alignment of the unit cell with respect to the long axis of assemblies is needed. A key feature of cross-β structure is that β-sheets are oriented parallel to the long fiber axis and fibril width defined by the number of laminated β-sheets[38,39]. Powder x-ray diffraction (Figure 2-17) does not define the directionality of β-sheets, but this information is available via electron diffraction of aligned fibers and nanotubes.

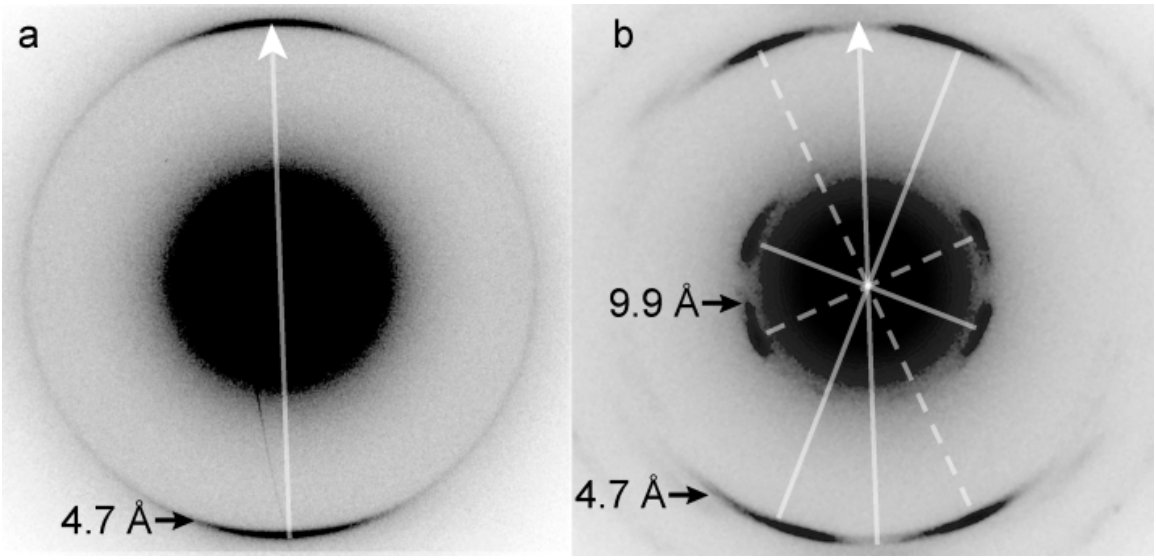

Figure 2-27: Electron diffraction of aligned Aβ(16-22) fibers (a) and nanotubes (b). Arrows indicate the orientation of the fiber/tube long-axis with electron beam oriented perpendicular to this axis. Solid and dotted crosses indicate independent sets of 4.7Å and 10Å d-spacings. Each cross-β pattern is tilted 25±2° from the nanotube long axis.

A comparison of electron diffraction from aligned fibers and nanotubes (Figure 2-27) indicates: (1) appearance of intense 9.9Å d-spacing, and (2) the splitting of arcs into two equally intense sets. The intensity of 9.9Å d-spacing is assigned to the increased number of repeated laminated

β-sheets. The KLVFFAE fiber contains a 4.7Å d-spacing and indicates that the β-sheets run parallel to the long fiber axis, but the lamination reflection is too weak to be observed. However, in nanotubes the same 4.7Å d-spacing and 9.9Å is split into two equally intense cross-β patterns. This doubling, similar to crystal twinning is most consistent with electron diffraction through 2 equivalent layers of a flattened hollow nanotube (Figure 2-28).

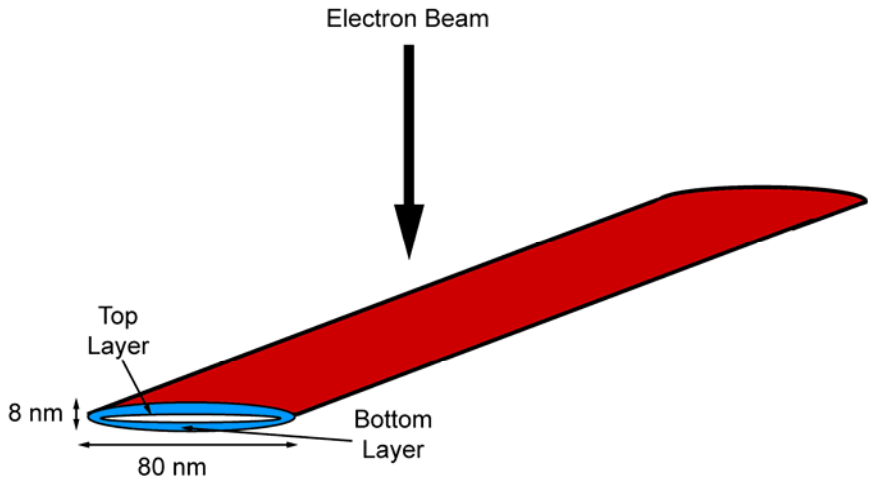

Figure 2-28: Electron beam diffraction occurs through two distinct layers of the hollow KLVFFAE nanotubes.

Figure 2-28 illustrates how the diffraction through a single layer of tube is composed of individual cross-β patterns with three major observed d-spacings: 4.7Å, 9.9Å, and 4.3Å. The 4.7Å d-spacing indicates the distances between hydrogen-bonded peptides, that is orthogonal to 9.9Å d-spacing coming from laminated β-sheets. The unique splitting and distances of the 4.3Å d-spacing report on the angle between the hydrogen bonding and lamination diffraction planes. And in this case, the 4.3Å d-spacing is consistent with peptides laminating directly on top giving an angle of 90° between each plane. The angle between the two sets of cross-β patterns in the nanotubes reveals that laminated β-sheets are offset by 25±2° and helically spiral around the long axis. Similar arc splitting has been observed in an array of helically oriented materials ranging

from DNA,[40] to α-helical peptide coiled-coils[41] and carbon nanotubes[42,43]. These measurements indicate that Aβ(16-22) nanotubes form a helical cross-β structure, in contrast to the typically twisted β-sheets, that runs along the long nanotube axis (Figure 2-30).

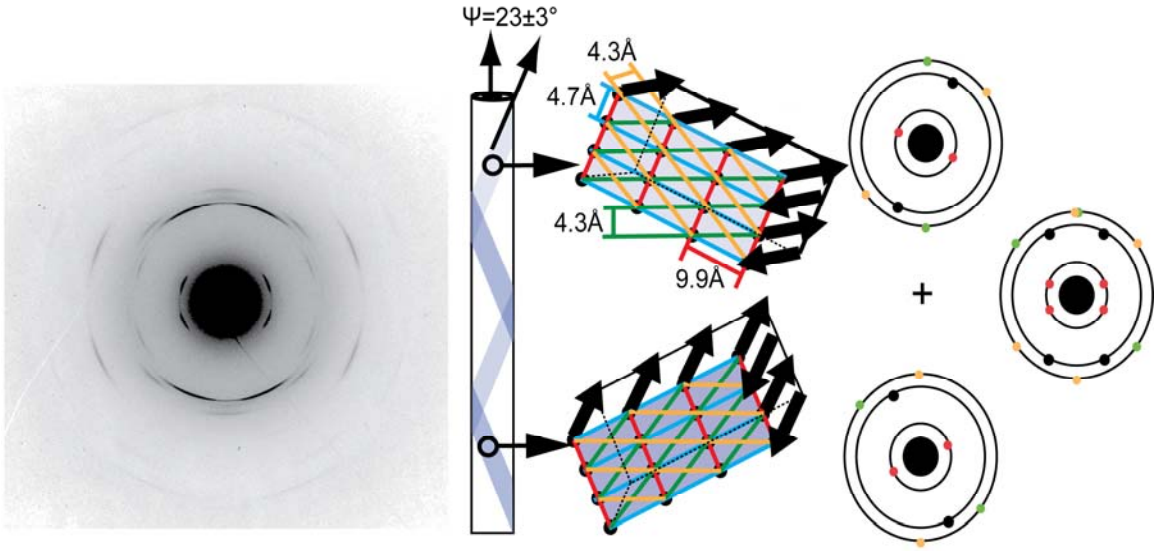

Figure 2-29: Detailed Analysis of Nanotube diffraction explaining the cross-beta peptide arrangement of peptides within a 4 nm layer gives rise to the observed electron diffraction. The summation of two equally intense diffraction patterns gives rise to the observed diffraction pattern.

The angle between the two sets of cross-β patterns in the nanotubes reveals that laminated β-sheets are offset by 25±2° and helically spiral around the long axis. Similar arc splitting has been observed in an array of helically oriented materials ranging from DNA,[40] to α-helical peptide coiled-coils[41] and carbon nanotubes[42,43]. These measurements indicate that Aβ(16-22) nanotubes form a helical cross-β structure, in contrast to the typically twisted β-sheets, that runs along the long nanotube axis (Figure 2-30). Full structural models of twisted

cross-β fibers and helical cross-β nanotubes consistent with solid-state NMR and electron diffraction are shown in Figure 2-30.

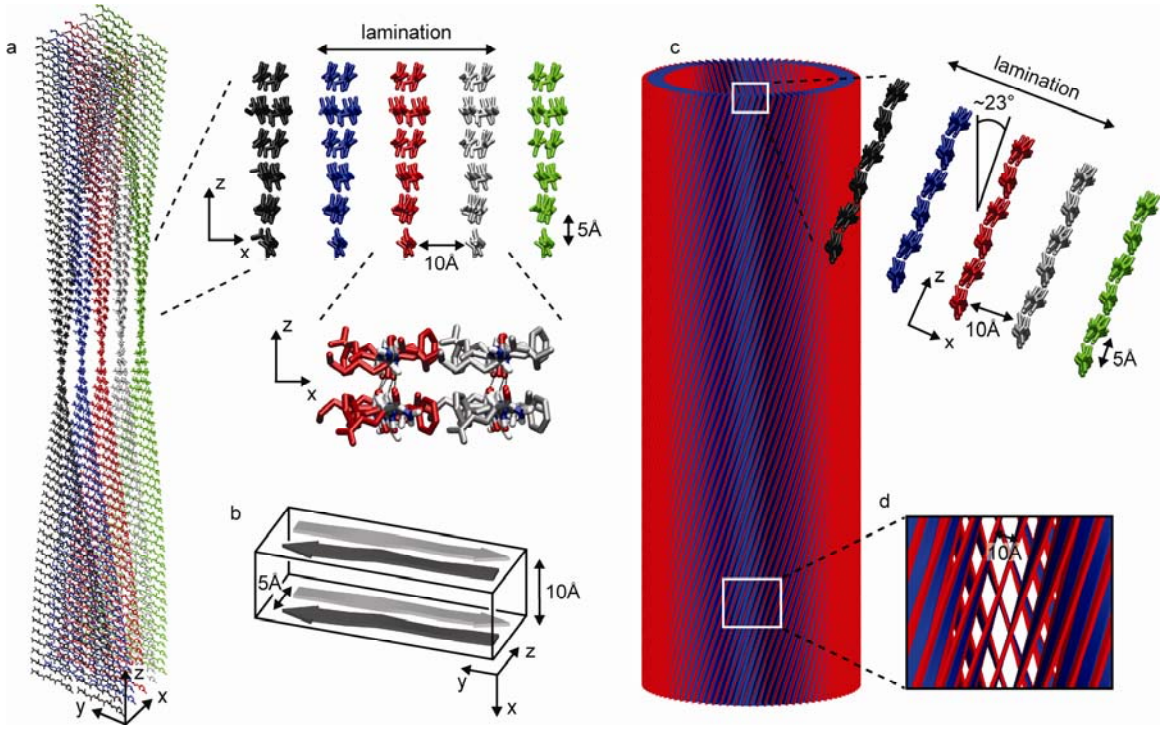

Figure 2-30: Structural model for Aβ(16-22) fibers (left) and nanotubes (right). Five β-sheets are individually colored with a twisted pitch of 1.6°. Expansion illustrates the side-chain lamination of 5 β-sheets (9.9 Å) and hydrogen bonding (4.7 Å). (b) A minimal unit cell with β-strands illustrated as arrows, where final morphology can be controlled by directed relative growth in x,y, and z directions. (c) Under acidic condition Aβ(16-22) nanotubes where extended β-sheet lamination of 140±10 β-sheets in the x-direction. Each β-sheet helically spirals around the nanotube axis at an angle of 25±2° with respect to the nanotube axis.

Discussion

While extensive evidence now exists for diverse amyloid forms and biological strains within neurodegenerative disease plaques, the structural basis of these strains remains ill-defined. Here,

we have examined the molecular level origins of morphological variation of two radically different morphologies, fibers and nanotubes. At neutral pH, charged K16 and E22 residues cross-strand pair and direct assemblies as anti-parallel β-sheets, while deprotonation of E22 or mutation to leucine results in anti-parallel out-of-register β-sheets (Figure 2-16). A systematic evaluation of the V18 position revealed β-branched residues (valine, isoleucine) prefer to pack against the less bulky A21 over the bulky aromatic F20[37]. Introduction of glutamine cross-strand side-chain hydrogen bonding will also direct Aβ(16-22) to be parallel[44]. These results suggest that, in the case of KLVFFAE, cross-strand pairing rules can be ranked as Q-Q cross-strand pairing > K-E salt bridges > β-branched residues (e.g. V) preference for packing against a non-bulky residue. The directing potential of K-E salt bridges is similar to K-D salt bridges. Indeed, it now appears that β-sheet cross-strand pairing plays a significant role in directing β-sheet registry and overall cross-β strain architecture.

A K-E Cross-Strand Pairing

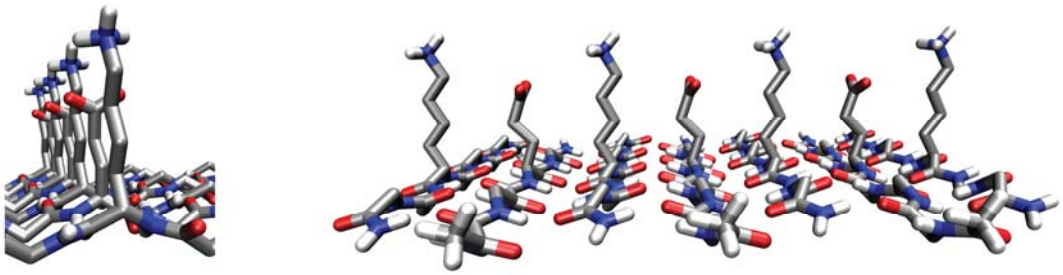

B V-A Cross-Strand Pairing

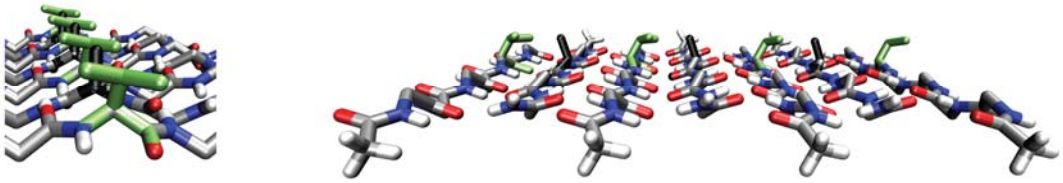

C Q-Q Cross-Strand Pairing

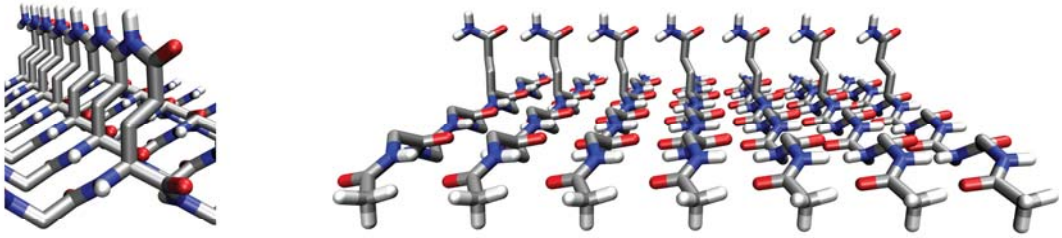

D Metal H-H Cross-Strand Pairing

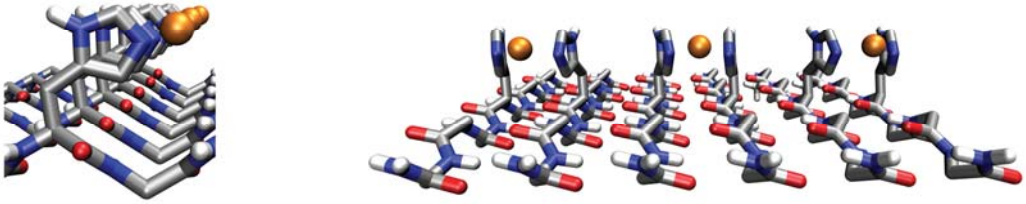

Figure 2-31: Cross-strand pairings that have been observed to play crucial role in amyloid β-sheet registry. A) Cross-strand pairing between oppositely charged residues (K-E)[33]. B) Packing of β-branched residues (V, I) against less bulky residues (A). C) Glutamine side-chain hydrogen bonding directs parallel assemblies.[44] D) His-His cross-strand paring directed by metals (Zn,Cu).[45,46]

Morphologically, the most striking difference is the degree of β-sheet lamination for fibers (6±1) and nanotubes (140±10). Differences in lamination can be attributed to side-chain complementarity across β-sheets. A mere one-residue registry shift has a profound effect of modulating the side-chain distribution on each β-sheet face. The lipophillic potential surfaces (Figure 2-21) of fiber in-register peptide dimers have different numbers of side-chains on each surface (six vs. eight). The result creates distinct β-sheet faces, one with a large hydrophobic surface area (residues L17, F19, and A21), and the opposite face contains a central hydrophobic patch composed of residues V18 and F20 flanked by two charged residues (K16, E22) at each terminus. MD reveals that these two surfaces face each other and are held together by aromatic interactions, yet slight destabilized by charged surfaces at the edges can significantly alter their growth and apparent stability.

In contrast, the nanotube's out-of-register organization places an equal number (seven) of residues on each β-sheet face. Intriguingly, the registry shift exposes the positively charged lysine to solution and results in two nearly identical large hydrophobic surface areas that come into contact. The symmetric highly hydrophobic nature of each β-sheet face appears to contribute to the observed extended lamination

Secondly, MD simulations for both fibers and nanotubes contain a central core of aromatic π-π stacking interactions. With the minimal 2 x 2 system the anti-parallel fibers contain two Phe19-Phe20 edge-to-face π stacking interactions. In contrast, the nanotubes contain a more centralized aromatic network consisting of two interacting aromatic residues (Phe-19 and Phe 20), and an additional offset interaction across strands. This unique Phe zipper arrangement in the absence of a polar laminate interface contributes to the extended β-sheet lamination. This unique Phe-Phe arrangement appears to contribute significantly to extended lamination. Indeed it has been found that incorporation of specific directing molecular interactions across β-sheet faces via H-bonding or metal coordination dyads appear to promote extended lamination needed for nanotube formation.

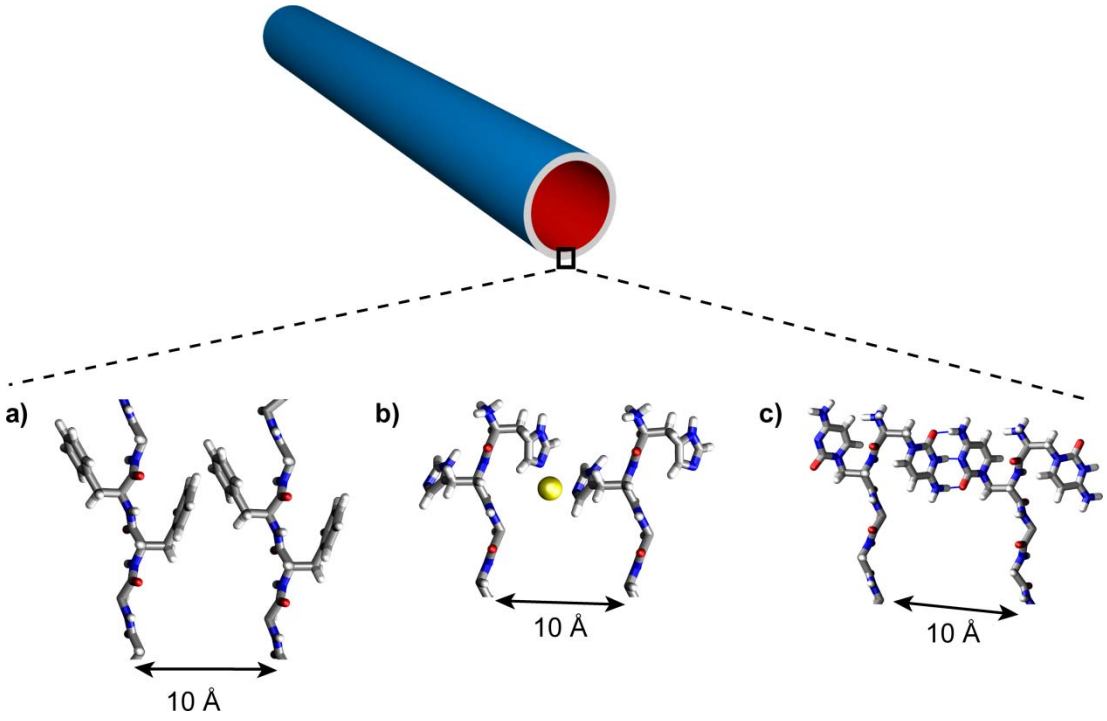

Figure 2-32: Incorporation of intra-sheet interactions that have resulted in extended beta-sheet lamination: a) KLVFFAE displaying the Phe-Phe dyad, b) HHQALVFFA + Zn^{2+} displaying His-Zn-His interaction that bridges laminates, c) ccQALVFFA displaying the cytosine i-motif interaction across laminates.

This simple example of KLVFFAE illustrates how subtle changes in sequence or assembly conditions can result in a wide assortment of amyloid/prion strains. Structural models of Aβ(16-22) fibers and nanotube have revealed the critical nature of optimizing cross-strand pairing (e.g. K-E > V-A) and cross-sheet pairing (F-F) to direct amyloid strain architectures. Combining the rules of β-sheet cross-strand pairing may help predict β-sheet registry of more complicated peptide systems as was predictive in the simplifying example of KLVFFAED assembly. Similar structural analysis will be crucial for revealing the differences between prion strains and why amyloids appear to have varying degrees of toxicity. Our studies of the model system Aβ(16-22) reveals that the plastic nature of the cross-β scaffold can be molded via cross-strand and cross-sheet interactions to yield a rich array of cross-β strains for construction of nanoarchitectures.

References

1. Walker LC, LeVine H, Mattson MP, Jucker M (2006) Inducible proteopathies. Trends in Neurosciences 29: 438-443.

2. Petkova AT, Leapman RD, Guo Z, Yau WM, Mattson MP, et al. (2005) Self-Propagating, Molecular-Level polymorphism in Alzheimer's b-Amyloid Fibrils. Science 307: 262-265.

3. Derkatch IL, Chernoff YO, Kushnirov VV, Inge-Vechtomov SG, Liebman SW (1996) Genesis and Variability of [*PSI*] Prion factors in *Saccharomyces cerevisiae*. Genetics 144: 1375-1386.

4. Walker LC, Rosen RF, Levine H (2008) Diversity of A beta deposits in the aged brain: a window on molecular heterogeneity? Romanian Journal of Morphology and Embryology 49: 5-11.

5. Rosen RF, Ciliax BJ, Wingo TS, Gearing M, Dooyema J, et al. (2010) Deficient high-affinity binding of Pittsburgh compound B in a case of Alzheimer's disease. Acta Neuropathologica 119: 221-233.

6. Collinge J, Clarke AR (2007) A general model of prion strains and their pathogenicity. Science 318: 930-936.

7. Lu K, Jacob J, Thiyagarajan P, Conticello VP, Lynn DG (2003) Exploiting amyloid fibril lamination for nanotube self-assembly. J Am Chem Soc 125: 6391-6393.

8. Dong J, Lu K, Lakdawala A, Mehta AK, Lynn DG (2006) Controlling amyloid growth in multiple dimensions. Amyloid 13: 206-215.

9. Samuel-Landtiser M, Zachariah C, Williams CR, Edison AS, Long JR (2007) Current Protocol Protein Science.

10. Lu K, Guo L, Mehta AK, Childers WS, Dublin SN, et al. (2007) Macroscale assembly of peptide nanotubes. Chem Commun (Camb) 2729-2731.

11. Lu K (2005) Discovery of Diverse Peptide Nanotube Architecture from the Self-assembly of Designed Amyloid-β Cassettes. Atlanta: Emory University. 257 p.

12. Pan Y, Gullion T, Schaefer J (1990) Determination fo C-N internuclear distances by Rotational-Echo Double Resonance NMR of Solids Journal of Magnetic Resonance 90: 330-340.

13. Sinha N, Schmidt-Rohr K, Hong M (2004) Compensation for pulse imperfections in rotational-echo double-resonance NMR by composite pulses and EXORCYCLE. J Magn Reson 168: 358-365.

14. Gullion T, Vega S (1992) A Simple Magic Angle Spinning NMR Experimeng for the Dephasing of Rotational Echoes of Dipolar Coupled Homonuclear Spin Pairs Chemical Physics Letters 194: 423-428.

15. Gullion T, Baker DB, Conradi MS (1990) New, Compensated Carr-Purcell Sequences. Journal of Magnetic Resonance 89: 479-484.

16. Fung BM, Khitrin AK, Ermolaev K (2000) An improved broadband decoupling sequence for liquid crystals and solids. J Magn Reson 142: 97-101.

17. Lindahl E, Hess B, van der Spoel D (2001) GROMACS 3.0: a package for molecular simulation and trajectory analysis. Journal of Molecular Modeling 7: 306-317.

18. Van der Spoel D, Lindahl E, Hess B, Groenhof G, Mark AE, et al. (2005) GROMACS: Fast, flexible, and free. Journal of Computational Chemistry 26: 1701-1718.

19. Berendsen HJC, Postma JPM, van Gunsteren WF, Hermans J (1981) Interaction models for water in relation to protein hydration. Intermolecular Forces. Dordrecht: Reidel Publishing Company. pp. 331-342.

20. Kaminski GA, Friesner RA, Tirado-Rives J, Jorgensen WL (2001) Evaluation and reparametrization of the OPLS-AA force field for proteins via comparison with accurate quantum chemical calculations on peptides. J Phys Chem B 105: 6474-6487.

21. Hess B, Bekker H, Berendsen HJC, Fraaije JGEM (1997) LINCS: A linear constraint solver for molecular simulations. J Comp Chem 18: 1463–1472.

22. Essmann U, Perera L, Berkowitz ML, Darden T, Lee H, et al. (1995) A Smooth Particle Mesh Ewald Method. J Chem Phys 103: 8577-8593.

23. Berendsen HJC, Vanderspoel D, Vandrunen R (1995) Gromacs - a Message-Passing Parallel Molecular-Dynamics Implementation. Comp Phys Comm 91: 43-56.

24. Paul C, Axelsen PH (2005) beta sheet structure in amyloid beta fibrils and vibrational dipolar coupling. Journal of the American Chemical Society 127: 5754-5755.

25. Miyazawa T (1960) Perturbation Treatment of the Characteristic Vibrations of Polypeptide Chains in Various Configurations. J Chem Phys 32: 1647-1652.

26. Benzinger TLS, Gregory DM, Burkoth TS, Miller-Auer H, Lynn DG, et al. (1998) Propagating structure of Alzheimer's β -amyloid(10-35) is parallel beta -sheet with residues in exact register. Proc Natl Acad Sci U S A 95: 13407-13412.

27. Gregory DM, Benzinger TLS, Burkoth TS, Miller-Auer H, Lynn DG, et al. (1998) Dipolar recoupling NMR of biomolecular self-assemblies: determining inter- and intrastrand distances in fibrilized Alzheimer's [beta]-amyloid peptide. Solid State Nuclear Magnetic Resonance 13: 149-166.

28. Burkoth TS, Benzinger TLS, Urban V, Morgan DM, Gregory DM, et al. (2000) Structure of the beta-Amyloid (10-35) Fibril. J Am Chem Soc 122: 7883-7889.

29. Gregory DM, Mehta MA, Shiels JC, Drobny GP (1997) Determination of local structure in solid nucleic acids using double quantum nuclear magnetic resonance spectroscopy. Journal of Chemical Physics 107: 28-42.

30. Bernard GM, Miskolzie M, Kotovych G, Wasylishen RE (2004) A solid-state NMR investigation of orexin-B. Canadian Journal of Chemistry-Revue Canadienne De Chimie 82: 1554-1563.

31. Garbow JR, McWherter CA (1993) Detemination of the Molecular Conformation of Melanostatin using C-13, N-15 REDOR NMR Spectroscopy Journal of the American Chemical Society 115: 238-244.

32. Neal S, Nip AM, Zhang HY, Wishart DS (2003) Rapid and accurate calculation of protein H-1, C-13 and N-15 chemical shifts. Journal of Biomolecular Nmr 26: 215-240.

33. Mehta AK, Lu K, Childers WS, Liang Y, Dublin SN, et al. (2008) Facial Symmetry in Protein Self-Assembly. J Am Chem Soc 130: 9829-9835.

34. Balbach JJ, Ishii Y, Antzutkin ON, Leapman RD, Rizzo NW, et al. (2000) Amyloid Fibril Formation by Ab16-22, a Seven-Residue Fragment of the Alzheimer's b-Amyloid Peptide, and Structural Characterization by Solid State NMR. Biochemistry 39: 13748-13759.

35. Fraser; RDB, MacRae TP (1973) Conformation in Fibrous Proteins. New York: Academic Press.

36. Makin OS, Atkins E, Sikorski P, Johansson J, Serpell LC (2005) Molecular basis for amyloid fibril formation and stability. Proc Natl Acad Sci 102: 315-320.

37. Liang Y, Pingali SV, Jogalekar AS, Snyder JP, Thiyagarajan P, et al. (2008) Cross-strand pairing and amyloid assembly. Biochemistry 47: 10018-10026.

38. Eanes ED, Glenner GG (1968) X-ray diffraction studies on amyloid filaments. J Histochem Cytochem 16: 673-677.

39. Geddes AJ, Parker KD, Atkins EDT, Beighton E (1968) "Cross-b" Conformation in Proteins. J Mol Biol 32: 343-358.

40. Watson JD CF (1953) The Structure of DNA. Cold Spring Harbor Symposia on Quantitative Biology 18: 123-131.

41. Crick FHC (1953) The Packing of a-Helices: Simple Coiled-Coils. Acta Crystallographica 6: 689-697.

42. Qin LC (2006) Electron diffraction from carbon nanotubes. Reports on Progress in Physics 69: 2761-2821.

43. Lambin P, Lucas AA (1997) Quantitative theory of diffraction by carbon nanotubes. Physical Review B 56: 3571-3574.

44. Ni R (2010): Emory.

45. Dong J, Canfield JM, Mehta AK, Shokes JE, Tian B, et al. (2007) Engineering metal ion coordination to regulate amyloid fibril assembly and toxicity. Proc Natl Acad Sci 104: 13313-13318.

46. Dong J, Shokes JE, Scott RA, Lynn DG (2006) Modulating amyloid self-assembly and fibril morphology with Zn(II). J Am Chem Soc 128: 3540-3542.

Chapter 3 : Amyloid Peptides Organized as a Bilayer Membrane[1]

Biology's most critical chemistry ranging from oxidative phosphorylation[1] to photosynthesis[2] relies on the localization of proteins with a two-dimensional cellular membrane matrix[3,4]. The cellular membrane architecture is made up of phospholipids that organize to form a bilayer membrane with hydrophobic tails separated from water and buried at the bilayer center and charged head groups exposed to water[4,5]. Intriguingly, a range of short peptides appear able to organize as structural[6,7] membrane replacements. Short amphiphilic peptide sequences composed of a stretch of 6-8 hydrophobic residues followed by 1-2 charged residues assemble into hollow tubes and vesicles and have been proposed to organize as bilayers (Figure 3-1).

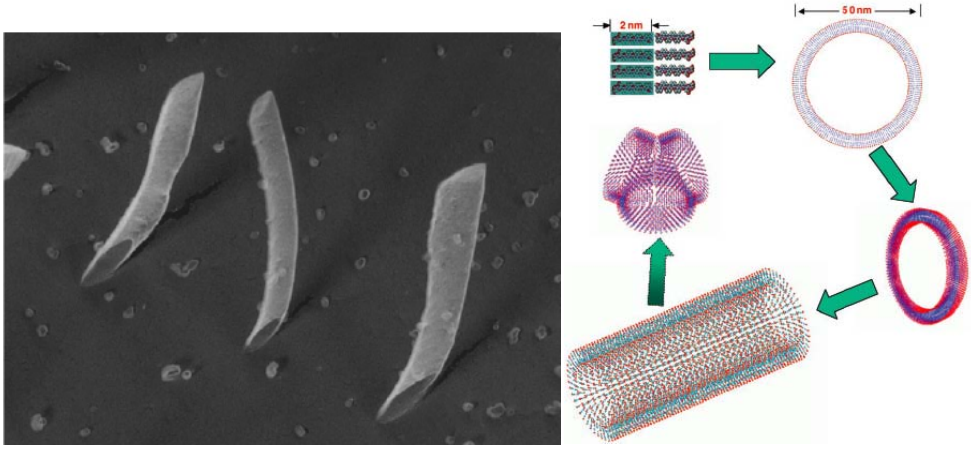

Figure 3-1: Cryo-etch HRSEM image of Ac-VVVVVVVD-OH peptide surfactant nanotubes[8]. Proposed model of peptide surfactants organized as a bilayer membrane[6].

As shown in the previous chapter, the nucleating core of the Alzheimer's Disease peptide, Aβ(16-22), assembled into hollow nanotubes. A bilayer model was originally proposed for the peptide nanotubes as small angle x-ray scattering (SAXS) revealed a 4.3±0.3 nm wall[7] thickness that is approximately twice the length of the extended peptide (2x2.4±0.2Å). Also

[1] Results published as Childers, W. S., A. K. Mehta, et al. (2010). "Peptides Organized as Bilayer Membranes." Angewandte Chemie International Edition 49(24): 4104-4107.

consistent with a parallel membrane like bilayer, the nanotube's surface can bind negatively charged gold particles[9] as shown in Figure 3-2.

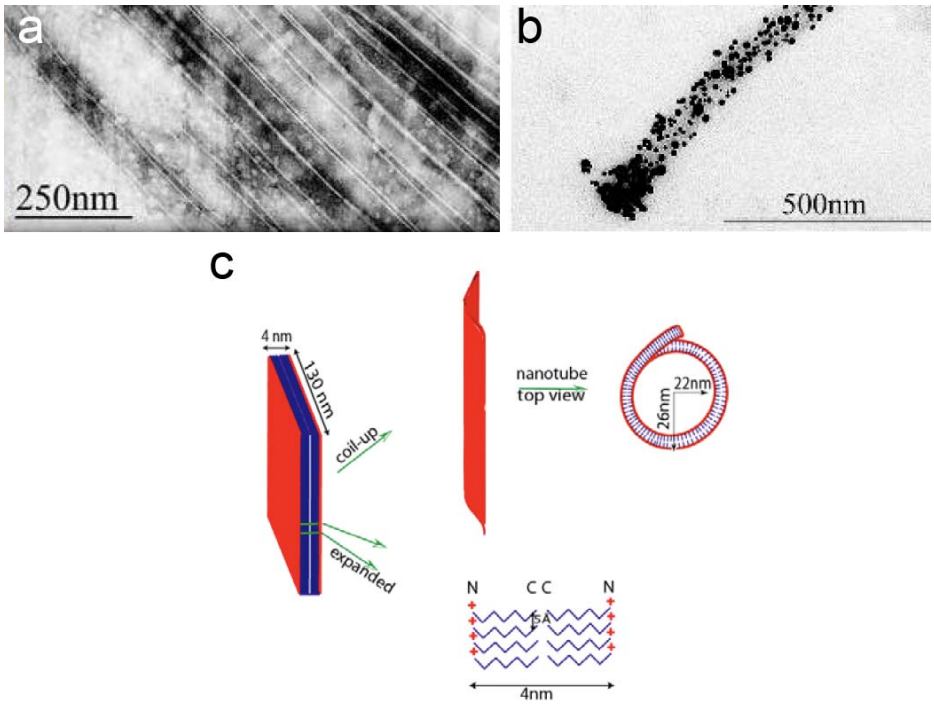

Figure 3-2: (a) Negatively stained TEM micrograph of KLVFFAE nanotubes assembled under acidic conditions in 40% acetonitrile[10]. (b) Binding of gold nanoparticles to nanotubes after deposition of the anionic polystryrene sulfonate PSS on the positively charge surface[10] (c) First generation proposed parallel peptide bilayer for KLVFFAE nanotubes.

From these observations it was proposed that KLVFFAE peptides organized just like a lipid membrane by two parallel β-sheets interacting through termini interactions to form a bilayer that exposes N-terminal lysines and buries the C-terminus (Figure 3-2). However, little direct evidence exists for the end-to-end peptide termini interactions in the proposed models[6,7,11,12,13,14,15]. In this chapter, solid-state NMR approaches are developed to probe peptide termini interactions and account for the tube wall thickness.

Methods

Peptide Assembly Preparation

Peptides were synthesized via microwave assisted solid-phase peptide synthesis as described in Chapter 2. After FMOC deprotection of the N-terminal lysine the resin was washed 5 times with dimethylformamide. For incorporation of ^{13}C carbonyl isotopes into N-terminal acetates, 5 mL of 20% [2,2'-^{13}C] acetic anhydride (Cambridge Isotope Laboratories) in dimethylformamide (DMF) was added and allowed to react for 12 hours, then resin was washed 5 times with dichloromethane and allowed to air dry. Peptides were cleaved and purified following procedures detailed in Chapter 2.

Peptides were assembled in 40% acetonitrile under with acidic conditions (nanotubes) or neutral conditions (fibers) at 4°C. After two weeks of assembly, maturation was verified by β-sheet CD signature and assemblies were visualized by TEM. For fast sodium sulfate bundling procedures a single aliquot of sodium sulfate was added to 1.3 mM KLVFFAE peptide nanotube solution to a final concentration of 9 mM sodium sulfate. Fast bundling does not induce the previously observed SAXS signature of bundled nanotubes[16], consistent with a more disorganized tube-tube arrangement. In comparison, slow sulfate/phosphate bundling procedures were modeled after the addition of sodium sulfate during monitoring of bundling by small angle x-ray scattering (SAXS)[16]. Briefly, the addition of concentrated sodium sulfate solution (100 mM) was broken up into 9 equivalent aliquots added once per hour to gradually raise the sodium sulfate concentration to 9 mM to titrate away surface bound TFA and induce nanotube bundling.

Cross-Section Embedded TEM

KLVFFAL peptide samples were bundled using sodium hydrogen phosphate[16] and aggregates were pelleted and reconstituted to concentration of ~50 mg/mL. This solution (15 μL) was placed on a glass slide and inverted over a 50% gluteraldehyde solution at 60°C for 30 minutes, then placed further over 4% OsO_4 for 30 minutes in a closed glass Petri dish. The resulting sample was incubated in 2.5% gluteraldehyde in 0.1 M phosphate buffer (pH 7.4) for 30 minutes, followed by a H_2O rinse, and further incubation in 2% OsO_4 for 30 minutes. This sample was washed with H_2O, stained with 4% uranyl acetate in 50% ethanol for 10 minutes, dehydrated through an ethanol series, ending at 100% and gradually embedded with 812 Epoxy resin by: (1) 60 minute incubation in 1:1 Ethanol: 812 epoxy resin, (2) 60 minutes 1:2 Ethanol: 812 epoxy resin, and (3) 60 minutes in 100% 812 epoxy resin. Samples were then thin (70 to 80nm) sectioned using a diamond knife and a RMC MT-7000 ultramicrotome, placed on TEM grids and post-stained with uranyl acetate and Reynold's lead citrate stain. TEM micrographs were recorded with a Philips 410 TEM using a tungsten filament at an accelerating voltage of 80 kV.

Cryo-etch High Resolution SEM

The nanotube solution was plunge-frozen in liquid ethane, transferred to a precooled (−170 °C) Gatan 3500 CT cryostage, fractured with a prechilled blade, and washed with liquid nitrogen. The cryostage was transferred to a Denton DV-602 chromium (Cr) coater. The temperature was increased to −105 °C and held for 20−30 min at 0.2 μTorr to allow exposed ice to sublime (etch). The sample was then cooled to −170 °C and sputter-coated with Cr at a rate of 0.3 Å/s at a current of 50 mA at 300 V under 5 mTorr Ar atmosphere, resulting in a 2 nm Cr film. The Cr-coated sample was transferred to a DS-130F field emission scanning electron microscope (SEM), and temperature was equilibrated at −120 °C for 30 min.

DQF-DRAWS

Double Quantum Filtered Dipolar Recoupling with a windowless sequence (DQF-DRAWS)

experiments[17,18] were implemented, with the addition of spin-temperature alternation of the initial ^{1}H $\pi/2$ pulse to the pulse sequence and phase cycling previously described[19] with a 41.225 kHz ^{13}C RF field measured by fitting a sine function with a decaying exponential to a ^{13}C nutation curve (Figure 3-3).

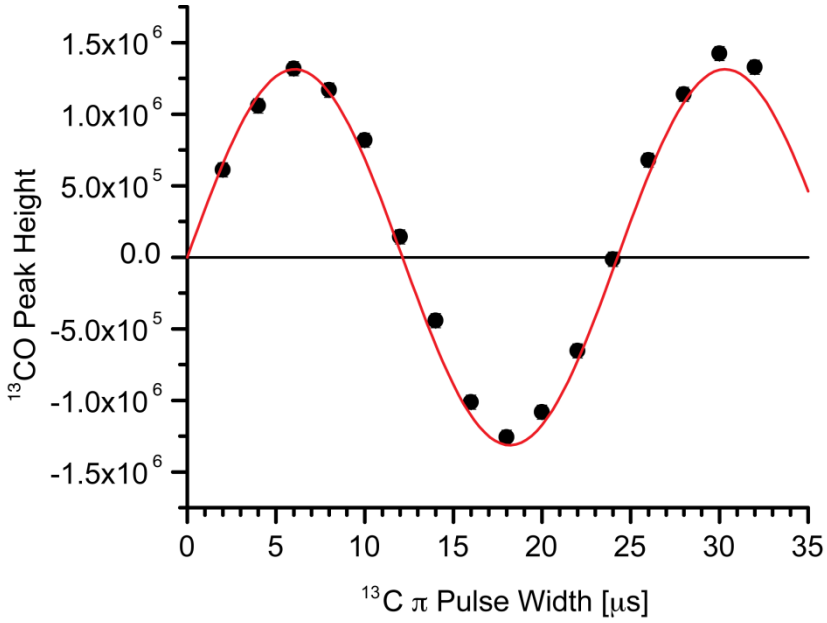

Figure 3-3: An example ^{13}C DQF-DRAWS nutation curve in which ^{13}C carbonyl peak height is plotted versus ^{13}C π pulse width. Data is fit to an exponentially decaying sine curve (red line) with $A=1.32\text{x}10^{6}$, $w=12.1\pm0.1$ μs, $t_1=2.1\text{x}10^{14}$ μs.

SPINAL-64[20] ^{1}H (600.3 MHz) decoupling at 128 kHz was used during both dipolar evolution and acquisition and the rotor period (206.2μs → ν_r = 4.85 kHz) was set to 8.5 times the ^{13}C π pulse length. A T_2DQ of 6.8ms was measured in a separate experiment by placing a composite 90x-90y-90x DQ coherence refocusing pulse between the two DRAWS evolution periods[21] which were fixed at 32-Tr, resulting in maximum DQ coherence excitation efficiency.

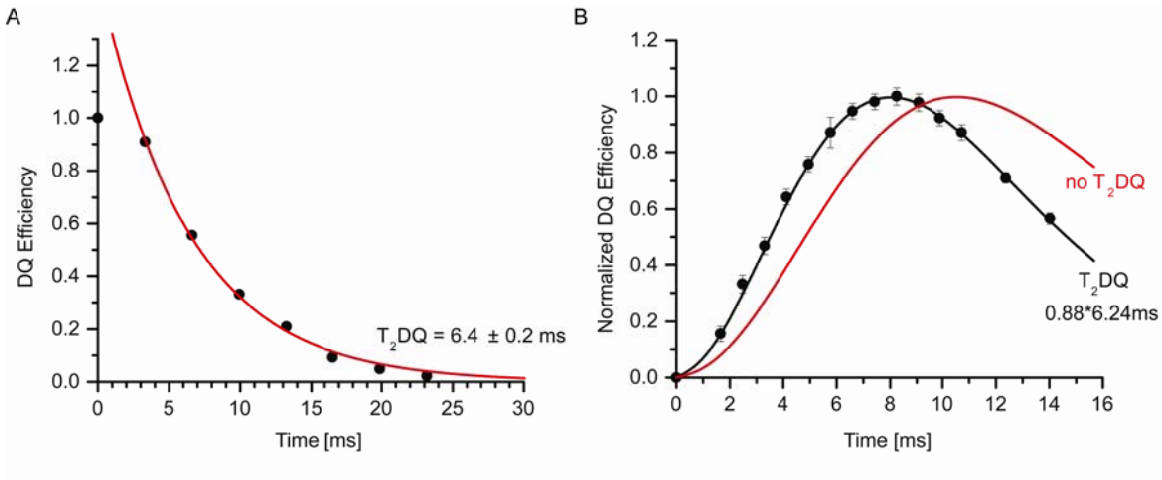

Figure 3-4: A Typical T_2DQ experiment for [1-^{13}C]CH_3CO-KLVFFAE nanotubes. Line fit (red line) to an exponentially decaying curve $y=A_1*\exp(-x/T_2DQ)$ with $A_1=1.55\pm0.05$ and $T_2DQ=6.24\pm0.2$ms (B) Application of T_2DQ correction in fitting of DQF-DRAWS experimental data.

Data points are the ratio of the sum of center- and sideband integrated peak intensities for each evolution time to the ^{13}C CP-MAS intensities. Error bars were calculated using the noise of each spectrum as the maximum peak height deviation. DQF-DRAWS curves were calculated using SIMPSON[22], where an array of ^{13}C spins were approximated with a three spin "infinite-loop" model[21] and chemical shift tensor components δ_{11}=74.1ppm, δ_{22}=6.0ppm and δ_{33}=-80.1ppm which were measured from the ^{13}C CP-MAS spectra. The effects of DQ-relaxation were approximated by multiplying the calculated SQ intensity with a decaying exponential[21] of the form $e^{-\frac{t}{2*T_2DQ}}$. Although the T_2DQ sequence provides an accurate measurement of the relaxation parameters, it does not account for the effects of RF inhomogeniety. Samples with an infinite array of carbonyl carbons separated and a known distance of 4.63 Å, as measured by x-ray powder diffraction[23], indicate that the effects of RF inhomogeniety can be approximated by decreasing the measured T_2DQ by ~85 to 90%. As a result, the calculated DQF-DRAWS curves

were multiplied by $e^{-\frac{t}{2*0.88*6.8ms}}$. The resolution limits of DRAWS appears to be dipolar couplings that correspond to distances shorter than 6Å as illustrated in simulated DRAWS curves below (Figure 3-5).

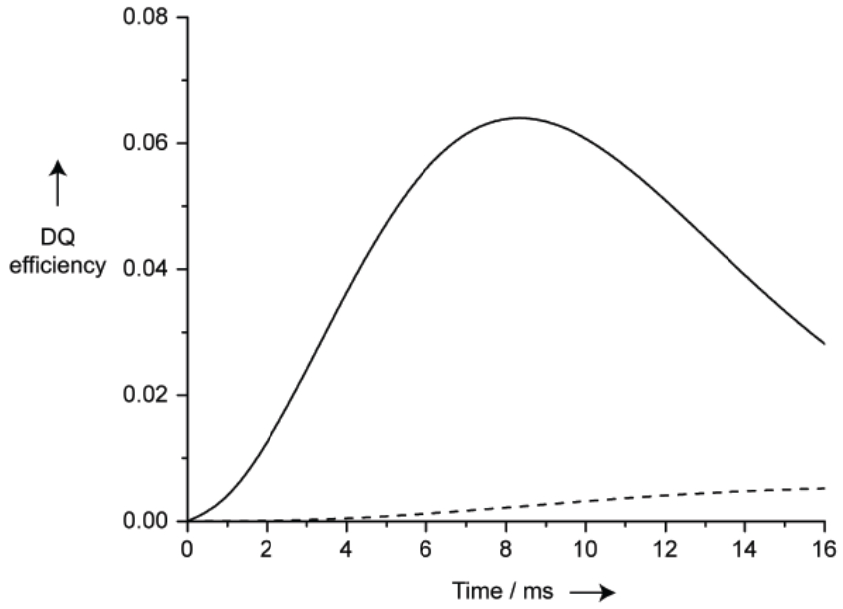

Figure 3-5: Simulated DQF-DRAWS buildup curves for ^{13}CO-^{13}CO separated by 5.2Å (solid line) and 9.4Å (dotted line). The longer distance is far too weak to be observed experimentally.

Spin Counting Using $^{13}C\{^{19}F\}$ REDOR

A $^{13}C\{^{19}F\}$-REDOR pulse sequence[24] with EXORCYCLE phase cycling[25] of the single-observe 6 μs ^{13}C (150.8 MHz) π-pulse was used to minimize re-introduction of ^{13}C-^{13}C homonuclear dipolar coupling[26,27]. To compensate for pulse imperfections the 5.3 μs ^{19}F REDOR rotor-synchronized dephasing π pulses were *xy*8 phase cycled[28]. 83 kHz Spinal64[20] ^{1}H (600.13 MHz) decoupling was applied during REDOR evolution and acquisition. REDOR data points are the integrated sum of center- and sideband peaks. Error bars were calculated using the noise of each spectrum as the maximum peak height deviation.

Example of spin-counting from REDOR spectra for three ^{13}C nuclei (green) close to an

^{19}F spin (blue) and one ^{13}C (red) far from an ^{19}F is illustrated in Figure 3-6. The REDOR experiment results in two spectra, the full-echo (S_0) spectrum where pulses were only applied to the observe spins (^{13}C), and the dephased (S) spectrum in which pulses were applied to both observe (^{13}C) and dephasing (^{19}F) spins. The S_0 spectrum (Figure 3-6b) has the chemical shift resolved signals from all the ^{13}C nuclei in the sample, including both the ^{13}CO's that are close (green line) and far (red line) from an ^{19}F. Application of REDOR dephasing pulses results in attenuation of the signal for the ^{13}C nuclei that are dipolar coupled (i.e. close) to a ^{19}F (Figure 3-6c).

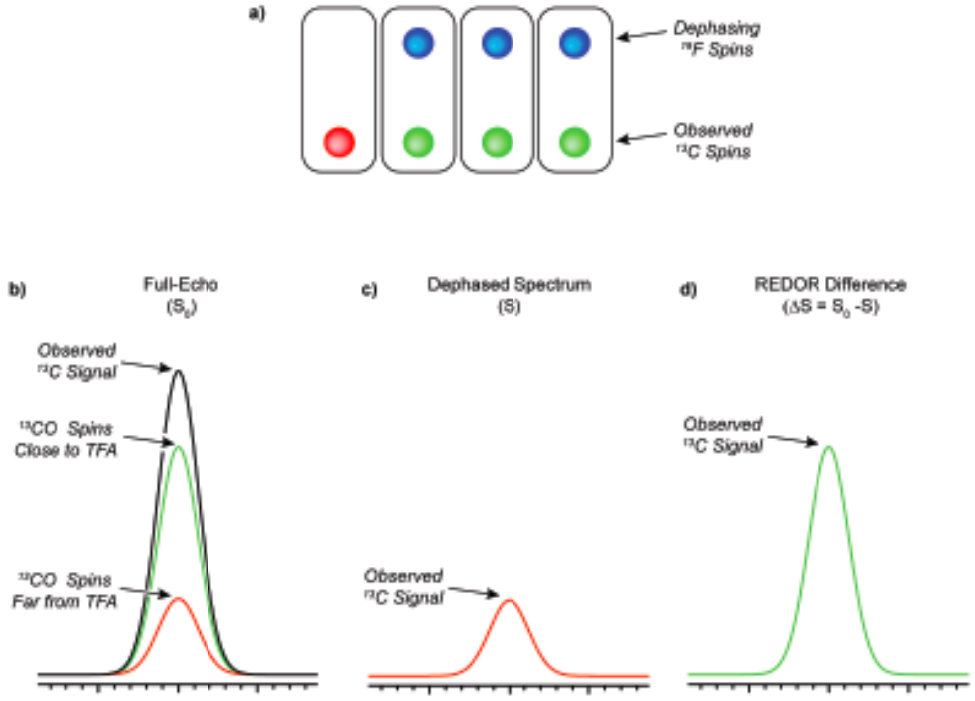

Figure 3-6: Illustration of concept of spin counting using REDOR.

If the S spectrum has no signal, this indicates that all the ^{13}C nuclei are close to a ^{19}F. In the current example, the S spectrum has 25% of the intensity of the S_0 spectrum, which is from the ^{13}C nuclei that have not been dephased – indicating that 25% of the ^{13}C nuclei are not close to

a ^{19}F. REDOR difference spectrum (ΔS) arising from the ^{13}C nuclei that are close to a ^{19}F (Figure 3-6d). The ratio of the ΔS to the S_0 spectrum corrects for spin-spin relaxation of the observe ^{13}C spins and in this case will be 0.75, indicating that 3 out of every 4 ^{13}C nuclei are close to a TFA. Incomplete refocusing of the pulses in the actual REDOR experiment will lower the actual observed value of $\Delta S/S_0$. This value can be measured in a separate experiment using a sample in which the positions of all nuclei are known and where all of the ^{13}C spins are close to a ^{19}F spin. For the REDOR experiments presented in this chapter, this value was measured to be 0.98 using fluoropyruvate.

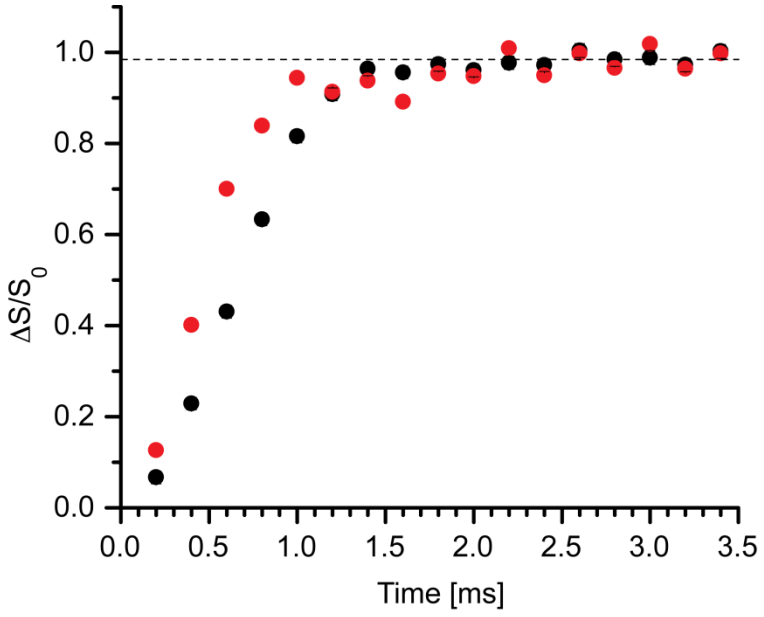

Figure 3-7: $^{13}C\{^{19}F\}$ REDOR curve of fluoropyurvate to determine REDOR scaling factor. Red circles (CO), black circles (COOH), and dashed line signifies the measured plateau level (0.98).

The natural abundance amide ^{13}CO spins have a similar chemical shift as the acetate CO and will also contribute to both the dephased and non-dephased signal. Assuming that all the peptide amide carbonyl groups are not close to a TFA, this will reduce the maximum $\Delta S/S_0$ by

99/(99+7*1.1)=0.92, where the 99 is the percent enrichment of the acetate carbonyl carbon, and 1.1 is the percent of natural abundance ^{13}C. If all of the natural abundance ^{13}C carbonyl groups are near TFA, the REDOR $\Delta S/S_0$ plateau would be 0.964. The actual natural abundance dephasing should be between 0.92 and 0.964, therefore an average value of 0.94 was selected. Including this factor, the expected REDOR plateau where 3 out of every 4 acetate groups are close to a TFA is 0.75*0.94 = 0.71.

Results

Development of Microscopy approaches to visualize nanotube walls

As shown by TEM images, the hollow nanotube morphology of KLVFFAE assemblies under acidic conditions is not apparent (Figure 3-2a). During a 3-5 minute uranyl acetate incubation time, stain can both accumulate outside the hollow nanotubes and diffuse inside the hollow nanotubes (Figure 3-8a). The resulting negative stain yields two parallel white lines that are 4.5±1.0 nm wide, similar to the wall thickness observed by SAXS[7]. The appearance of white lines is consistent with peptide-rich nanotube walls that exclude uranyl acetate stain. Additionally, during TEM sample preparation the drying down of samples on the TEM grid surface causes the flexible hollow nanotubes to flatten to an observed width of 70-85 nm (~1/2 the circumference of a 52 nm diameter nanotube determined by SAXS[7]).

In order to clearly visualize the hollow nanotube walls, methods were developed to capture nanotubes in various orientations while avoiding any flattening of the flexible nanotubes. Cross sectioning of epoxy resin embedded KLVFFAL nanotubes directly visualizes the nanotubes down the hollow center (Figure 3-8b). Addition of the epoxy resin displaces the aqueous solvent at the nanotubes center, and avoids nanotube collapse that occurs during sample dehydration. From TEM images, KLVFFAL nanotubes have a 45±10 nm diameter and a wall thickness of 4±1 nm.

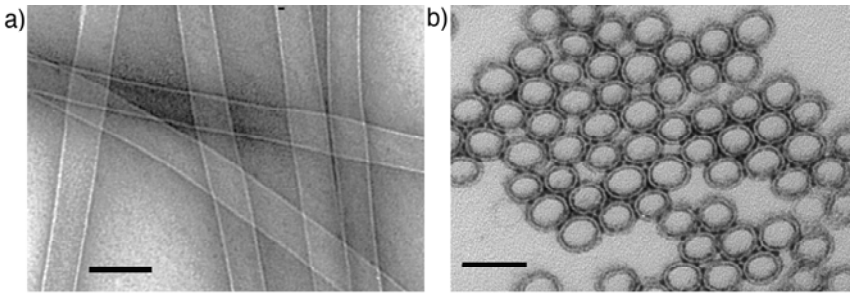

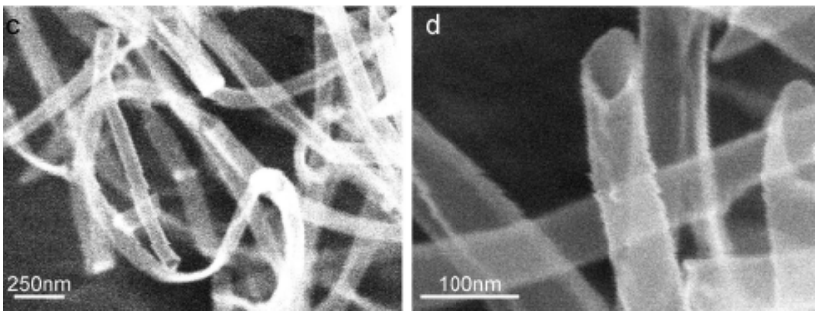

Figure 3-8: Various electron microscopy methods used to visualize 1.3 mM KLVFFAE nanotubes under acidic conditions. (a) Uranyl acetate negatively stained TEM image of dried and flattened KLVFFAL nanotubes, (b) cross-sectioned epoxy resin embedded assemblies oriented perpendicular to the tube long axis. (c) and (d) cryoetch HR-SEM.

For cryo-etch HR-SEM samples were flash frozen in liquid ethane to avoid crystallized water and promote vitreous ice formation. The solution was then etched under sublimation conditions to remove bulk water and coated with a thin 2nm layer of chromium. Cryo-etch HR-SEM images (Figure 3-8c,d) highlight the flexible nature of the hollow peptide nanotubes.

Probing Bilayer Structure

As a preliminary NMR study of bilayer structure ^{13}C CP-MAS spectrum was recorded for KLVFFAE and KLVFFAL nanotubes assemblies and KLVFFAE fibers (Figure 3-9). The acetate carbonyl chemical shift varies between 172-175 ppm. The most notable difference is comparison of wet versus lyophilized KLVFFAE fibers, as a new chemical shift emerges downfield at 175 ppm. Therefore, it appears the acetate carbonyl chemical shift is sensitive to the degree of hydration but only effects a partial population of acetate carbonyls. The significant broadness of chemical shifts for nanotube assemblies could also be due to a combination of chemical environments that vary in degree of solvent exposure.

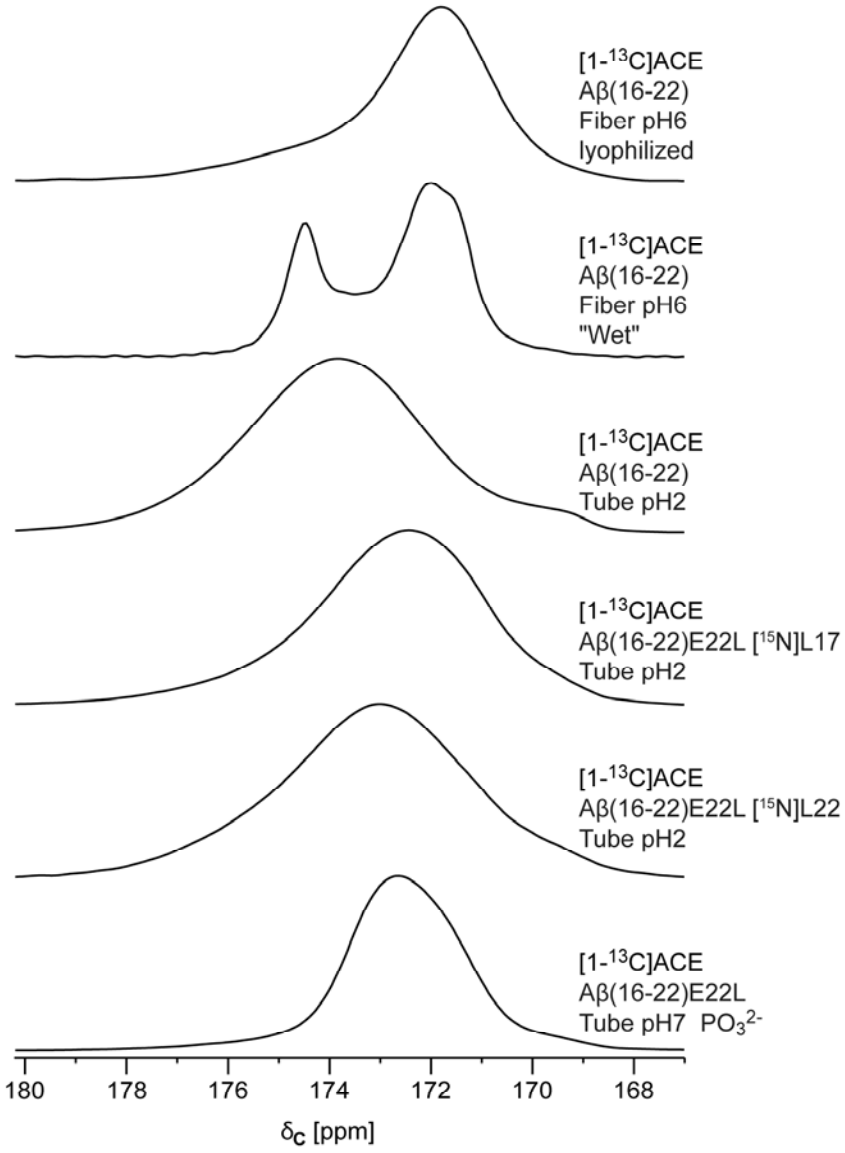

Figure 3-9: Chemical Shifts of [1-^{13}C]CH_3CO-KLVFFAX.

As shown in Chapter 2, $^{13}C\{^{15}N\}$ REDOR measurements have indicated that the acidic KLVFFAE peptides form extended anti-parallel out-of-register β-sheets that are approximately 2.4±0.2 nm wide[29]. TEM micrographs (Figure 3-8) indicate a wall thickness of 4.5±1.0 nm consistent with SAXS measurements (4.3±0.2 nm[7]). It then appears that the termini stacking of two amyloid sheets (2 x 2.4±0.2 nm = 4.8 ± 0.4 nm) could account for the wall thickness.

Additionally, neutral KLVFFAE peptides form fibers (Chapter 2) with widths of 5±1 nm may also consistent with peptides organized as a bilayer interface[29]. To test for termini interactions within fiber and nanotube assemblies ^{13}C labels were incorporated into the N-terminal acetate carbonyl. As shown in Figure 3-10, incorporation of ^{13}C labels within an anti-parallel β-sheet scaffold regularly spaces the ^{13}C isotopes 9.4Å in the hydrogen-bonding dimension. While side-chain interactions separate laminated β-sheets by 9.9Å. Within this cross-β scaffold N-terminal acetate ^{13}C carbonyls are spaced too far away to have any observed dipolar couplings in the hydrogen bonding and lamination directions. Therefore, any observed dipolar couplings can be assigned to ^{13}C acetate carbonyls in close proximity in the termini direction.

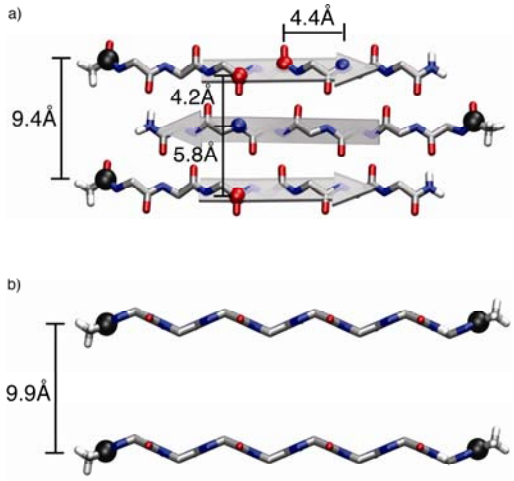

Figure 3-10: (a) β-Sheet structural model with distance constraints (diffraction and NMR via red and blue spheres). Acetate carbonyl labeling scheme (black spheres) to probe the bilayer interface. The distance between the acetate carbonyls is 9.4 Å/9.9Å is too far to have any significant dipolar coupling. (b) β-Sheet structural model rotated 90° to visualize the lamination of two sheets.

Prior to probing the bilayer interface with ^{13}C acetate carbonyls, it was necessary to orient the N-terminal acetate with respect to the central peptide backbone. To test the orientation of the N-terminal acetate a [1-^{13}C]CH_3CO-K[^{15}N]LVFFAE-NH_2 labeling scheme was designed to

measure the distance between the ^{13}C acetate carbonyl and ^{15}N backbone nitrogen of leucine-17. Previous REDOR measurements (Chapter 2) indicated that L17 had a β-sheet conformation and was hydrogen bonded to E22[29]. BS-REDOR analysis of ^{13}C {^{15}N } REDOR data points indicate 30% of the acetates are bent, while 70% are arranged as extended β-sheets.

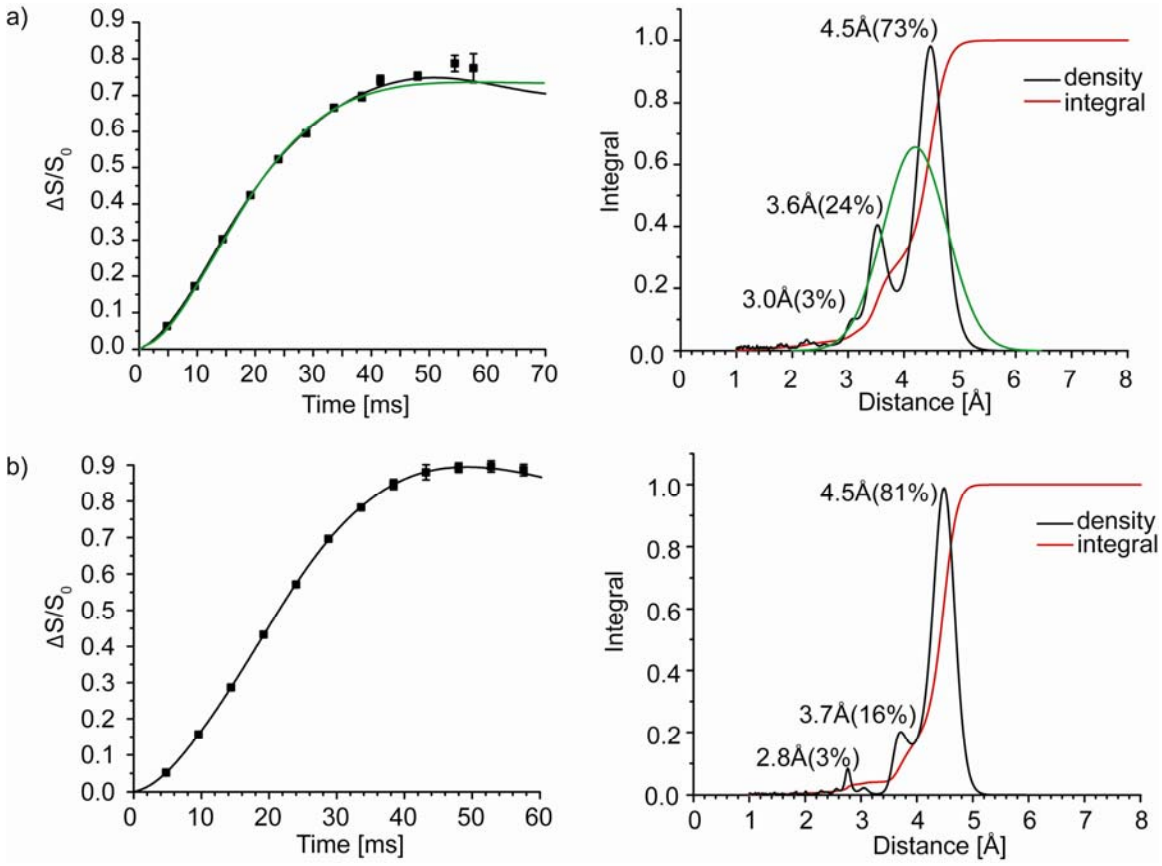

Figure 3-11: ^{13}C {^{15}N } REDOR of [1-^{13}C]CH_3CO-K[^{15}N]LVFFAE-NH_2 (a) nanotubes and (b) fibers.

Upon initial inspection, the REDOR data could be fit to a single Gaussian distribution (green curve). However, an unbiased fit to the data using Boltzmann-Statistics maximum entropy approach indicates the presence of two major distance distributions. These two populations are consistent with two conformational populations of the N-terminal acetate as observed in a conformational search (Figure 3-12).

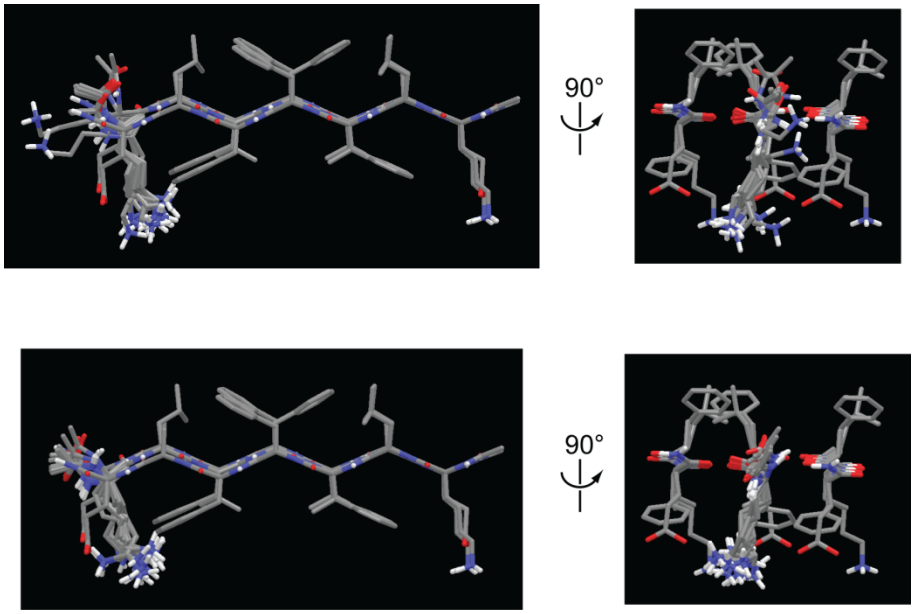

Figure 3-12: Family of structures from MMFFs conformational search consistent with acetate ^{13}CO -^{15}N-L17 fiber distances of 3.6Å (top) and 4.5Å (bottom).

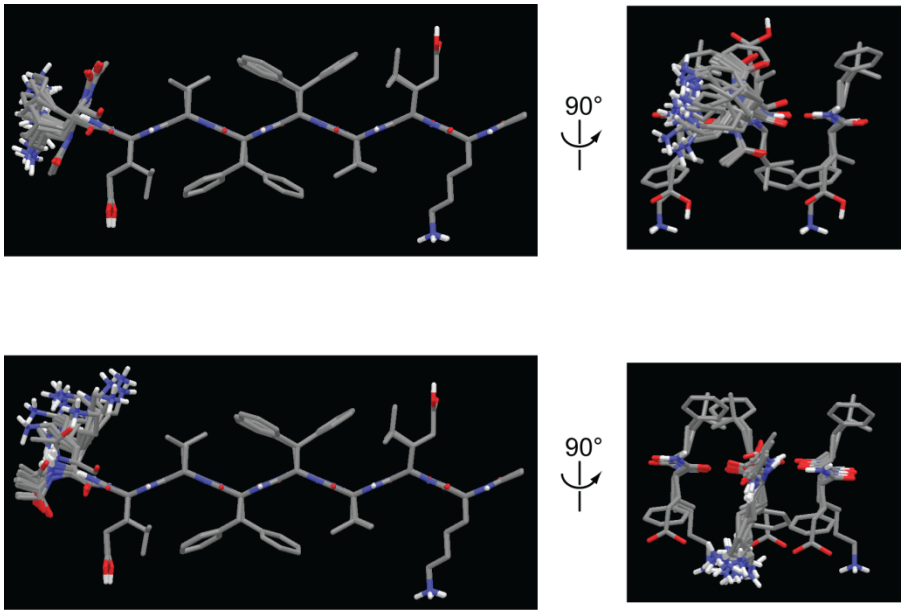

Figure 3-13:Family of Structures from MMFFs conformational search consistent with KLVFFAE nanotube acetate ^{13}CO -^{15}N-L17 distances of 3.6Å (top) and 4.5Å (bottom).

Given that the acetate group appears to be in an extended conformation at the bilayer interface, it provides a good probe for peptide termini interactions at the bilayer interface. In the proposed labeling scheme acetate carbonyls are spaced 9.4Å within hydrogen-bonded β-sheets, and 9.9Å across laminated β-sheets. This spacing between known closest peptide neighbors are too long to have any observable couplings, therefore any observable homonuclear dipolar couplings can be attributed to acetates in close proximity (<6Å) at the bilayer interface. DQF-DRAWS measured observable dipolar couplings and DQ buildup curves were fit to an infinite array of acetate carbonyl spins with ^{13}CO-^{13}CO distances of 5.1Å ±0.2Å for nanotubes and 4.9Å ±0.2Å for fibers. These results provide direct evidence for interaction of termini in close proximity creating a bilayer interface.

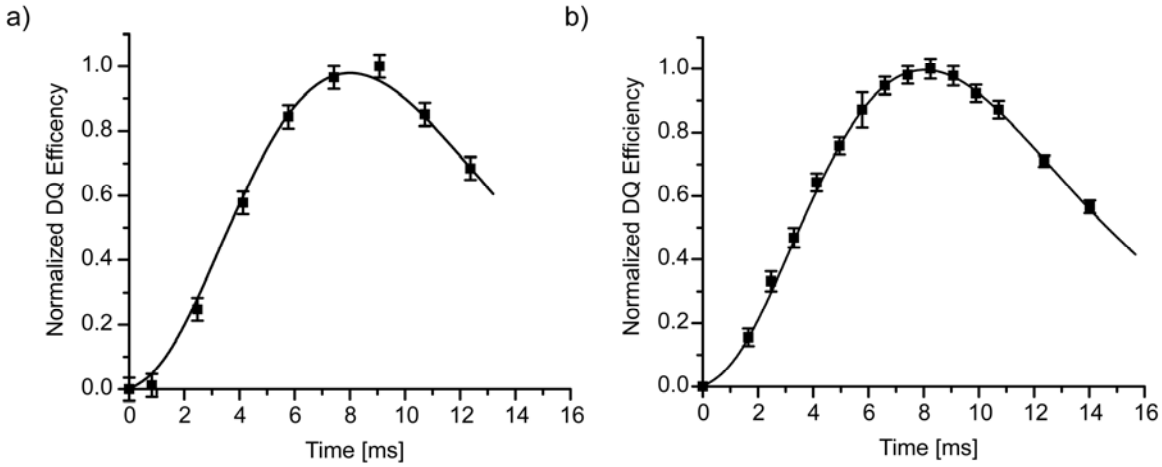

Figure 3-14: a) ^{13}C DQF DRAWS of 1.0 mM [1-^{13}C]CH_3CO-K[^{15}N]LVFFAE-NH_2 peptide nanotubes assembled in 40% acetonitrile 0.1% TFA and bundled with Na_2SO_4. Solid line is simulated DQF-DRAWS curve for a ^{13}C -^{13}C distance of 5.1 Å and T_2DQ = 6.4 ms. b) and fibers assembled under neutral conditions in 40% acetonitrile. Solid line is simulated DQF-DRAWS curve for a ^{13}C -^{13}C distance of 4.9 Å and T_2DQ = 7.7 ms

To further characterize and quantify peptide termini interactions both ^{13}Cs and ^{15}Ns [1-^{13}C]CH_3CO-KLVFFAE-[^{15}N]NH_2 were incorporated at the N-termini and C-termini respectively. The Isotopically enriched peptides were synthesized, purified and allowed to assemble in 40% acetonitrile under acidic conditions.

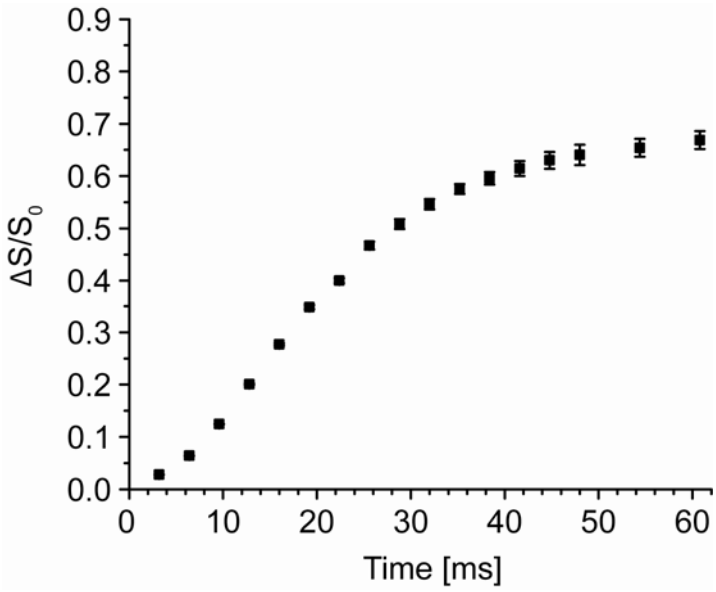

Figure 3-15: ^{13}C{^{15}N} REDOR of 1.3 mM [1-^{13}C]CH_3CO-KLVFFAE-[^{15}N]NH_2 in 40% acetonitrile 0.1% TFA.

Analysis of REDOR measurements indicates data does not fit a simple two-spin system within a bilayer interface as $\Delta S/S_0$ plateaus at 0.7. These differences may be attributed to three distinct types of termini interfaces: (1) buried bilayer interface, (2) bundled tube interface, and (3) solvent exposed surfaces. Design of future experiments to distinguish these interfaces is needed to aid in fitting of sample to more complex spin systems.

Probing the inner and outer bilayer surfaces

In contrast to lipid bilayers, KLVFFAE peptide bilayers contain a polar bilayer interface with a high density of positively charged lysines. Stabilization of the positively charged lysine may depend upon cooperative K-E cross-leaflet interactions. To test if K-E interactions are critical to bilayer formation E22 was mutated to leucine (E22L). KLVFFAL also have wall thicknesses that could accommodate two extended peptides[29], however no residue within the sequence is capable of passivating lysine's buried positive charge. To test, [1-^{13}C]CH_3CO-K[^{15}N]LVFFAL-NH_2 peptide was synthesized, purified and assembled in 40% acetonitrile under acidic conditions. DQF-DRAWS measured observable dipolar couplings that could be fit to an infinite array of acetate carbonyl spins with ^{13}CO-^{13}CO distances of 5.2Å ±0.2Å.

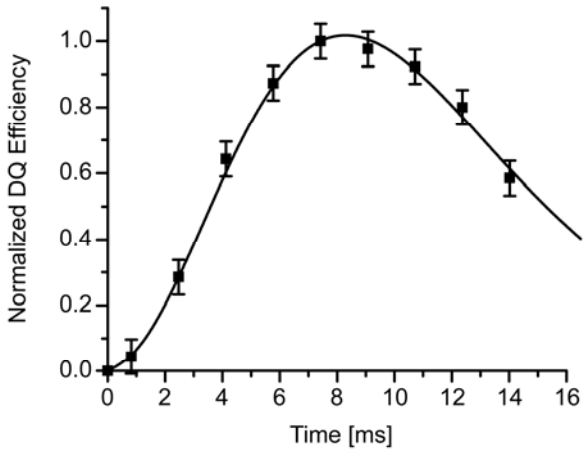

Figure 3-16: a) ^{13}C DQF-DRAWS of 1.3 mM [1-^{13}C]CH_3CO-K[^{15}N]LVFFAL-NH_2 peptide nanotubes assembled in 40% acetonitrile 0.1% TFA and bundled with Na_2SO_4. Solid line is simulated DQF-DRAWS curve for a ^{13}C -^{13}C distance of 5.2 Å and T_2DQ = 12 ms.

As KLVFFAL nanotubes contain termini interface, it suggests cooperative K-E interactions are not required for bilayer formation. Among solved protein structures, lysine is the least frequently buried residue and its charge must be passivated at the bilayer interface. A potential candidate for lysine's counter ion is TFA, as it used for peptide cleavage from solid-phase synthesis resin and TFA is also used as counterion during HPLC purification. To test if

TFA (CF_3COO^-) served as lysine's counter ion, ^{13}C was incorporated near lysine-16 into the N-terminal acetate carbonyl and $^{13}C\{^{19}F\}$REDOR was used to detect ^{13}C-^{19}F dipolar couplings.

However, Figure 3-17 indicates $\Delta S/S_0$ plateau at 0.94 indicating nearly all lysines utilize CF_3COO^- as a counter ion. It is possible that surface bound TFA could be displaced during the bundling process with HPO_4^{2-} or SO_4^{2-}. Potentially, the instantaneous increase in sodium sulfate from 0 to 9 mM would immediately bundle tubes together and trap TFA ions at the surface between nanotubes. To test this idea, the weaklier bundling Na_2HPO_4 was added via a slow addition rate (2mM/Hr) to a final concentration of 9 mM.

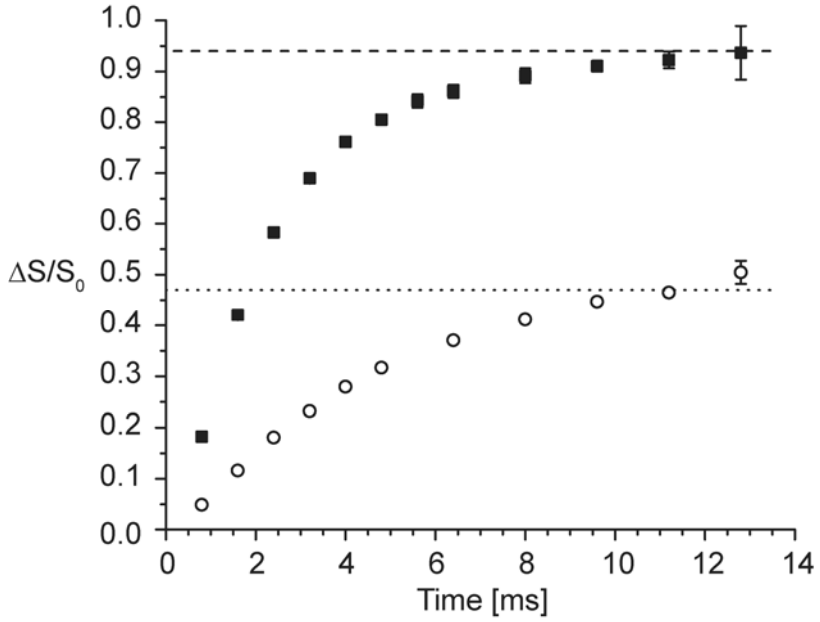

Figure 3-17: $^{13}C\{^{19}F\}$ REDOR of [1-^{13}C]CH_3CO-KLVFFAL-NH_2 tubes in 40% acetonitrile containing 0.1% TFA. Black squares are for tubes bundled with a single aliquot of Na_2SO_4 and hollow circles are for bundling by slow addition of Na_2HPO_4. The dashed black horizontal line at a $\Delta S/S_0$ value of 0.94 represents dephasing of 100% of the acetate carbonyl ^{13}C nuclei (see Experimental Section). The dotted horizontal line at a $\Delta S/S_0$ value of 0.47 (50% of 0.94)

indicates the maximum dephasing if only half of the acetate carbony ^{13}C nuclei are close to a CF_3COO^- ion. Unless shown, error bars are the size of the data points.

Bundling the nanotubes[16] at a slower rate resulting in only 50% of the N-terminal acetate carbonyls being near a CF_3COO^-. This analysis indicates most of the CF_3COO^- anions on the surface have been displaced by phosphate, whereas remaining half of CF_3COO^- anions remained buried at the bilayer interface. Figure 3-18 compares different leaflet models in which the number of layers is increased from one to four.

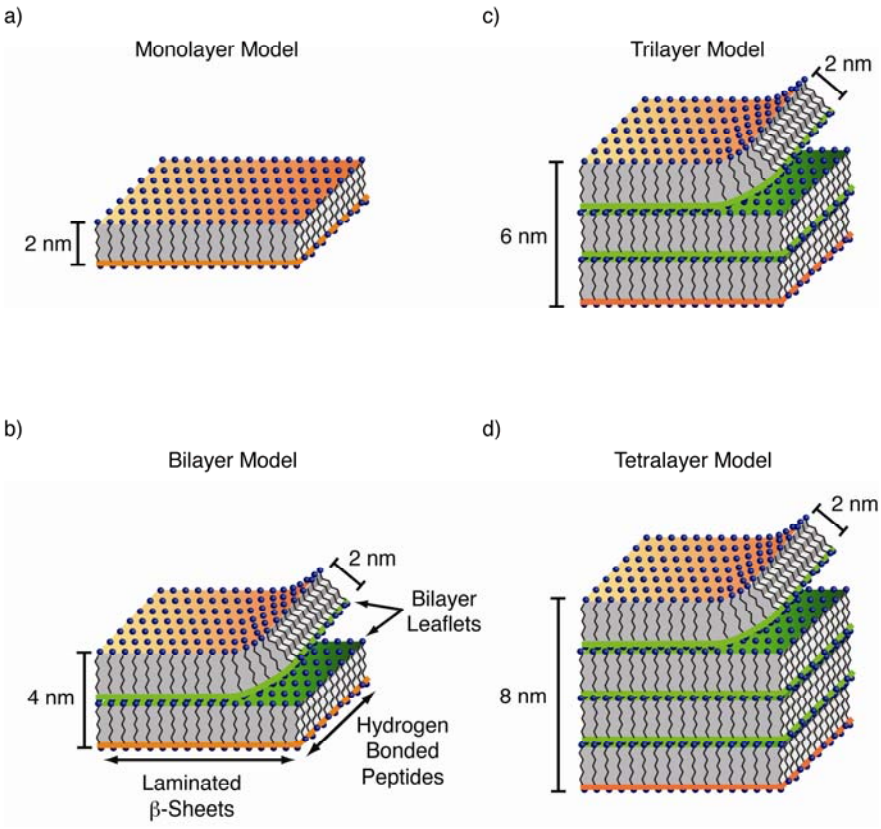

Figure 3-18: Location of sulfate or phosphate (orange) and TFA (green) ions for peptide (**a**) monolayer, (**b**) bilayer, (**c**) trilayer and (**d**) tetralayer after slow bundling as shown in Fig.5b – main text. Wall thickness measured by AFM height, SAXS and TEM are 4 ± 1 nm and consistent with a bilayer model (**b**).

The ability of phosphate to displace TFA would depend on surface exposure for monolayer (100% displaced – 0.0 $\Delta S/S_0$), bilayer (50% displaced – 0.47 $\Delta S/S_0$), trilayer (33% displaced – 0.62 $\Delta S/S_0$) and tetralayer models (25% displaced – 0.71 $\Delta S/S_0$). As shown in Figure 3-19, the actual REDOR dephasing values are consistent with bilayer interface and reveals two distinct equal population chemical environments for the N-terminal acetate: a buried bilayer interface and a solvent exposed interface.

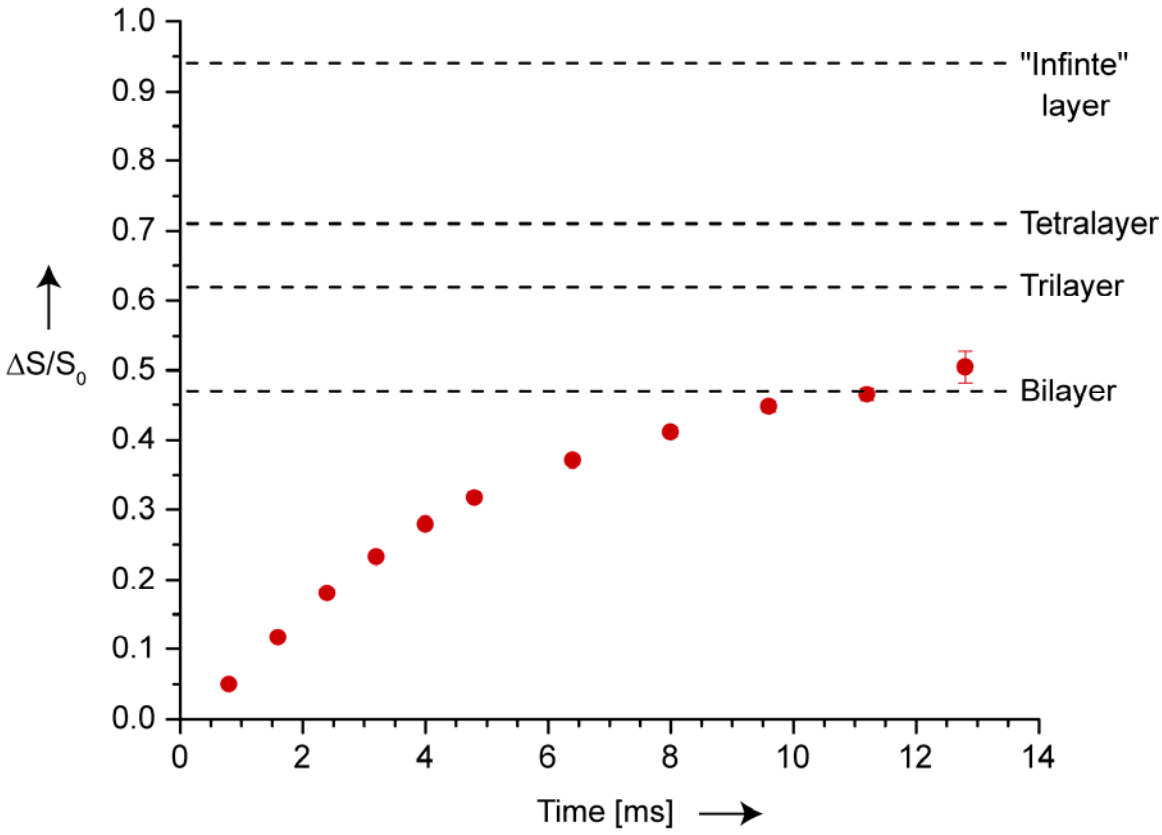

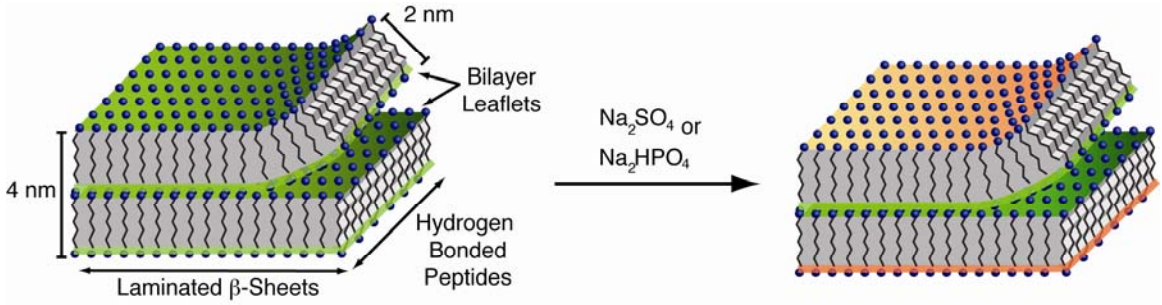

Figure 3-19: Theoretical $^{13}C\{^{19}F\}$REDOR dephasing plateaus for models of slowly bundled [1-^{13}C]CH_3CO-KLVFFAL-NH_2 tubes shown in Figure S4. Dotted lines represent expected REDOR dephasing for titration of surface bound TFA in 4 different models: "infinite" layer, tetralayer, trilayer, and bilayer models. Bottom panel shows model of titration of surface bound TFA ions (green) with sulfate or phosphate ions (orange), and a buried bilayer interface containing TFA ions that passivate lysine's positive charge.

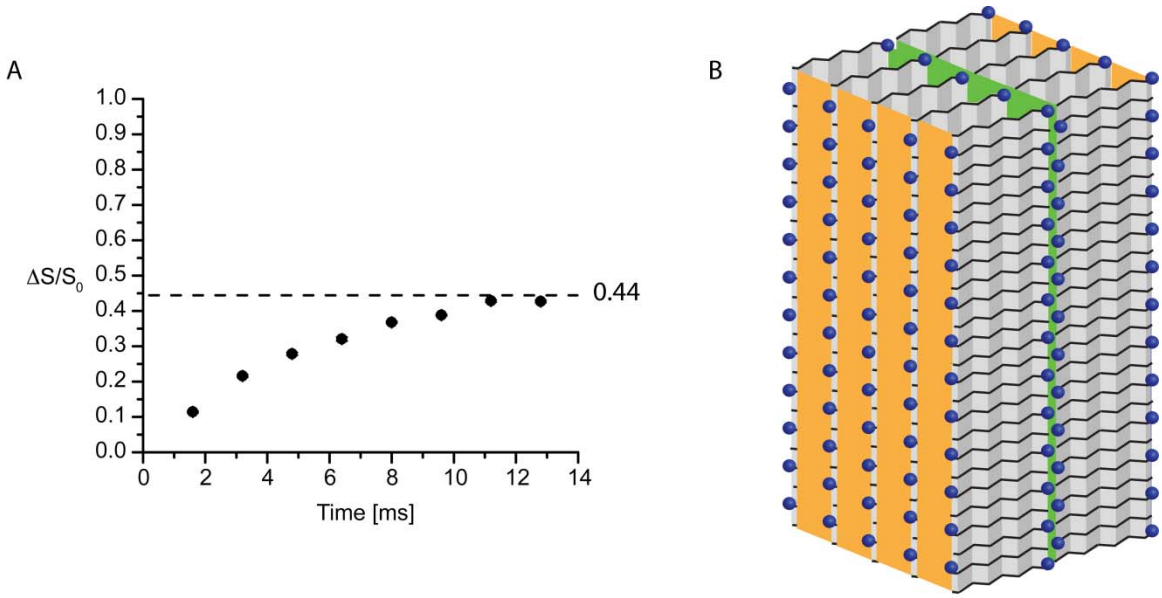

Figure 3-20: (A) $^{13}C\{^{19}F\}$ REDOR of [1-^{13}C]CH_3CO-KLVFFAE-NH_2 assembled in neutral conditions (B) Cartoon Model of KLVFFAE fiber of 5 β-sheets laminated together and form a bilayer structure. [1-^{13}C] acetates (blue spheres), TFA rich bilayer interface (green), and TFA free solvent exposed surface (orange).

Calculation of Surface-to-Volume Ratio

While the primary sequence of amyloid peptides are traditionally thought of as highly hydrophobic, here we report an amyloid structure with a charge burial rate of 8 %, compared with

typical well-folded globular proteins with charge burial rates 4-7%[30]. Previously, it was shown that the peptide $+NH_3$-KLVFFAE-NH_2 containing 2+ charge/peptide assembled into hollow nanotubes with a ~4 nm wall under acidic condition[10]. If both ionizable groups remain charged, then ~13% of buried residues would be charged – nearly double the average burial rate of globular protein[30]. Analysis of buried ionizable residue frequency within crystal structures indicates a correlation with a protein's surface area to volume ratio (SVR)[31]. Generally, larger protein cores can more easily accommodate penalties from burial of ionizable groups. Typical globule proteins have a SVR=0.19-0.45 Å-1, where those with lower SVR are observed to have more ionizable groups within the buried core relative to proteins with higher SVR values[31].

An estimation of the exposed surface area at the termini was obtained by building a 10 hydrogen bonded x10 laminated peptide system based off previous Molecular Dynamics results. The accessible solvent surface was calculated using standard 'rolling ball' algorithms[32,33] that probe the accessible surface along that termini surface. The surface area was calculated for the laminate surface(162±21Å^2), hydrogen bonding surface (406±22Å^2) and the termini surface(75±11Å^2).

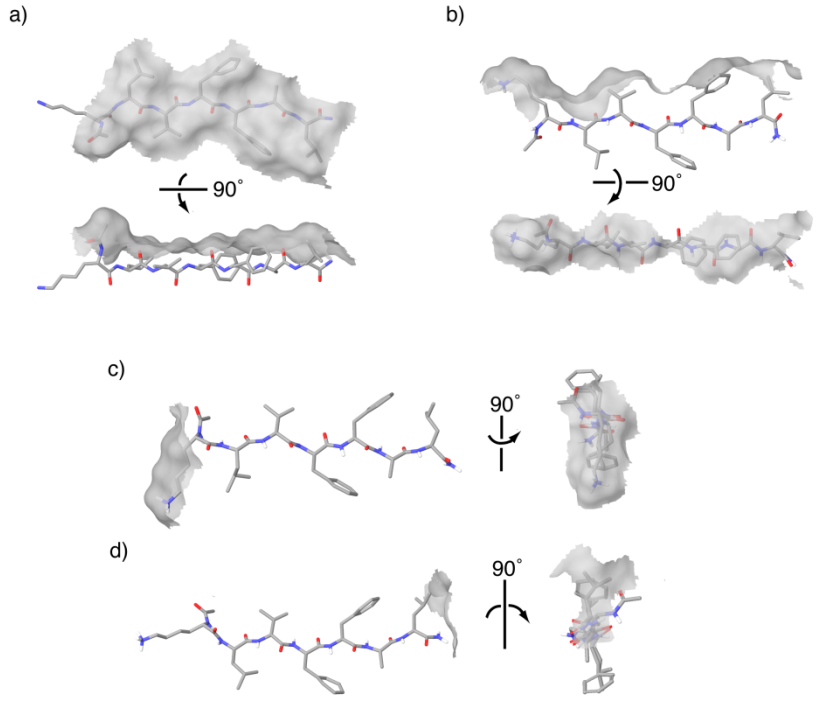

Figure 3-21: Illustration of surfaces that would be desolvated upon two peptides interacting through (a) backbone hydrogen bonding, (b) beta-sheet lamination, and (c) termini interactions.

The surface area for a smooth 52 nm diameter hollow cylinder with a wall thickness of 4 nm and a height of 1000 nm is 3.0x10^{7}Å^2 and a volume of 6.0 x10^{8}Å^2. To correct for the rugged nature of the peptide nanotube the ratio of the accessible solvent surface (ASA) for the termini surface (75±11Å^2) to the expected smooth surface for one peptide (4.7Å*9.9Å=46.5 Å^2) was used to give a corrected surface area of 4.9x10^{7}Å^2. Using the corrected surface area, the SVR for peptides organized as a bilayer nanotube is 0.08±0.01 Å^{-1}. A similar calculation for a micro long

fiber yields a SVR of 0.13±0.02 $Å^{-1}$. In contrast to globular proteins the SVR for cross-β organization of KLVFFAE nanotubes is approximately 2-fold lower (SVR=0.08Å-1). Therefore, the enlarged inter-molecular protein core of cross-β structures makes amyloid less susceptible to destabilization by buried charge than common intramolecular folds of globular proteins.

Conclusions

Here we have provided direct evidence that short amyloid peptides can organize into a bilayer structure with similar long rang organization, yet the local arrangement is quite different. The anti-parallel β-sheet organization places lysines on the outer solvent exposed surface like a phospholipid membranes, but in contrast also places half of the lysines at the center of the bilayer creating a polar bilayer interface composed with high positive charge density passivated by TFA counterions. Unlike passive phospholipid bilayers, peptide bilayers may be able the functionality of the bilayer interior as well as the grid-like surface for construction of unique nanomaterials.

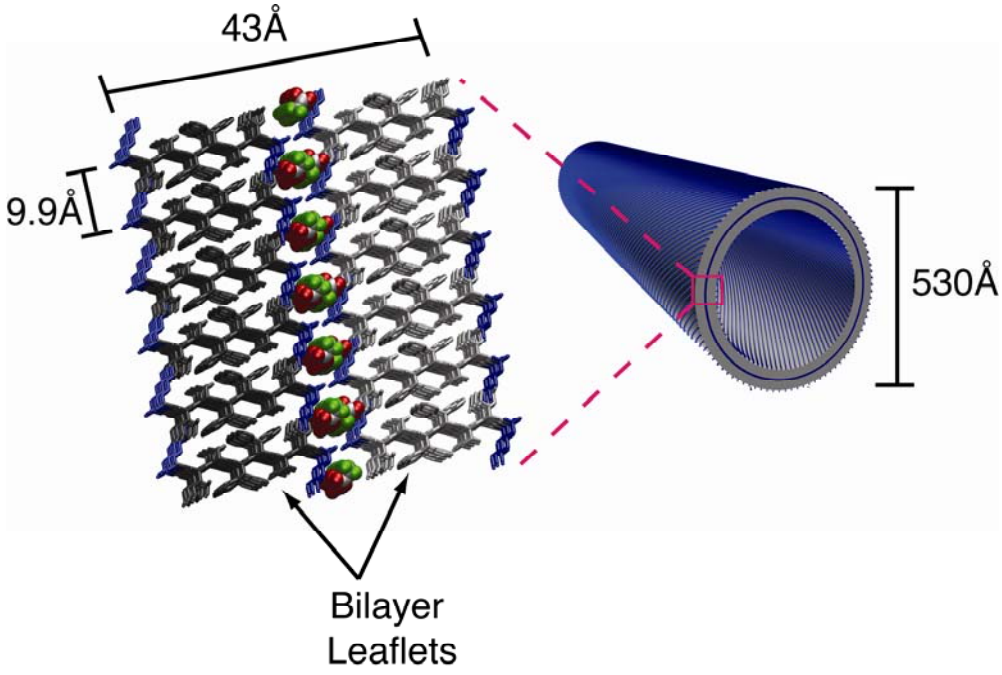

Figure 3-22: Bilayer structural model. Outer leaflet residues are colored black, inner leaflet residues are colored gray. Anti-parallel β-sheets place lysines (blue) at the surface and buried within the bilayer interface. TFA ions (colored by atom type – F(green), C(silver), O(red)) sufficiently passivate lysines. The resulting organization yields a patterned surface illustrated by stripes that helically spiral along the long tube.

Unlike lipids, the amyloid peptide bilayers are created from paracrystalline β-sheet secondary structure. KLVFFAL peptides associate through backbone hydrogen bonding which provides a large hydrophobic surface area of contact (406±22Å^2). The long hydrogen bonded β-sheets helically wrap around the long tube axis with a pitch angle of 25±2°. Association of 140±10 β-sheet faces (162±21Å^2) through lamination contributes to the 52 nm diameter of the hollow tubes. While an end-to-end termini surface (75±11Å^2) interaction forms the bilayer interface. The relative differences in desolvated surfaces areas likely gives rise to the anisotropic growth needed to form a long hollow nanotube composed of just a bilayer. In contrast the bending of laminating β-sheets to form helical ribbons would result in the inner leaflet being more compressed than the

outer leaflet. Therefore this bending likely limits association of additional leaflets and sets the wall thickness at 4.3±0.3 nm.

In comparison to SVR of globular protein folds (0.19-0.45$Å^{-1}$)[31], the intermolecular association of peptides into a cross-β structure results in a significantly lower SVR (0.08-0.13). Analysis of buried ionizable residue frequency within crystal structures indicates a correlation with a protein's surface area to volume ratio (SVR)[31]. Generally, larger protein cores can more easily accommodate penalties from burial of ionizable groups. Typical globule proteins have a SVR=0.19-0.45 $Å^{-1}$, where those with lower SVR are observed to have more ionizable groups within the buried core relative to proteins with higher SVR values[31]. In contrast to globular proteins the SVR for cross-β organization of KLVFFAE nanotubes is approximately 2-fold lower (SVR=0.08$Å^{-1}$). Therefore, the enlarged protein core of cross-β structures' makes amyloid less susceptible to destabilization by buried charge and a potential common structural fold for all proteins. Taken together construction of bilayer membranes out of simple peptides opens the door to the design new patterned bilayer surfaces with the local order of an enzyme and the long-range morphology of a cellular membrane.

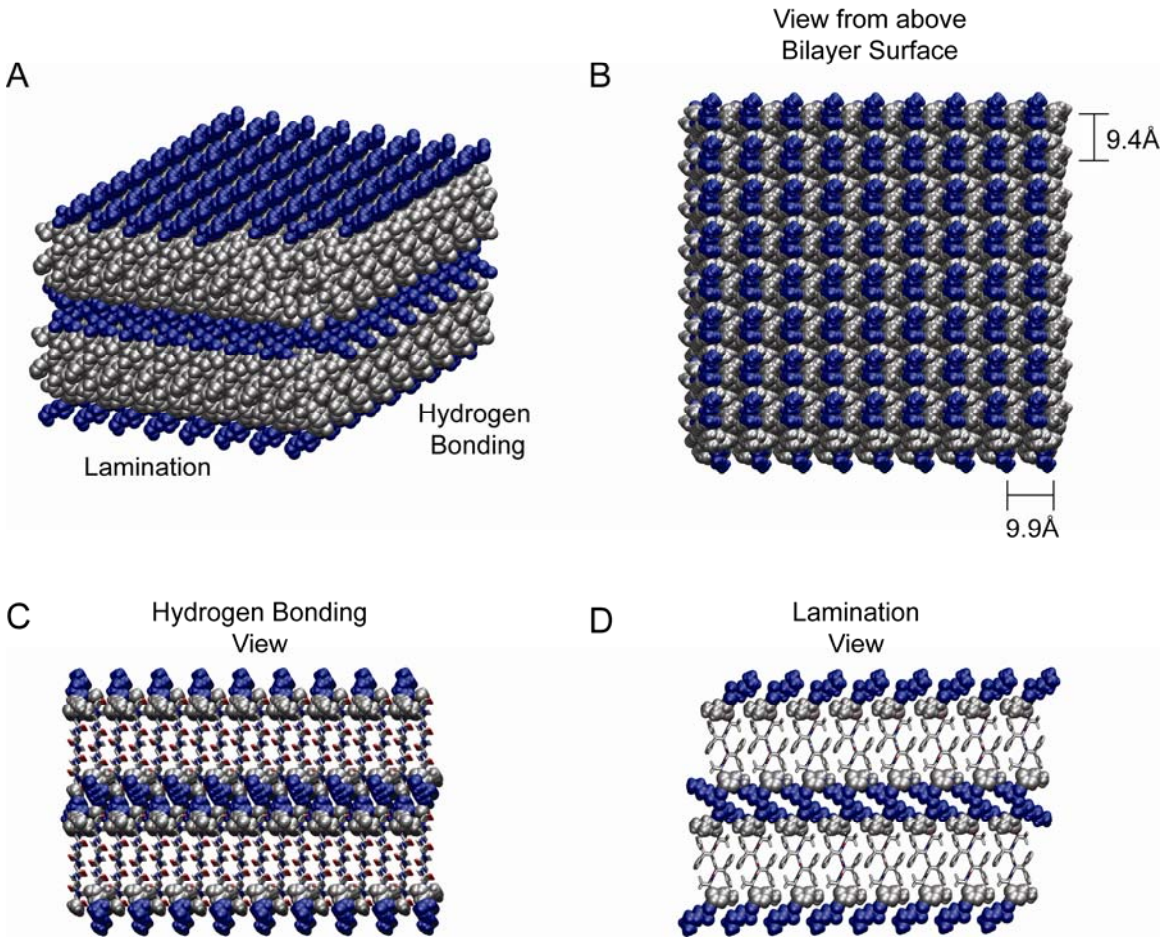

Figure 3-23: KLVFFAE Peptide Bilayer as a patterned surface grid. (A) Overall view of the bilayer structure, (B) Top view highlighting the patterned surface where positively charged lysines (blue) emerging from a hydrophobic surface (gray) that are spaced 9.4Å in the hydrogen bonding direction and 9.9Å in the lamination direction. View of bilayer surface directly perpendicular to the hydrogen-bonding dimension (C) and lamination dimension (D).

References

1. Vonck J, Schafer E (2009) Supramolecular organization of protein complexes in the mitochondrial inner membrane. Biochimica Et Biophysica Acta-Molecular Cell Research 1793: 117-124.

2. Amunts A, Nelson N (2009) Plant Photosystem I Design in the Light of Evolution. Structure 17: 637-650.

3. Singer SJ, Nicolson GL (1972) Fluid Mosaic Model of the structures of the cell-membranes Science 175: 720-&.

4. Hianik T (2006) Structure and physical properties of biomembranes and model membranes. Acta Physica Slovaca 56: 687-806.

5. Santoso S, Hwang W, Hartman H, Zhang SG (2002) Self-assembly of surfactant-like peptides with variable glycine tails to form nanotubes and nanovesicles. Nano Letters 2: 687-691.

6. Vauthey S, Santoso S, Gong HY, Watson N, Zhang SG (2002) Molecular self-assembly of surfactant-like peptides to form nanotubes and nanovesicles. Proceedings of the National Academy of Sciences of the United States of America 99: 5355-5360.

7. Lu K, Jacob J, Thiyagarajan P, Conticello VP, Lynn DG (2003) Exploiting amyloid fibril lamination for nanotube self-assembly. J Am Chem Soc 125: 6391-6393.

8. Yang YL, Khoe U, Wang XM, Horii A, Yokoi H, et al. (2009) Designer self-assembling peptide nanomaterials. Nano Today 4: 193-210.

9. Lu K, Conticello VP, Lynn DG (2004) In: Conticello VP, Chilkoti A, Atkins E, Lynn DG, editors. Mater Res Soc Synp Proc 826E. Warrendale, PA. pp. V1.6.

10. Lu K (2005) Discovery of Diverse Peptide Nanotube Architecture from the Self-assembly of Designed Amyloid-β Cassettes. Atlanta: Emory University. 257 p.

11. de la Paz ML, Goldie K, Zurdo J, Lacroix E, Dobson CM, et al. (2002) De novo designed peptide-based amyloid fibrils. Proceedings of the National Academy of Sciences of the United States of America 99: 16052-16057.

12. Balbach JJ, Ishii Y, Antzutkin ON, Leapman RD, Rizzo NW, et al. (2000) Amyloid Fibril Formation by Aβ16-22, a Seven-Residue Fragment of the Alzheimer's β-Amyloid Peptide, and Structural Characterization by Solid State NMR. Biochemistry 39: 13748-13759.

13. Marshall KE, Hicks MR, Williams TL, Hoffmann SV, Rodger A, et al. (2010) Characterizing the Assembly of the Sup35 Yeast Prion Fragment, GNNQQNY: Structural Changes Accompany a Fiber-to-Crystal Switch. Biophysical Journal 98: 330-338.

14. Castelletto V, Hamley IW, Harris PJF, Olsson U, Spencer N (2009) Influence of the Solvent on the Self-Assembly of a Modified Amyloid Beta Peptide Fragment. I. Morphological Investigation. Journal of Physical Chemistry B 113: 9978-9987.

15. Castelletto V, Hamley IW, Hule RA, Pochan D (2009) Helical-Ribbon Formation by a beta-Amino Acid Modified Amyloid beta-Peptide Fragment. Angewandte Chemie-International Edition 48: 2317-2320.

16. Lu K, Guo L, Mehta AK, Childers WS, Dublin SN, et al. (2007) Macroscale assembly of peptide nanotubes. Chem Commun (Camb) 2729-2731.

17. Gregory DM, Mehta MA, Shiels JC, Drobny GP (1997) Determination of local structure in solid nucleic acids using double quantum nuclear magnetic resonance spectroscopy. Journal of Chemical Physics 107: 28-42.

18. Bower PV, Oyler N, Mehta MA, Long JR, Stayton PS, et al. (1999) Determination of torsion angles in proteins and peptides using solid state NMR. Journal of the American Chemical Society 121: 8373-8375.

19. Mehta MA, Eddy MT, McNeill SA, Mills FD, Long JR (2008) Determination of peptide backbone torsion angles using double-quantum dipolar recoupling solid-state NMR Spectroscopy. Journal of the American Chemical Society 130: 2202-2212.

20. Fung BM, Khitrin AK, Ermolaev K (2000) An improved broadband decoupling sequence for liquid crystals and solids. J Magn Reson 142: 97-101.

21. Gregory DM, Benzinger TL, Burkoth TS, Miller-Auer H, Lynn DG, et al. (1998) Dipolar recoupling NMR of biomolecular self-assemblies: determining inter- and intrastrand distances in fibrilized Alzheimer's β-amyloid peptide. Solid State Nucl Magn Reson 13: 149-166.

22. Bak M, Rasmussen JT, Nielsen NC (2000) SIMPSON: A general simulation program for solid-state NMR spectroscopy. Journal of Magnetic Resonance 147: 296-330.

23. Liu P, Ni R, Mehta AK, Childers WS, Lakdawala A, et al. (2008) Nucleobase-Directed Amyloid Nanotube Assembly. Journal of the American Chemical Society 130: 16867-16869.

24. Pan Y, Gullion T, Schaefer J (1990) Determination fo C-N internuclear distances by Rotational-Echo Double Resonance NMR of Solids Journal of Magnetic Resonance 90: 330-340.

25. Sinha N, Schmidt-Rohr K, Hong M (2004) Compensation for pulse imperfections in rotational-echo double-resonance NMR by composite pulses and EXORCYCLE. J Magn Reson 168: 358-365.

26. Gullion T, Vega S (1992) A Simple Magic Angle Spinning NMR Experimeng for the Dephasing of Rotational Echoes of Dipolar Coupled Homonuclear Spin Pairs Chemical Physics Letters 194: 423-428.

27. Wooley KL, Klug CA, Tasaki K, Schaefer J (1997) Shapes of dendrimers from rotational-echo double-resonance NMR. Journal of the American Chemical Society 119: 53-58.

28. Gullion T, Baker DB, Conradi MS (1990) New, Compensated Carr-Purcell Sequences. Journal of Magnetic Resonance 89: 479-484.

29. Mehta AK, Lu K, Childers WS, Liang Y, Dublin SN, et al. (2008) Facial Symmetry in Protein Self-Assembly. J Am Chem Soc 130: 9829-9835.

30. Miller S, Janin J, Lesk AM, Chothia C (1987) Interior and Surface of Monomeric Proteins Journal of Molecular Biology 196: 641-656.

31. Shirota M, Ishida T, Kinoshita K (2008) Effects of surface-to-volume ratio of proteins on hydrophilic residues: Decrease in occurrence and increase in buried fraction. Protein Science 17: 1596-1602.

32. Connolly ML (1983) Analytical Molecular-Surface Calculation Journal of Applied Crystallography 16: 548-558.

33. Shrake A, Rupley JA (1973) Environment and Exposure of protein atoms - lysozyme and insulin Journal of Molecular Biology 79: 351-371.

Chapter 4 : The Phases of Peptide Oligomerization

Surfactant molecules display complex phase behavior when dispersed as a liquid colloid in aqueous environments. Above a certain critical micelle concentration (CMC), phases emerge that include micelle, ellipsoid, cylinder, and bilayer[1]. The molecular structure and concentration of the amphiphilic as well as temperature, ionic strength, pH and solvent conditions all impact the phase behavior and propagate into long-range paracrystalline assemblies.

Analysis of amyloid peptide assembly pathways have identified numerous intermediates that appear to have the structural diversity observed in surfactant phases, yet unlike surfactants these phases only appear as transient intermediates as opposed to thermodynamically stable surfactant phases. For example, amyloid monomers have been observed to assemble into short metastable filaments[2,3,4,5,6,7,8] and 5-25 nm spherical oligomers[2,9,10,11,12,13,14] that have been observed to structurally transition into mature elongated fibrils. The oligomers have been suggested to be neurotoxic and etiologically relevant to many amyloid diseases[13,15,16,17]. Yet, the environmental conditions that bias and stabilizes the neurotoxic oligomer remains unclear.

The nucleating core of the Aβ peptide of Alzheimer's disease, Aβ(16-22) or KLVFFAE, may now be the simplest and best-studied model for amyloidogenic assembly[18,19,20,21,22,23,24,25,26,27,28,29,30]. Molecular dynamics (MD) studies of its assembly[23] reveal low-energy folded conformations, that unlike native proteins, maintain hydrophobic surfaces that are only partially buried. Monte Carlo simulations with 30 KLVFFAE peptides suggest the initial formation of disordered aggregates that accommodates the hydrophobic surfaces, then at later stages through inter-chain hydrogen bonding transition into ordered β-sheet assemblies[31]. Coarse-grained models[32,33] enabled analyses of even larger peptide populations (up to 200)[33] and these too quickly collapse into disordered oligomers and reorganize into β-sheet rich assemblies[32,33].

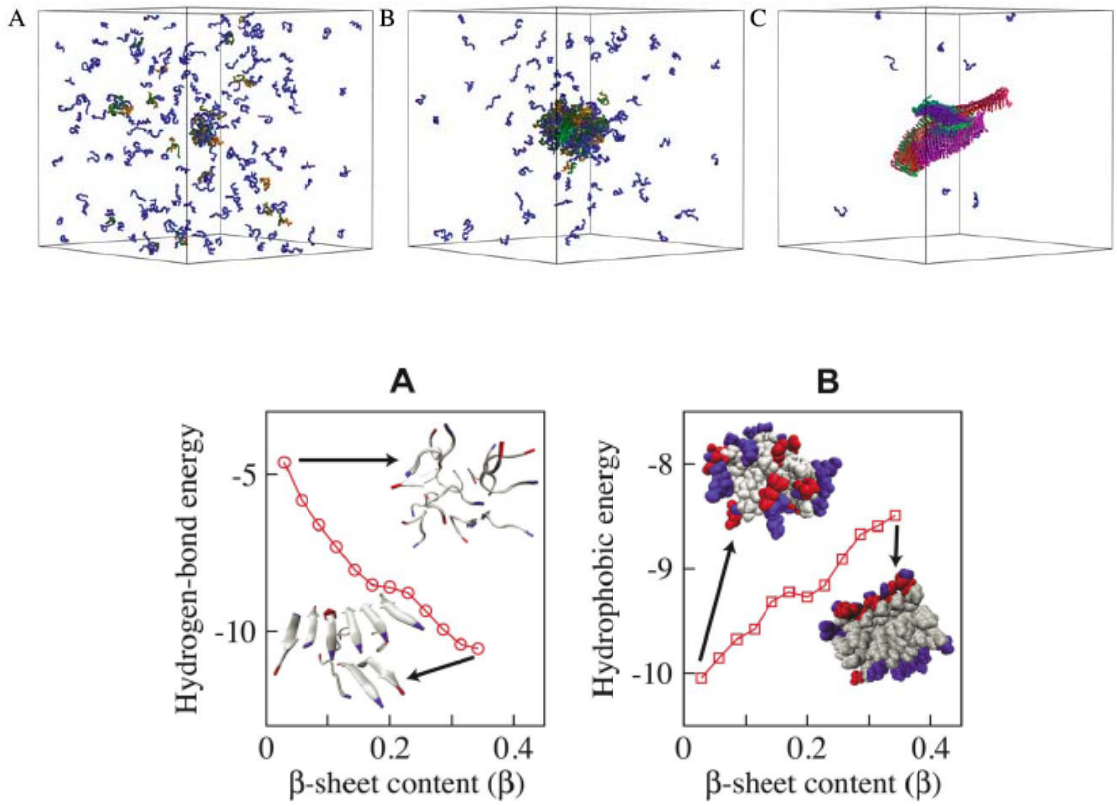

Figure 4-1: Monte Carlo simulations of a model 12-residue peptide. Simulation contains 216 peptides in a (A) starting solvated state t=1000, (B) hydrophobic collapse into a disordered state at t=5000, and (C) reorganization into an amyloid assembly at t=30 000[33]. Competition between hydrogen bonding (A) and hydrophobic energy upon increasing β-sheet content of Aβ(16-22) oligomers[26].

Further Langevin dynamics models[27] of amphiphilic peptides argue that these transient oligomer intermediates that transition into β-sheet rich assemblies reflect temperature-dependent phase boundaries and that peptides with a low β-sheet propensity form amorphous oligomers over a broader range of temperatures than peptides with higher β-sheet propensity[27].

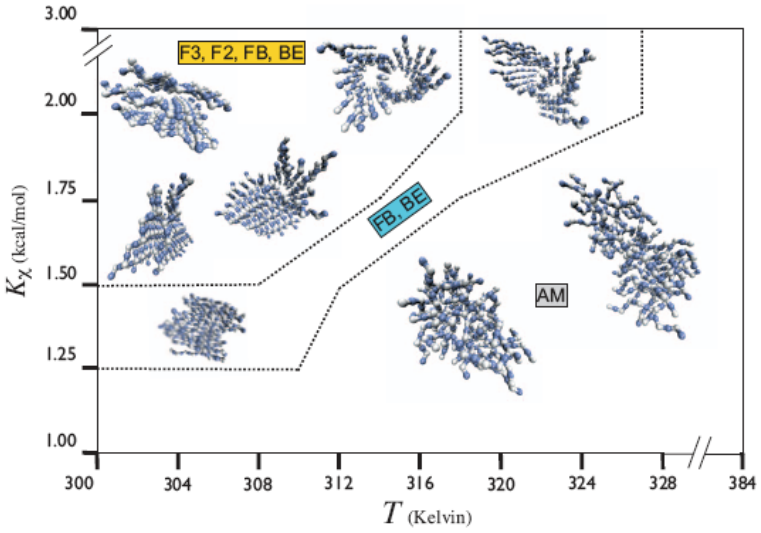

Figure 4-2: Peptide aggregation as a function of temperature and β-sheet propensity. Diagram of β-sheet propensity (Kχ) versus temperature proposes phase boundaries between fibrillar states (F2, F3), barrel like intermediates (FB, and BE) and amorphous aggregates (AM)[27]. Reprinted with permission from Bellesia G, Shea JE (2009) Effect of beta-sheet propensity on peptide aggregation. Journal of Chemical Physics 130. Copyright 2009, American Institute of Physics.

Recent experimental evidence has established that KLVFFAE peptides indeed aggregate in a concentration-dependent manner into micron sized oligomers that were directly observed to serve as major, if not exclusive, nucleation sites for a amyloid nanotube assemblies[22]. The observed oligomers can be best characterized as intermolecular molten globules as fluorescent photobleaching experiments indicate the oligomers exchange rapidly and appear similar to the fluid phases of lipid surfactants, while mature nanotubes assemblies exchanged slowly during photobleach experiments consistent with a crystalline state[22]. Furthermore, these short peptides have been shown to structurally organize as a bilayer similar to lipid surfactants[34]. To examine the extent to which these amyloid peptides have surfactant-like phase behavior we have developed environmental control of the phase boundaries and developed experimental constraints on the phase space that gives rise to the final KLVFFAE amyloid assemblies[20,21,34].

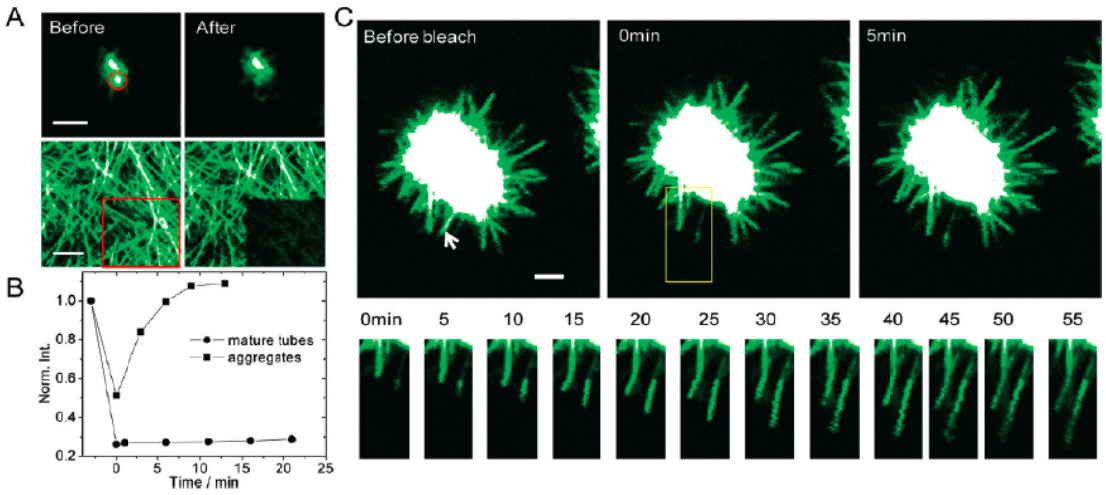

Figure 4-3: Fluorescence microscopy study of rhodamine-1722/KLVFFAE (1:250)[22]. (A) Fluorescent images after photobleaching spot (circled in red), (B) recovery of normalized fluorescent intensity for mature tubes (squares) and aggregates (circles), (C) time course of recovery after photobleaching of an emerging nanotube (boxed in yellow) . Arrow points to tube emerging from oligomer.

Methods

Peptide Synthesis and Purification

Peptides were synthesized using a Liberty CEM Microwave Automated Peptide Synthesizer (NC, USA) and a FMOC-Rink Amide MBHA Resin (AnaSpec, CA, USA). FMOC-Rink Amide MBHA Resin was swollen using dimethylformamide for 15 minutes. Microwave assisted FMOC deprotection was completed using 20% piperdine and 0.1M N-Hydroxybenzotriazole (HOBt) in dimethylformamide at 45-55°C for 180 sec, followed by 3X dimethylformamide flushes. Each FMOC-amino acid coupling step was performed using 0.1M FMOC protected amino acid and activated with 0.1 M 2-(1H-Benzotriazole-1-yl)-1,1,3,3-tetramethyluronium hexafluorophosphate (HBTU), and 0.2M N,N – Diisopropylethylamine (DIEA) in DMF. Coupling temperatures using microwave were maintained between 75-82°C for 300 sec, then rinse three aliquots of

dimethylformamide. Final acetylation of the N-terminus was achieved by addition 20% acetic anhydride in dimethylformamide.

Resin was filtered and washed with dichloromethane and allowed to air dry. Peptides were cleaved from the resin using trifluoroacetic acid/thioanisole/1,2-ethanedithiol/anisole (90: 5 : 3 : 2, v/v/v/v) at room temperature for 3 hrs. The cleaved peptide-TFA solution was filtered, and precipitated by drop-wise addition of cold (-20°C) diethyl ether. Precipitated product was centrifuged at 3000 rpm for 3 min, and the pellet was further washed using 3 times with cold diethyl ether. Dried peptides were dissolved in minimal volume of 40% acetonitrile + 0.1% trifluoroacetic acid and purified by RP-HPLC using a C18-reverse phase column with an acetonitrile-water gradient. Molecular weight was confirmed by MALDI-TOF using a 2,5-dihydroxybenzoic acid matrix.

Aβ(16-22) (1.3 mM) was dissolved in 40% CH_3CN/H_2O with 0.1% TFA using vortexing and sonication at room temperature. Solutions were then split and stored under quiescent conditions and temperature was controlled at 4°C, 28°C, and 37°C for 1 month. Concentrated Aβ(16-22) assemblies in methanol water mixtures were initially dissolved in 20% methanol with 0.1% TFA using vortexing and sonication. Then assemblies were diluted with methanol or water to adjust the aliquot methanol concentration from 20-70% methanol. Each aliquot was then stored at 4°C for 1-month incubation period. To study the internal structure of the observed oligomers, 1.3 mM KLVFFAE peptides were assembled by adding 2 wt% uranyl acetate as a contrast agent.

Transmission Electron Microscopy Imaging

Upon addition to TEM grids, the amyloid peptide assemblies were allowed to adsorb for 1 min. Excess peptide solution was wicked away with filter paper. The 2-wt % uranyl acetate (pre incubated at 4°C, 28°C, and 37°C) were added to TEM grids and incubated for 3-5 minutes. Samples were then placed in a dessicator overnight. TEM micrographs were recorded with a

Philips 410 TEM at magnifications ranging from 7100x to 69 000x with a Tungsten filament at an accelerating voltage of 80 kV. Negatives were scanned at 2000 dpi resolution on an Agfa DuoScan flatbed scanner (Agfa Corp., Ridgefield Park, NJ).

Circular Dichroism and Melting Temperatures

An aliquot (15-70 μL) of amyloid nanotube and oligomer assemblies was placed in 0.1 mm path length demountable window cell with Teflon tape wrapped around the window edges to minimize evaporation. Initially, CD at 215 nm was recorded over a 15 minute period at controlled temperature (4°C, 28°C, or 37°C) until CD signature of solution stabilized. After temperature incubation, wavelength scans over 185-300 nm were recorded. For melting temperature profiles, the ellipticity at 215 nm was recorded as a function of temperature in increments of 2°C and fit to the sigmoidal form of the Boltzmann equation.

RESULTS

Initial Phase Transition

The temperature dependence of the transition barriers predicted by computational modeling[27,33,35] and constrained by the initial experimental analyses were explored initially by following the assembly of Ac-KLVFFAE-NH_2[22] at 4°, 28°, and 37°C. The peptide was solublized in 40% acetonitrile containing 0.1% TFA, and the solution was split into three equal aliquots and each incubated at one temperature until thermodynamic equilibrium was achieved as indicated by CD. Figure **4-4** contains the transmission electron microscopy (TEM) images of uranyl acetate stained hollow nanotubes that formed at both 4° and 28°C. However, only spherical particle structures were found at 37°C, and by TEM, these assemblies diameter have a bimodal Gaussian distribution at 88 and 197 nm (Figure 4-5) and were an order of magnitude smaller than the transient intermolecular molten globules reported at room temperature[22].

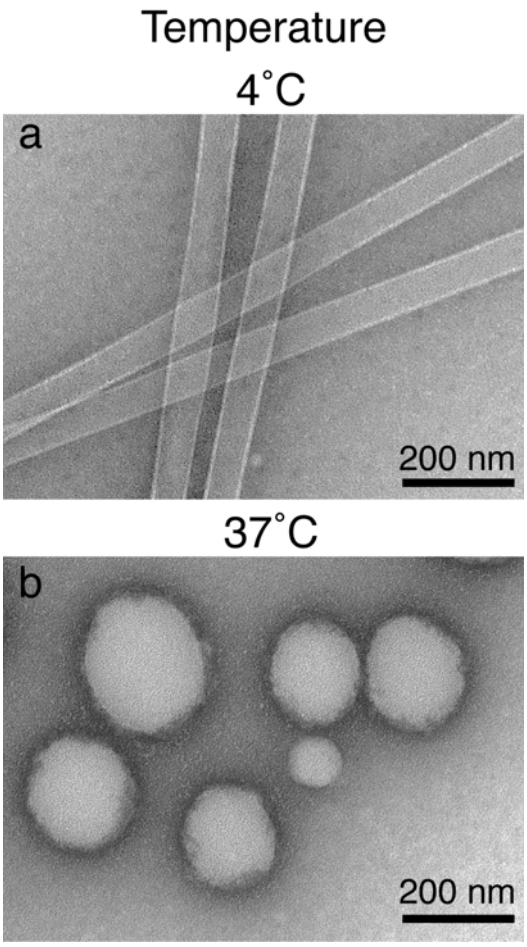

Figure 4-4: TEM images of 1.3 mM KLVFFAE assembled at (a) 4°C and (b) 37°C at 40% acetonitrile and 1.3 mM KLVFFAE assembled at (c) 30% methanol and (d) 60% methanol at 4˚C.

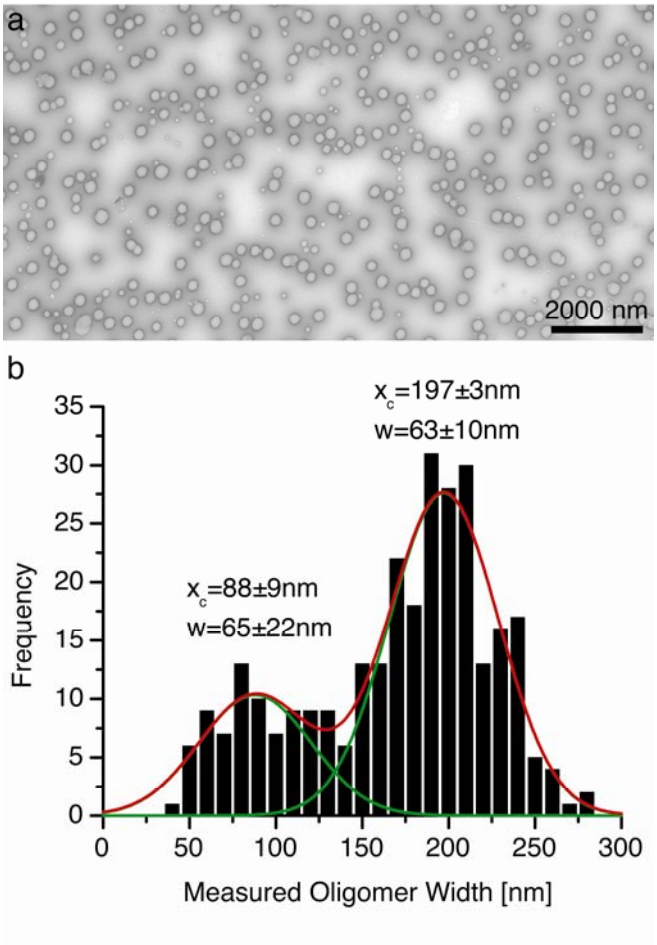

Figure 4-5: Size distribution of KLVFFAE particle assemblies at 37°C as measured by TEM.

While the effect of temperature on particle size will require further analyses, at 1.3 mM KLVFFAE in 40% acetonitrile temperatures above ~30°C clearly inhibit either the transition to paracrystalline order or the propagation of those structures into nanotubes at 1.3 mM peptide concentration. And further slight increases in temperature (>45˚C) completely inhibit oligomer formation.

The conditions for nanotube assembly have been optimized at 1.3 mM KLVFFAE as a minimal concentration in 40% acetonitrile acidified with trifluoroacetic acid (TFA),[25,26] and subtle changes to these conditions resulted in transitions through different phase barriers. In 20%

acetonitrile (Figure **4-6**) and in H_2O, both containing 0.1% TFA at 4°C, the transitions occur considerably faster, but result in more heterogeneous mixtures of tubes and sheets. In both 60% and 80% acetonitrile, small populations of oligomers accompanied the nanotubes, and a range of oligomer sizes were observed (Figure **4-6**).

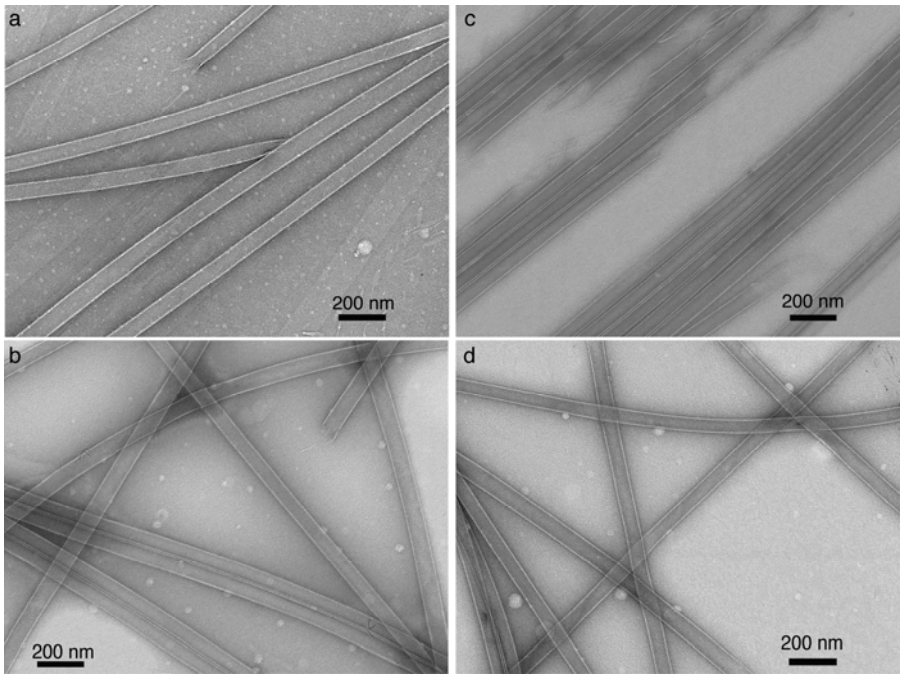

Figure 4-6: 1.3 mM KLVFFAE assembled at (a) 20%, (b) 40%, (c) 60%, and (d) 80% acetonitrile.

In methanol, the same peptide concentration gave markedly different structures. Between 20-40% methanol, nanotubes assembled (**Figure 4-7**) as they did in acetonitrile, but in 40-60% methanol, oligomers accumulated and at 60% only oligomers were observed (**Figure 4-7**). The particle size again varied in diameter, from 40-190 nm, but most strikingly, each contained a single small spot with a lighter phase contrast, resulting in an "eyeball" or "budding vesicle" appearance. The dimensions of these smaller spots were more homogenous, ranging in diameter from 25-65 nm (Figure 4-8).

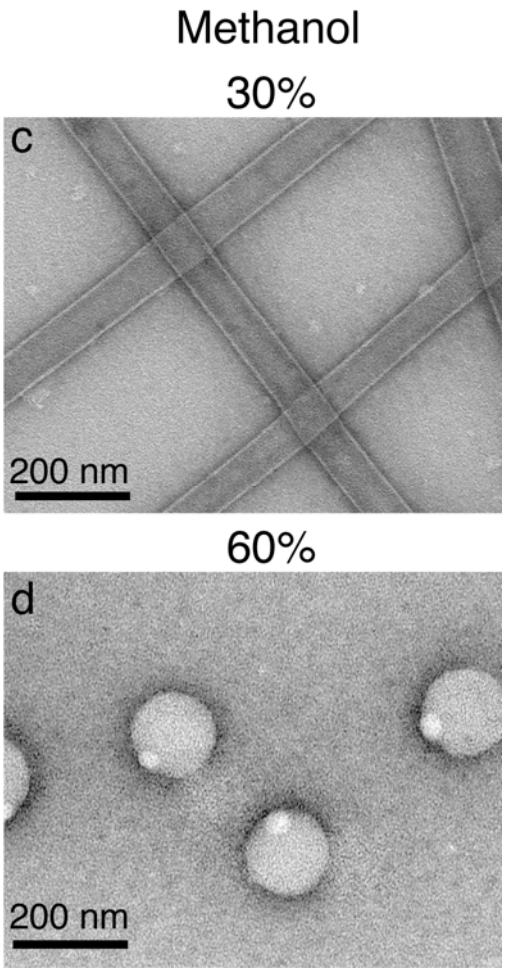

Figure 4-7: TEM images of 1.3 mM KLVFFAE assembled at (a) 30% methanol and (b) 60% methanol at 4˚C.

To better understand the morphology of the entire oligomer population (n=250), oligomer widths (Figure 4-8b), and inner particle widths (Figure 4-8c) were measured and analyzed. The oligomer population can be grouped into small oligomers (w=51±25 nm) and large oligomers (w=133±43 nm). The inner particles can be fit to a Gaussian size distribution of 37±16 nm. Given the similarities in size between the small oligomers (w=51±25 nm) and the observed inner particles (37±16 nm), it is tempting to speculate that the two populations may be related. One possible model is that the inner particles bud off to form the smaller oligomers populations,

similar to budding observed in lipid surfactants[36]. Further characterization will be needed to understanding the significance of this correlation.

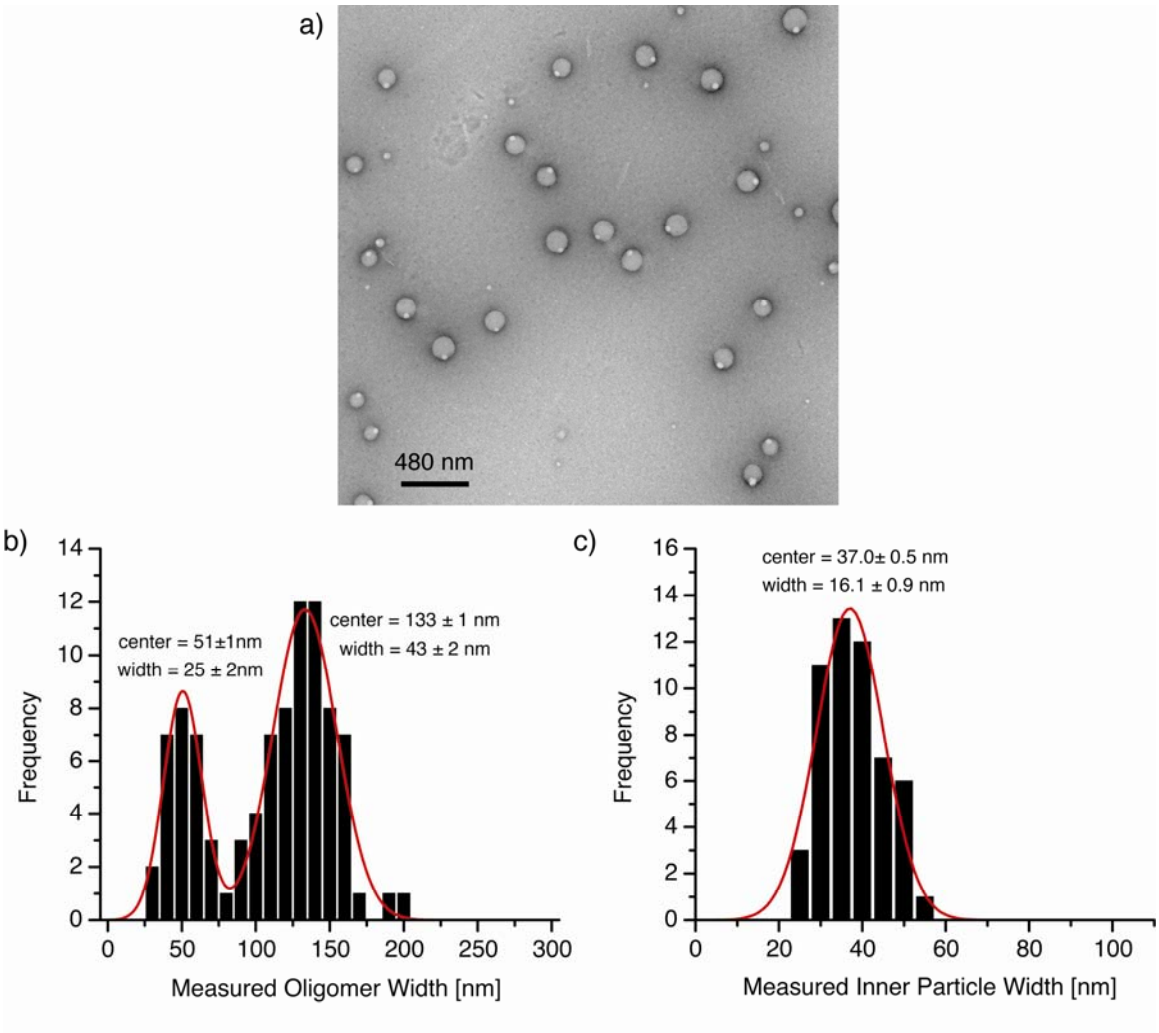

Figure 4-8: a) TEM Image of 1.3 mM KLVFFAE oligomers in 60% methanol + 0.1% TFA at 4˚C b) Gaussian Distribution of measured oligomer widths fit to the sum (red line) and c) distribution of inner particle widths.

Internal Oligomer Structure

Within the oligomers the local peptide concentration has increased significantly,[28] creating a more desolvated environment that could favor crystallization. On the other hand, either the concentration difference in the solution or a solvation energy difference could slow

emergence of the crystalline phases from the oligomer. Indeed, the appearance of budding from particles in methanol may be due to resuspension in water during uranyl acetate staining (Figure 4-7), which may promote crystalline growth or budding on the oligomer surface. To test this idea, we attempted to probe crystallinity within the particles by allowing the KLVFFAE peptide to assemble in the presence of 1 wt% uranyl acetate. The TEM images of the assembly incubated at 37°C for 2 weeks in 40% acetonitrile is shown in Figure **4-9**. The presence of uranyl acetate had no apparent impact on KLVFFAE assembly, but the stain was inhomogeneously distributed throughout the oligomer (Figure **4-9**). Short filament-like structures, consistent with the surface localized buldging eyeballs seen in methanol (Figure 4-7), excluded the uranyl acetate stain and stretched from one end of the particle to the other. A single such filament stretching across each oligomer and emerging at the surface would be consistent with the eyeball appearance seen in TEM.

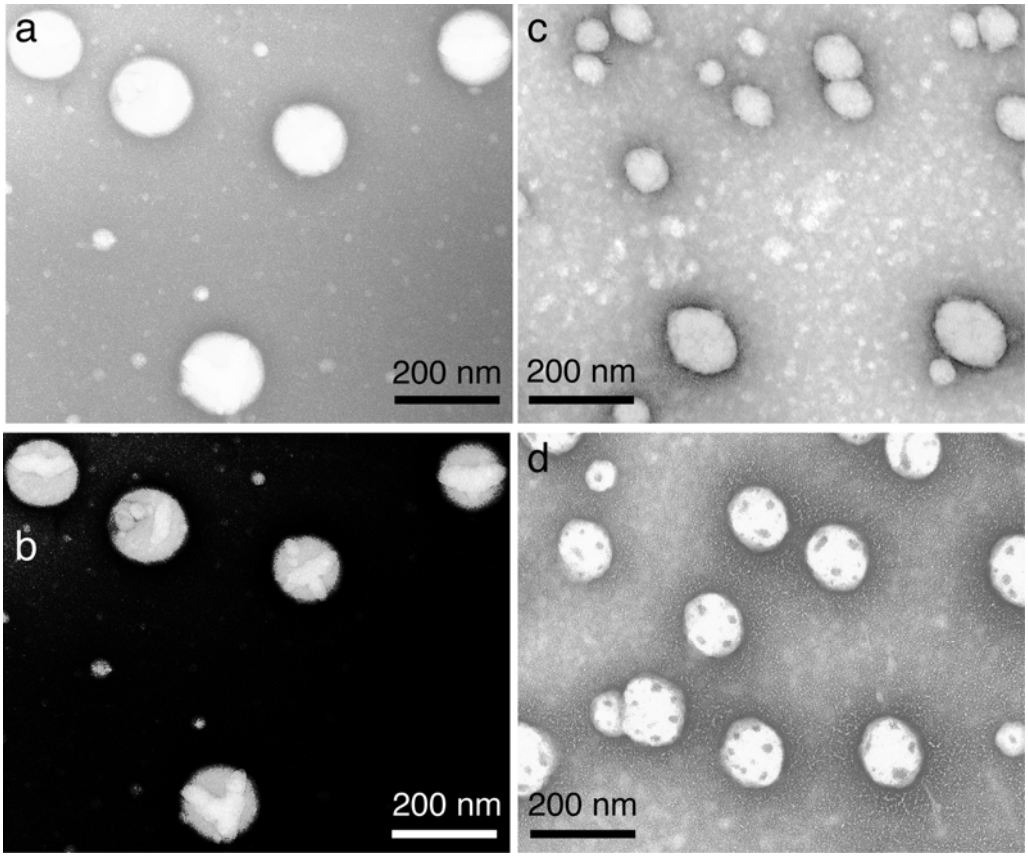

Figure 4-9: KLVFFAE monomers incubated with 2 wt% uranyl acetate at 37°C for 2 weeks. Images presented are the same, except image on left has been processed using typical input levels. Adobe Photoshop input levels on right image have been adjusted to clearly visualize differences in uranyl acetate staining within particle assemblies.

When the temperature of the KLVFFAE nanotube assemblies formed at 4°C was increased to 37°C and allowed to incubate there for 2 weeks, oligomer assemblies are again observed (Figure **4-9**). When this nanotube solution is heated in the presence of 2-wt% uranyl acetate, the oligomers show distinct regions with uranyl acetate contrast and many more crystalline regions that exclude stain. It appears that in contrast to oligomers formed from monomers, oligomers formed from heating nanotubes contain a significantly greater density of organized assemblies (Figure **4-9**).

To assess whether the observed structures within the oligomers included paracrystalline domains, the assemblies were compared by CD. As seen in Figure **4-10**, a β-sheet minimum at 215 nm dominated all assemblies studied (4°C, 28°C, and 37°C), however, the magnitude of this diagnostic β-structure ellipticity at 28°C is only 33% and the 37°C oligomer only 20% of the 4°C nanotubes. While this difference in ellipticity is expected to be both a function of the degree of assembly, lowest for the oligomers, and the nature of the structures, as the fibers are known to give weaker signatures that tubes, the signatures for all three assemblies are very similar to that of the known nanotube structure.[26] Each assembly displayed a cooperative melt on heating, however the melting temperatures (T_m) were different. The nanotube assemblies formed at 4°C and 28°C melted at the same temperature, 46.1±4.9°C and 48.6±4.6°C respectively (Figure **4-10**), while the oligomer assemblies formed at 37°C melted cooperatively at a 63.2±2.9°C (Figure **4-10**). The chemical and architectural environments of β-sheets within the oligomers are different, and this difference in solvation may account for their higher T_m.

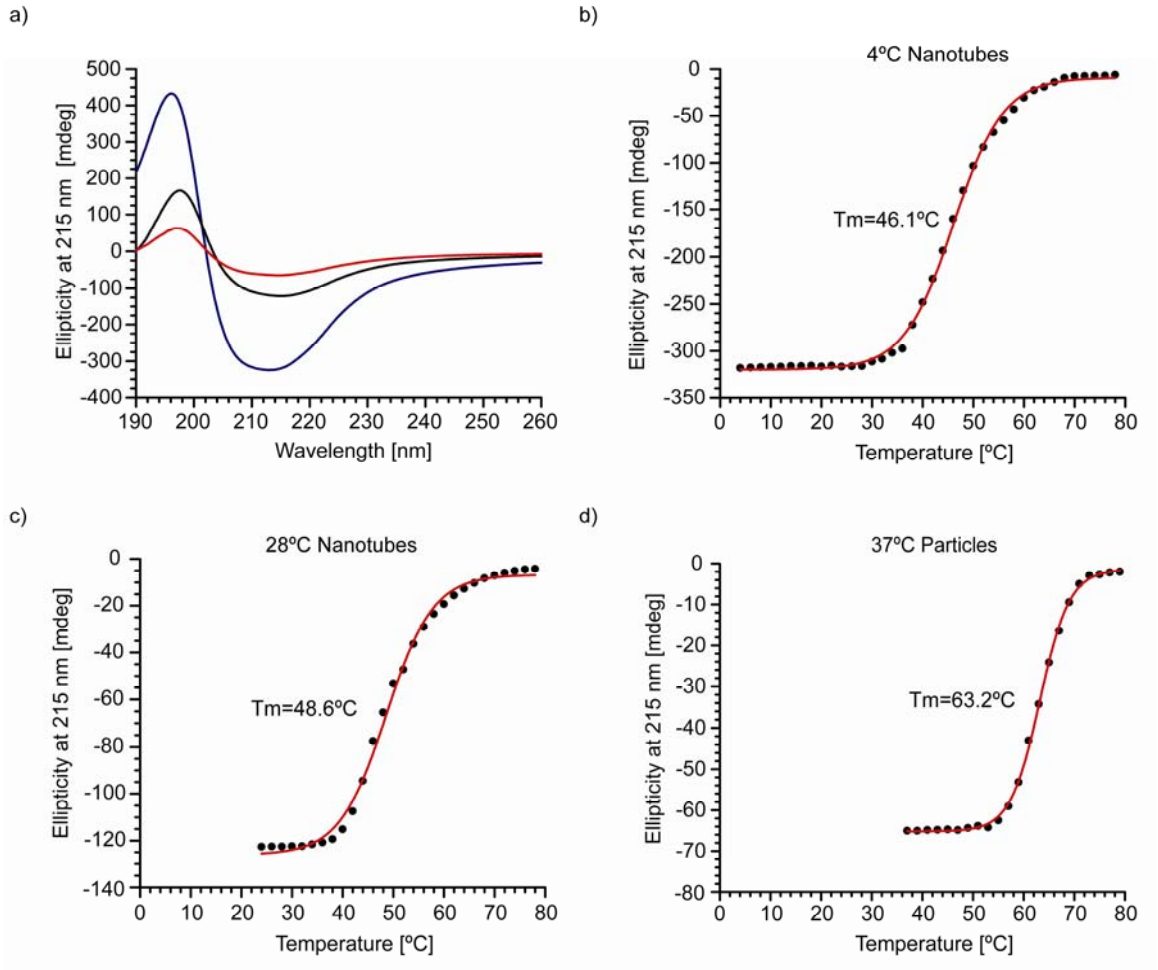

Figure 4-10: CD for KLVFFAE assemblies at 4°C (blue line), 28°C (black line), and 37°C (red line) and melting profiles for 4°C nanotubes (b), 28°C nanotubes (c) and 37°C particles (d). Each melting curve was fit using the sigmoidal form of the Boltzmann equation. The melting curve for nanotubes assembled at 4°C were fit to the equation y=-8.98+(-320.1+8.98)/(1+exp((T-46.1)/4.9)), 28°C nanotube melting fit to the equation y=-6.69+(-126.1+6.69)/(1+exp((T-48.6)/4.6)), and the particles found at 37°C fit to the equation y=-1.42+(-65.1+1.42)/(1+exp((T-63.2)/2.9)).

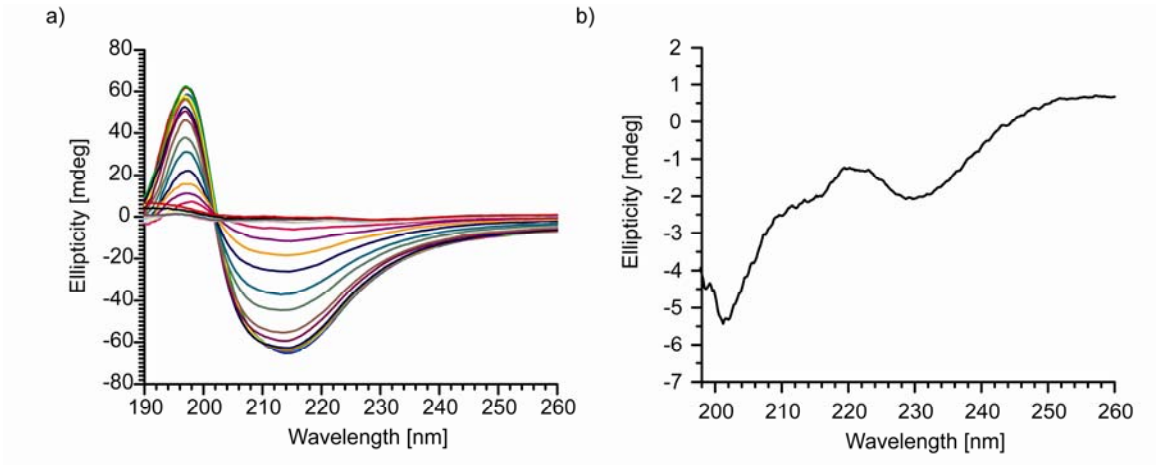

Figure 4-11: (a) CD Wavelength scans of melting 37°C globules from 37°C to 78°C. (c) Zoom-in wavelength scans of final melted structure at 78°C.

Overall, the presented TEM and CD analysis suggests that oligomers are mixtures of a β-sheet rich phase and more fluid liquid regions. The ability of oligomers to transition into β-sheet assemblies may depend on peptide propensities. To test if the particle-nanotube transition can be modulated by changes in sequence, three KLVFFAE variants were evaluated: KLVFFAL, KLVFFAV (Figure **4-13**) and KLVGFAE (Figure 8). Using amyloid structure prediction algorithm, TANGO[37,38,39], both KLVFFAL (TANGO Score 542) and KLVFFAV (TANGO Score 560) have a greater amyloid propensity than KLVFFAE (TANGO Score 420), while the F19G substitution is predicted to drastically impact the peptide's ability to form amyloid (TANGO Score 19). Indeed Figure **4-13** indicates that both KLVFFAL and KLVFFAV readily assemble into nanotube structures over a range of 4-37°C, and above 55°C the peptides assemble only into oligomers. Solutions of 1.3 mM KLVFFAL peptide assemblies at 4°C and 37°C are consistent with the presence of β-sheet secondary structure (Figure **4-13**), while assemblies at 55°C are indicative of a melted secondary structure (Figure **4-13**). Given assemblies do not display a classical random coil CD signature, the observed CD could be a mixture of β-sheet and

random coil structures. A second possibility is that CD signature is influenced by intrapeptide aromatic interactions[40] from the Phe-Phe dyad.

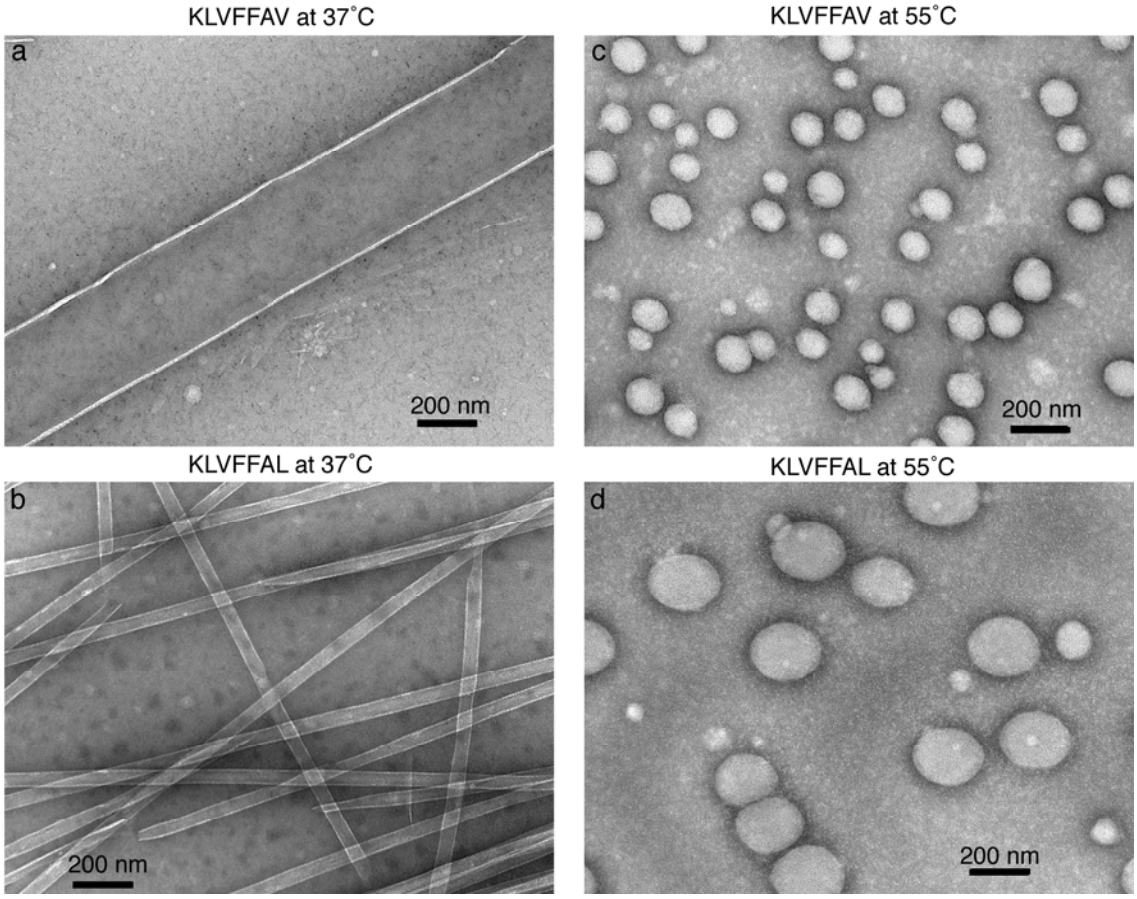

Figure 4-12: TEM micrographs of 1.3 mM KLVFFAV assembled in 40% acetonitrile with 0.1% TFA at (a) 37°C and (b) 55°C. TEM micrographs of 1.3 mM KLVFFAL assembled in 40% acetonitrile with 0.1% TFA at (c) 37°C and (d) 55°C.

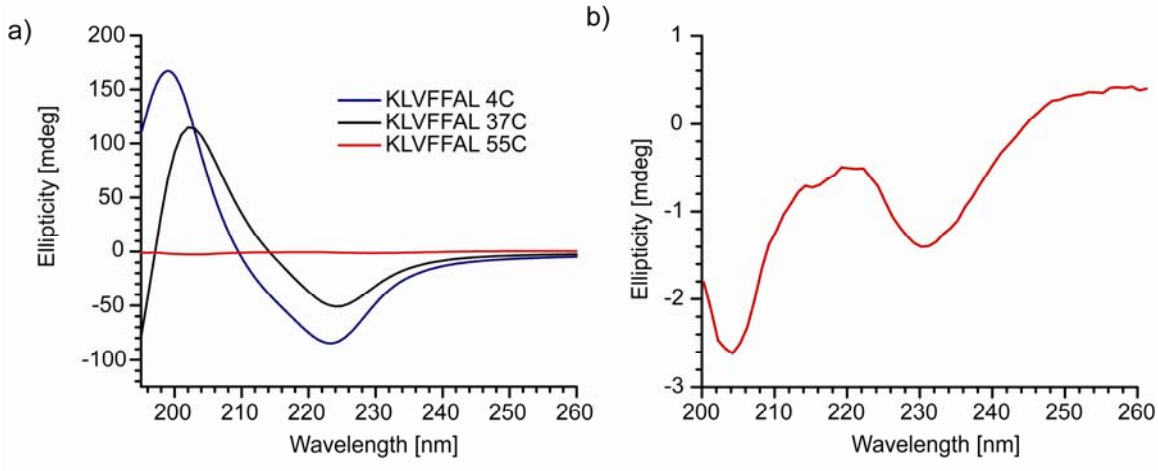

Figure 4-13: Comparison of CD for 1.3mM KLVFFAL assembled at 4°C (blue line), 37°C (black line), and 55°C (red line) and (b) zoom-in of CD of KLVFFAL assembled at 55°C.

KLVGFAE on the other hand does not transition to β-structure under these conditions, and the oligomer structures form at all temperatures tested, sequesters uranyl acetate, and forms no detectable amyloid structures (Figure **4-14**). At least under these conditions, the ability to aggregate into oligomers is largely a function of sequence hydrophobicity, and peptide sequences with weaker β-sheet propensities appear unable to transition into β-sheet aggregates and form amyloid structures, and are arrested at the oligomer state.

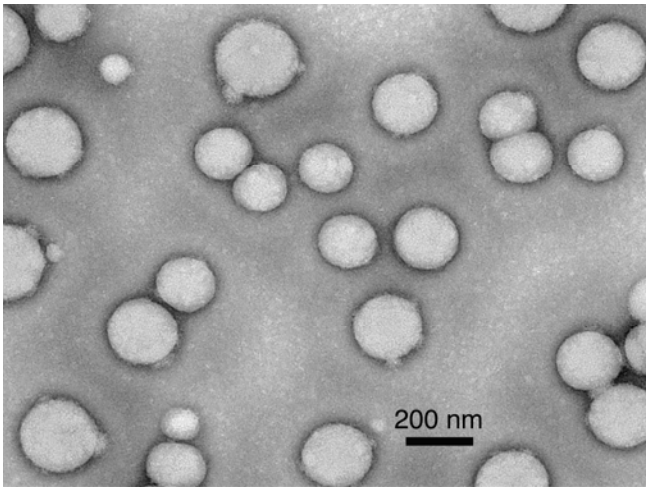

Figure 4-14: TEM Image of negatively stained 1.3 mM KLVGFAE assemblies in 40% acetonitrile and 0.1% TFA at 4˚C.

Creating Nanotubes and Fibers from Oligomers

The core KLVFFAE peptide has the advantage of forming two amyloid morphologies, fibers and nanotubes,[18,20] and it is the transition to fibers that has been associated with disease. The temperature of the preformed oligomer solution was decreased from 37°C to 4°C and maintained for 1 week. During this time, the 215 nm ellipticity changed from -64 nm to -271 nm (Figure S5), and this change was accompanied by the growth of ordered assemblies.

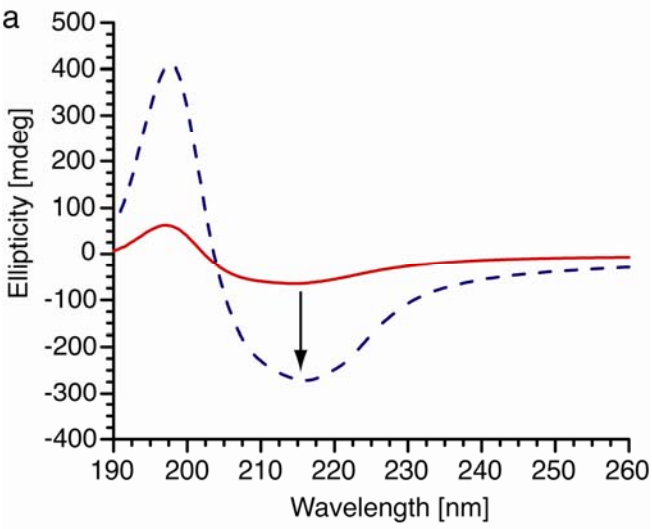

Figure 4-15: CD of mature 1.3 mM KLVFFAE oligomers (red line) after incubation at 4˚C for 2 weeks (dotted blue line).

At early times, the structures appear as particles connected by thin filaments or sheets, a "beads on a string" pattern (Figure **4-16**b-d) that eventually develops into typical nanotubes (Figure **4-16**e). Given the previous real time analyses,[28] the pattern may arise via nucleation within one oligomer, and the growing assembly, with widths of 10-150 nm, and connecting to other oligomers as it grows (Figure **4-16**c,d). As these structures are observed only during the temperature transition from preformed particles, these structures are unlikely to be surface affects[14]. However, unlike the transient oligomers formed at lower temperatures, these smaller oligomers seem capable of nucleating a range of crystalline forms that include fibers and tubes.

To create conditions more compatible with fiber stability,[18,20] oligomers preformed under acidic conditions at 37°C were adjusted to neutral pH. At intermediate times ordered structures associated with the oligomers began forming and while most appeared fiber-like (Figure **4-16**h), the widths at times were as large as 200 nm (Figure **4-16**g). As the assemblies matured, fibers with homogenous widths of 10-30 nm (Figure **4-16**j) dominated the images. The larger fibers that did exist showed striations (Figure **4-16**j) along their surface suggesting that extended laminations may well form within the oligomers, but once solvent exposed, fibril stability dominated the assemblies.

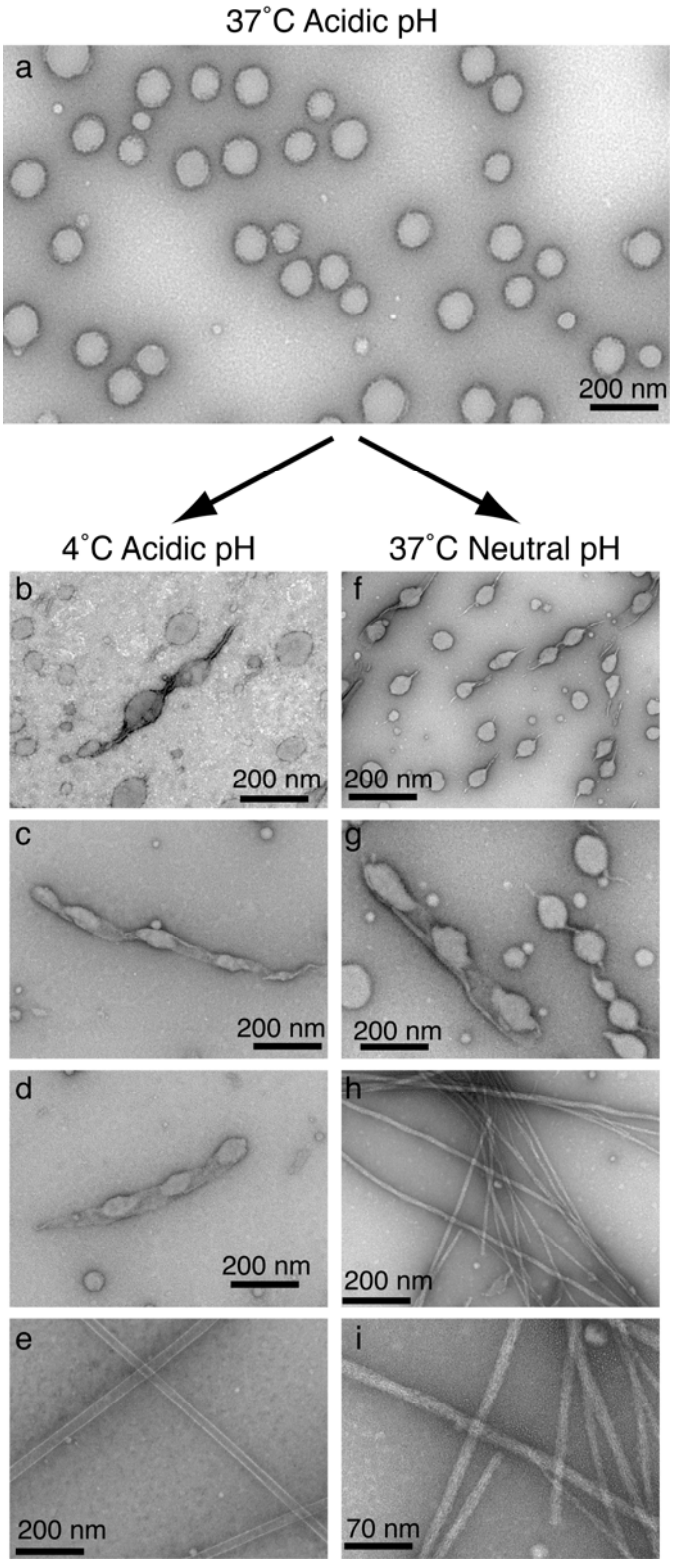
37˚C Acidic pH
a
200 nm
4˚C Acidic pH
37˚C Neutral pH
b
200 nm
f
200 nm
c
200 nm
g
200 nm
d
200 nm
h
200 nm
e
200 nm
i
70 nm

Figure 4-16: TEM image of mature KLVFFAE oligomers formed at 37°C for 1 month (a) and TEM images after assembly conditions changed to 4˚C for 2 weeks (b-e), and pH titrated to neutral conditions and incubated for 1 week (f, g) and 2 weeks (h,i).

To quantify the impact of changing assembly conditions of the matured 37°C oligomer solution from 37°C to 4°C or pH 2 to pH 7, a population of structures before and after the assembly change were compared. As shown in Figure **4-17**a the initial oligomer population (n=299) was composed of 71% large oligomers (w > 100 nm) and 29% small oligomers (w < 100 nm). Upon changing the assembly conditions of the matured oligomer solution at 37°C to 4°C and allowed to incubate at these conditions for 1 week the observed morphology population (n=739) could be grouped as 11% large oligomers (w>100 nm), 66% small oligomers (w<100 nm), 20% oligomers nucleating wide sheets (w>20 nm), and 2% oligomer nucleating thin filaments (w<20 nm). From these observations the populations of large oligomers appears to dramatically decreased and has begun nucleating wide sheets and thin filaments, while the population of small oligomers has increased. This observation is consistent with large oligomers having the capacity to nucleate ordered amyloid structures, while smaller oligomers are incapable of amyloid nucleation.

Upon changing the assembly conditions of the matured oligomer solution at 37°C and pH 2 to pH 7 and allowed to incubate at these conditions for 1 week the observed morphology population (n=1374) could be grouped as 27% large oligomers (w>100 nm), 42% small oligomers (w<100 nm), 14% oligomers nucleating wide sheets (w>20 nm), and 17% oligomer nucleating thin filaments (w<20 nm). In comparison to the solution adjusted to 4°C, the population adjusted to pH 7 displayed a significantly larger population of oligomer nucleating small filaments (2% versus 17%).

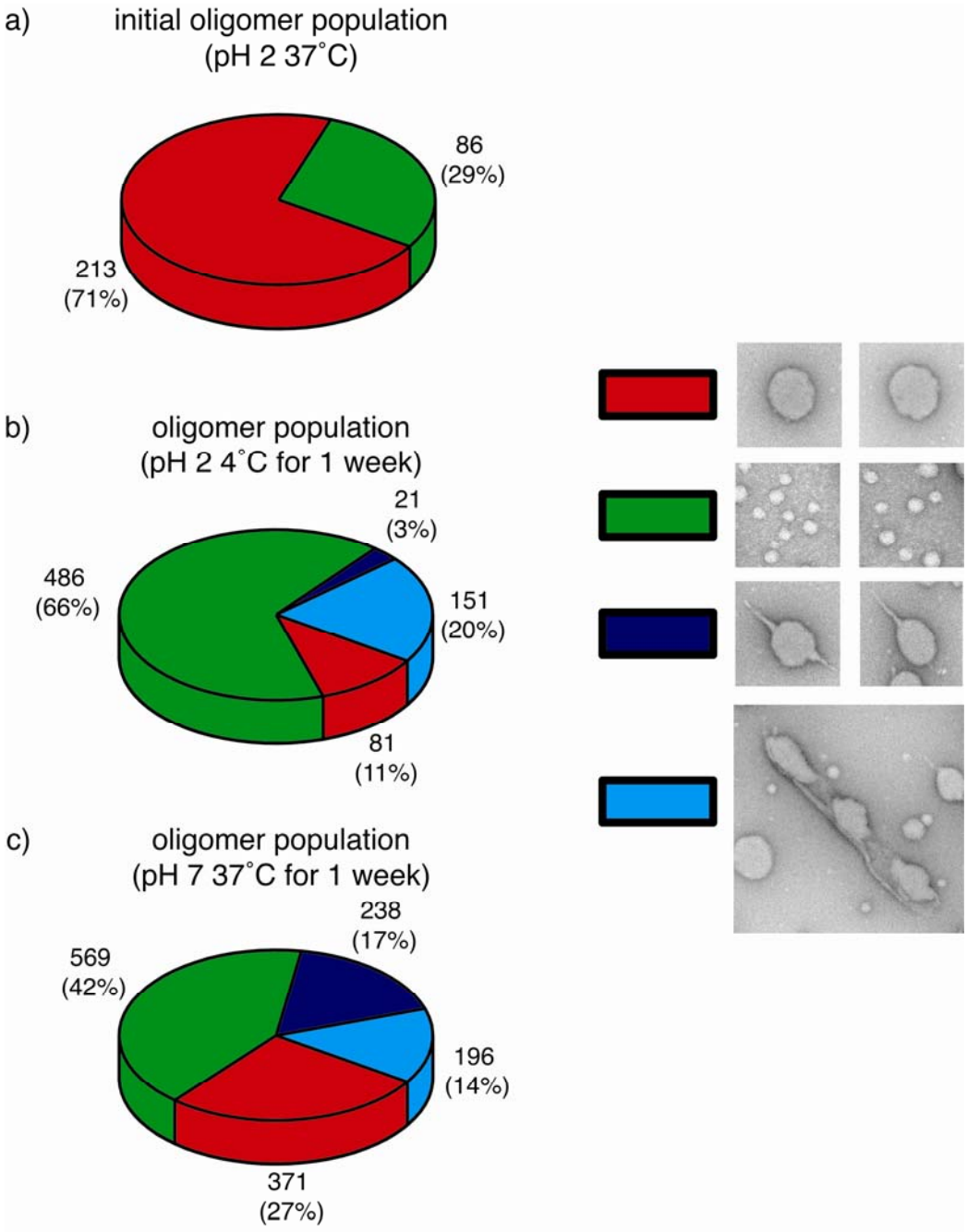

Figure 4-17: (a) Population Distribution of 1.3 mM KLVFFAE mature oligomers formed at 37˚C under acidic conditions in 40% acetonitrile after conditions and analyzed by TEM. (b) oligomer population distribution after pH conditions were changed to pH 7 at 37˚C and incubated for 1 week, and (c) oligomer population distribution after temperature conditions were changed 4˚C at pH 2 and incubated for 1 week. In the pie charts oligomers were characterized into 4 categories:

large oligomers with widths >140 nm (red), small oligomers with widths <140 nm (green), large oligomers that nucleate thin filaments with <35 nm widths (navy), and large oligomers that nucleate thick filaments (cyan).

Given the apparent difference in observed filament widths nucleating from oligomers adjusted from 37°C to 4°C at constant pH compared with assembly adjusted from pH 2 to pH 7 at constant temperature, the widths of nucleating assemblies were measured and analyzed. As shown in Figure 4-18 the mature 37°C oligomers incubated at 4°C for 1 week contained oligomers with the capacity to nucleate ordered amyloid assemblies with a width of 64±47 nm. In contrast, mature 37°C oligomer solutions incubated at pH 7 for 1 week contained oligomers with the capacity to nucleate ordered amyloid assemblies that could be fit into width populations of 27±21 nm and 93±117 nm.

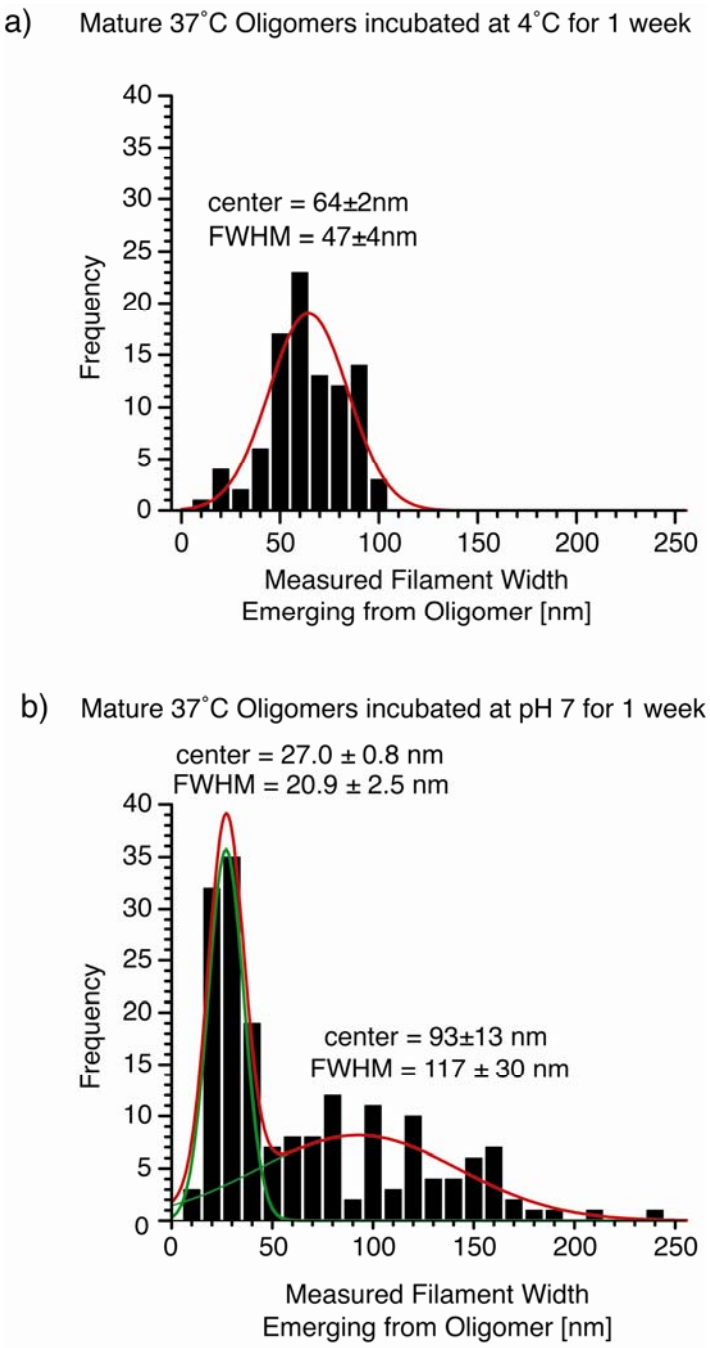

Figure 4-18: (a) Population distribution of filament widths emerging from 1.3 mM KLVFFAE mature oligomers formed at 37˚C under acidic conditions in 40% acetonitrile (a) after temperature conditions were changed to 4˚C at pH 2 and incubated for 1 week and (b) after pH conditions were changed to pH 7 at 37˚C and incubated for 1 week.

Impact of Filament Width on Morphology

Given the distribution of filament widths that were observed a population of ribbons with varying widths was analyzed. Initial observations indicated two types of ribbon morphologies: ribbons that twisted and ribbons that coiled. For each ribbon the width was measured and compared with the tilt angle of the ribbon. By definition tilt angle is the angle between the direction of the filament and the long ribbon axis. For twisted ribbons, each filament runs parallel to the ribbon axis, therefore the tilt angle equal to zero. Interestingly, as the ribbon width was increased from 15-160 nm, a phase change from twisted ribbons to helical ribbons with a tilt angle of 25±5° was observed at a critical ribbon width of ~40 nm. Therefore, increasing number of laminated β-sheets switches the ribbon morphology from a twisted phase to helical phases. Furthermore, addition of 1 mM KLVFFAE peptide monomers then converted all of the ribbons into hollow nanotubes.

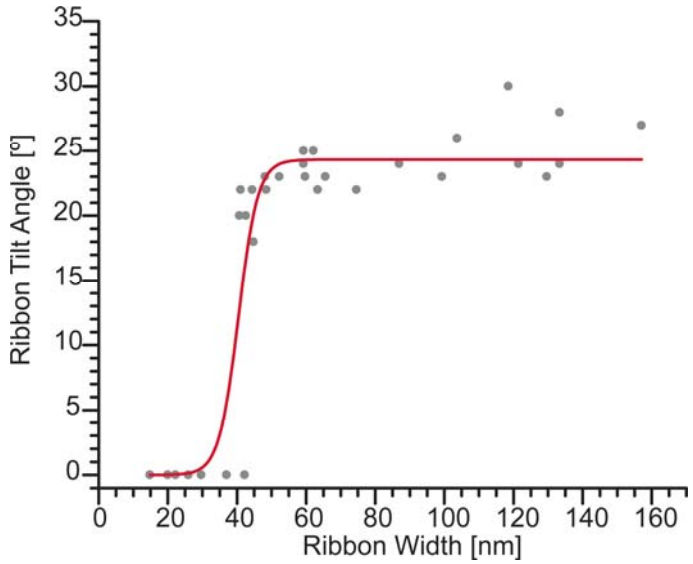

Figure 4-19: Transition from twisted ribbon phase to helical ribbon phase as a function of filament width. Ribbons undergo this transition at a critical width of ~ 40 nm (or 40 laminated β-sheets).

Influence of Salts on Peptide Oligomerization

Surfactant phase changes are also heavily influenced by salt content. For example, experimental and computation studies have shown sodium chloride alters the phase properties of lipid bilayer membranes driving them towards a more crystalline state[41]. The melting temperature of crystalline nanotubes was measured as a function of sodium chloride concentration. Indeed addition of sodium chloride improved the thermostability of nanotubes and appeared to follow Debye-Huckle equation (Figure 4-20). The influence of salt may also be attributed to exchange of TFA counterions with chloride ions at high concentration of NaCl as has been observed with other model amyloid peptides[42].

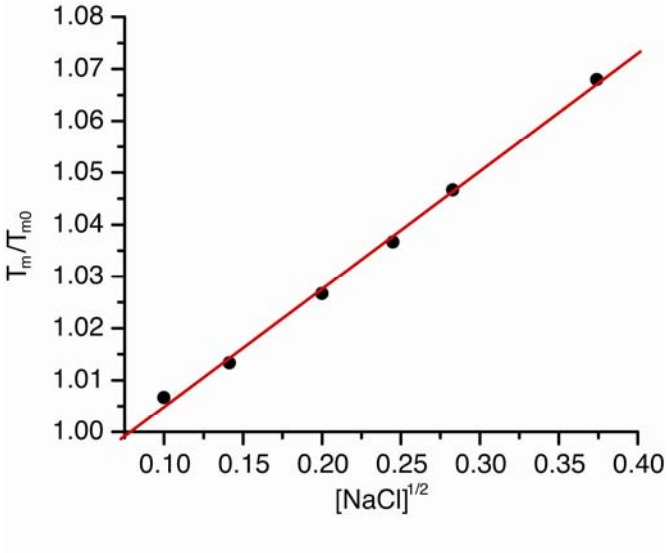

Figure 4-20: Influence of NaCl on thermostability of KLVFFAE nanotubes. The impact of increased salt concentration on the amyloid assemblies fits to a Debye–Hückel model. Apparent melting temperature normalized to 1.0 mM KLVFFAE at 0 M NaCl (300 K) against the square root of the ionic strength. Linear correlations: $y=0.982 + 0.227\ [NaCl]^{1/2}$.

Intriguingly, addition of divalent ions directed hollow tubes to bundle together into a lamellar-like phase (Figure 4-21). Further studies of this salt induced phase change, revealed the shift towards a bundled nanotube phase occurred between the range of 3-9 mM[43].

Additionally, divalent salts such as sodium hydrogen phosphate, sodium sulfate, and potassium chromate can direct the bundling of nanotubes, while monovalent anions require a high concentration (>150 mM) to observe similar effects. Therefore, the apparent phase change appears to be driven by electrostatic screening of the positively charged nanotube surface with divalent anions[43].

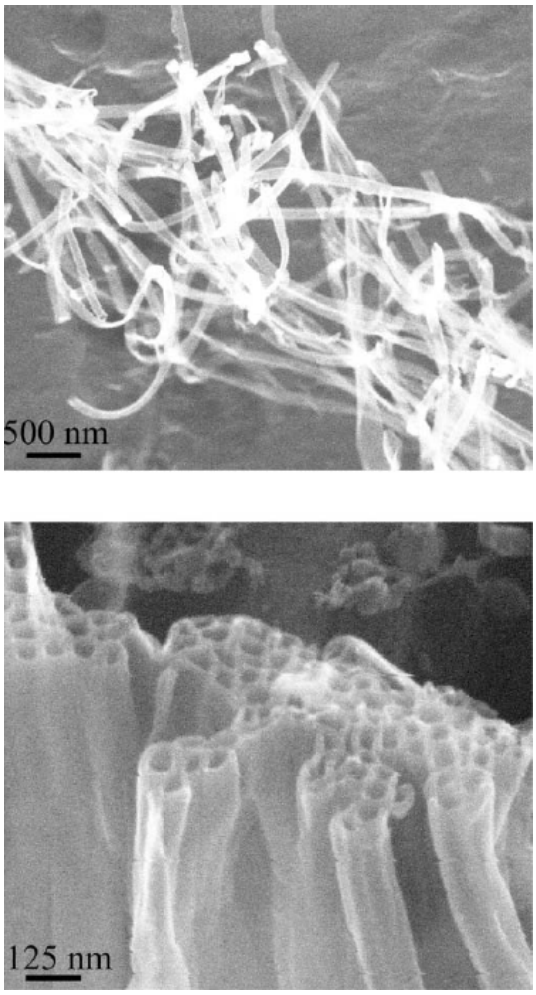

Figure 4-21: Cryo-etch high-resolution scanning electron microscopy (cryoetch HRSEM) images of chromium sputter-coated Aβ(16–22) peptide nanotubes before (top) and after (bottom) sulfate bundling. Within these reversibly forming macroassemblies, the nanotubes are deformed with non-circular cross-sections maximizing the contact surface-area through lamellar-like packing (bottom).

Discussion

Almost 100 years ago James William McBain postulated the existence of "colloidal ions" that are now generally recognized as micelles[44]. Since that time, the rich phase behavior of surfactant molecules has impacted our understanding of supramolecular assemblies ranging from biological membranes to soaps and been exploited in practical applications in engineering, medicine, and manufacturing. The simple peptides described here display a phase behavior similar to but distinct from the lipid amphiphiles, and quite possibly with an even richer array of morphological forms. The de-solvating entropic forces that drive micelle formation appear equally important for peptide oligomerization, requiring a critical concentration for the phase transition. Computer simulations suggest that the functionality of the peptide backbone gives rise to a less ordered phase within the oligomer than seen in the micelle, one more similar to that of the molten globule discussed in protein folding[22], but one that is likely to transition directly into the crystalline β-structures known in folded proteins. However, ordered propagation of these β-structured nuclei occurs not only within the oligomer but also in the solution where the adsorption of soluble peptides occurs at the ordered template end (Fig 6).[28]

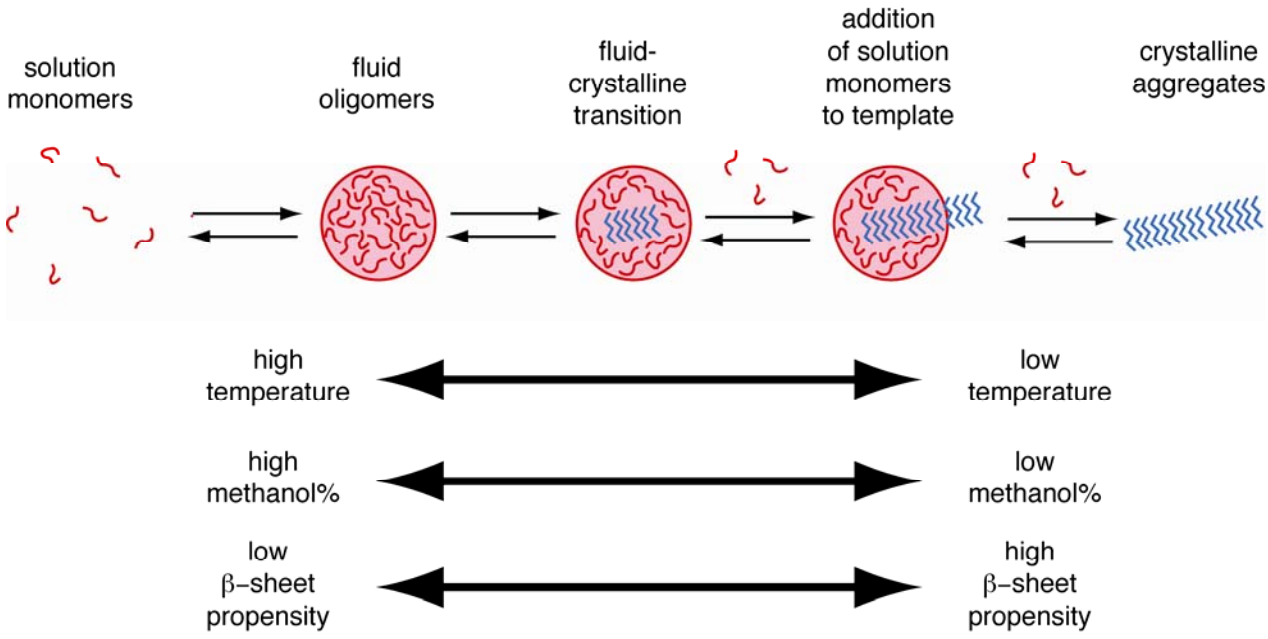

Figure 4-22: Model for the phase transition from monomeric state to disordered oligomer to an ordered crystalline state. Red denotes unstructured KLVFFAE peptides and blue represents the transition to the more crystalline KLVFFAE β-sheets.

The crystallization that occurs within the oligomers may take many forms depending on the environment and the state of the peptide. We suggest that the almost 17°C difference in the melting temperature of the assemblies within the oligomer relative to the final nanotube is primarily due to solvation differences within the oligomers and/or to different forms. Fully formed tubes can emerge from the oligomers,[28] and when oligomers preformed at 37°C are cooled to allow for crystallization, with fibers and ribbons emerging as prevalent structures. Certainly when the propagation media favors fiber growth, e.g., at more neutral pH values for KLVFFAE, then fibers are formed even though they appear from the oligomers as sheets and bundles. Such bundles may simply be the result of multiple nucleation events emerging from one or multiple oligomers or simply tangling of the fibers during deposition on the EM grids. Clearly, further analysis of these early phase transitions and propagation events will be required.

The crystalline phase is rich in morphological forms. In this chapter we have shown KLVFFAE peptides undergoes diverse surfactant-like phases of fibers, helical and twisted ribbons, oligomers with varying degrees of order, hollow nanotubes, and lamellar tube bundles. Each of the observed phases can be modulated by assembly conditions (pH, temperature, peptide concentration, and salt) as well the degree of laminated β-sheets can induce distinct morphological changes. Each of these arise from growth along the three orthogonal planes, β-sheet, lamination, and end-to-end stacking accessible to the extended peptides[45]. As these peptides get longer, the array of structural forms will undoubtedly expand, and it is certainly possible that some of these many forms could compromise cell function as an etiological basis of protein misfolding diseases. It therefore becomes important to understand the phase behavior of peptide assemblies not only in solution, but also in the complex milieu of the eukaryotic cell. In such complex media, the phase behavior will certainly be reflected in the physical state of the peptide, the complex environment of both cytoplasm and extracellular matrix, and the many surfaces presented by macromolecules and the ordered amphiphiles of biological membranes[46]. The phase behavior that has emerged from lipid amphiphiles will certainly provide the foundation on which the phase diagrams of the more functionally rich peptides can be simulated, experimentally evaluated, and practically exploited.

References

1. Lipowsky R, Sackmann E, editors (1995) Polymorphism of Lipid-Water Systems: Elsevier Science B.V.
2. Lu K (2005) Discovery of Diverse Peptide Nanotube Architecture from the Self-assembly of Designed Amyloid-β Cassettes. Atlanta: Emory University. 257 p.
3. Harper JD, Wong SS, Lieber CM, Lansbury PT (1997) Observation of metastable A beta amyloid protofibrils by atomic force microscopy. Chemistry & Biology 4: 119-125.

4. Walsh DM, Hartley DM, Kusumoto Y, Fezoui Y, Condron MM, et al. (1999) Amyloid beta-protein fibrillogenesis - Structure and biological activity of protofibrillar intermediates. Journal of Biological Chemistry 274: 25945-25952.

5. Kelly JW (1996) Alternative conformations of amyloidogenic proteins govern their behavior. Curr Opin Struct Biol 6: 11-17.

6. Goldsbury C, Frey P, Olivieri V, Aebi U, Muller SA (2005) Multiple assembly pathways underlie amyloid-beta fibril polymorphisms. Journal of Molecular Biology 352: 282-298.

7. Hill SE, Robinson J, Matthews G, Muschol M (2009) Amyloid Protofibrils of Lysozyme Nucleate and Grow Via Oligomer Fusion. Biophysical Journal 96: 3781-3790.

8. Harper JD, Wong SS, Lieber CM, Lansbury PT (1999) Assembly of A beta amyloid protofibrils: An in vitro model for a possible early event in Alzheimer's disease. Biochemistry 38: 8972-8980.

9. Wu JW, Breydo L, Isas JM, Lee J, Kuznetsov YG, et al. (2010) Fibrillar Oligomers Nucleate the Oligomerization of Monomeric Amyloid beta but Do Not Seed Fibril Formation. Journal of Biological Chemistry 285: 6071-6079.

10. Hoshi M, Sato M, Matsumoto S, Noguchi A, Yasutake K, et al. (2003) Spherical aggregates of beta-amyloid (amylospheroid) show high neurotoxicity and activate tau protein kinase I/glycogen synthase kinase-3 beta. Proceedings of the National Academy of Sciences of the United States of America 100: 6370-6375.

11. Sorci M, Grassucci RA, Hahn I, Frank J, Belfort G (2009) Time-dependent insulin oligomer reaction pathway prior to fibril formation: Cooling and seeding. Proteins-Structure Function and Bioinformatics 77: 62-73.

12. Bitan G, Kirkitadze MD, Lomakin A, Vollers SS, Benedek GB, et al. (2003) Amyloid beta-protein (A beta) assembly: A beta 40 and A beta 42 oligomerize through distinct pathways. Proceedings of the National Academy of Sciences of the United States of America 100: 330-335.

13. Kayed R, Head E, Thompson JL, McIntire TM, Milton SC, et al. (2003) Common structure of soluble amyloid oligomers implies common mechanism of pathogenesis. Science 300: 486-489.

14. Dong JJ, Apkarian RP, Lynn DG (2005) Imaging amyloid beta peptide oligomeric particles in solution. Bioorganic & Medicinal Chemistry 13: 5213-5217.

15. Lambert MP, Barlow AK, Chromy BA, Edwards C, Freed R, et al. (1998) Diffusible, nonfibrillar ligands derived from A beta(1-42) are potent central nervous system neurotoxins. Proceedings of the National Academy of Sciences of the United States of America 95: 6448-6453.

16. Haass C, Selkoe DJ (2007) Soluble protein oligomers in neurodegeneration: lessons from the Alzheimer's amyloid beta-peptide. Nature Reviews Molecular Cell Biology 8: 101-112.

17. Glabe CG, Kayed R (2006) Common structure and toxic function of amyloid oligomers implies a common mechanism of pathogenesis. Neurology 66: S74-S78.

18. Balbach JJ, Ishii Y, Antzutkin ON, Leapman RD, Rizzo NW, et al. (2000) Amyloid Fibril Formation by Ab16-22, a Seven-Residue Fragment of the Alzheimer's b-Amyloid Peptide, and Structural Characterization by Solid State NMR. Biochemistry 39: 13748-13759.

19. Lu K, Jacob J, Thiyagarajan P, Conticello VP, Lynn DG (2003) Exploiting amyloid fibril lamination for nanotube self-assembly. J Am Chem Soc 125: 6391-6393.

20. Mehta AK, Lu K, Childers WS, Liang Y, Dublin SN, et al. (2008) Facial Symmetry in Protein Self-Assembly. J Am Chem Soc 130: 9829-9835.

21. Liang Y, Pingali SV, Jogalekar AS, Snyder JP, Thiyagarajan P, et al. (2008) Cross-strand pairing and amyloid assembly. Biochemistry 47: 10018-10026.

22. Liang Y, Lynn DG, Berland KM (2010) Direct Observation of Nucleation and Growth in Amyloid Self-Assembly. Journal of the American Chemical Society 132: 6306-6308.

23. Klimov DK, Thirumalai D (2003) Dissecting the assembly of A beta(16-22) amyloid peptides into antiparallel beta sheets. Structure 11: 295-307.

24. Santini S, Mousseau N, Derreumaux P (2004) In silico assembly of Alzheimer's A beta(16-22) peptide into beta-sheets. Journal of the American Chemical Society 126: 11509-11516.

25. Petty SA, Decatur SM (2005) Experimental evidence for the reorganization of beta-strands within aggregates of the a beta(16-22) peptide. Journal of the American Chemical Society 127: 13488-13489.

26. Cheon M, Chang I, Mohanty S, Luheshi LM, Dobson CM, et al. (2007) Structural reorganisation and potential toxicity of oligomeric species formed during the assembly of amyloid fibrils. Plos Computational Biology 3: 1727-1738.

27. Bellesia G, Shea JE (2009) Effect of beta-sheet propensity on peptide aggregation. Journal of Chemical Physics 130.

28. Castelletto V, Hamley IW, Harris PJF, Olsson U, Spencer N (2009) Influence of the Solvent on the Self-Assembly of a Modified Amyloid Beta Peptide Fragment. I. Morphological Investigation. Journal of Physical Chemistry B 113: 9978-9987.

29. Castelletto V, Hamley IW, Hule RA, Pochan D (2009) Helical-Ribbon Formation by a beta-Amino Acid Modified Amyloid beta-Peptide Fragment. Angewandte Chemie-International Edition 48: 2317-2320.

30. Hamley IW, Nutt DR, Brown GD, Miravet JF, Escuder B, et al. (2010) Influence of the Solvent on the Self-Assembly of a Modified Amyloid Beta Peptide Fragment. II. NMR and Computer Simulation Investigation. Journal of Physical Chemistry B 114: 940-951.

31. Cheon M, Favrin G, Chang I, Dobson CM, Vendruscolo M (2008) Calculation of the free energy barriers in the oligomerisation of A beta peptide fragments. Frontiers in Bioscience 13: 5614-5622.

32. Auer S, Dobson CM, Vendruscolo M (2007) Characterization of the nucleation barriers for protein aggregation and amyloid formation. Hfsp Journal 1: 137-146.

33. Auer S, Meersman F, Dobson CM, Vendruscolo M (2008) A Generic Mechanism of Emergence of Amyloid Protofilaments from Disordered Oligomeric Aggregates. Plos Computational Biology 4.

34. Childers WS, Mehta AK, Ni R, Taylor JV, Lynn DG (2010) Peptides Organized as Bilayer Membranes. Angewandte Chemie International Edition 49: 4104-4107.

35. Bellesia G, Shea JE (2009) Diversity of kinetic pathways in amyloid fibril formation. Journal of Chemical Physics 131.

36. Hianik T (2006) Structure and physical properties of biomembranes and model membranes. Acta Physica Slovaca 56: 687-806.

37. Linding R, Schymkowitz J, Rousseau F, Diella F, Serrano L (2004) A Comparative Study of the Relationship Between Protein Structure and [beta]-Aggregation in Globular and Intrinsically Disordered Proteins. Journal of Molecular Biology 342: 345-353.

38. Fernandez-Escamilla A-M, Rousseau F, Schymkowitz J, Serrano L (2004) Prediction of sequence-dependent and mutational effects on the aggregation of peptides and proteins. Nat Biotech 22: 1302-1306.

39. Rousseau F, Schymkowitz J, Serrano L (2006) Protein aggregation and amyloidosis: confusion of the kinds? Current Opinion in Structural Biology 16: 118-126.

40. Sreerama N, Manning MC, Powers ME, Zhang JX, Goldenberg DP, et al. (1999) Tyrosine, phenylalanine, and disulfide contributions to the circular dichroism of proteins: Circular dichroism spectra of wild-type and mutant bovine pancreatic trypsin inhibitor. Biochemistry 38: 10814-10822.

41. Bockmann RA, Hac A, Heimburg T, Grubmuller H (2003) Effect of sodium chloride on a lipid bilayer. Biophysical Journal 85: 1647-1655.

42. Castelletto V, Hamley IW, Cenker C, Olsson U (2010) Influence of Salt on the Self-Assembly of Two Model Amyloid Heptapeptides. The Journal of Physical Chemistry B 114: 8002-8008.

43. Lu K, Guo L, Mehta AK, Childers WS, Dublin SN, et al. (2007) Macroscale assembly of peptide nanotubes. Chem Commun (Camb) 2729-2731.

44. McBain JW (1913) Mobility of highly charged micelles. Transactions of the Faraday Society 9: 99-102.

45. Dong J, Lu K, Lakdawala A, Mehta AK, Lynn DG (2006) Controlling amyloid growth in multiple dimensions. Amyloid 13: 206-215.

46. Spitzer J, Poolman B (2009) The Role of Biomacromolecular Crowding, Ionic Strength, and Physicochemical Gradients in the Complexities of Life's Emergence. Microbiology and Molecular Biology Reviews 73: 371-388

Chapter 5 : Specificity in Amyloid Self-Assembly

Nature's simplest organisms rely heavily on mixtures of peptides that co-assemble via multi-step processes to create complex nanomachines ranging from bacterial mitotic-like spindles[1,2,3] to bacterial actins that orchestrate cell wall growth[4,5,6] to proteins for construction of viral capsids[5,7]. In contrast steps towards de novo self-assembly have largely centered on well-defined rules of DNA base pairing (Figure **5-1**) to construct intricately complex multi-component assemblies[8,9,10].

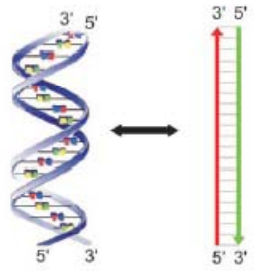

Figure 5-1: The DNA double helix (top) is composed of two antiparallel oligonucleotides that have high sequence specificity as a result of Watson–Crick hydrogen bonding patterns. The choice of suitable DNA sequences allows the generation of complex motifs which contain double-helical regions, sticky ends, bulge loops, hairpin loops, junctions, and crossovers. Combing the appropriate DNA sequences has led to the rationale design of complex nanoarchitectures[11].

Specificity within peptides assemblies is less understood and de novo assemblies have not yet approached the full complexity of Nature's nanomachines[1,2,3]. Emerging interactions in de novo peptide assemblies has centered on charge directed interactions to direct the cooperative assembly of monomer to form a range for fibril assemblies from coiled-coil[12] to

amyloid fibers[13]. Recent advances have shown that mixtures of helical peptides have adequate specificity to assemble specifically even within complex mixtures where promiscuous coiled-coil binding could take place, [14,15] thus laying the foundation for construction of increasingly complex nanomachines (Figure **5-2**).

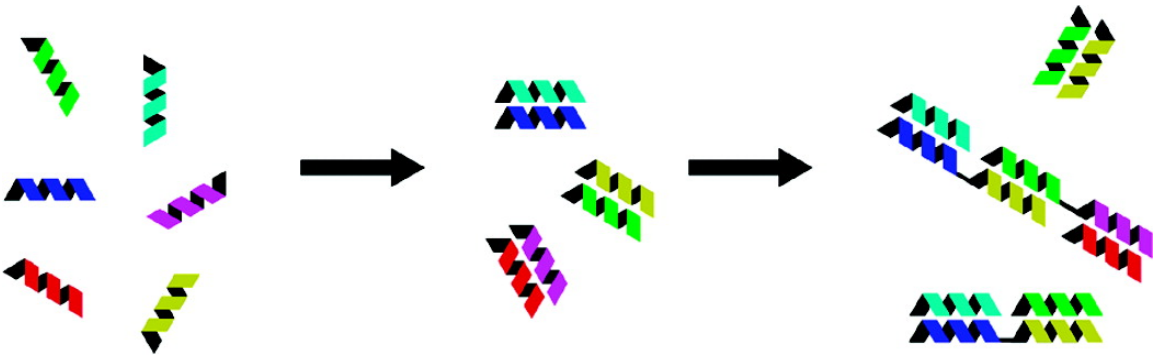

Figure 5-2: Concept specificity within mixtures of alpha-helical coiled-coil peptide building blocks. Within the cartoon specific binding between coiled coil pairs directs precise assemblies even within complex chemical systems[14,15].

Specificity within mixtures of β-sheet forming peptides is far less understood. The cross-β scaffold provides a unique structural scaffold that seeds the formation of an array of morphologies ranging from typical twisted fibers to hollow nanotubes[13] as shown in Chapter 2. Astonishingly, peptides differing by a single methylene (KLVFFAL vs KLVFFAV) form nanotubes with drastically different diameters (38 nm vs 278 nm)[13,16]. The two β-sheet forming peptides present an intriguing model system as the pure peptide assemblies are easily distinguishable by TEM and present an interesting specificity challenge as individual peptides differ only by a single methylene. In our attempts to better understand the energetic surfaces which direct these different assemblies, we have investigated the competitive assembly of mixed peptide solutions and here demonstrate that a single "CH_2" is able to drive phase separation into two radically different assemblies.

Results and Discussion

Preliminary Evaluation of Peptide Mixing Compatibility

Previously, in Chapter 2 I showed that the registry of KLVFFAE β-sheets was sensitive to peptide sequence at the level of a single "H" as in-register anti-parallel fibers formed under neutral conditions and out-of-register anti-parallel nanotubes when the terminal glutamate is protonated. KLVFFAL and KLVFFAV form nanotubes independent of pH, consistent with the protonatable E terminal residue driving the morphology switch. The FTIR spectra of both assemblies (Figure **5-3**) contain the hallmark signatures of anti-parallel β-sheet secondary structure, most notably the intense amide stretcth at 1627cm^{-1} and the weaker mode at 1693 cm^{-1} [17,18]. The differences in relative intensity between 1660 and 1680 cm^{-1} may be the result of varying levels of antisymmetric COO- stretching vibration of trifluoroacetetic acid (TFA).

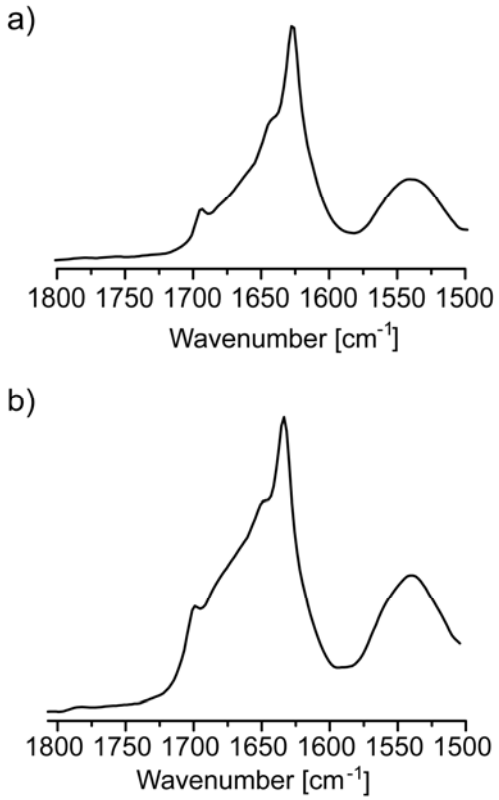

Figure 5-3: FT-IR of (a) 1.3 mM KLVFFAL nanotubes and (b) 1.3 mM KLVFFAV nanotubes assembled in 40% acetonitrile +0.1% TFA at 4°C.

Further analysis using isotope-edited IR have indicated both E22L and E22V are composed of the anti-parallel out-of-register β-sheets[19] shown in Figure **5-4**. Most striking however, the KLVFFAL and KLVFFAV peptides form different diameter nanotubes as seen in Figure **5-5**a and b. Given that the two peptides differ in molecular weight by a mere 14 amu, and maintain the same strand registry we have sought to understand the molecular recognition events that dictate the tube size differences.

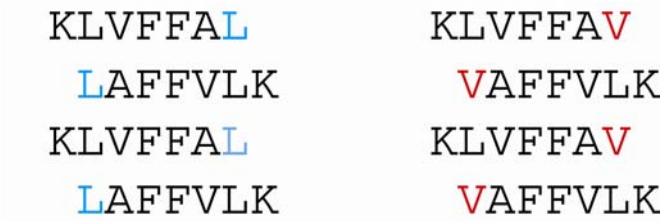

Figure 5-4: β-sheet registry of 1.3 mM KLVFFAL and 1.3 mM KLVFFAV nanotubes assembled in 40% acetonitrile + 0.1% TFA as determined by isotope-edited IR[19].

The Co-Assembly of KLVFFAL and KLVFFAV

To test whether KLVFFAL and KLVFFAV peptides could co-assemble, the two peptides were mixed together at 0.65 mM each in 40% acetonitrile + 0.1% TFA at 4°C and allowed to assemble for a total of 3 months. The micrographs in Figure **5-5**, indicates that KLVFFAL assembles into 40 nm diameter tubes, while KLVFFAV assembled into 280 nm diameter tubes consistent with previous SAXS results[13]. Interesting, after 1 month incubation the 1:1 co-assembly formed only a heterogenous mixture of filaments and sheets (Figure **5-5**c). However, after further incubation, small tubes and large tubes (Figure **5-5**e,f) as well as a population of short filaments had emerged (Figure **5-5**d).

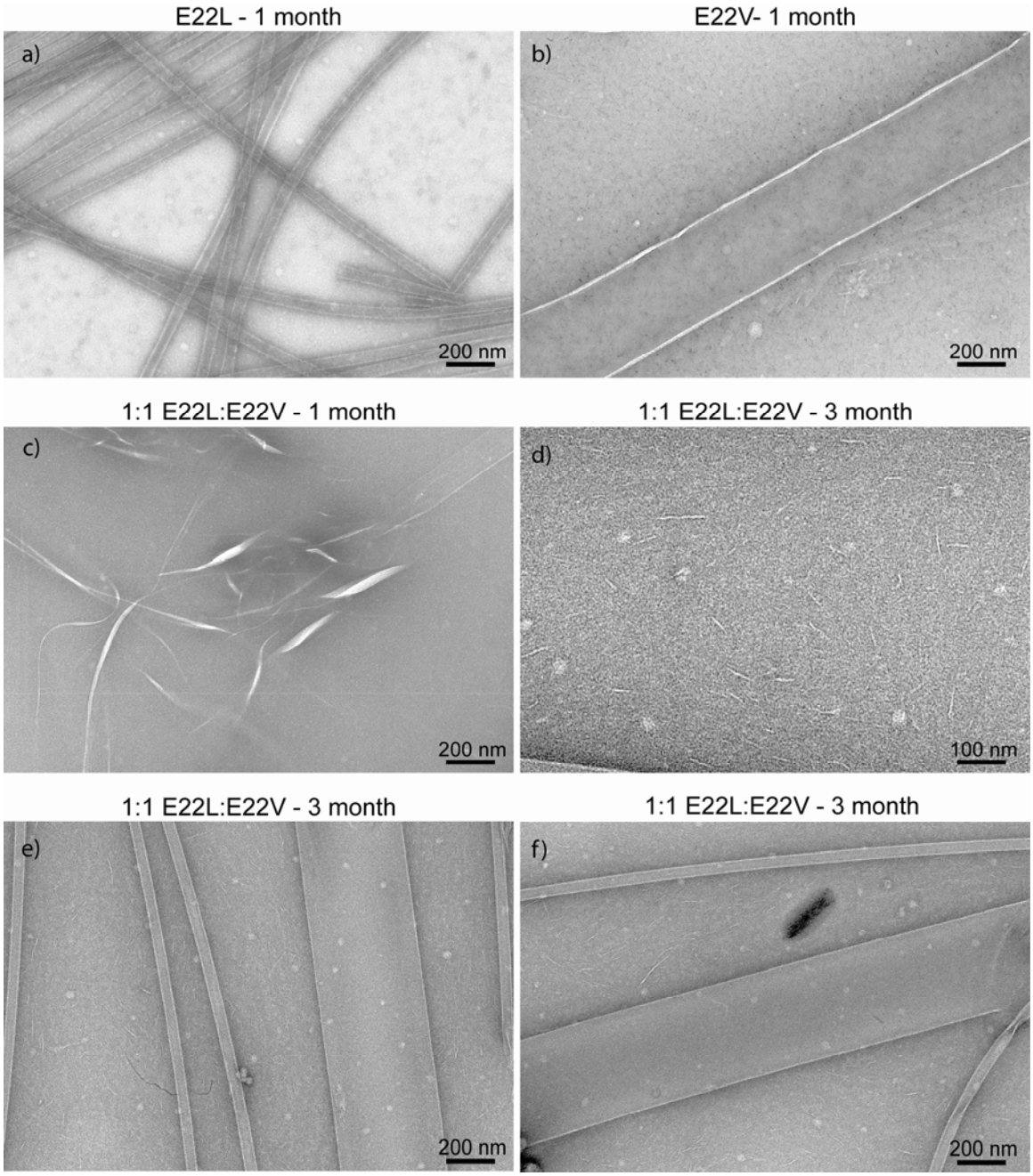

Figure 5-5: TEM Micrographs of (a) pure 1.3 mM KLVFFAL assemblies and (b) pure KLVFFAV assemblies and (c) 1:1 (0.65 mM:0.65mM) KLVFFAL:KLVFFAV assembled in 40% acetonitrile containing 0.1% TFA at 4°C after 1 month incubation and after three month incubation three species observed short filaments (d) and small tubes and large tubes (e and f).

Most reasonably, the CD for the two pure peptide assemblies appear as almost mirror images of each other Figure **5-6**a indicates KLVFFAL nanotubes (blue) and KLVFFAV (red). The KLVFFAL assemblies display a characteristic β-sheet signature with a minimum at 225 nm and a maximum at 205 nm, while KLVFFAV assemblies contain a minimum at 203 nm and a positive cotton effect at 221 nm. CD measurements of the 1:1 mixture qualitatively appear to be a simple 1:1 summation of E22L and E22V CD curves (Figure 4b).

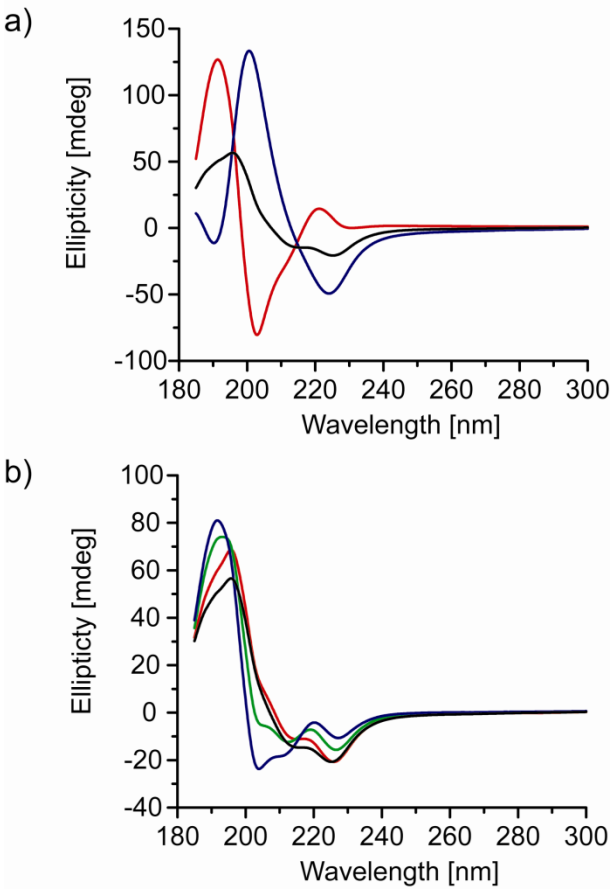

Figure 5-6: a) CD of mature 1.3 mM KLVFFAL nanotubes (blue line), 1.3 mM KLVFFAV (red line) and 0.65 mM KLVFFAL:0.65 mM KLVFFAV (black line) allowed to assembly for 3 months. B) Simulated fit of the experimental KLVFFAL:KLVFFAV CD (black line) assuming a 40:60 KLVFFAL:KLVFFAV composition (green line), 50:50 KLVFFAL:KLFFAV (red line), and 60:40 KLVFFAL:KLFFAV (blue line).

To fit the CD for the mixed peptide solution, simulated CD curves were calculated assuming various compositions of the measured pure KLVFFAV and KLVFFAL CD curves shown in Figure **5-6**. The experimental 1:1 peptide mixture fits best to a 50:50 summation of KLVFFAL and KLVFFAV CD spectra, slight deviation exists in the range of 210-220 nm and below 200 nm. These deviations may be attributed to the small filaments observed by TEM (Figure **5-5**c,d).

Probing the Degree of Phase Separation via Solid-State NMR

Solid-state NMR experiments were designed to probe whether peptides were mixed at the molecular level (i.e. KLVFFAL peptides were directly backbone hydrogen bonded to KLVFFAV peptides). In an isotope labeling scheme, KL[^{15}N]VFF[1-^{13}C]AL, was previously used to show that V18 backbone amide hydrogen bonds with A21's backbone carbonyl on another strand[20]. Using this labeling scheme it is possible to determine the percentage of KLVFFAL peptides that backbone hydrogen bond with other KLVFFAL peptides by spin counting (Figure **5-7**). To observe the number of KLVFFAV peptides that are hydrogen bonded to KL[^{15}N]VFF[1-^{13}C]AL peptides a ^{13}C isotope was synthetically incorporated into the A21's methyl to yield KLVFF[3-^{13}C]AV, a spin label which is chemical shift resolved from A21's ^{13}C carbonyl (Figure **5-8**a). This labeling scheme (Figure **5-7**) can detect both pure E22L domains as well as mixed domains of E22L and E22V peptides. Since the E22V peptide does not contain a ^{15}N, pure E22V domains will not be detected using this labeling scheme.

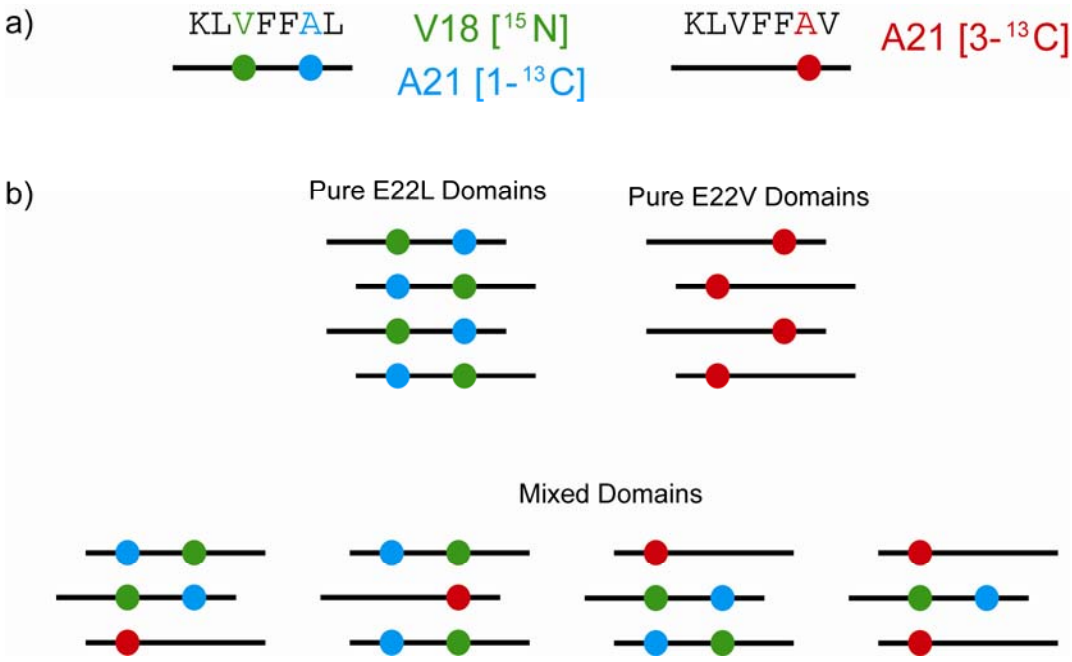

Figure 5-7: Conceptual Design of $^{13}C\{^{15}N\}$ REDOR Experiment to detect the degree of mixing at the molecular level. (a) The following labeling schemes were employed incorporating a ^{13}C and ^{15}N in E22L (KL[^{15}N]VFF[1-^{13}C]AL) and only a ^{13}C in E22V (KLVFF[3-^{13}C]AV). Using this labeling scheme pure E22L domains can be detected as well as mixed domains of E22L and E22V peptides. Since the E22V peptide does not contain a ^{15}N, pure E22V domains cannot be detected.

The two isotopically labeled peptides were synthesized using standard FMOC solid-phase peptide synthesis, and purified by HPLC. To ensure a 1:1 mixing ratio, the amount of peptide was quantified by HPLC. The peptides were then allowed to assemble for 3months. Sodium sulfate was added to the mature sample (Figure **5-5**b-d), and it was pelleted at 3000g, the pellet was frozen in liquid nitrogen, and the solvent was removed by lyophilization.

$^{13}C\{^{15}N\}$REDOR of mature assemblies of a 1:1 mixture of KL[^{15}N]VFF[1-^{13}C]AL and KLVFF[3-^{13}C]AV confirmed peptide mixing. Nearly 30% of the A21 ^{13}C labeled methyls were close to a KL[^{15}N]VFF[1-^{13}C]AL peptide. While the ^{13}C carbonyl REDOR plateau level, indicated that 70% of the KL[^{15}N]VFF[1-^{13}C]AL peptides are near other KL[^{15}N]VFF[1-^{13}C]AL.

Our current proposal is that the tube population, which maintain the morphology of pure peptide, are indeed pure “L” and “V” nanotubes. The mixed sample arises from the fibers which would account for roughly 1/3 of the peptides. Exactly why the fibers can accommodate the methylene “defect” and the tubes show greater selectivity will need to be determined. That said, fluorescence microscopy data[21] indicates the degree of mixing within nanotube assemblies for a rhodamine labeled peptides was up to 1%, however the upper bound on detected incorporation remain unknown at this point.

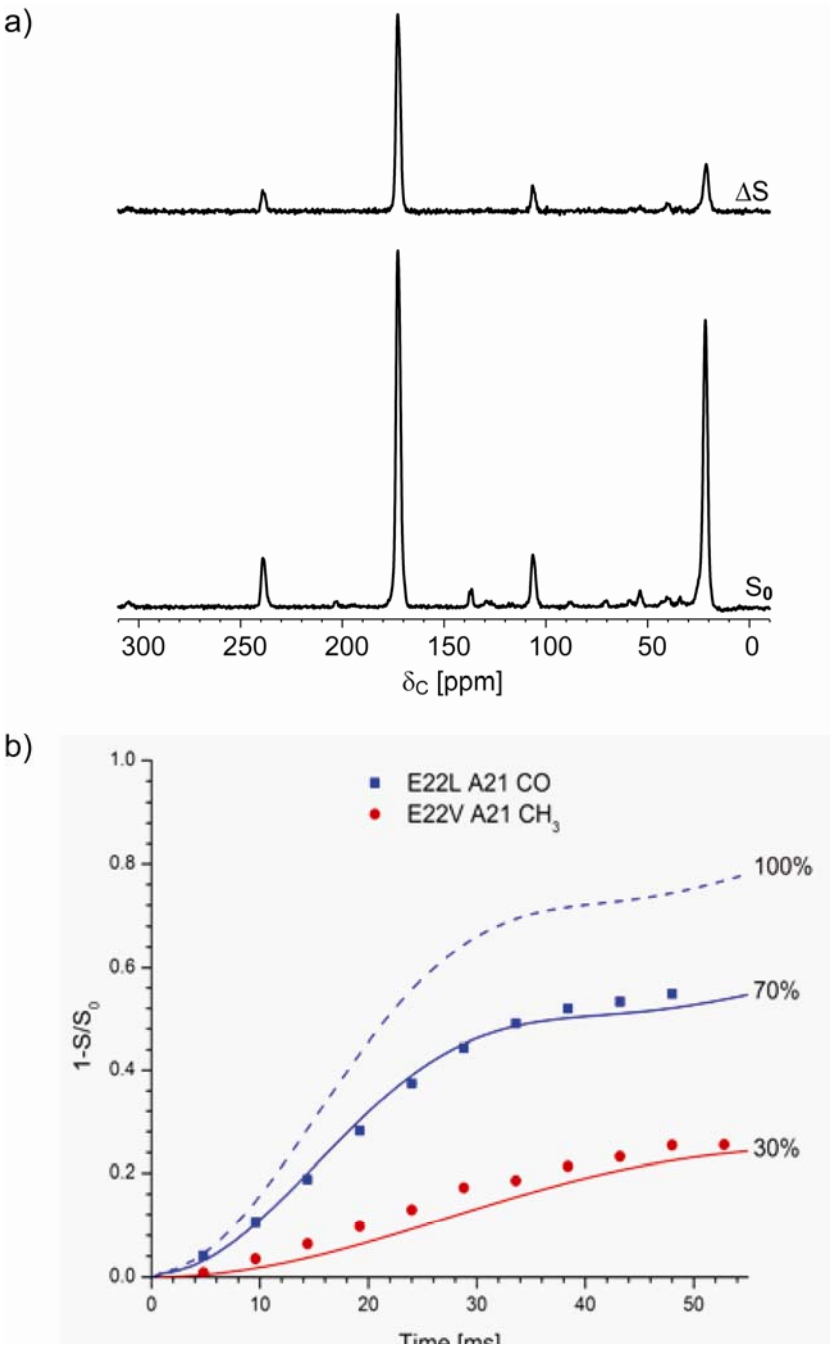

Figure 5-8: (a) $^{13}C\{^{15}N\}$REDOR full echo and REDOR difference spectra at 336-Tr spectrum for a 1:1 mixture of KL[^{15}N]VFF[1-^{13}C]AL and KLVFF[3-^{13}C]AV indicating the ^{13}C are well resolved to allow $^{13}C\{^{15}N\}$REDOR collection for two REDOR curves within a single sample (b) $^{13}C\{^{15}N\}$REDOR dephasing of a 1:1 mixture of KL[^{15}N]VFF[1-^{13}C]AL and KLVFF[3-^{13}C]AV assemblies. The complete 100% dephasing curve (dotted blue line), 70% dephasing curve (solid

blue line) and 30% dephasing curve (solid red line) is compared with experimental observed data for KLVFFAL's A21 CO (blue squares) and KLVFFAV's A21 CH_3 (red circles).

Probing the Secondary Structural Differences of Assemblies

As shown in Figure **5-6**, KLVFFAL and KLVFFAV display distinct CD signatures. The CD of both peptides is the summation of effects from both peptide amide and –FF- aromatic electronic transitions. Clusters of aromatic side-chains within 9Å have been shown to strongly influence protein CD transitions and calculations indicated that the observed CD signature is sensitive to the phenylalanine side-chain arrangements[22]. This suggests that the Phe arrangement in E22V is distinctly different from that of E22L. A second possibility is that E22V assemblies are composed of altered peptide secondary structures; however isotope edited FT-IR indicates that both pure assemblies are composed of anti-parallel out-of-register β-sheets[19]. Therefore, the observed CD signature differences (Figure **5-6**) may be the result of side-chain conformational changes that arise from differences in β-sheet lamination.

Probing the Peptide Organization Differences in Assemblies

To test if both E22L and E22V β-sheets laminate similarly, diffraction patterns of aligned nanotubes were collected and analyzed. While the electron diffraction E22L and E22V nanotube were distinct (Figure **5-9**), the KLVFFAL nanotubes diffraction pattern was consistent with two superimposed equally intense cross-β patterns that are each offset 13±2° from the long nanotube axis. Each cross-β pattern is composed of 4.7Å d-spacing from H-bonded β-sheet strands and a 10.1Å d-spacing coming from extended β-sheet lamination. In comparison, the KLVFFAV nanotube diffraction also appears to be composed of two equally intense diffraction patterns offset by 34±3°. A 4.7 Å d-spacing assigned to extended array of hydrogen bonded β-sheet peptides is present, but no 10Å lamination d-spacing was observed in the E22V pattern. Instead,

the diffraction pattern contained unique d-spacing at 5.3Å that has been previously attributed to β-sheet pleats shifted by one pleat as illustrated in Figure **5-10**[23].

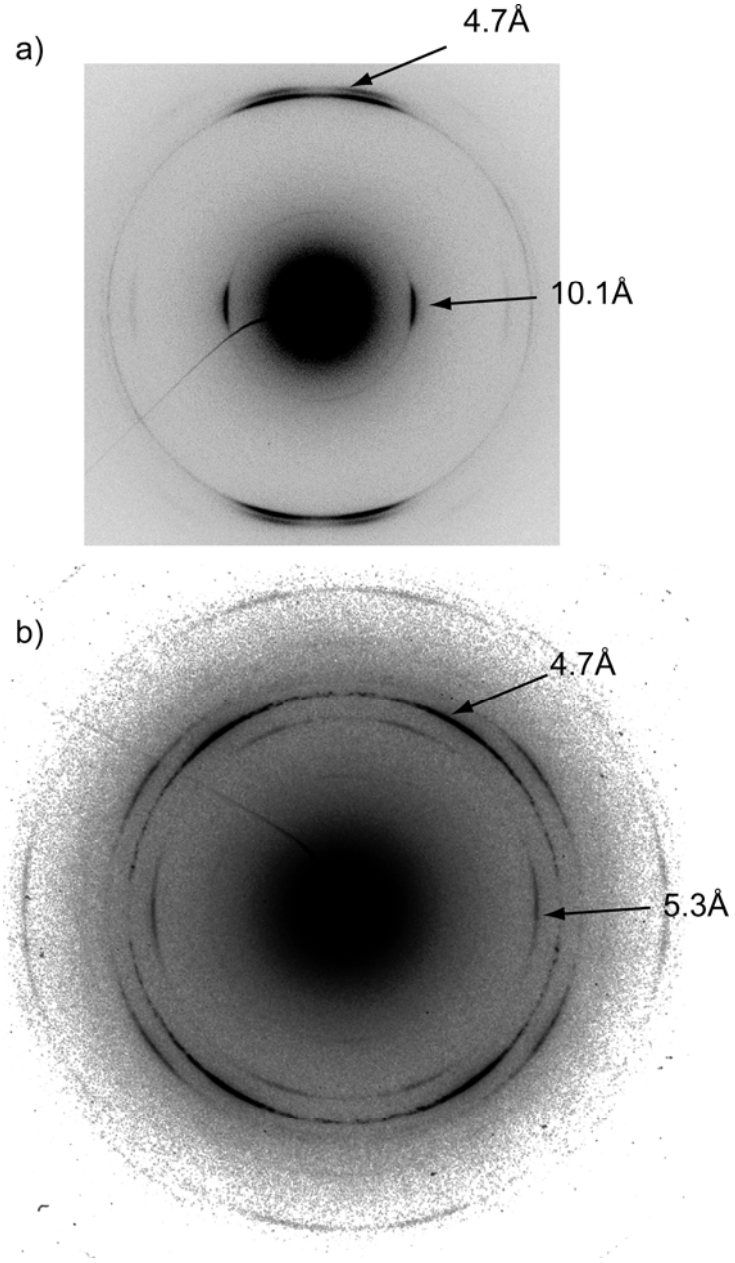

Figure 5-9: Comparison of aligned electron diffraction of (a) KLVFFAL and (b) KLVFFAV nanotubes.

To simplify analysis of the E22V nanotube diffraction (Figure **5-9**), diffraction of a similar peptide E22A which forms only sheets was analyzed. The simplicity of amyloid sheet

diffraction is that electrons only diffract through one layer of peptide, relative to two layers of peptide for a hollow nanotube. The electron diffraction of aligned E22A sheets is shown in Figure **5-10**. To assign the structural origins of the 5.3 Å d-spacing, CLEARER amyloid diffraction[24], simulation software was used to simulate unit cells corresponding to a=9.4Å, b=6.9Å, c=11Å, α=90°, β=90°, and γ was varied between 125-150°. The corresponding simulations are displayed in Figure **5-10**, and experimental 5.3Å d-spacing is most consistent with a two pleat shift.

In an earlier study a wide-angle x-ray scattering (WAXS) found that E22V nanotubes from a powder sample contained a broad lamination d-spacing at 11.0Å relative to a much sharper 10.1 Å d-spacing for the E22L nanotubes[19]. In these samples, the hydrogen bonding 4.7Å d-spacing for E22L and E22V contain similar line widths, indicating the broadness is not the result of overall sample heterogeneity[19]. Similar differences in the broadness of lamination d-spacing were also observed when KLVFFAE nanotube (150 laminated sheets) and fiber (5-6 laminated sheets) x-ray powder diffraction were compared in Chapter 2[13]. In this case due to the low number of laminates of KLVFFAE each fiber contained very few laminates resulting in an observed broad lamination d-spacing. Therefore, the observed E22V WAXS lamination broadness is consistent with fewer lattice repeats than observed in E22L WAXS. In contrast E22V contains several relatively sharp d-spacings at 7.7Å, 5.3Å, and 4.3Å that are not observable in E22L (Figure **5-9**) and Aβ(16-22) fiber and nanotubes[13]. Each of these d-spacings can however be indexed to reflections associated with an extended array of β-sheet pleats[25].

Based upon differences in the observed diffraction, the structural model of E22V nanotube assemblies is consistent with a high number of pleat repeats. Such an extended pleat arrangement would alter the extended growth from lamination (E22L) to end-to-end assembly (E22V) as shown in Figure **5-10**.

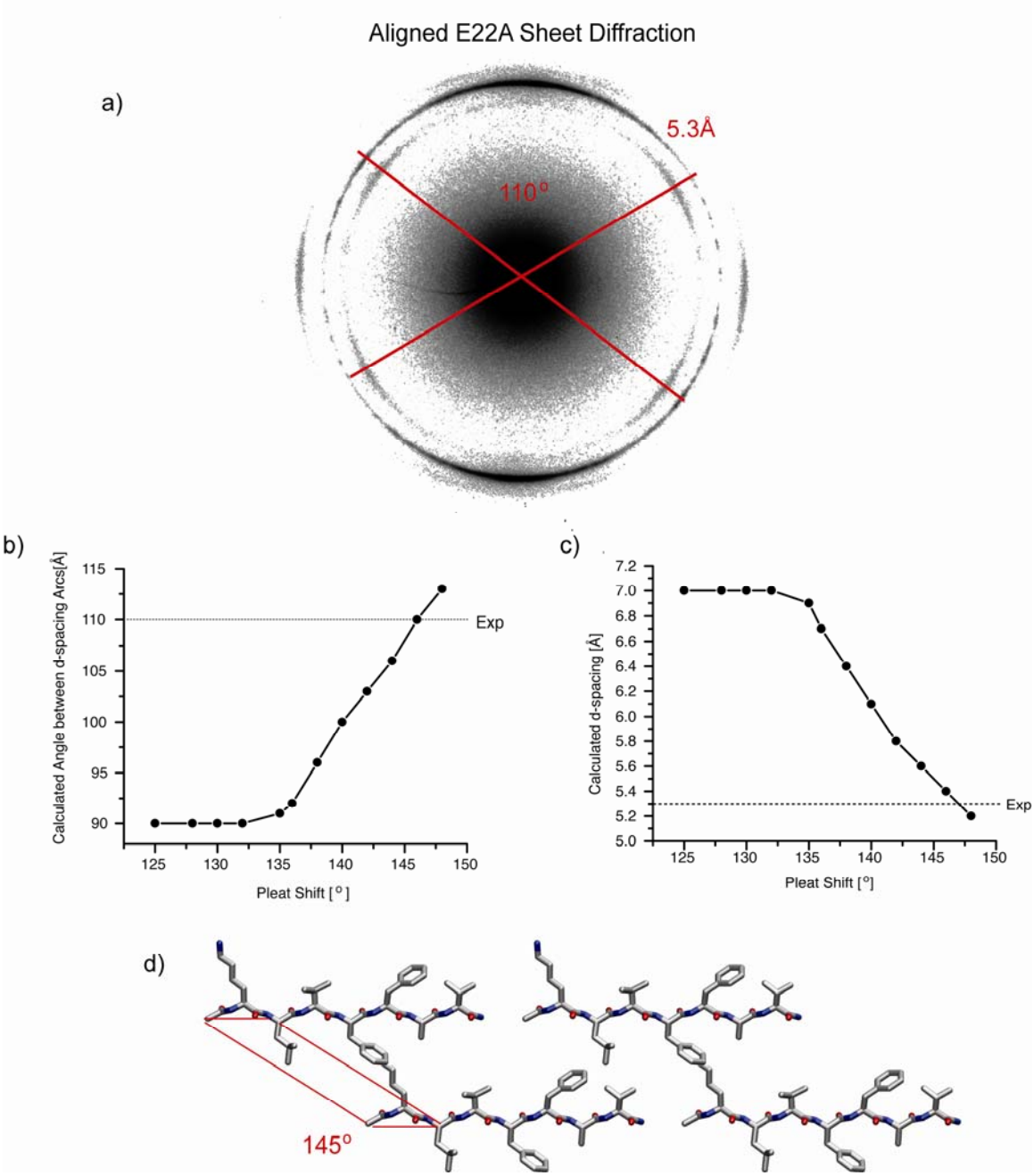

Figure 5-10: (a) Electron diffraction of aligned E22A sheets highlighting the 5.3Å d-spacings that corresponds to pleat organization[26]. CLEARER[24] simulated (b) angle between d-spacing arcs and (c) d-spacings as a function of varying the pleat shift from 125-150°. The experimental diffraction is most consistent with a (d) model in which laminates shift by two pleats.

Probing peptide organization with respect to the tube walls

This new model for peptide organization raises many more questions and the most important focuses on how many laminates construct the nanotube wall. SAXS and AFM measurements indicate that the wall thickness of E22V and E22L assemblies is 3-5 nm[16,19]. The following labeled peptides were synthesized, purified, and assembled in 40% acetonitrile at a concentration of 1.3 mM: [1-^{13}C]CH_3CO-KLVFFA[^{15}N]X. To probe for end-to-end interactions ^{13}C at the N-terminal acetate carbonyl is too far away from ^{13}C in neighboring hydrogen-bonded peptides (9.4Å) as well as the nearest peptides between laminates (>10Å) for ^{13}C DQF-DRAWS, which measures 13C-13C dipolar couplings, to observe any significant dephasing. Indeed, as shown Figure 9 below both [1-^{13}C]CH_3CO-KLVFFA[^{15}N]L and [1-^{13}C]CH_3CO-KLVFFA[^{15}N]V contain ^{13}Cs in close proximity. After applying a T2DQ correction, the distance between acetate carbonyls within E22L nanotube assemblies is 5.2±0.2Å, while it is 4.9±0.2Å within E22V nanotube assemblies.

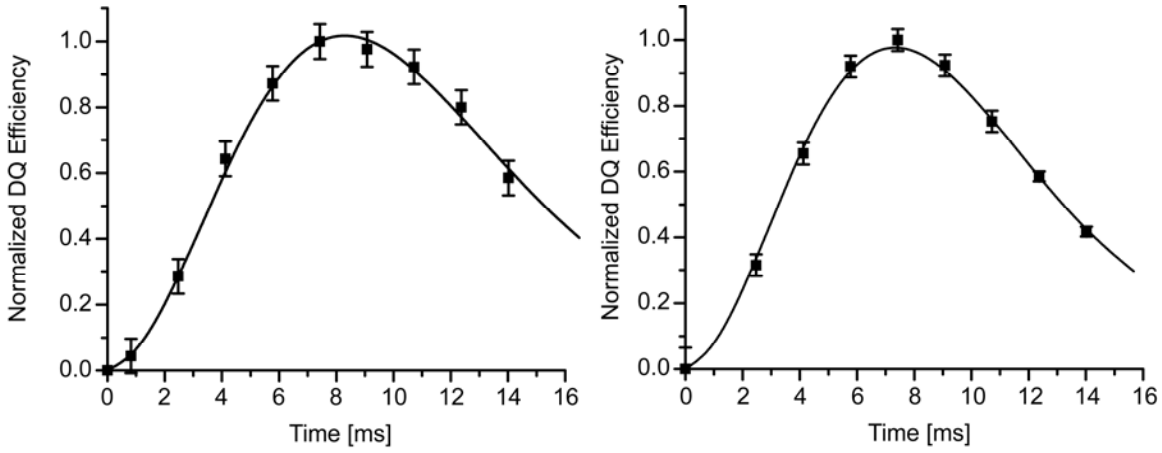

Figure 5-11: DQF-DRAWS comparing (a) [1-^{13}C]CH3CO-KLVFFA[^{15}N]L nanotubes with a T2DQ=12 ms correction applied and (b) [1-^{13}C]CH3CO-KLVFFA[^{15}N]V nanotubes with a T2DQ=4.6 ms correction applied.

The 4nm wall thickness determined by SAX, SANS, and AFM would then be most consistent with 4 laminates. Within the 4 laminate model, 75% test how many β-sheets laminate together to form E22V's nanotube walls slow sodium phosphate was used to titrate away surface

bound TFA and bundle nanotubes together for solid-state NMR analysis. To test how many β-sheets laminate to form E22V nanotube walls, slow addition of sodium phosphate was used to titrate surface bound TFA and bundle the nanotubes for solid-state NMR analysis. $^{13}C\{^{19}F\}$ REDOR dephasing in Figure **5-12** plateaued at 75% consistent with a 4 laminate model.

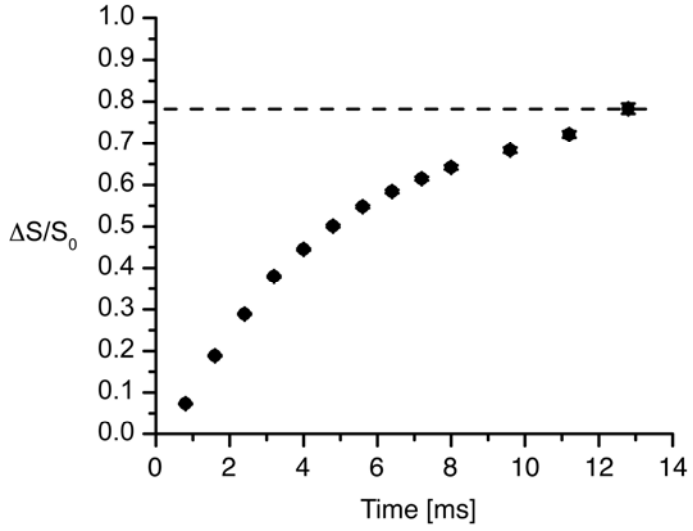

Figure 5-12: $^{13}C\{^{19}F\}$ REDOR of phosphate bundled [1-^{13}C]CH3CO-KLVFFA[^{15}N]V nanotubes assembled in 40% acetonitrile + 0.1% $C^{19}F_3COO^-$.

Testing the effect of Decreasing Side-Chain Length

With the data in hand, there are sufficient constraints to begin building structural models for MD analysis. These models suggest that the long leucine residue does not allow the L17-F19 pleat sit on top of F20 due to L22 steric clashes. The shorter valine side-chain however can be accommodated this pleat shift (Figure **5-10**). This model then predicts that shortening the E22 side-chain is a root cause of the structural change, and a series of congeners at the E22 position ranging in side-chain length (glutamic acid, leucine, isoleucine, valine, alanines, and glycines) were characterized by electron diffraction. As shown in Figure **5-13**, the electron diffraction patterns can be grouped into 2 categories: those with observable 10Å d-spacing and those with an observable 5.3Å d-spacing. Peptide assemblies (E22, E22I, E22L) with observable 10Å d-

spacing indicate the wide nanotubes diameter is made up of extended β-sheet lamination, while peptide assemblies (E22V, E22A, E22G) with 5.3Å d-spacing indicate end-to-end termini interactions.

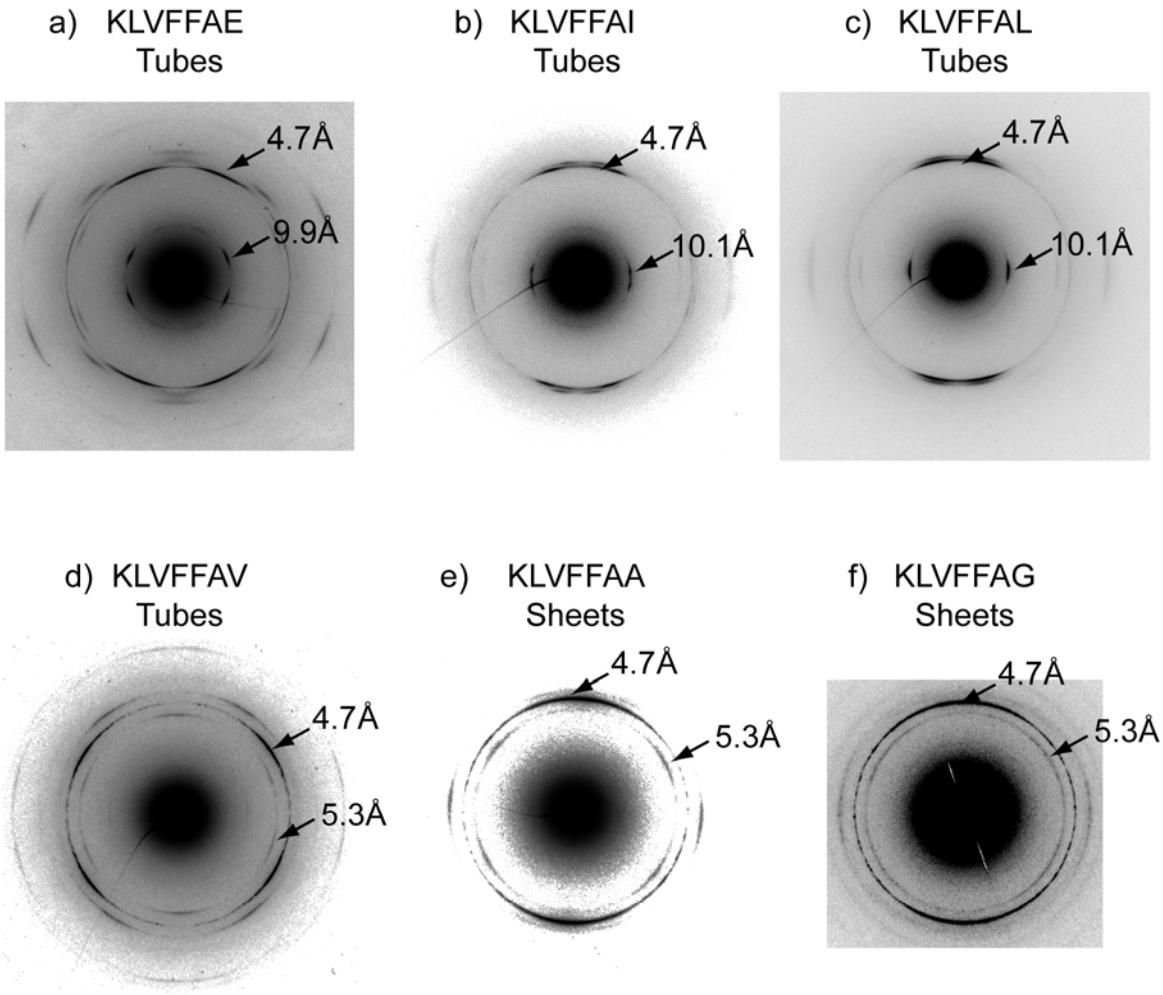

Figure 5-13: Electron diffraction of aligned peptide assemblies of (a) KLVFFAE, (b) KLVFFAI, (c) KLVFFAL, (d) KLVFFAV, (e) KLVFFAA, and (f) KLVFFAG. D-spacing signatures of extended hydrogen bonding (4.7Å), extended lamination (~10Å), and extended termini stacking (5.3Å) are identified if present in each electron diffraction pattern.

This division of the peptide assemblies into two broad categories of extended lamination (E22, E22L, and E22I) and end-to-end associations (E22V, E22A, and E22G) argues that side-

chain shortening drives the observed pleat shift, and it appears that E22L-E22V provides the switching point between these two architectures.

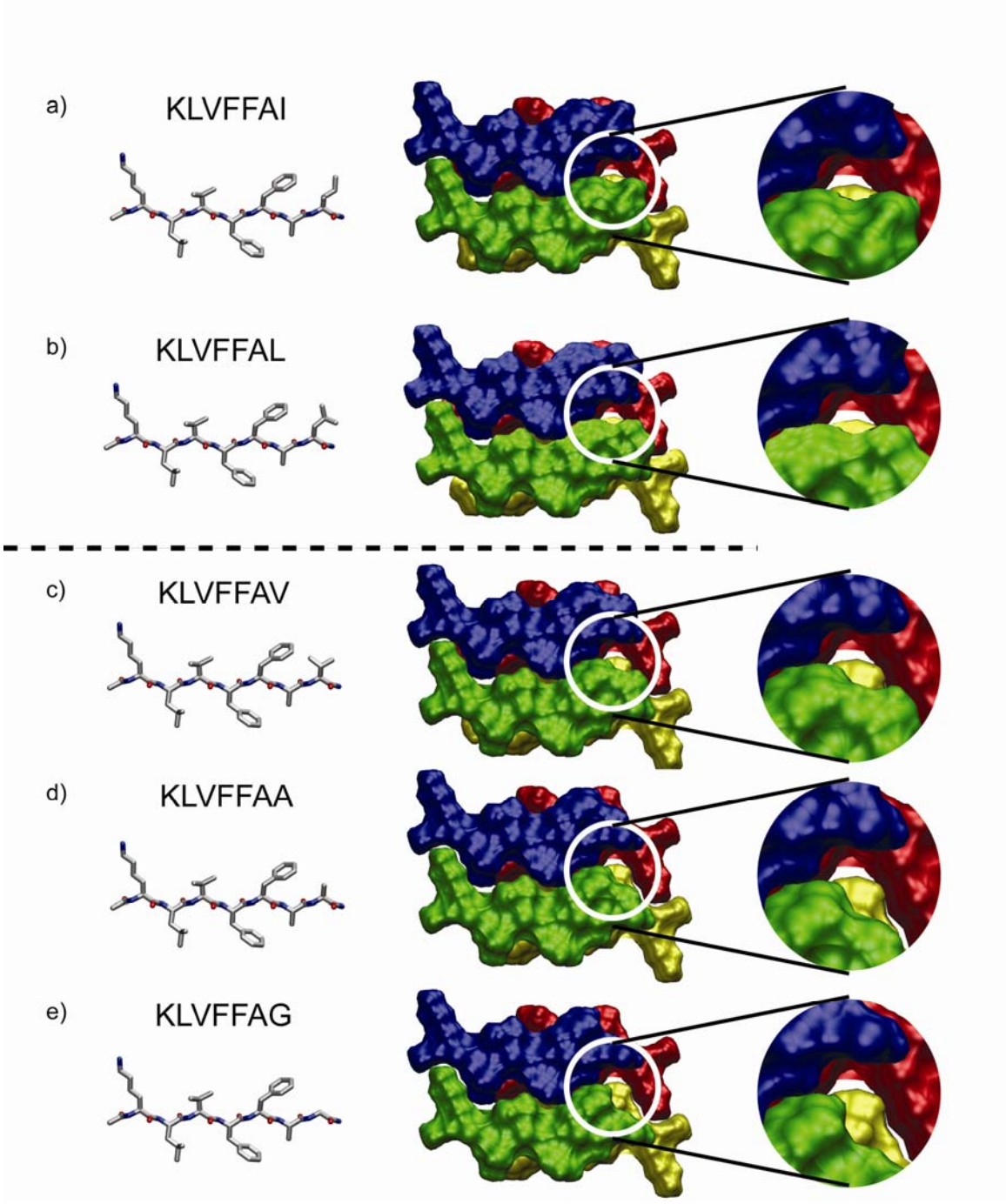

Figure 5-14: The overall impact of decreasing the E22 side-chain length creates a void space that allows the L17-F19 pleat to shift and rest above F20 pleat. Lengthy side chains (E22, E22I, and

E22L) do not allow this pleat shift, while shorter side-chains permit the pleat shift (E22V, E22A, and E22G).

Conclusions

Decoding the rules of specificity in self-assembly will be necessary for robust construction of functional biological and chemical systems. Well defined Watson-Crick base pairing has enabled genomic encoding of entire organisms.[27] In contrast to the simplified 2 base pairs of oligonucleotides, polypeptides containing 20 natural amino acids offers a rich, yet poorly understood, molecular language to encode complex specificity.

Here two radically different β-sheet peptide assembly configurations (extended lamination versus sticky end assembly - Figure **5-10**) is encoded at the molecular level of a single methylene change from leucine to valine. The source of this change in peptide configuration is shortening the C-terminal leucine enables peptide building blocks to shift by one pleat as illustrated by a series of E22 mutants (Figure **5-14**). Relative to the blunt ends of KLVFFAL nanotube assemblies, the E22V pleat shift creates a larger surface area that can be desolvated upon stacking peptides in the termini direction. Similar complementarity has been seen in the modulation the number of alpha-helices that bundle together where single residue substitutions can also modulate steric interactions[28,29,30].

Unlike nucleic acids, dissecting the peptide specificity code will require extensive studies of how peptides sequence encode specificity through tertiary steric interactions. Earlier studies[14,31,32] have explored coiled-coil sequence space and have begun to develop rules of coiled-coil specificity. Here we have provided an early example of how subtle changes in peptide sequence can direct β-sheet configurational changes that direct peptide behaviour. Further understanding of β-sheet specificity combined with coiled-coil assembly energetics will enable unprecedented de novo design of complex nanomachines and systems chemistry.

Within β-sheet assemblies, this is of critical importance importance in the context of neurodegenerative prion diseases. As an example, yeast prions exhibit species barriers that are directed at the level of a single amino acid substation[33,34]. Furthermore, in the context of human disease similar species barriers appear to exist[35]. While all peptides have the capacity to form amyloid assemblies[36,37], side-chain interactions direct specificity for the construction of a wide away of prion strain architectures. Dissecting this β-sheet specificity code will be critical to our understanding of prion strains and amyloid forms within the complex cellular environment.

References

1. Kruse T, Bork-Jensen J, Gerdes K (2005) The morphogenetic MreBCD proteins of Escherichia coli form an essential membrane-bound complex. Molecular Microbiology 55: 78-89.

2. Gerdes K, Howard M, Szardenings F (2010) Pushing and Pulling in Prokaryotic DNA Segregation. Cell 141: 927-942.

3. Moller-Jensen J, Jensen RB, Lowe J, Gerdes K (2002) Prokaryotic DNA segregation by an actin-like filament. Embo Journal 21: 3119-3127.

4. Cabeen MT, Jacobs-Wagner C (2005) Bacterial cell shape. Nature Reviews Microbiology 3: 601-610.

5. Briggs JAG, Wilk T, Welker R, Krausslich HG, Fuller SD (2003) Structural organization of authentic, mature HIV-1 virions and cores. Embo Journal 22: 1707-1715.

6. Dye NA, Pincus Z, Theriot JA, Shapiro L, Gitai Z (2005) Two independent spiral structures control cell shape in Caulobacter. Proceedings of the National Academy of Sciences of the United States of America 102: 18608-18613.

7. Mateu MG (2009) The capsid protein of human immunodeficiency virus: intersubunit interactions during virus assembly. Febs Journal 276: 6098-6109.

8. He Y, Ye T, Su M, Zhang C, Ribbe AE, et al. (2008) Hierarchical self-assembly of DNA into symmetric supramolecular polyhedra. Nature 452: 198-U141.

9. Cai MA, Wang QB (2010) Structural DNA Nanotechnology. Progress in Chemistry 22: 975-982.

10. Winfree E, Liu FR, Wenzler LA, Seeman NC (1998) Design and self-assembly of two-dimensional DNA crystals. Nature 394: 539-544.

11. Feldkamp U, Niemeyer CM (2006) Rational design of DNA nanoarchitectures. Angewandte Chemie-International Edition 45: 1856-1876.

12. Zimenkov Y, Dublin SN, Ni R, Tu RS, Breedveld V, et al. (2006) Rational design of a reversible pH-responsive switch for peptide self-assembly. Journal of the American Chemical Society 128: 6770-6771.

13. Mehta AK, Lu K, Childers WS, Liang Y, Dublin SN, et al. (2008) Facial Symmetry in Protein Self-Assembly. J Am Chem Soc 130: 9829-9835.

14. Bromley EHC, Sessions RB, Thomson AR, Woolfson DN (2009) Designed alpha-Helical Tectons for Constructing Multicomponent Synthetic Biological Systems. Journal of the American Chemical Society 131: 928-930.

15. Reinke AW, Grant RA, Keating AE (2010) A Synthetic Coiled-Coil Interactome Provides Heterospecific Modules for Molecular Engineering. Journal of the American Chemical Society 132: 6025-6031.

16. Lu K (2005) Discovery of Diverse Peptide Nanotube Architecture from the Self-assembly of Designed Amyloid-β Cassettes. Atlanta: Emory University. 257 p.

17. Nilsson MR (2004) Techniques to study amyloid fibril formation in vitro. Methods 34: 151-160.

18. Paul C, Wang JP, Wimley WC, Hochstrasser RM, Axelsen PH (2004) Vibrational coupling, isotopic editing, and beta-sheet structure in a membrane-bound polypeptide. Journal of the American Chemical Society 126: 5843-5850.

19. Liang Y (2009) Energetic Contributions of Amyloid Self-Assembly: Emory University. 213 p.

20. Mehta MA, Eddy MT, McNeill SA, Mills FD, Long JR (2008) Determination of peptide backbone torsion angles using double-quantum dipolar recoupling solid-state NMR Spectroscopy. Journal of the American Chemical Society 130: 2202-2212.

21. Liang Y, Guo P, Pingali SV, Pabit S, Thiyagarajan P, et al. (2008) Light harvesting antenna on an amyloid scaffold. Chemical Communications: 6522-6524.

22. Sreerama N, Manning MC, Powers ME, Zhang JX, Goldenberg DP, et al. (1999) Tyrosine, phenylalanine, and disulfide contributions to the circular dichroism of proteins: Circular dichroism spectra of wild-type and mutant bovine pancreatic trypsin inhibitor. Biochemistry 38: 10814-10822.

23. Sikorski P, Atkins EDT, Serpell LC (2003) Structure and texture of fibrous crystals formed by Alzheimer's A beta(11-25) peptide fragment. Structure 11: 915-926.

24. Makin OS, Sikorski P, Serpell LC (2007) CLEARER: a new tool for the analysis of X-ray fibre diffraction patterns and diffraction simulation from atomic structural models. Journal of Applied Crystallography 40: 966-972.

25. Sikorski P, Atkins EDT, Serpell LC (2003) Structure and Texture of Fibrous Crystals Formed by Alzheimer's Aβ(11-25) Peptide Fragment. Structure 11: 915-926.

26. Sikorski P, Atkins ED, Serpell LC (2003) Structure and texture of fibrous crystals formed by Alzheimer's Ab(11-25) peptide fragment. Structure 11: 915-926.

27. Lartigue C, Vashee S, Algire MA, Chuang RY, Benders GA, et al. (2009) Creating Bacterial Strains from Genomes That Have Been Cloned and Engineered in Yeast. Science 325: 1693-1696.

28. Betz S, Fairman R, Oneil K, Lear J, Degrado W (1995) Design of 2-stranded and 3-stranded coiled-coil peptides Philosophical Transactions of the Royal Society of London Series B-Biological Sciences 348: 81-88.

29. Harbury PB, Kim PS, Alber T (1994) Crystal-Structures of an isoleucine-zipper trimer. . Nature 371: 80-83.

30. Zhu BY, Zhou NE, Kay CM, Hodges RS (1993) Packing and hydrophobicity effects on protein folding and stability - effects of beta-branced amino acids, valine, and isoleucine, on the formationa nd stability of 2-stranded alpha helical coiled coil leucine zippers Protein Science 2: 383-394.

31. Walters RFS, DeGrado WF (2006) Helix-packing motifs in membrane proteins. Proc Natl Acad Sci 103: 13658-13663.

32. Gratkowski H, Lear JD, DeGrado WF (2001) Polar side chains drive the association of model transmembrane peptides. Proceedings of the National Academy of Sciences of the United States of America 98: 880-885.

33. Chen BX, Bruce KL, Newnam GP, Gyoneva S, Romanyuk AV, et al. (2010) Genetic and epigenetic control of the efficiency and fidelity of cross-species prion transmission. Molecular Microbiology 76: 1483-1499.

34. Chen BX, Newnam GP, Chernoff YO (2007) Prion species barrier between the closely related yeast proteins is detected despite coaggregation. Proceedings of the National Academy of Sciences of the United States of America 104: 2791-2796.

35. Collinge J, Clarke AR (2007) A general model of prion strains and their pathogenicity. Science 318: 930-936.

36. Guijarro JI, Sunde M, Jones JA, Campbell ID, Dobson CM (1998) Amyloid fibril formation by an SH3 domain. Proceedings of the National Academy of Sciences of the United States of America 95: 4224-4228.

37. Dobson CM (1999) Protein misfolding, evolution and disease. Trends Biochem Sci 24: 329-332.

Chapter 6 : Templating Molecular Arrays in Amyloid's Cross-β Grooves[1]

Initial classification of unbranched fibrous assemblies as amyloid has relied heavily upon the histochemical dye Congo Red(CR)[1]. In commonly used histological protocols[2,3] CR stains amyloid materials even in complex fibrous or tissue samples. When the CR stained sample is viewed under crossed polarized light, a characteristic "apple-green" birefringence is observed, which can be more appropriately termed apple-green interference color[4,5,6]. And somewhat less dramatic the electronic transition show a red-shifted UV profile for CR bound to amyloid relative to unbound CR[7]. For more than 80 years[1,3,7,8] these CR histological staining protocols have served as a universal diagnostic of cross-β structure. Not only has CR been used in the diagnostics of amyloid related neurodegenerative disease[7] it has also identified cross-β structures regardless of primary sequence in misfolded globular proteins[9], functional amyloid forms[10,11,12], and truncated synthetic amyloid peptides[13,14]. Indeed, radically different peptide sequences and various amyloid configurations[15,16,17,18,19,20,21] all yield similar spectroscopic signatures of CR binding, implying common CR binding mode. Despite extensive biophysical characterization[5,22,23,24,25], the intertwined nature of CR amyloid binding and cross-β structure remains ill-defined.

Solid-state NMR[19,26,27,28,29,30,31], fiber diffraction[32,33,34,35,36,37] and x-ray crystallography of amyloid crystallites[18,38] have independently characterized amyloids of radically different sequences as being composed of a cross-β spine in which long hydrogen bonded β-sheets with peptides separated by 4.6-4.8Å run parallel to the long fiber axis and laminate together with each sheet separated by ~10Å to yield a 50 Å width. The grid-like spacing

[1] Results published as Childers, W. S., A. K. Mehta, et al. (2009). Templating Molecular Arrays in Amyloid's Cross-β Grooves. JACS **131**(29): 10165-10172.

of peptides yields two orthogonal reflections to create amyloid's cross-β pattern. In amyloid's simplest form, the solvent accessible surfaces can be approximated as a rectangular solid (Figure **6-1**) with two distinct faces: a surface with side-chains emerging from the β-sheet pleats (i.e. pleat surface - yellow) and surfaces composed of N- and C-terminal residues (i.e. termini surface - blue). Using this simplified scaffold as a model, the pleat surface (yellow) has two possible CR binding orientations: (a) parallel to β-strands separated by 4.6-4.8Å[23,24], and packed within the ~7Å β-sheet pleats[39]. In contrast the termini surface (blue) is formed by β-sheets that laminate together separated by ~10Å result in solvent exposed laminate grooves[8,40]. In addition, the fiber ends also present two low stoichiometry binding sites for each fiber. This complex surface dimensionality (Figure **6-1**) of the cross-β structure has stymied assignment of ligand binding sites[41,42], which has further complicated the de novo design of amyloid diagnostic and therapeutic agents.

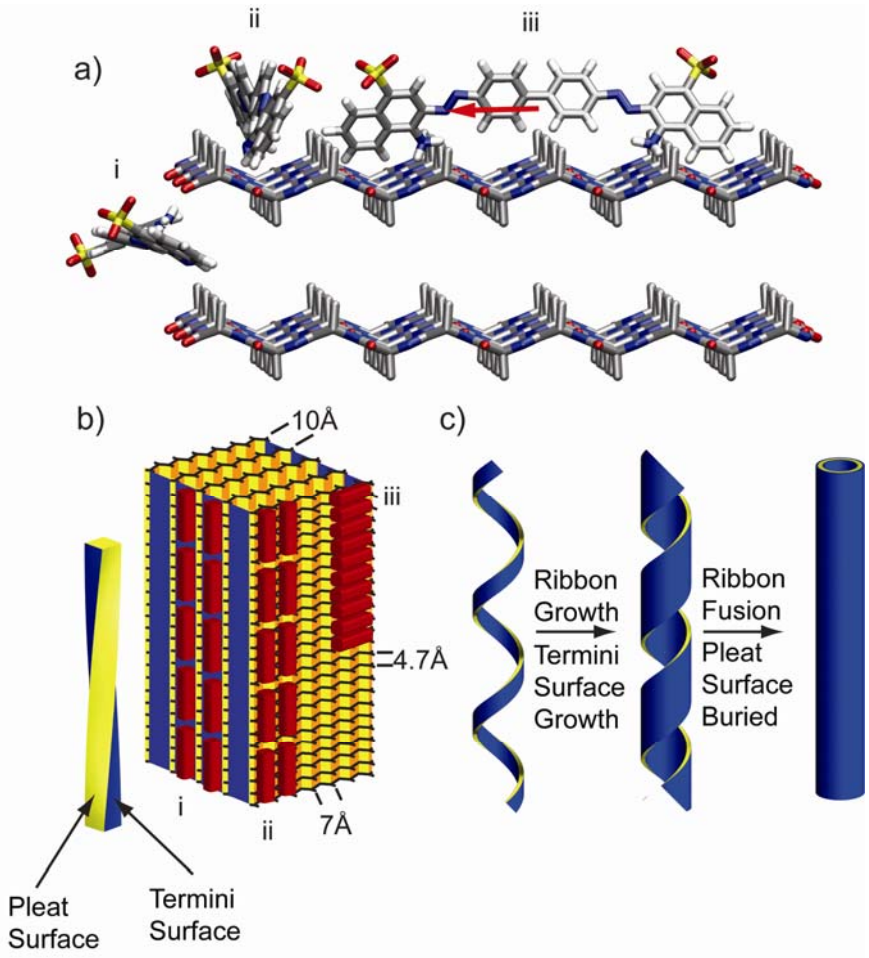

Figure 6-1: Proposed CR-amyloid binding modes. The calculated transition dipole is shown as a red arrow along binding mode iii. (a) The cross-β structure contains three possible binding sites: (i) laminate groove, (ii) pleat groove, and (iii) between two β strands. (b) Amyloid fibers contain two distinct solvent accessible surface: β-sheet pleat surface (yellow) and the termini surface (blue). CR (red blocks) contains a single binding mode organized end-to-end within laminate grooves (i). Along the β-sheet pleat surface (yellow) there are two potential binding modes: within the pleats (ii) organized end-to-end or between peptide strands organized side-by-each perpendicular to the fiber axis. (c) Transformation of KLVFFAL ribbons into nanotubes that display the termini surface (blue) and bury the β-sheet pleat surface (yellow)

To reduce the surface complexity of amyloid fiber assemblies, we have focused on the critical nucleating core of the Alzheimer's disease peptide. ^{16}KLVFFA^{22}E or Aβ(16-22) forms typical cross-β fibers under neutral conditions (similar to Figure **6-1**b), and forms helical cross-β nanotubes under acidic conditions (Figure **6-1**c). In Chapter 5, the structures of KLVFFAL and KLVFFAV were assembled via extended in-register lamination and extended out-of-register lamination. As a result of KLVFFAL's extended in-register lamination, the β-sheet pleat surface (yellow) is completely buried and exposed only the termini surface (blue). In KLVFFAV's extended out-of-register lamination, the termini surface (blue) becomes buried and exposes the β-sheet pleat surface (yellow). Therefore E22L and E22V nanotubes provide simplified model amyloid surfaces that reduce the complex surface dimensionality observed in twisted amyloid fibers (Figure **6-1**). Within this chapter, I will use these model cross-β surfaces to determine CR's affinity to the pleat and termini surfaces, and the laminate groove binding site will be characterized in detail.

Methods

Peptide Synthesis and Purification

Peptides were synthesized using standard FMOC NMM/HBTU protocols for solid-phase synthesis and capped with a N-terminal CH_3CO- and a C-terminal $-NH_2$ as described in Chapter 2 Methods Section. Peptides were purified via RP-HPLC using C18-reverse phase with an acetonitrile−water gradient. MALDI-TOF with a 2,5-dihydroxybenzoic acid matrix confirmed molecular weight. Aβ(16−22)E22L (1.3 mM) dissolved in 2:3 CH_3CN/H_2O with 0.1% TFA (pH 2). Dissolution of sample was assisted using vortexing and sonication until solution became clear. Peptide solutions were then assembled at 4 °C until mature by CD, ~2 weeks[19]. Assemblies were titrated to neutral conditions using 0.1 M NaOH in 40% CH_3CN.

Transmission Electron Microscopy and Electron Diffraction

TEM micrographs were recorded with a Philips 410 TEM using Tungsten filament at an accelerating voltage of 80 kV. Upon sample addition to TEM grids (200 mesh with a thin carbon film support – Electron Microscopy Sciences, Hatfield, PA), the KLVFFAL assemblies were allowed to adsorb for 1 min. Excess peptide solution was wicked away with filter paper. Then a 2 wt % uranyl acetate incubation time (1-5 minutes) was optimized for negative staining both inside and outside of the hollow nanotubes. Prior to EM studies, grids were placed in a desiccator overnight to remove any residual solvents. The resulting samples were viewed and imaged at magnifications between 7100× and 69 000×. Negatives were scanned at 2000 dpi resolution on an Agfa DuoScan flatbed scanner (Agfa Corp., Ridgefield Park, NJ).

For electron diffraction, the film exposure time was optimized at approximately 0.2 s to minimize exposure of the bright center spot while allowing adequate exposure time to capture the diffraction pattern. Additionally, to minimize impact of center spot, the smallest aperture and spot size settings were used. For electron diffraction *d*-spacing was calculated using $d = \lambda L/R$, where

R is the distance (mm) from the central bright spot to one of the rings, *L* (mm) is the distance between specimen and photographic film, and λ is the electron wavelength (80 kV). Camera length was calibrated using an aluminum polycrystalline standard (Ted Pella, Inc., Redding, CA). Since evaporated aluminum standard contained *d*-spacings at shorter distances than amyloid nanotube samples, an additional standard with *d*-spacings comparable to KLVFFAL nanotubes was required. Aβ(16−22) nanotubes with *d*-spacings of 4.7 and 9.9 Å, confirmed by fiber X-ray diffraction, were employed as a standard.[19] In each case, the Aβ(16−22) nanotube standard confirmed that the camera constant calculated using evaporated aluminum could be extrapolated to longer d-spacings.

UV−Vis Absorption and Circular Dichroism

UV−vis absorption spectra were recorded with a Jasco V-530 UV spectrophotometer using a 2 mm cuvette path length to collect absorptions at higher CR concentrations. Dissolving CR in 40% acetonitrile at pH 7 shifted the λ_{max} from 498 to 505 nm. CR molar absorptivity at 505 nm was determined to be 39 239 L mol^{-1} cm^{-1} in 40% acetonitrile at pH 7 and was found to be insensitive from pH 6−8. Both UV and CD spectra were background subtracted using KLVFFAL/KLVFFAV nanotubes in the absence of CR to minimize scattering effects. CD spectra were measured on a Jasco V-810 CD polarimeter with a 1 mm cuvette.

Hill Plot

Molar absorbtivity at 532 nm was 56 604 L mol^{-1} cm^{-1} for bound CR under conditions with excess nanotubes, while the molar absorbtivity for free CR was 39 239 L mol^{-1} cm^{-1}. After correction for scattering, an isobestic point was identified at 406 nm with a molar absorbtivity of 15 195 L mol^{-1} cm^{-1}. The moles of bound CR were calculated following protocols[7] established for CR UV−vis absorption spectral assays[7]. The amount of bound CR was calculated as $(A_{532}/39\,239 - A_{406}/15\,195)/((56\,604/39\,239) - 1)$ for each saturation point in the Hill plot. θ in the Hill plot is the fraction of occupied binding sites (CR bound)/(total CR), where total CR binding

was determined from the maximum. Hill plot error bars represent the standard deviation of three independent trials, and each trial is the average of three scans.

Linear Dichroism

LD reports on orientation of molecules by measuring the difference in absorption of linearly polarized light parallel and perpendicular to the orientation axis (e.g. the long nanotube/fiber axis).

$$LD = A_{\parallel} - A_{\perp}$$

Advances in micro-volume Couette flow cells[43,44] has allowed investigation of molecular orientations in various assembled architectures including fibers with less interference from light scattering[45]. A Couette flow cell is composed of an inner cylinder surrounded by a larger outer cylinder that rotates creating laminar flow in the hollow cavity between the cylinders[43]. Long hollow nanotubes orient well in the direction of laminar flow. The reduced linear dichroism (LD_R) is related to orientation of the CR's transition dipole with respect to the amyloid nanotube axis (α) and an orientation factor (S) as shown in Equation 2[43].

$$LD^R=(A_{\parallel}-A_{\perp})/A=3/2S(3\cos^2\alpha-1)$$

LD was recorded using a micro-volume cuvette with a path length of 50 μm[44] and a rotation speed of 3000 rpm to establish Couette flow. The background for each sample was recorded by measuring the LD spectra of samples at 0 rpm under isotropic conditions to capture potential scattering effects from self-assembled structure. To correct for observed light scattering empirical methods developed by Nordh subtract out the contribution due to the turbidity of the amyloid nanotube sample[46] and quantifies the background turbidity dichroism LD_T as a function of two constants, α and k.

$$LD^T(\lambda)=\alpha\lambda^{-k}$$

Typical values of k are between 2.8 and 3.5, and here 3.5 was used to quantify the turbidity dichroism[46].

Polarizing Microscopy

KLVFFAL nanotubes have a diameter of 38 nm[19] and are below the resolution of optical microscopy (~200 nm). Addition of divalent anions (e.g., sulfate) to the positively charged nanotubes creates micron sized nanotube bundles that are large enough to be visualized by optical microscopy[47]. Following published methods[2], the sulfate bundled nanotubes were stained with CR. The sulfate bundled peptide nanotube solution (3 μL) was air-dried on a glass microscope slide, then a 100 μM CR staining solution (100 μL) was added and allowed to air-dry. The slide was then washed with double distilled H_2O to remove unbound CR and again allowed to air-dry. Optical microscopy images were collected with an Olympus BX60 differential interference contrast microscope with sample between crossed polarizers at a magnification of 40×. Bright field images were obtained by tuning the angle between polarizers to 0°.

Quantum Calculations

All calculations were performed with Gaussian 03[48]. The DFT 6-31+G(d,p)/B3LYP geometry optimized Congo Red monomer was fixed when creating the dimers, trimers, and tetramers. ZINDO/S[49,50] calculations of vertical electronic transitions were limited by memory requirements to a maximum of 4 CR molecules. Exciton coupling is the difference between the calculated vertical transition energies for the multimers relative to monomer.

Results

Preliminary Analysis of E22L and E22V Nanotubes

Compared with the complex surface dimensionality of amyloid fibers containing both a pleat surface and a termini surface (Figure **6-1**), E22L and E22V nanotubes simplify the study of small molecule binding as there structure presents only one type of surface: E22L (termini surface) and E22V (pleat surface). Figure **6-2** below analyzes the grid like surface of each type of nanotube based upon the solved structures of E22L and E22V nanotubes discussed in Chapter 5. The grid surface for E22L (Figure **6-2**a) places the N-terminal lysines 9.4Å apart in the hydrogen bonding direction and ~10Å apart in the lamination direction. The hydrophobic surface (blue) of this grid is composed of residues at or near the termini, and in the case of KLVFFAL these are L17 and L22. In comparison the grid surface of E22V nanotubes (Figure **6-2**b) the N-terminal lysines are spaced by 9.4Å in the hydrogen bonding direction and ~24 Å in the peptide chain direction. And E22V's hydrophobic pleat surface (yellow) is composed of side-chains emerging from the pleats, and due to the anti-parallel peptide arrangment this alternates from one peptide containing K-V-F-V side-chains, and the next peptide chain containing L-F-A side-chains. Along the pleat surface each pleat has different chemical composition dictated by the emerging side-chains and could potentially serve as unique pleat binding sites. As illustrated in Figure **6-1**aii, the CR molecules could also bind parallel to the β-strands[23,24].

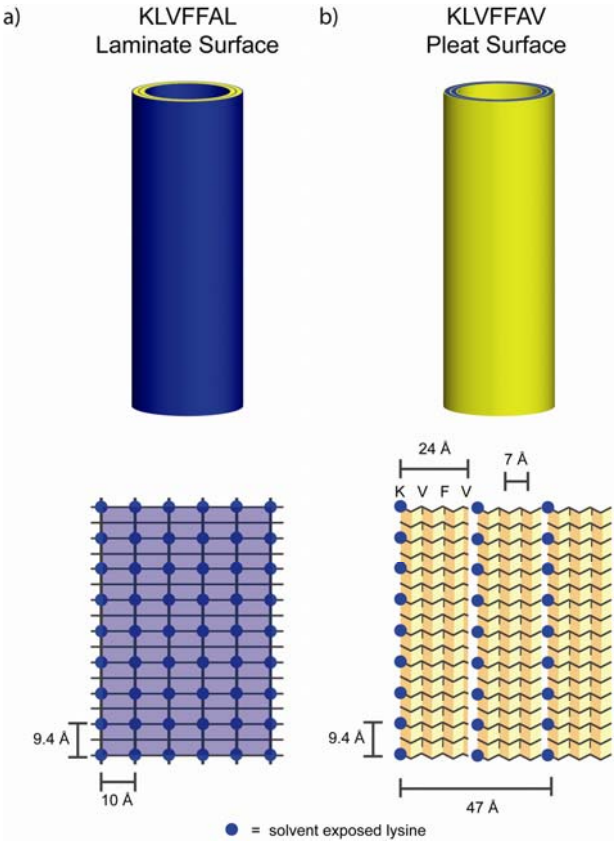

Figure 6-2: A comparison of the surface of E22L (termini surface) tubes with E22V (pleat surface) tubes.

Using these unique amyloid morphologies, CR binding to the termini (E22L) and pleat (E22V) surfaces can be directly compared. Upon addition of CR to both E22L and E22V nanotubes the UV-Vis absorption red-shifts relative to free CR (Figure **6-3**a), a diagnostic signature of CR binding to amyloid structures[8]. Additionally, the achiral unbound CR molecule has no CD signature in solution, but with either E22L or E22V an induced CD is observed (Figure **6-3**b). The differences in CR induced CD for E22L and E22V may be the result of binding to distinct molecular environments or unique CR binding conformations. These results support the idea that CR has multiple binding sites along the amyloid surface[41] and E22L and E22V presents unique sub-domains of that surface. Given that the termini surface contains only

a single type of binding site relative to the pleat surface (Figure **6-1**), this chapter provides a detailed biophysical characterization of CR binding to E22L nanotubes.

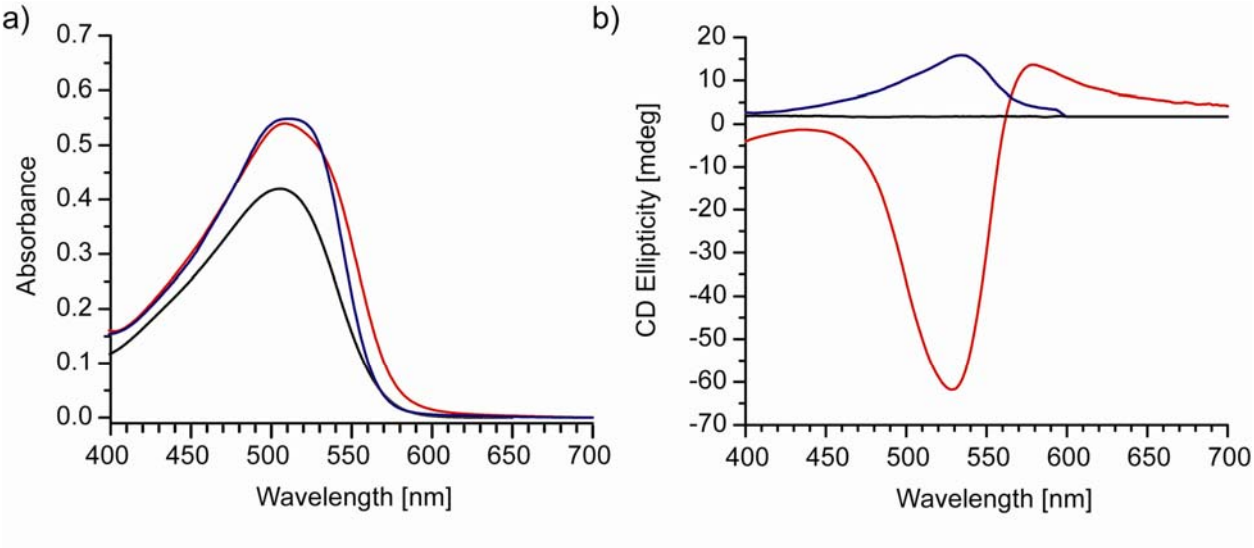

Figure 6-3: Survey of CR Binding to E22L nanotubes and E22V nanotubes using UV-Vis Absorption (a) and Circular Dichroism (b). In each plot free 40 μM CR (black), 40 μM CR + 650 E22V nanotubes (red), 40 μM CR + 650 E22V nanotubes (blue).

CR Binds to E22L Nanotubes that expose the termini surface

To visualize the 38 nm diameter E22L nanotubes by optical microscopy, sodium sulfate was added to bundle the nanotubes, yielding a bundle diameter of approximately 1 μm[47]. CR appears to accumulate along each E22L nanotube bundle (Figure **6-4**a) and when the sample is placed between crossed polarizers, it displays the characteristic apple-green interference (Figure **6-4**b) diagnostic of amyloid assemblies[1,2].

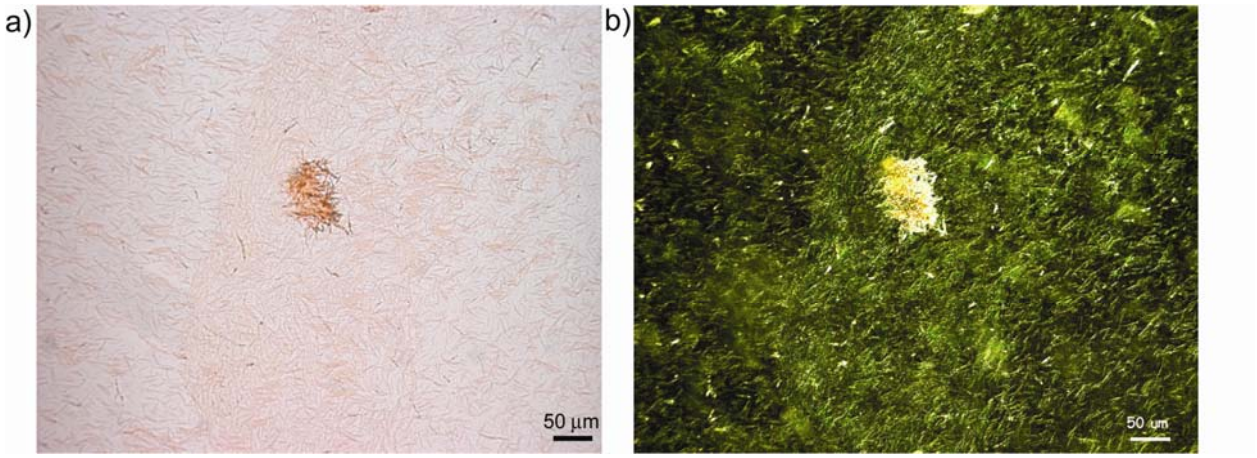

Figure 6-4: Image of 1.3mM KLVFFAL nanotube assemblies in 40% acetonitrile bundled together with 18 mM sodium sulfate and stained with 100µM CR viewed in (a) bright field and (b) between crossed polarizers.

To reduce scattering effects for UV-vis absorbance, the peptide concentration was reduced to 200 µM. Figure **6-5** compares 10µM CR to 10µM CR + 200 µM KLVFFAL and upon binding there is an apparent red-shift and intensity increase as is typically observed for CR binding to amyloid assemblies[7]. To determine CR:KLVFFAL binding ratio, the CR spectral shift assay[7,8] was modified to study binding of CR to KLVFFAL nanotubes in 40% acetonitrile. At saturation, the E22L:CR binding ratio was estimated to be 6.1±0.5. Hill plot analysis (Figure **6-5**b) indicated a Hill coefficient of 1.2±0.2 and a K_d of 1.9±0.5 µM consistent with non-cooperative binding to a single site along the solvent exposed laminate grooves. At high CR concentrations, deviations from linearity may be due to increased light scattering, an alteration of bound CR molar absorbtivity, or even binding of a second CR molecule within the laminate groove.

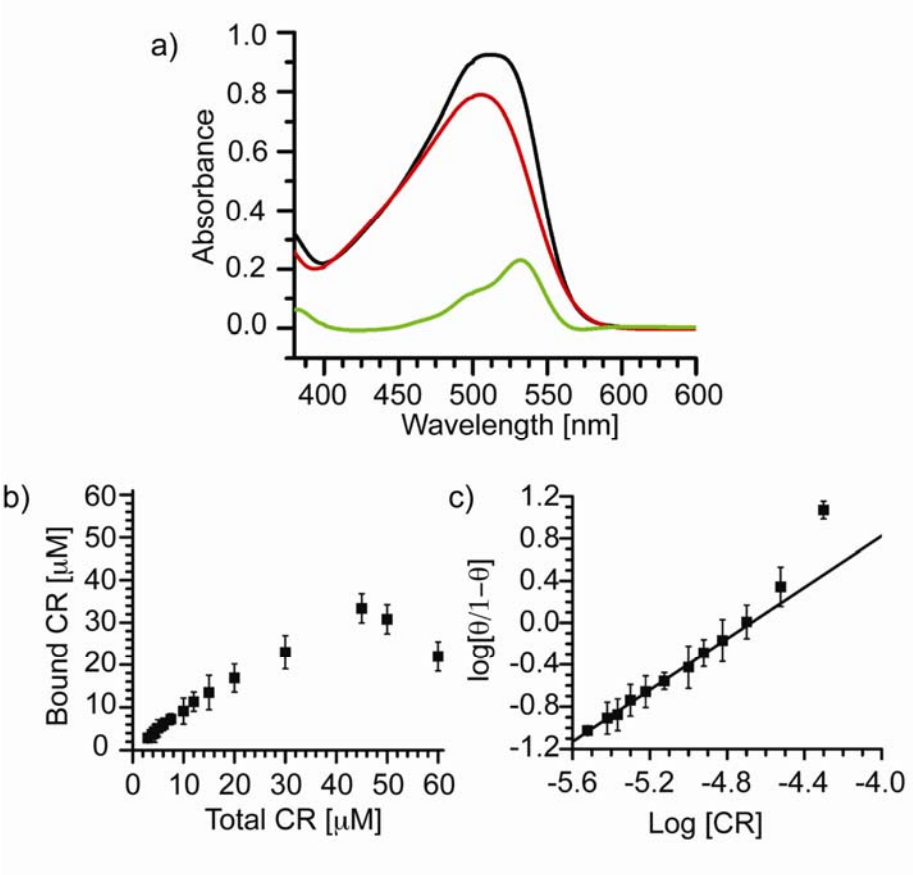

Figure 6-5: (a) UV-Vis absorbance comparison of 10 μM CR (red), 10 μM CR + 200 μM KLVFFAL (black) and difference (green). (b) The concentration of bound CR versus total CR concentration upon addition to + 200 μM KLVFFAL nanotube assemblies. Bound CR was calculated based upon λ of maximal difference between bound and unbound CR (532 nm) and an isobestic point (416 nm) – see Methods for details of calculation. Maximum binding to 200 μM E22L occurred at 33.4 μM CR (c) Hill plot analysis of CR binding gave a slope of 1.2 ±0.2 and a y-intercept of 5.71.

CR binding does not alter the KLVFFAL's cross-β structure

A potential concern is the addition of CR to KLVFFAL nanotubes would modify the KLVFFAL morphology and change the surface of the nanotubes. If this change occurs, it would be difficult to localize the CR binding site. Under neutral conditions in 40% acetonitrile, KLVFFAL assembles into hollow nanotubes with diameters of 38 nm. Upon saturation of the

KLVFFAL nanotube surface with CR, no apparent change to E22L tubular morphology was observed by TEM (Figure **6-6**).

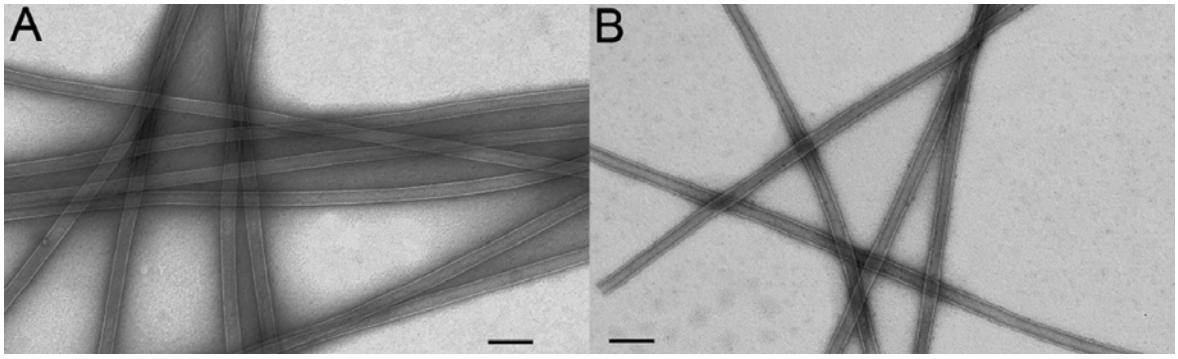

Figure 6-6: TEM micrographs of uranyl acetate negatively stained (A) 0.65 mM KLVFFAL assembled in 40% acetonitrile + 0.1% TFA, then titrated to neutral conditions using 200 mM NaOH in 40% acetonitrile (B) Addition of 0.1 mM CR to the KLVFFAL nanotube assemblies after incubation for 1 week period.

Greater precision can be obtained by comparison of electron diffraction patterns of oriented KLVFFAL nanotubes with and without the CR, and again no apparent structural changes occur at the level of the cross-β pattern (Figure **6-7**). Each pattern displays the superposition of two equally intense cross-β patterns that arise from both the top and bottom layers of a flattened hollow nanotube. Individual cross-β patterns are composed of a 4.7Å d-spacing assigned to hydrogen bonded peptides and an orthogonal 10.2Å d-spacing assigned to the distance between laminated β-sheets and is offset 13±2º from the nanotube long axis.

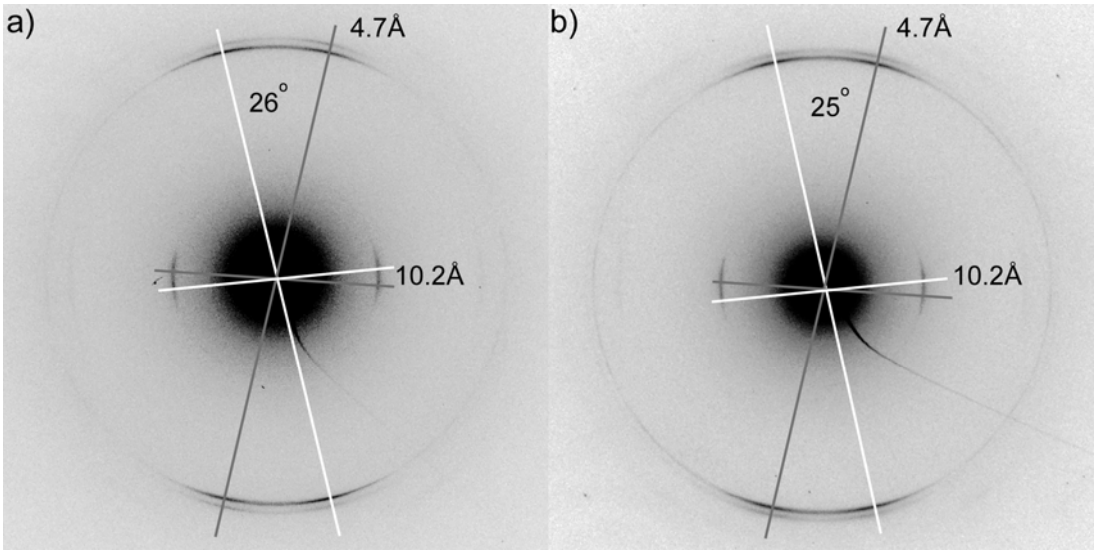

Figure 6-7: Electron diffraction comparing a) aligned 650 μM KLVFFAL nanotubes and (b) 650 μM KLVFFAL nanotubes + 65 μM CR. Each diffraction pattern is the sum of two equally intense cross-β patterns represented by gray and white crosses.

CR is oriented along the Nanotube Surface

To interrogate the orientation of CR with respect to the nanotube long axis surface linear dichroism (LD) was measured using a Couette flow cell[43]. Initially, the KLVFFAL nanotubes alone were analyzed to investigate the orientation of the β-sheets with respect to the nanotube axis. The electronic transition dipole of the amide π-π* transition lies along the C=O bond vector[45,51] collinear with β-sheet hydrogen bonds. Consistent with electron diffraction analysis (Figure **6-7**), under couette flow the nanotubes display a positive LD signature indicating the C=O bond vectors within β-sheets run roughly parallel to the nanotube axis (Figure **6-8**a).

ZINDO/S calculations indicate CR's low energy π-π* transition runs parallel to the long molecular axis (Figure **6-1**), consistent with previous calculations[5]. UV-vis absorption indicates this transition spans 400-650 nm, and KLVFFAL nanotubes have no absorption in the range of 400-650 nm and contain no LD signature (Figure **6-8**b). Additionally, CR alone has a weak positive LD signature which may be the result of couette flow orienting[51] a small percentage of linear CR molecules (Figure **6-8**b). Upon addition of CR to KLVFFAL nanotubes,

the LD displays a strong positive signature with a λ_{max} of 515 nm, indicating CR's long molecular axis is oriented roughly parallel to the nanotube axis. With a calculated orientation factor (S) between 0.8-1.0, the CR transition dipole is oriented within 0-14º of the nanotube axis placing it co-linear with the laminate grooves offset 13±2º from the nanotube axis.

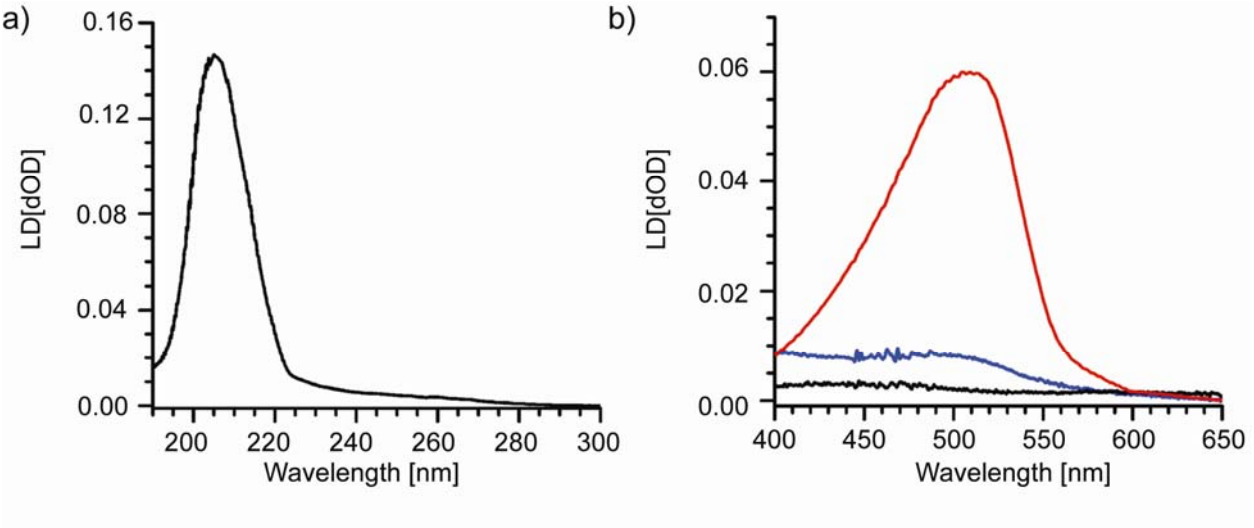

Figure 6-8: Couette flow LD of (a) KLVFFAL nanotubes only in the wavelength range of the amide transition, (b) 65 µM CR (blue) and 65 µM CR + 650 µM KLVFFAL. The positive LD indicates that the electronic transition dipoles are oriented parallel to the direction of flow.

CR Docking Model

Models of the laminate groove binding site were created based upon electron diffraction d-spacing and solid-state NMR ^{13}C-^{15}N distance constraints. No structural constraints were applied during the MD studies, and all models consistent with diffraction and solid-state NMR experimental data were retained. The model of the laminate groove is formed by two laminated β-sheets, where each β-sheet is composed of 6 hydrogen bonded β-strands (Figure **6-9**).

The surface of the laminate grooves forms an amphiphilic binding site composed of a hydrophobic base composed of leucine-17 (orange), leucine-22 (yellow) with positively charged lysines (blue) emerging from the surface every 9.4Å. Within the groove, CR was manually

docked and to accomplish charge complementarity between the negatively charged sulfates and the positively charged lysines, then energy minimized with implicit water (Figure **6-9**). CR, with a length of ~19Å, spans parallel to 6 hydrogen bonded peptides (5x4.7Å=23.5 Å). This binding is consistent with the 6.1±0.5 binding ratio calculated earlier (Figure **6-5**) and also consistent with earlier charge directed CR-amyloid models[8].

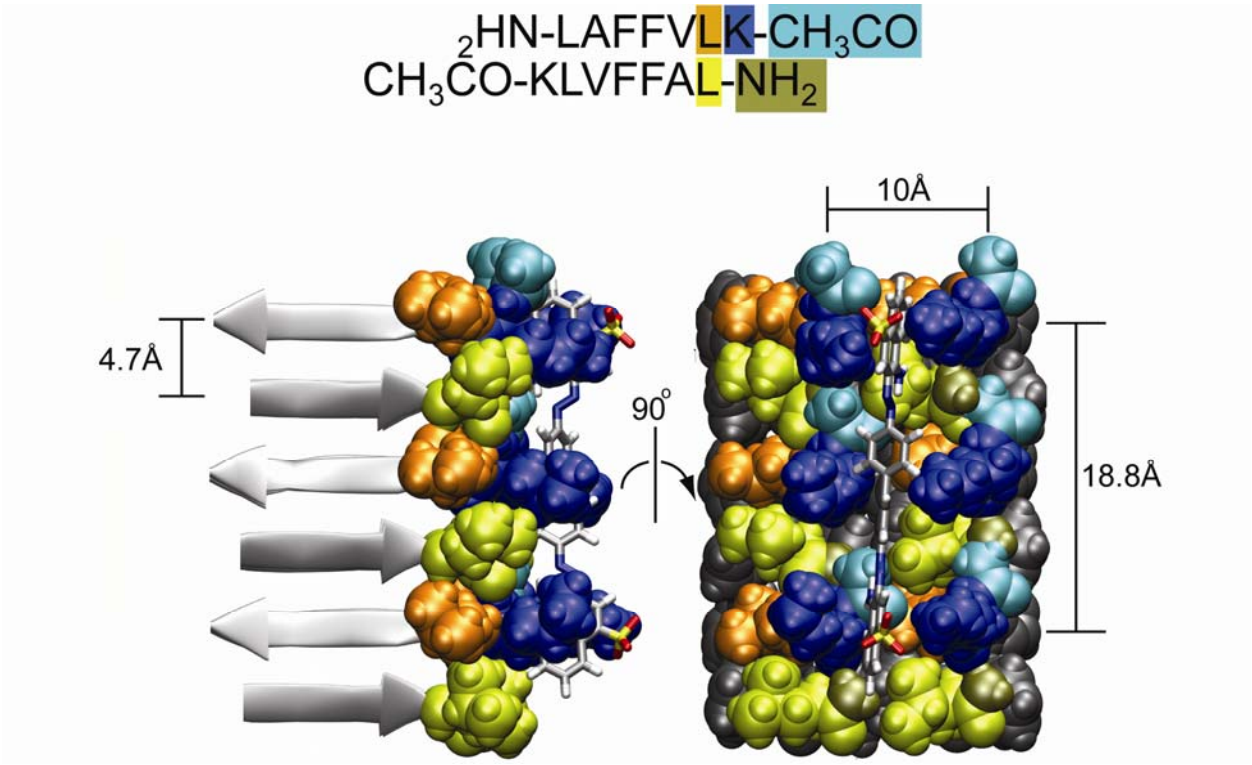

Figure 6-9: Structural model of the CR binding to the KLVFFAL laminate groove binding site. The residues in close proximity to CR are shown in space-filling format: CH_3CO N-terminal capping group (cyan), Lys-16 (blue), Leu-17 (orange), Phe-19 and Phe-20 (gray), Leu-22 (yellow) and C-terminal $–NH_2$ capping group (brown). CR is shown in stick format with C (gray), O (red), N (blue), H (white) and S (yellow).

CR Binds at High Density

To test for CR-CR interactions UV-vis and CD spectra were collected as a function of KLVFFAL:CR ratio (Figure **6-10**). Both UV-vis and CD spectra display a concentration

dependent red-shift. The induced CD reports only on CR molecules bound to the amyloid chiral environment and as the concentration increases there is an observed red-shift and change in the band shape which is consistent with coupled oscillator interaction between neighboring CR electronic transition dipoles. Exciton coupling theory[52,53], predicts a λ_{max} red-shift for electronic transition dipoles oriented end-to-end as J-aggregates and a blue shift for transition dipoles organized side-by-side as H-aggregates.

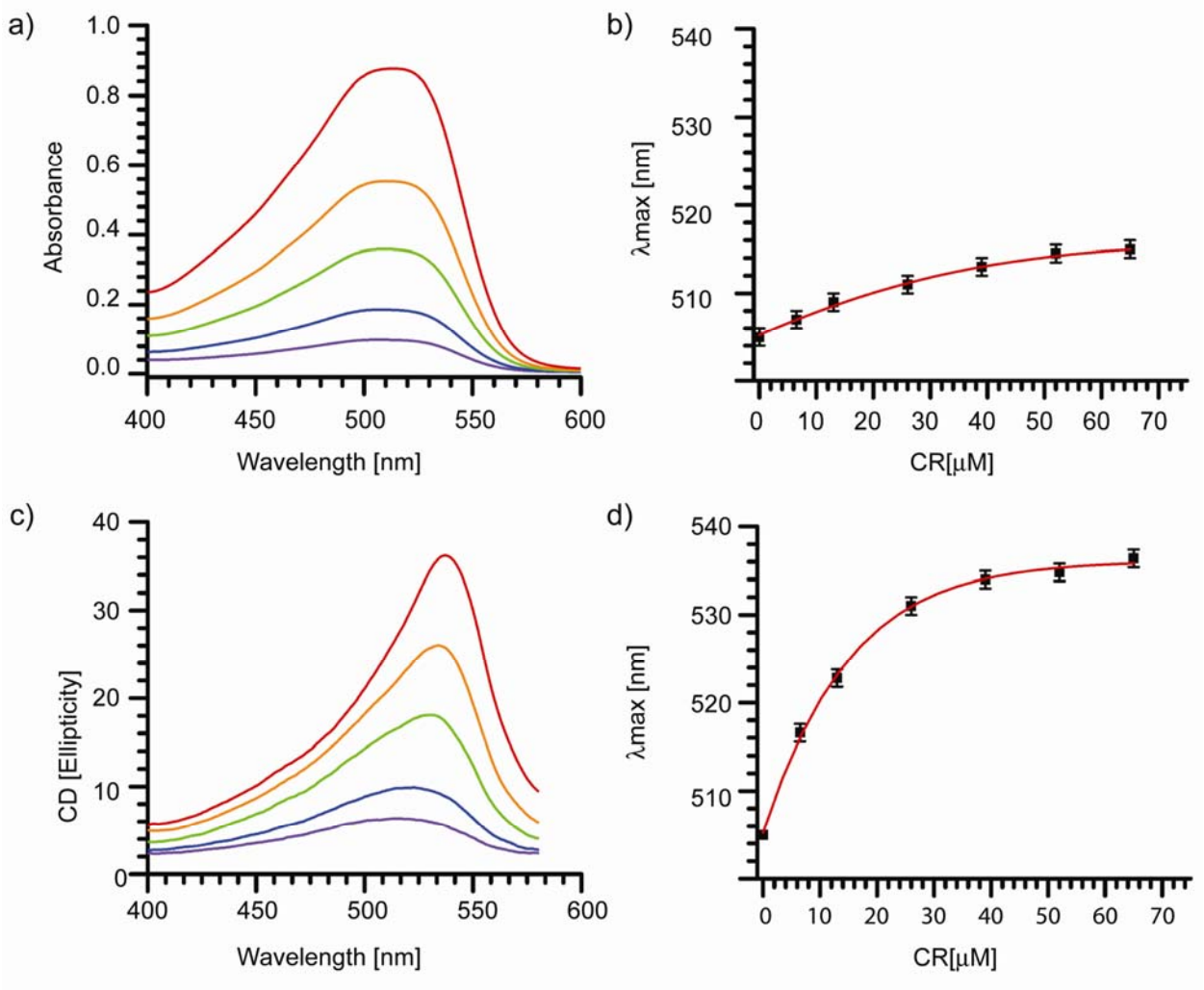

Figure 6-10: a) UV-Vis and c) CD spectra at different KLVFFAL:CR binding ratios with KLVFFAL peptide concentration set at 650 μM: black (65μM CR only),violet (100:1), blue (75:1), green (50:1), orange (20:1), and red (10:1). Graph of UV-vis λ_{max} and CD λ_{max} versus CR concentration.

Quantum chemical calculations were employed to investigate the observed UV-vis spectral changes as a function of number and orientation of molecules. Due to the number of atoms in CR, semi-empirical quantum-chemical calculations (ZINDO/S[49,50]) were employed as the method has low computational costs while maintaining a level of accuracy, and has been commonly used to predict the impact of exciton coupling on electronic transitions in molecular aggregates[54,55,56].

ZINDO/S calculations of CR molecules organized as J-aggregates (Figure **6-11**A) and H-aggregates (Figure **6-11**B) are consistent with predictions from exciton coupling theory[52,53]. As expected the calculated exciton coupling energy (ΔE) increases as the center-to-center distance is decreased. In the simplifying case of a pure H-aggregate (Figure **6-11**A) or a pure J-aggregate organization (Figure **6-11**B), neither fit the observed UV-vis as it appears to red-shift and blue-shift with respect to unbound CR. Fixing the CR molecules in one laminate and varying the position of a CR molecule in the neighboring laminate(Figure **6-11**C and D), indicates an orientation dependence of exciton coupling. The pure H-character becomes more J-like as the center-to-center distance is increased. In Figure **6-11**D a molecular system containing a 3-molecule J-aggregate and a 2-molecule H-aggregate was studied. The resulting ZINDO calculations indicate both red-shifted and blue shifted transitions (Figure **6-11**D). Even though saturated binding is approximated by 4 CR molecules the effects of exciton coupling are on the same magnitude as that observed in UV-vis absorption spectrum. As a further test, to examine the helical nature of nanotube surface a planar trimer was compared with a helical trimer and little difference was detected (Figure **6-12**).

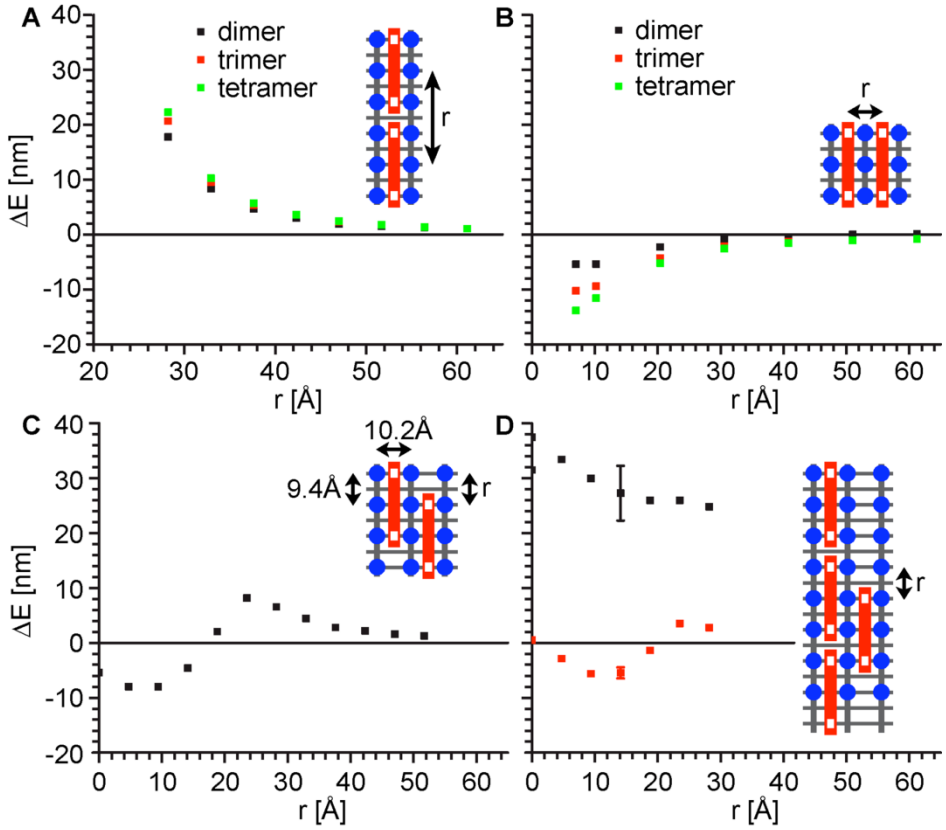

Figure 6-11: Calculated ZINDO/S exciton coupling energy (DE) of (A) CR organized as J-aggregates and (B) CR organized as H-aggregates as center-to-center distance is varied. In (C) the registry within H-aggregates is varied, and in (D) the registry of a monomer relative to a CR J-aggregate trimer is evaluated. The red and blue dashed horizontal lines represent the observed red and blue shifts for bound CR. The inset represents a laminate groove where β-sheets are separated by 10.2Å and H-bonded peptides by 4.7Å, where lysines (blue circles) and congo red molecules (red rectangles) with sulfates (white squares) are shown.

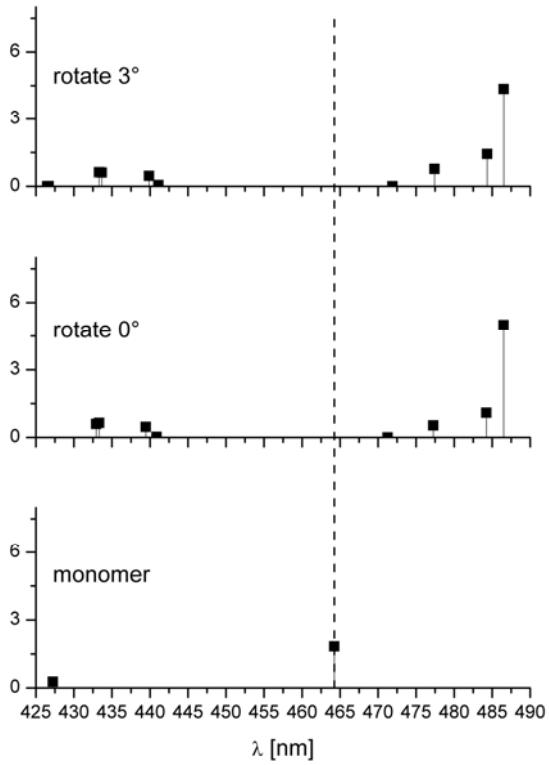

Figure 6-12: Calculated ZINDO electronic transitions for Congo Red monomer (bottom), tetramer (middle and top) with a center-to-center distance of 28.2 Å. In the top spectrum each molecule was rotated by 3°. Vertical axis is the calculated oscillator strength.

Potential Influence of Biphenyl Conformational Change

To test the impact of conformational changes on the CR UV spectra, ZINDO/S spectra were calculated for the CR monomer as a function of biphenyl orientation. The geometry optimized 6-31G+(d,p)/B3LYP conformation has a biphenyl dihedral angle of 144°. Each spectra were calculated using ZINDO/S as the starting structure and applying rotation around the biphenyl. These calculations are consistent with rotations around the biphenyl of CR monomers inducing only an 8nm red-shift and a 15nm blue shift. Although the blue shift is large enough to account for the 10nm blue-shift observed upon CR binding to amyloid, the calculated red-shift cannot

account for the observed red-shift. Therefore it is unlikely that the experimentally observed intensity increase and shift in λ_{max} arises solely from conformational changes in CR.

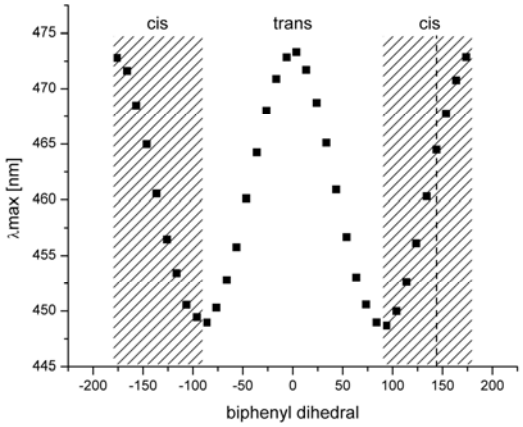

Figure 6-13: λ_{max} for Congo Red monomer as function of biphenyl orientation calculated with ZINDO/S. Initial structure was optimized with DFT 6-31G+(d,p)/B3LYP and has a dihedral angle of 144° (indicated with a dashed vertical line).

Discussion

For more than 80 years, CR has provided a diagnostic of cross-β structure that seems completely independent of primary sequence[1,2,8]. The KLVFFAL nanotube morphology simplifies analysis of CR binding relative to amyloid fibers as it presents a surface containing only cross-β laminate grooves. Upon addition of CR to amyloid nanotubes, an apple-green interference (Figure **6-4**) and a red-shifted low energy transition (Figure **6-5**) are observed as diagnostic features. Investigations with ab intio[5] and ZINDO/S (Figure **6-1**) calculations indicate the transition dipole moment of CR lies parallel to the long molecular axis regardless of biphenyl conformation. Both LD and electron diffraction analysis position CR co-linear with E22L's laminate grooves. Along a single 38 nm diameter E22L nanotube multiple 1 nm wide laminate grooves run parallel to each other providing a capacity to bind numerous CR molecules in close proximity (<10Å) and within the range of distance-dependent exciton coupling for J-aggregates (<45Å) and H-aggregates (< 30 Å) as indicated in Figure **6-11**.

The calculated exciton coupling (ΔE) for a CR J-aggregate tetramer separated by 28Å is 23 nm, and consistent with the 25 nm red shift observed for the CR-E22L at saturation. However, UV-vis absorption is broad over a range of 450-600 nm, extended to lower wavelengths than free CR (λ_{max}=505 nm). Such broadening is distinct from the sharp red-shifted UV-vis profile of isolated J-aggregates (Figure **6-14**) observed in other chromophore systems[57,58]. Similarly, if the cross-β structure organizes CR side-by-side as isolated H-aggregates, then only a blue-shift would be observed (Figure **6-14**). The combined organization of CR organized as both J- and H-aggregates best approximates experimentally observed UV-Vis absorption of CR bound to amyloid. An offset in H-aggregate registry of 14.1Å best fits the experimental data and is consistent with optimizing charge complementation. However, current computation limitations make this assignment tenuous.

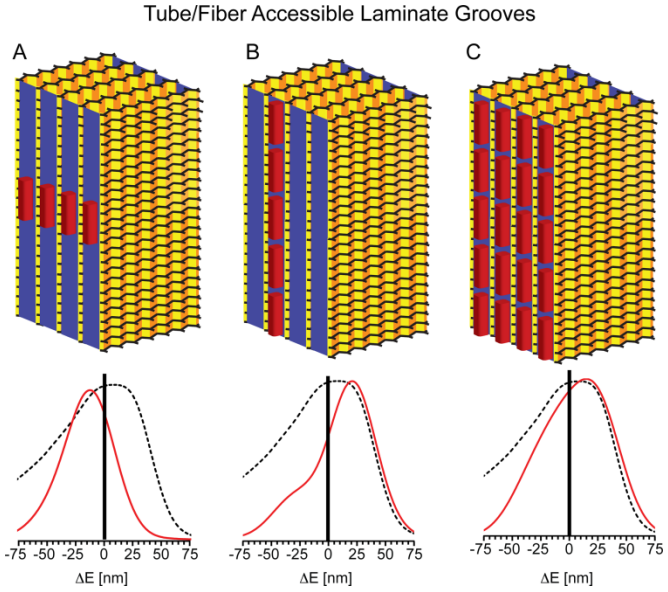

Figure 6-14: Simulated UV-Vis of different CR binding arrangements along on the laminate groove surface as a: (a) isolated H-aggregate tetramer, (b) an isolated J-aggregate tetramer, and (c) a saturated laminate groove surface with both J- and H-aggregate organization. The solid red curves represent calculated UV-vis spectrum compared with experimental UV-vis absorption (dotted black line) for KLVFFAL:CR binding ratio of 10:1.

An overall structural model of CR-KLVFFAL complex at saturation illustrates the central hydrophobic residues LVFFAL in gray and the N-terminal lysines (blue) with bound CR (red). The laminate groove can be characterized as a hydrophobic base mostly composed of leucine residues with positive charged lysines emerging from the surface like knobs roughly every 10Å in a grid-like arrangement due to cross-β organization. CR molecules have been manually docked along this surface so that the negatively charged sulfates are properly positioned to interact with the positively charged lysines. Each CR molecule occupies the termini surface created by 6 hydrogen peptides (6x4.7Å), so that the center-to-center distance between neighboring CR molecules within a laminate groove is 28Å. In addition each KLVFFAL nanotube contains a 40Å wall in which binding to both the inner and outer surfaces of the nanotubes would create H-aggregates that would contribute only a slight 1 nm blue shift to the UV-Vis spectrum (Figure **6-11**).

As illustrated in Figure 6-13, a biphenyl conformation change extending CR's conjugation could also contribute to the observed red-shift[59]. However, the CR binding saturation experiment is inconsistent with just a single optically active conformation. Here we propose a CR-CR exciton coupling model to account for the spectral shift changes observed upon CR binding to amyloid. The CR template assembly presented here is consistent with polarizing microscopy results acquired on various amyloid plaques which indicate CR binds parallel to the fiber axis[25] resulting in well defined densely packed J-aggregates. This CR-laminate groove model is also consistent with previous proposals that CR interacts with the peptide termini and parallel to the fiber axis[8]. In fact the pH dependence of CR binding to a variety of Aβ(1-40) truncations indicates histidines may influence CR binding and suggest a His13-His14-Gln15-Lys16 CR binding motif. This CR binding motif is localized within the laminate grooves of the most highly resolved structural models for Aβ(1-40)[15,16]. However, CR binding to KLVFFAV nanotubes also indicates CR may have affinity for pleat grooves (Figure **6-3**),

consistent with the idea that CR has multiple binding sites along the amyloid fiber surface. Indeed, multiple CR binding modes that yield similar UV-Vis profiles may be the source of CR's universal binding to all amyloid.

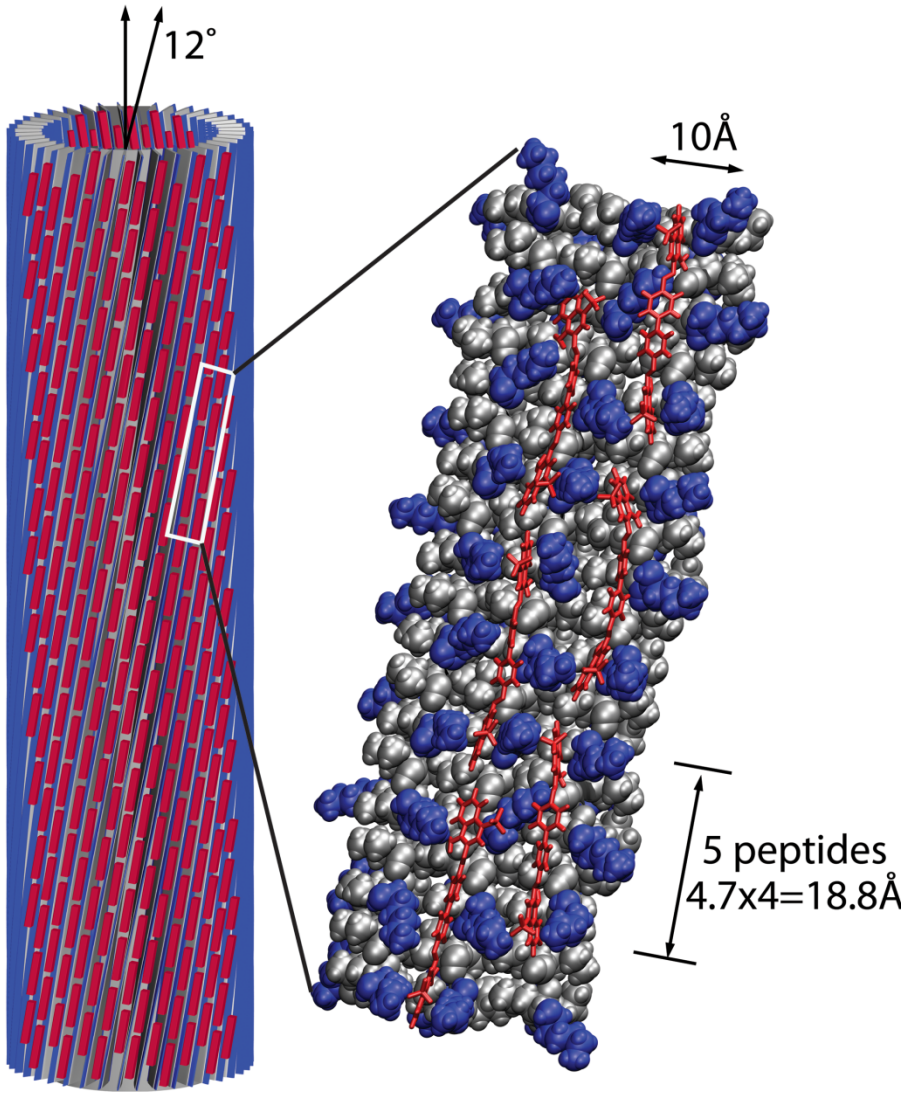

Figure 6-15: Structural Model of KLVFFAL amyloid nanotubes saturated with CR, where CR (red blocks), positively charged lysines (blue), hydrophobic leucines (gray).

Previously, the short amyloid peptide HAQKLVFFA was shown to form toxic amyloid fibers containing histidines in the laminate grooves that template Cu (II) ions into linear arrays separated by 9.4Å. Indeed, amyloid's ability to organize molecular entities into arrays ranging from metal ions[60,61] to CR may be the key to its functional significance. A recent discovery identified such a functional role of Pmel17 amyloid in melanosome[12] as the amyloid surface appears to organize substrates linearly for melanin polymerization. With this foundational insight into amyloid templating capabilities, primary sequence variations localized in amyloid laminate and pleat grooves may serve as diagnostic fingerprints[62] of amyloid strains and even distinguish between "toxic", "functional" and "benign" amyloid forms.

References

1. Divry P FM (1927) The optic properties of amyloid. Omptes rendus des seances de la societie de biologie et de ses filiales 97: 1808-1810.
2. Nilsson MR (2004) Techniques to study amyloid fibril formation in vitro. Methods 34: 151-160.
3. Ladewig P (1945) Double-refringence of the amyloid-congo red-complex in histological sections Nature 156: 81-82.
4. Howie AJ, Brewer DB (2009) Optical properties of amyloid stained by Congo red: History and mechanisms. Micron 40: 285-301.
5. Kurimoto M, Mueller B, Kaminsky W, Kahr B, Jin L-W (2002) Dyeing Crystals to Dyeing Tissues: Congo Red in Anisotropic Media. Mol Cryst Liq Cryst 389: 1.
6. Kaminksy W, Jin LW, Powell S, Maezawa I, Claborn K, et al. (2006) Polarimetric imaging of amyloid. Micron 37: 324-338.
7. Klunk WE, Jacob RF, Mason RP, Ronald W (1999) [19] Quantifying amyloid by congo red spectral shift assay. Methods in Enzymology: Academic Press. pp. 285-305.

8. Klunk WE, Pettegrew JW, Abraham DJ (1989) Quantitative evaluation of congo red binding to amyloid-like proteins with a β-pleated sheet conformation. J Histochem Cytochem 37: 1273-1281.

9. Guijarro JI, Sunde M, Jones JA, Campbell ID, Dobson CM (1998) Amyloid fibril formation by an SH3 domain. Proceedings of the National Academy of Sciences of the United States of America 95: 4224-4228.

10. Glover JR, Kowal AS, Schirmer EC, Patino MM, Liu J-J, et al. (1997) Self-Seeded Fibers Formed by Sup35, the Protein Determinant of [PSI+], a Heritable Prion-like Factor of S. cerevisiae. 89: 811-819.

11. Iconomidou VA, Vriend G, Hamodrakas SJ (2000) Amyloids protect the silkmoth oocyte and embryo. FEBS Letters 479: 141-145.

12. Fowler DM, Koulov AV, Alory-Jost C, Marks MS, Balch WE, et al. (2006) Functional Amyloid Formation within Mammalian Tissue. PLoS Biology 4: e6.

13. Inouye H, Nguyen JT, Fraser PE, Shinchuk LM, Packard AB, et al. (2000) Histidine residues underlie Congo red binding to Aβ analogs. Amyloid 7: 179-188.

14. Tenidis K, Waldner M, Bernhagen Jr, Fischle W, Bergmann M, et al. (2000) Identification of a penta- and hexapeptide of islet amyloid polypeptide (IAPP) with amyloidogenic and cytotoxic properties. Journal of Molecular Biology 295: 1055-1071.

15. Petkova AT, Ishii Y, Balbach JJ, Antzutkin ON, Leapman RD, et al. (2002) A structural model for Alzheimer's β-amyloid fibrils based on experimental constraints from solid state NMR. Proc Natl Acad Sci 99: 16742-16747.

16. Petkova AT, Yau WM, Tycko R (2006) Experimental Constraints on Quaternary Structure in Alzheimer's Beta-Amyloid Fibrils. Biochemistry 45: 498-512.

17. Wasmer C, Lange A, Van Melckebeke H, Siemer AB, Riek R, et al. (2008) Amyloid Fibrils of the HET-s(218-289) Prion Form a β Solenoid with a Triangular Hydrophobic Core. Science 319: 1523-1526.

18. Sawaya MR, Sambashivan S, Nelson R, Ivanova MI, Sievers SA, et al. (2007) Atomic structures of amyloid cross-β spines reveal varied steric zippers. Nature 447: 453-457.

19. Mehta AK, Lu K, Childers WS, Liang Y, Dublin SN, et al. (2008) Facial Symmetry in Protein Self-Assembly. J Am Chem Soc 130: 9829-9835.

20. Tycko R, Sciarretta KL, Orgel JPRO, Meredith SC (2009) Evidence for Novel -Sheet Structures in Iowa-mutant -Amyloid Fibrils. Biochemistry 48: 6072-6084.

21. Sikorski P, Atkins ED, Serpell LC (2003) Structure and texture of fibrous crystals formed by Alzheimer's Ab(11-25) peptide fragment. Structure 11: 915-926.

22. Frid P, Anisimov SV, Popovic N (2007) Congo red and protein aggregation in neurodegenerative diseases. Brain Research Reviews 53: 135-160.

23. Carter DB, Chou KC (1998) A Model for Structure-Dependent Binding of Congo Red to Alzheimer β-Amyloid Fibrils. Neurobiology of Aging 19: 37-40.

24. Turnell (1992) Binding of the dye congo red to the amyloid pig insulin reveals novel homology amongst amyloid-forming peptide sequences. J Mol Biol 227: 1205-1223.

25. Jin L-W, Claborn KA, Kurimoto M, Geday MA, Maezawa I, et al. (2003) Imaging linear birefringence and dichroism in cerebral amyloid pathologies. Proc Natl Acad Sci U S A 100: 15294-15298.

26. Petkova AT, Ishii Y, Balbach JJ, Antzutkin ON, Leapman RD, et al. (2002) A structural model for Alzheimer's β-amyloid fibrils based on experimental constraints from solid state NMR. Proc Natl Acad Sci U S A 99: 16742-16747.

27. Petkova AT, Buntkowsky G, Dyda F, Leapman RD, Yau WM, et al. (2004) Solid state NMR reveals a pH-dependent antiparallel b-sheet registry in fibrils formed by a b-amyloid peptide. J Mol Biol 335: 247-260.

28. Burkoth TS, Benzinger TLS, Urban V, Morgan DM, Gregory DM, et al. (2000) Structure of the beta-Amyloid (10-35) Fibril. J Am Chem Soc 122: 7883-7889.

29. Bu ZM, Shi Y, Callaway DJE, Tycko R (2007) Molecular alignment within beta-sheets in A beta(14-23) fibrils: Solid-state NMR experiments and theoretical predictions. Biophysical Journal 92: 594-602.

30. Benzinger TL, Gregory DM, Burkoth TS, Miller-Auer H, Lynn DG, et al. (2000) Two-Dimensional Structure of b-Amyloid(10-35) Fibrils. Biochemistry 39: 3491-3499.

31. Balbach JJ, Ishii Y, Antzutkin ON, Leapman RD, Rizzo NW, et al. (2000) Amyloid Fibril Formation by Ab16-22, a Seven-Residue Fragment of the Alzheimer's b-Amyloid Peptide, and Structural Characterization by Solid State NMR. Biochemistry 39: 13748-13759.

32. Sikorski P, Atkins EDT, Serpell LC (2003) Structure and texture of fibrous crystals formed by Alzheimer's A beta(11-25) peptide fragment. Structure 11: 915-926.

33. Serpell LC, Smith JM (2000) Direct visualisation of the β-sheet structure of synthetic Alzheimer's amyloid. J Mol Biol 299: 225-231.

34. Marshall KE, Hicks MR, Williams TL, Hoffmann SV, Rodger A, et al. (2010) Characterizing the Assembly of the Sup35 Yeast Prion Fragment, GNNQQNY: Structural Changes Accompany a Fiber-to-Crystal Switch. Biophysical Journal 98: 330-338.

35. Makin OS, Atkins E, Sikorski P, Johansson J, Serpell LC (2005) Molecular basis for amyloid fibril formation and stability. Proc Natl Acad Sci 102: 315-320.

36. Eanes ED, Glenner GG (1968) X-ray diffraction studies on amyloid filaments. J Histochem Cytochem 16: 673-677.

37. Geddes AJ, Parker KD, Atkins EDT, Beighton E (1968) "Cross-b" Conformation in Proteins. J Mol Biol 32: 343-358.

38. Nelson R, Sawaya MR, Balbirnie M, Madsen AO, Riekel C, et al. (2005) Structure of the cross-b spine of amyloid-like fibrils. Nature 435: 773-778.

39. Krebs MRH, Bromley EHC, Donald AM (2005) The binding of thioflavin-T to amyloid fibrils: localisation and implications. J Struct Biol 149: 30-37.

40. William EK, Manik LD, Jay WP (1995) Chrysamine-G binding to Alzheimer and control brain: Autopsy study of a new amyloid probe. Neurobiology of aging 16: 541-548.

41. Levine IIIH (2005) Multiple ligand binding sites on Aβ(1-40) fibrils. Amyloid 12: 5-14.

42. Wu C, Wang Z, Lei H, Zhang W, Duan Y (2007) Dual Binding Modes of Congo Red to Amyloid Protofibril Surface Observed in Molecular Dynamics Simulations. J Am Chem Soc 129: 1225-1232.

43. Marrington R, Dafforn TR, Halsall DJ, Rodger A (2004) Micro-Volume Couette Flow Sample Orientation for Absorbance and Fluorescence Linear Dichroism. Biophys J 87: 2002-2012.

44. Marrington R, Dafforn TR, Halsall DJ, MacDonald JI, Hicks M, et al. (2005) Validation of new microvolume Couette flow linear dichroism cells. The Analyst 130: 1608-1616.

45. Dafforn TR, Rajendra J, Halsall DJ, Serpell LC, Rodger A (2004) Protein Fiber Linear Dichroism for Structure Determination and Kinetics in a Low-Volume, Low-Wavelength Couette Flow Cell. Biophys J 86: 404-410.

46. Nordh J, Deinum J, Nordén B (1986) Flow orientation of brain microtubules studies by linear dichroism. European Biophysics Journal 14: 113-122.

47. Lu K, Guo L, Mehta AK, Childers WS, Dublin SN, et al. (2007) Macroscale assembly of peptide nanotubes. Chem Commun (Camb) 2729-2731.

48. M. J. Frisch GWT, H. B. Schlegel, G. E. Scuseria, M. A. Robb, J. R. Cheeseman, J. A. Montgomery, Jr., T. Vreven, K. N. Kudin, J. C. Burant, J. M. Millam, S. S. Iyengar, J. Tomasi, V. Barone, B. Mennucci, M. Cossi, G. Scalmani, N. Rega, G. A. Petersson, H. Nakatsuji, M. Hada, M. Ehara, K. Toyota, R. Fukuda, J. Hasegawa, M. Ishida, T. Nakajima, Y. Honda, O. Kitao, H. Nakai, M. Klene, X. Li, J. E. Knox, H. P. Hratchian, J. B. Cross, V. Bakken, C. Adamo, J. Jaramillo, R. Gomperts, R. E. Stratmann, O. Yazyev, A. J. Austin, R. Cammi, C. Pomelli, J. W. Ochterski, P. Y. Ayala, K. Morokuma, G. A. Voth, P. Salvador, J. J. Dannenberg, V. G. Zakrzewski, S. Dapprich, A. D. Daniels, M. C.

Strain, O. Farkas, D. K. Malick, A. D. Rabuck, K. Raghavachari, J. B. Foresman, J. V. Ortiz, Q. Cui, A. G. Baboul, S. Clifford, J. Cioslowski, B. B. Stefanov, G. Liu, A. Liashenko, P. Piskorz, I. Komaromi, R. L. Martin, D. J. Fox, T. Keith, M. A. Al-Laham, C. Y. Peng, A. Nanayakkara, M. Challacombe, P. M. W. Gill, B. Johnson, W. Chen, M. W. Wong, C. Gonzalez, and J. A. Pople (2004) Gaussian. Wallingford, CT.

49. Bacon AD, Zerner MC (1979) Intermediate neglect of differential overlap theory for transition metal complexes - De, Co, and Cu chlorides Theoretica Chimica Acta 53: 21-54.

50. Thompson MA, Zerner MC (1991) A theoretical examination of the electronic-structure and spectroscopy of the photosynthetic reaction center from rhodopseudomonas-viridis J Am Chem Soc 113: 8210-8215.

51. Rodger A, Marrington R, Geeves MA, Hicks M, Alwis Ld, et al. (2006) Looking at long molecules in solution: what happens when they are subjected to Couette flow? Phys Chem Chem Phys 8: 3161-3171.

52. Kasha M (1959) Relation between Exciton Bands and Conduction Bands in Molecular Lamellar Systems. Reviews of Modern Physics 31: 162.

53. Harada NN, Nakanishi K (1983) Circular Dichroic Spectroscopy – Exciton Coupling in Organic Stereochemistry. Mill Valley, CA: University Science Books.

54. Wichard JDB, Tonu P (2004) Excitonic coupling in polythiophenes: Comparison of different calculation methods. The Journal of Chemical Physics 120: 2490-2495.

55. Beljonne D, Cornil J, Silbey R, Millie P, Bredas JL (2000) Interchain interactions in conjugated materials: The exciton model versus the supermolecular approach. The Journal of Chemical Physics 112: 4749-4758.

56. Howard IA, Zutterman F, Deroover G, Lamoen D, Van Alsenoy C (2004) Approaches to Calculation of Exciton Interaction Energies for a Molecular Dimer. The Journal of Physical Chemistry B 108: 19155-19162.

57. Ohno O, Kaizu Y, Kobayashi H (1993) J-aggregate formation of a water-soluble porphyrin in acidic aqueous media. J Chem Phys 99: 4128-4139.

58. Harrison WJ, Mateer DL, Tiddy GJT (1996) Liquid-Crystalline J-Aggregates Formed by Aqueous Ionic Cyanine Dyes. J Phys Chem 100: 2310-2321.

59. Miura T, Yamamiya C, Sasaki M, Suzuki K, Takeuchi H (2002) Binding mode of Congo Red to Alzheimer's amyloid β-peptide studied by UV Raman spectroscopy. J Raman Spectrosc 33: 530-535.

60. Dong J, Shokes JE, Scott RA, Lynn DG (2006) Modulating amyloid self-assembly and fibril morphology with Zn(II). J Am Chem Soc 128: 3540-3542.

61. Dong J, Canfield JM, Mehta AK, Shokes JE, Tian B, et al. (2007) Engineering metal ion coordination to regulate amyloid fibril assembly and toxicity. Proc Natl Acad Sci 104: 13313-13318.

62. Ashburn TT, Han H, McGuinness BF, Lansbury PT (1996) Amyloid probes based on Congo Red distinguish between fibrils comprising different peptides. Chemistry & Biology 3: 351-358.

Chapter 7 : Amyloid as a Catalyst

While lipid membrane assemblies are usually discussed in terms of long-range order and their ability to provide barriers for cellular components, amyloid assemblies are composed of polypeptides and have the potential for protein-like architectures and functions. Studies of congo red binding to KLVFFAL nanotubes in Chapter 5[1] indicate that amyloids bind and interact with small molecules much like an enzyme. As shown in Figure **7-1**, amyloid structures can bind small molecules in high density with individual small molecule binding sites organized side-by-side along the nanotube surface[1].

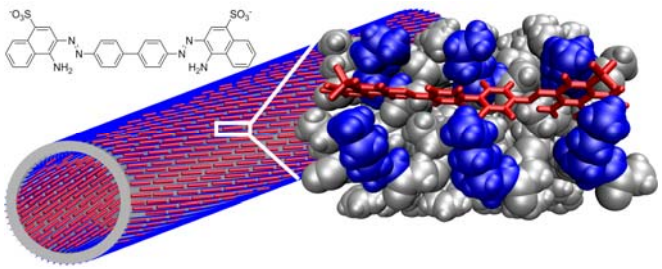

Figure 7-1: Binding of congo red arrays along the KLVFFAL nanotube surface. The nanotube surface is composed of individual small molecule binding sites in close proximity[1].

With amyloid's capacity to form small molecule binding sites, it raises the possibility that binding sites could also be catalytic. Given that KLVFFAL's congo red binding site contains one lysine per 0.61 nm^3 (1.0 nm x 0.94 nm x 0.65 nm=0.61 nm^3) with a calculated lysine concentration of 2.7 M along the nanotube surface, we proposed the surface may be suitable for amine catalyzed retro-aldol catalysis. Retro-aldol catalysis has been heavily researched in model systems ranging from catalytic antibodies[2] to rationally designed short peptides[3,4] to computationally designed enzymes[5]. To measure the retro-aldol activity, a fluorescence-based assay is used as retro-aldol cleavage of 4-hydroxy-4-(6-methoxy-2-naphthyl)-2-butanone yields the highly fluorescent 6-methoxy-2-naphthaldehyde[2]. As shown in Figure **7-2**, the general

strategy for catalyzing retro-aldol reactions is through a Schiff base intermediate as is used by Type I aldolases[6]. A detailed characterization of computationally designed[5] retroaldolase enzymes[7] revealed the essential features of the enzyme's catalysis were an ~14-fold enhancement due to the lysine pKa shift and nearly 10^3-fold enzymatic rate acceleration due to the hydrophobic substrate binding[7]. Given the major component of the catalytic enhancement was attributed to hydrophobic substrate binding, we proposed that KLVFFAL's lysine-rich hydrophobic surface may also achieve retro-aldol catalysis.

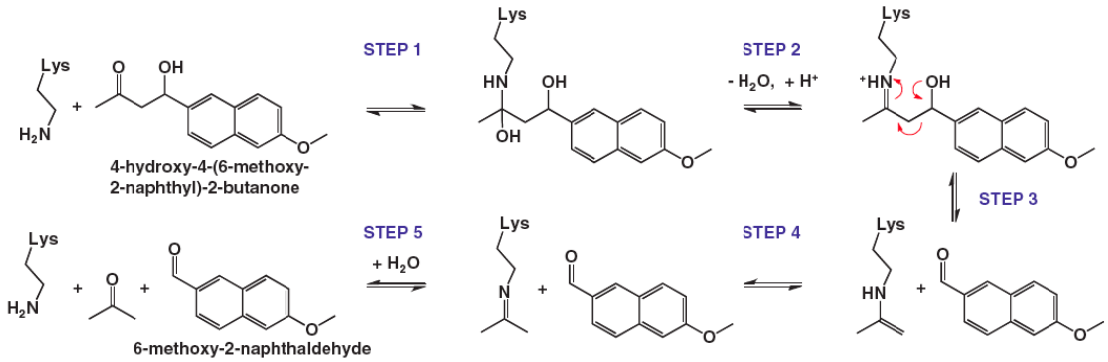

Figure 7-2: Steps in the amine-catalyzed retro-aldol reaction of 4-hydroxy-4-(6-methoxy-2-naphthyl)-2-butanone to form 6-methoxy-2-naphthaldehyde[7].

Methods

Microwave Assisted Solid-Phase Peptide Synthesis

Peptides were synthesized on a Liberty CEM Microwave Automated Peptide Synthesizer (NC, USA) utilizing a FMOC-Rink Amide MBHA Resin (AnaSpec, CA, USA). All FMOC protected amino acids were purchased from Anaspec, and remaining chemicals from Sigma-Aldrich. Each peptide synthesis was performed at 0.1 mmol using a 30 mL reaction vessel at a scale of 0.1 mmol. FMOC-Rink Amide MBHA Resin was initially swollen using ~7 mL dimethylformamide for 15 minutes. FMOC deprotection was achieved by addition of 20% piperdine 0.1 M N-Hydroxybenzotriazole (HOBt) in dimethylformamide with microwave power set to maintain

temperature between 45-55°C for 180 sec, followed by 3X flushing with dimethylformamide. Each coupling step was performed using 0.1M FMOC protected amino acid, and activated with 0.1 M 2-(1H-Benzotriazole-1-yl)-1,1,3,3-tetramethyluronium hexafluorophosphate (HBTU), and 0.2M N,N –Diisopropylethylamine (DIEA) in DMF. Coupling temperatures were maintained between 75-82°C by optimizing microwave power for 300 s. After coupling, the resin was rinsed with three aliquots of dimethylformamide. At the end of coupling steps, 20% acetic anhydride in dimethylformamide was added to acetylate the N-terminus of the peptides. The capping reaction was allowed to proceed for 3 hours at room temperature. Resin was filtered and washed with dichloromethane and allowed to air dry. Peptides were cleaved from the resin using trifluoroacetic acid/thioanisole/1,2-ethanedithiol/anisole (90: 5 : 3 : 2, v/v/v/v) at room temperature for 3 hrs. The cleaved peptide-TFA solution was filtered, and precipitated by dropwise addition of cold (-20°C) diethyl ether. Precipitated product was centrifuged at 3000 rpm for 3 min, and the pellet was subjected to 3 additional rounds of washing with cold diethyl ether. Precipitated product was desiccated overnight.

Dried peptides were dissolved in minimal volume of 40% acetonitrile + 0.1% trifluoroacetic acid and purified by RP-HPLC using a C18-reverse phase column with an acetonitrile-water gradient. Samples eluted from HPLC (10 μL) were mixed with 2,5-dihydroxybenzoic acid matrix (10 μL), 3x2 μL drops were placed on individual spots of MALDI plate and allow to dry in dessicator, and MALDI subsequently confirmed the molecular weight of each peptide used.

Peptides (1.3 mM) were dissolved in 4:6 CH_3CN/H_2O with 0.1% TFA for nanotube assemblies. Dissolution was assisted by ~2 minutes of continuous vortexing, followed by ~15 minutes of sonication until solution became clear. For fibril assemblies after peptides were dissolved in 4:6 CH_3CN/H_2O, solution was slowly titrated by drop-wise addition of 200 mM NaOH until solution became viscous (pH 6 as measured by pH paper). Peptides were allowed to

assemble for approximately 2 weeks at 4 °C until mature as monitored by CD β-sheet signature and homogenous population of hollow tubes visualized by TEM. Prior to kinetic analysis, peptide assemblies were centrifuged at 13,800g for 30 minutes and resuspended in water.

Synthesis of Methodol

Methodol[2], also referred to as 4-hydroxy-4-(6-methoxy-2-naphthyl)-2-butanone was synthesized following procedures[2,7] from acetone and 6-methoxy-2-napthaldehyde (Sigma-Aldrich). Purity was confirmed via ^{1}H NMR and fluorescence measurements to be 96%, containing 4% 6-methoxy-2-napthaldehyde.

Retro-Aldol Kinetic Measurements

Fluorescence measurements for retro-aldol kinetics were collected on a Synergy HT Multi-detection microplate reader. For each initial rate measurement triplicates were ran in each well with a volume of 250 μL and an excitation wavelength of 360 nm, and fluorescence emission observed at 460 nm at a sensitivity level of 50. Time point measurements were collected every 45 s, and plates were shaken for 20 s at an intensity level of 3. Catalytic efficiencies were measured at a fixed KLVFFAL nanotube concentration at 500 μM and varying the methodol concentration to obtain initial rates for 7 methodol concentrations. A graph of initial rates versus methodol concentration yielded a linear plot, where the slope reflected second order kinetic value of k_{cat}/K_M.

Results

To compare with other known catalyst, the retro-aldolase activity was measured in 50 mM sodium phosphate buffer containing 300 mM NaCl at pH 7.5 with 5% DMSO to assist with substrate solubility[7]. Given methodol's low solubility (~500 μM) in water, the amyloid assemblies were not saturated with substrate. Therefore, as with the previous characterization of Rosetta designed retro-aldolases[7], second-order rate constants were measured (k_{cat}/K_m) by monitoring initial rates as a function of initial substrate concentration. Peptides were initially assembled at 1.3 mM in 40% acetonitrile, and after the assemblies matured as verified by CD and TEM, the nanotubes were collected at 13,800g for 30 minutes and resuspended in water, and CD confirmed the presence of β-sheet secondary structure.

As a preliminary screen for catalysis of 50 μM methodol, 50 μM methodol with either 1 mM KLVFFAL or 1 mM RLVFFAL nanotubes, was separately incubated in 50 mM sodium phosphate buffer containing 300 mM NaCl for 30 hours at room temperature. Fluorescence end-point measurements were recorded to determine the extent of reactions (Figure **7-3**). Correcting for residual 6-methoxy-2-naphthaldehyde in the starting material, the KLVFFAL nanotubes catalyzed the conversion 13% of the methodol into 6-methoxy-2-naphthaldehyde over the course of 36 hours. Over the same time course, no 6-methoxy-2-naphthaldehyde production was generated from RLVFFAL nanotube assemblies, indicating the critical nature of the lysine amine for the retro-aldolase activity.

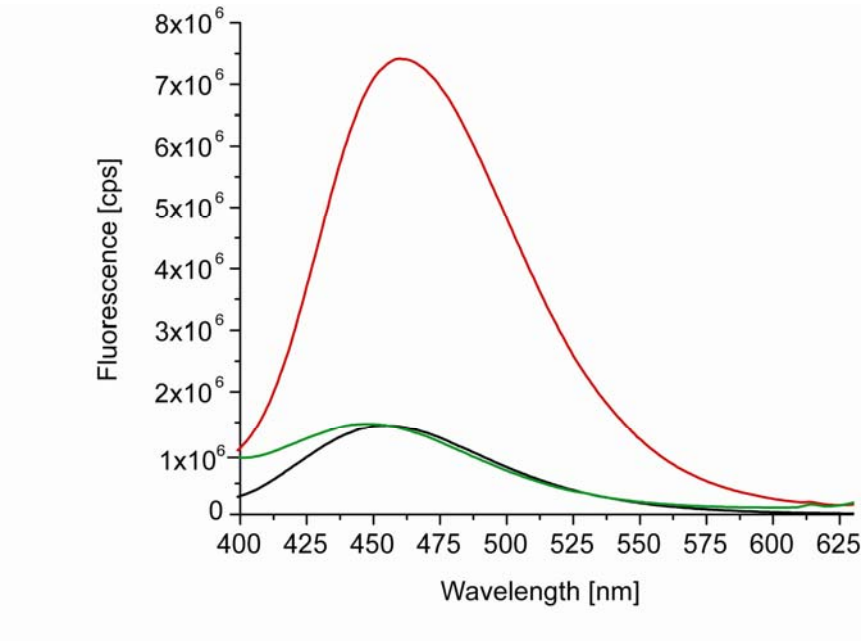

Figure 7-3: Fluorescence spectrum of 50 μM methodol (black line), 50 μM methodol with 1 mM KLVFFAL nanotubes (red line), and 50 μM methodol with 1 mM RLVFFAL nanotubes (green line) was separately incubated in 50 mM sodium phosphate buffer with 300 mM NaCl at pH 7.5 for 36 hours at room temperature.

Catalytic efficiency of lysine (100 mM-500 mM) served as a control and was found to be identical (2.4×10^{-6} M^{-1} s^{-1}) to previous measurements[7]. Under identical conditions, 500 μM KLVFFAL with the methodol followed a linear profile over a 10-50 μM concentration range and yielded a second-order rate constant (k_{cat}/K_m) of 8.8×10^{-3} $M^{-1}s^{-1}$, which is 3.7×10^3 greater than single amino acid lysine.

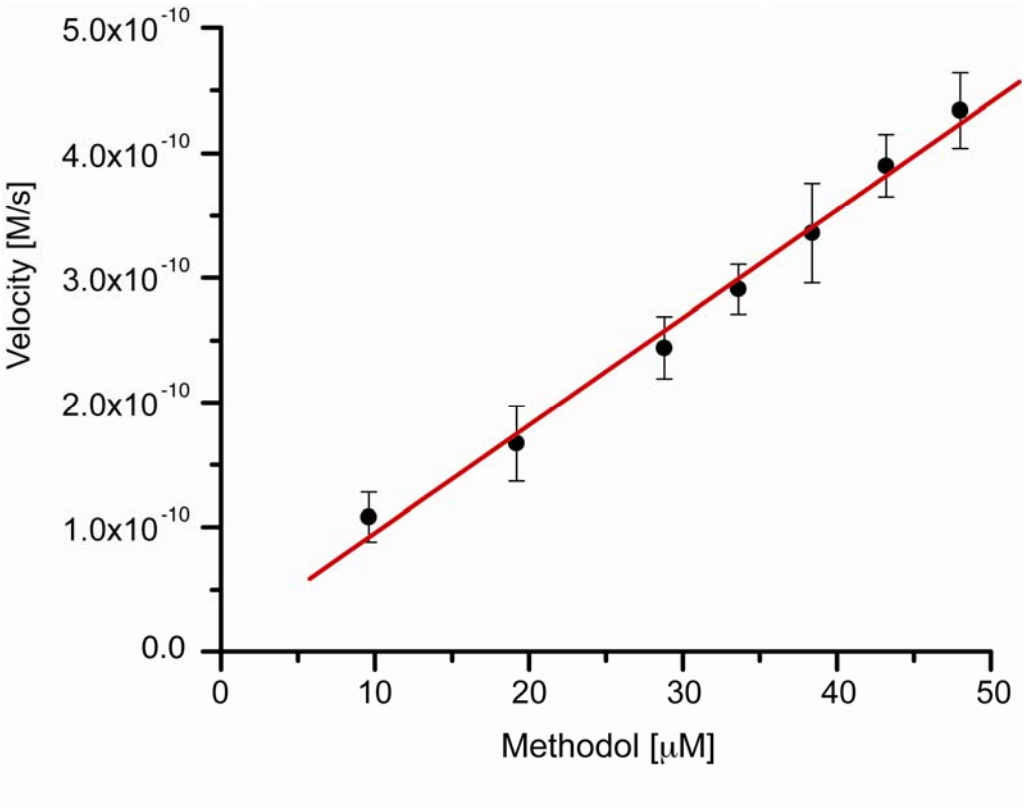

Figure 7-4: Production of 6-methoxy-2-naphthaldehyde as a function of methodol concentration. Reactions were performed in 50 mM phosphate buffer at 25°C with 300 mM NaCl at pH 7.5 with 500 μM KLVFFAL catalyst.

Given that 6-methoxy-2-naphthaldehyde could also form a Schiff base complex with lysine, the binding constants were determined to evaluate potential impact from product inhibition. The fluorescence emission at 452 nm, when excited at 330 nm, is completely lost as the Schiff base is formed[7]. To measure the K_d, a solution of 5.9 μM 6-methoxy-2-naphthaldehyde was titrated with KLVFFAL assemblies over 5-500 μM, yielding a Kd of 51±3 μM. Accordingly, product inhibition during kinetic measurements was minimized by using methodol substrate concentrations below 50 μM.

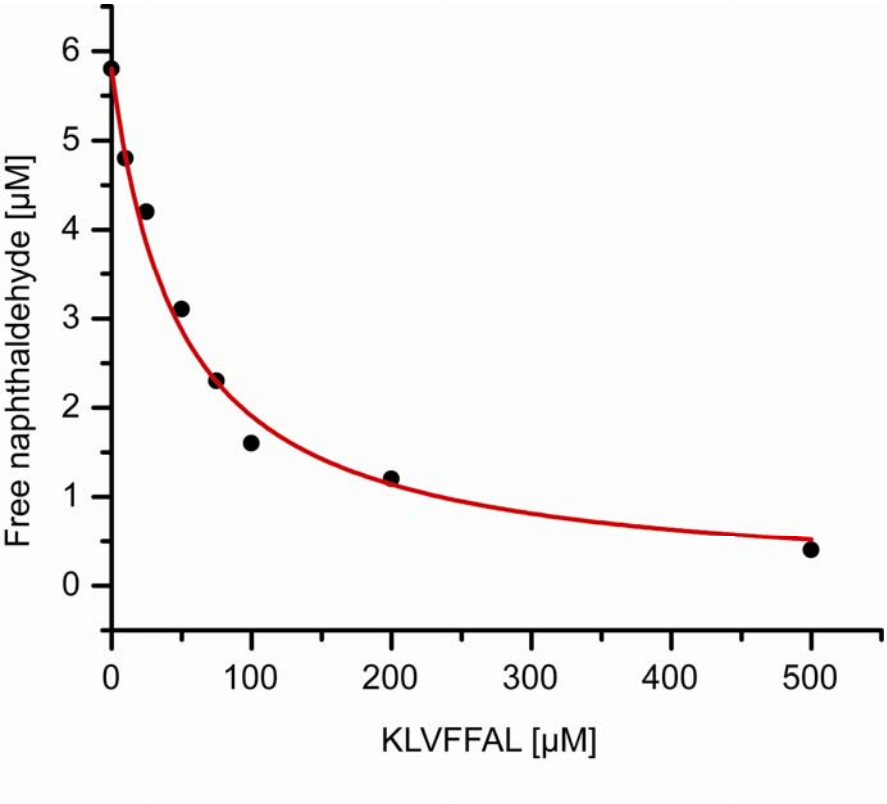

Figure 7-5: Measurement of free naphthaldehyde as a function of KLVFFAL assembly (peptide concentration) using 5.8 μM 6-methoxy-2-naphthaldehyde. The line is the fit of $[N]_f = (K_d[N]_t) / ([E]_t + K_d)$ to the experimental data where K_d is 52±2 μM.

To evaluate directly the impact of product inhibition on multiple turnovers, the ratio of free naphthaldehyde to KLVFFAL catalytic sites (2 peptides/site) was plotted as a function of time. As shown in the reaction progress curves (Figure 7-6), ~4 turnovers were observed for 10 μM KLVFFAL catalyst over 2000 minutes, however higher KLVFFAL concentrations (50 μM) were clearly impacted by product inhibition.

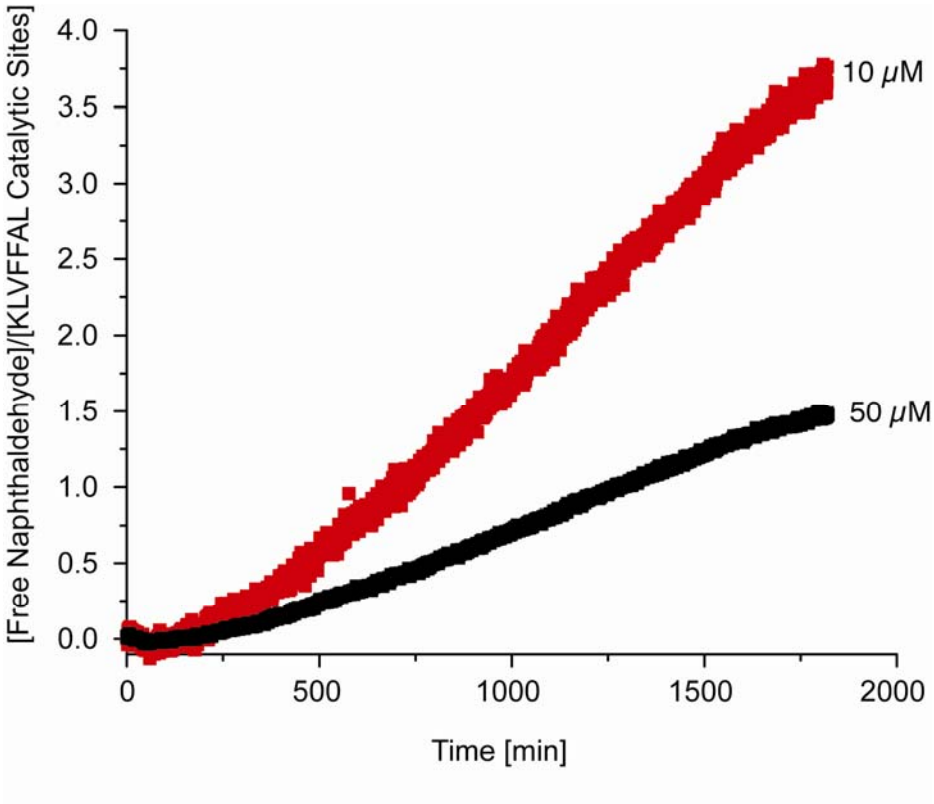

Figure 7-6: Reaction progress curves over multiple turnovers for KLVFFAL. Methodol substrate (400 μM) was mixed with the indicated KLVFFAL concentrations (10 μM and 50 μM) with 50 mM phosphate buffer and 300 mM NaCl, and 5% DMSO at pH 7.5.

Docking of Methodol to KLVFFAL Nanotube Surface

To better understand substrate/nanotube binding we manually docked the substrate with 1000 iterations of energy minimization using the MMFF force field to maximize favorable contacts and minimize van der Waals clashes. With a molecular length of ~10Å, a minimum of two hydrogen bonded β-sheet peptides are needed to construct a small molecule binding site for methodol. Each active site along the nanotube surface covers a surface area of ~180Å^2 and the center-to-center distance between active sites is ~10Å.

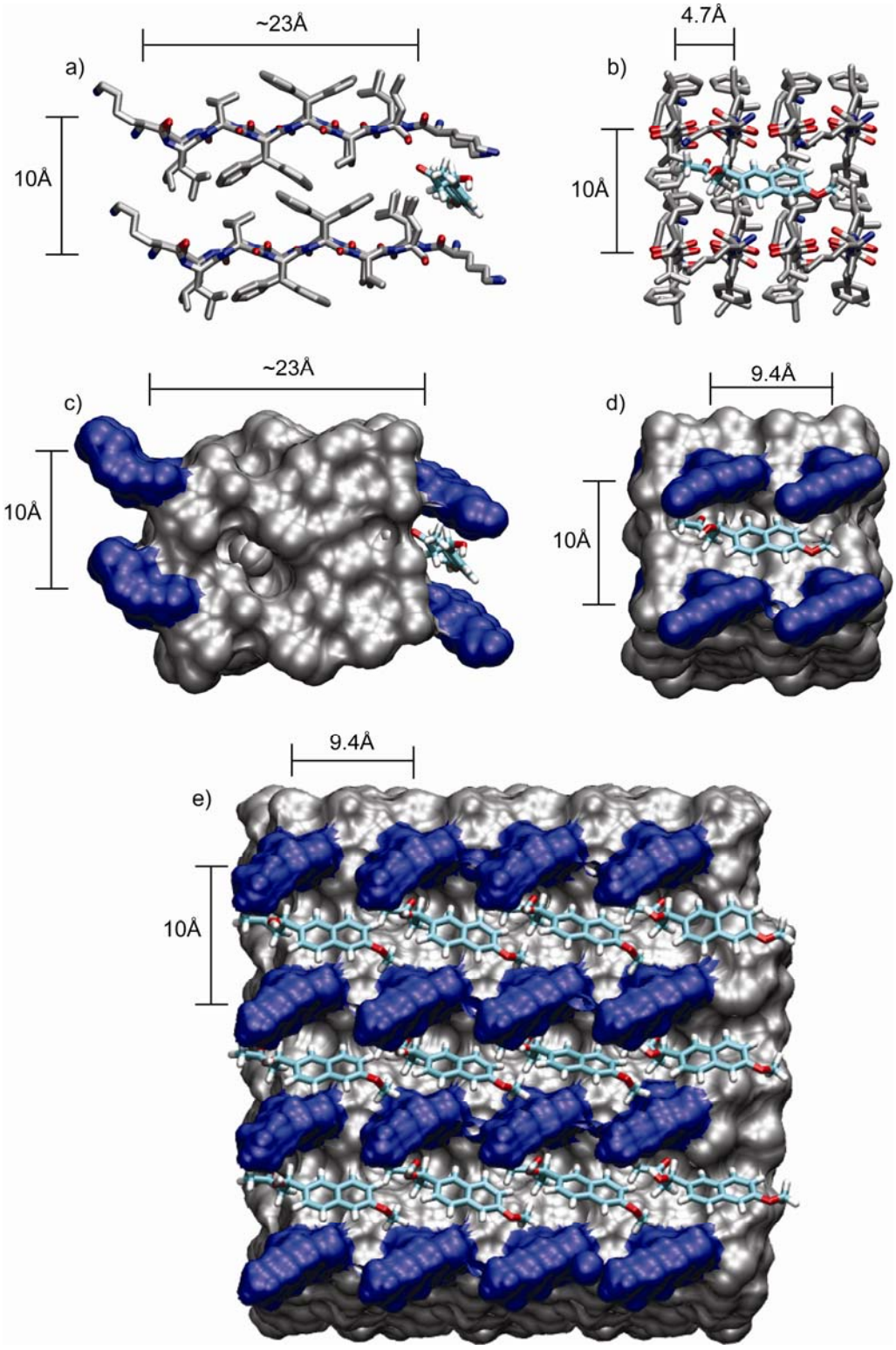

Figure 7-7: Manual docking of 4-hydroxy-4-(6-methoxy-2-naphthyl)-2-butanone (methodol) to KLVFFAL laminate grooves. After methodol was manually docked 1000 iterations of steepest

decent energy minimization using MMFF force field was carried out. Cartoon models of the methodol-KLVFFAL assembly (a) and (b) perpendicular to the peptide chain and (b) and (d) parallel to the peptide chain are presented. (e) Overall, the figure displays a 3 x 3 nm KLVFFAL laminate groove surface saturated with methodol.

To understand the accessibility of the lysine amine on the tube surface, a 1 ns molecular dynamics (MD) run was completed starting with a 5 H-bonded peptides x 5 laminates of KLVFFAL peptides. Given that KLVFFAL forms an anti-parallel out-of-register structure, the N-terminal lysine is not backbone hydrogen bonded and may display considerable conformational freedom. Indeed MD simulations indicate that individual lysines could be oriented in nearly any direction, placing the amine within 5-6.5Å of lysine's backbone alpha carbon. When the lysine conformational range is mapped onto a KLVFFAL laminate grid surface, it covers a significant fraction of the surface area (>40%) - Figure **7-8**. Assuming non-specific binding to the hydrophobic laminate surface, there is a greater than 40% probability of being in sufficiently proximal to a lysine amine to react.

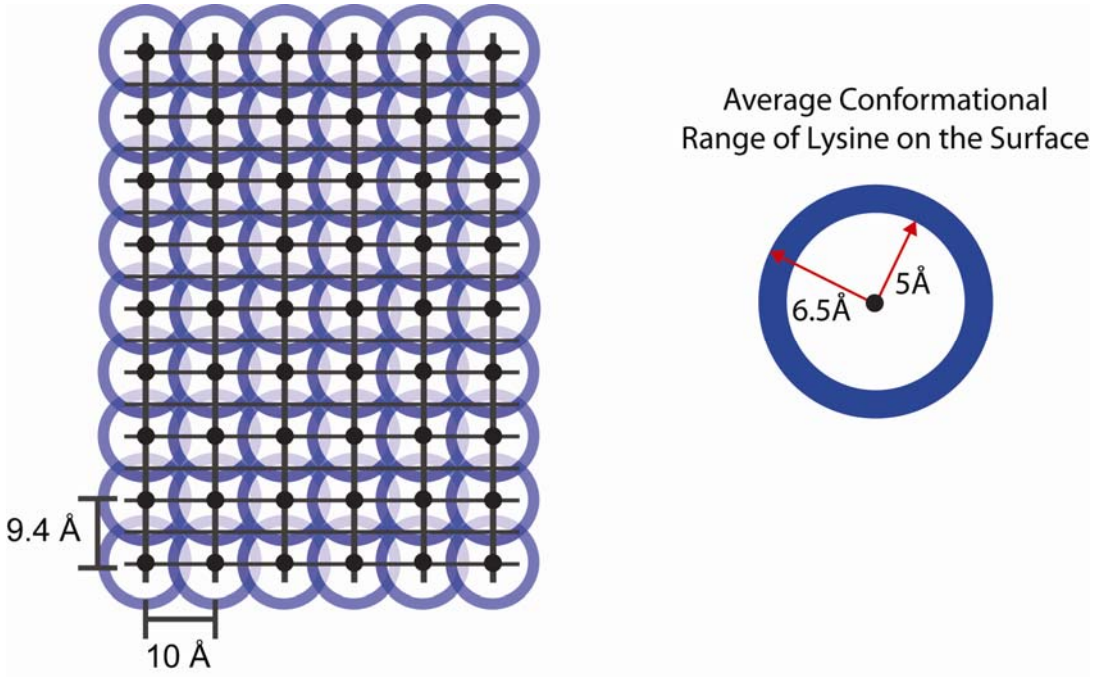

Figure 7-8: Cartoon image of KLVFFAL amyloid surface treated as a grid, where black spheres represent the periodic distribution of the lysine backbone α-carbon. Blue circles represent regions along the grid that have a high probability to be in proximity of the lysines amine as observed by 1 ns molecular dynamics simulation.

Structural Analysis and Catalysis

The most direct test for the role of the lysine in catalysis would be comparison to Aβ(16-22) K16R nanotube assemblies. Previously, it has been shown that RLVFFAL assemblies into nanotube assemblies that are morphologically indistinguishable than KLVFFAL nanotubes[8]. Therefore, the key structural differences between the two assemblies are RLVFFAL presents an arginine-rich surface. Consistent with the proposed amine catalyzed mechanism (Figure **7-2**), no product formation was detected for RLVFFAL nanotubes (Table 1). To dramatically modulate the surface of the nanotubes, Aβ(16-22) E22V were assembled to create nanotubes with a pleat-rich surface (Chapter 5). Intriguingly, E22V's pleat surface resulted in a 59% increase in catalytic activity, from 8.8 x 10^{-3} $M^{-1}s^{-1}$ (E22L) to 1.4 x 10^{-2} $M^{-1}s^{-1}$ (E22V).

Driven by K-E cross-strand pairing, a further dramatic change in binding site architecture results from analysis of KLVFFAE anti-parallel β-sheet fibers and the KLVFFAQ parallel β-sheet fibers driven by Q-Q cross-strand pairing. No detectable retro-aldol catalysis could be detected by either of these assemblies. Future substrate binding studies will help reveal the reasons for of the absence of catalysis for these fiber assemblies.

To further evaluate the importance of the nanotube surface, bundled assemblies were compared with unbundled assemblies. I speculated that bundling of KLVFFAL nanotubes would block ~50% of the catalytic surface. The addition of 200 mM sodium phosphate at pH 7.5 bundle the nanotubes, resulting in visible aggregates. When diluted to 50 mM and compared, the bundled nanotube assemblies displayed a catalytic efficiency of $1.4 \times 10^{-3}\ M^{-1}s^{-1}$, an 84% reduction in catalytic activity ($8.8 \times 10^{-3}\ M^{-1}s^{-1}$).

Table 1. Second-order rate constants at 25°C in 50 mM sodium phosphate, 300 mM NaCl and 5% DMSO, pH 7.5 and rate acceleration relative to lysine.

Catalyst	$(k_{cat}/K_M)_{obs}$, $(M^{-1} s^{-1})$	Rate acceleration relative to lysine	Reference
KLVFFAL bundled Tubes	1.4×10^{-3}	5.8×10^{2}	This Study
KLVFFAL Tubes	8.8×10^{-3}	3.6×10^{3}	This Study
KLVFFAV Tubes	1.4×10^{-2}	5.8×10^{3}	This Study
RLVFFAL Tubes	n.d.*	-	This Study
KLVFFAE Fibers	n.d.*	-	This Study
KLVFFAQ Fibers	n.d.*	-	This Study
Lysine	2.4×10^{-6}	(1)	This Study
Propargylamine[7]	1.7×10^{-5}	7	REF [7]
Trifluoroethlyamine[7]	7.0×10^{-6}	3	REF [7]
YKLLKELLAKLKWLLRKL Helical Peptide [3]	5.2×10^{-2}	2.0×10^{4}	REF [3]
Antibody 38C2[2]	1190	5.0×10^{8}	REF [2]
Rosetta Designed RA61[7]	0.49	2.0×10^{5}	REF [7]
Rosetta Designed RA60[7]	0.16	6.7×10^{4}	REF [7]
Rosetta Designed RA45[7]	0.11	4.6×10^{4}	REF [7]
Rosetta Designed RA34[7]	0.22	9.2×10^{4}	REF [7]

*None detectable in the range of RLVFFAL (<1.5 mM) and methodol (<500μM) solubility.

Conclusions

These initial examples reveal the catalytic potential of amyloid structures. In contrast to modern enzymes where specific binding creates highly specific catalytic effective single active sites, the amyloid assemblies contain multiple catalytic sites all arranged in close proximity. In the Rosetta designed RA61 enzyme, just 2% (128 $Å^2$) of the surface area (7280 $Å^2$) is available for substrate binding. Therefore, even though the catalytic site in amyloid is not optimized for chemistry, the repetitive cross-β structure does place numerous catalytic sites in close proximity, and increases the probability that a molecular collision might result in a chemical event.

Moreover, various amyloid conformational folds yield radically different catalytic activities. Not only do single amino acid substitutions impact the β-sheet registry and assembled morphology, the sequence changes have profound impact on the accessible chemistry. The KLVFFAE anti-parallel fibers[9] and KLVFFAQ parallel fibers[10] displayed no detectable retroaldolase activity, and this absence in observable activity could be due to a lack of substrate binding, binding to pleat surfaces away from the lysine, restricted conformation of lysine that is organized into an in-register β-sheet, or the absence of a suitable binding pocket. Further analysis of substrate binding will help reveal the origins of this difference.

While these amyloid catalysts are not optimized they already display catalytic efficiencies within 5-50 fold of de novo designed enzymes[5,7].

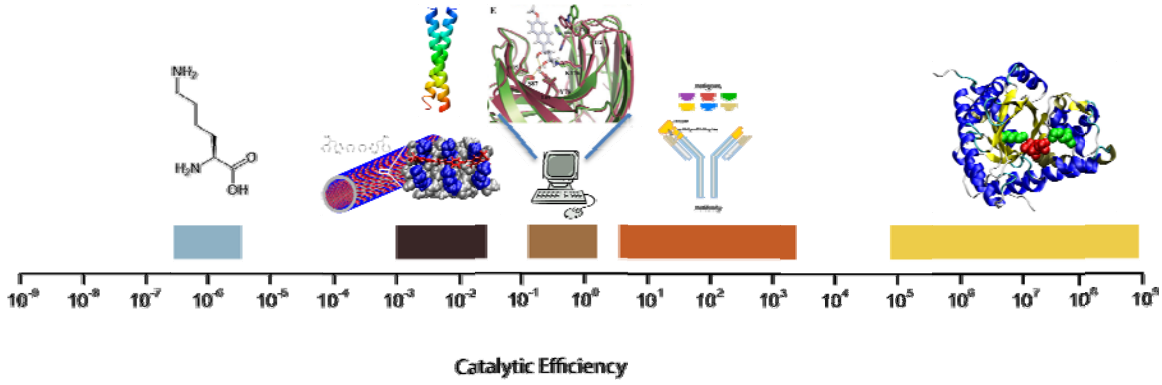

Figure 7-9: Comparison of KLVFFAL nanotubes to other known retro-aldolase catalyst, including from lowest to highest catalytic activity: lysine, amyloid, designed helical peptide, computationally designed enzymes, catalytic antibodies, and natural enzymes.

And their catalytic activity may have significant implications in neurodegenerative diseases, where plaques accumulate over the course of several decades. As observed with the catalysis of nanotube bundle assemblies, the accumulation of fibers into plaques may help block catalytic surfaces. Defining the depth of amyloid's catalytic repertoire may further reveal a wide array of functional amyloid assemblies and the catalysis from short simple amyloid forming peptides could have provided the necessary emergent catalyst to build a diverse prebiotic chemical inventory[11].

References

1. Childers WS, Mehta AK, Lu K, Lynn DG (2009) Templating Molecular Arrays in Amyloid's Cross-Beta Grooves. Journal of American Chemical Society 131: 10165-10172.

2. List B, Barbas CF, Lerner RA (1998) Aldol sensors for the rapid generation of tunable fluorescence by antibody catalysis. Proceedings of the National Academy of Sciences of the United States of America 95: 15351-15355.

3. Tanaka F, Barbas CF (2001) Phage display selection of peptides possessing aldolase activity. Chemical Communications: 769-770.

4. Tanaka F, Fuller R, Barbas CF (2005) Development of small designer aldolase enzymes: Catalytic activity, folding, and substrate specificity. Biochemistry 44: 7583-7592.

5. Jiang L, Althoff EA, Clemente FR, Doyle L, Rothlisberger D, et al. (2008) De novo computational design of retro-aldol enzymes. Science 319: 1387-1391.

6. Gefflaut T, Blonski C, Perie J, Willson M (1995) Class I aldolases: Substrate specificity, mechanism, inhibitors and structural aspects. Progress in Biophysics & Molecular Biology 63: 301-340.

7. Lassila JK, Baker D, Herschlag D (2010) Origins of catalysis by computationally designed retroaldolase enzymes. Proceedings of the National Academy of Sciences of the United States of America 107: 4937-4942.

8. Lu K (2005) Discovery of Diverse Peptide Nanotube Architecture from the Self-assembly of Designed Amyloid-β Cassettes. Atlanta: Emory University. 257 p.

9. Mehta AK, Lu K, Childers WS, Liang Y, Dublin SN, et al. (2008) Facial Symmetry in Protein Self-Assembly. J Am Chem Soc 130: 9829-9835.

10. Ni R (2010): Emory.

11. Childers WS, Ni R, Mehta AK, Lynn DG (2009) Peptide membranes in chemical evolution. Current Opinion in Chemical Biology 13: 652-659.

Chapter 8 : Conclusions - Amyloids as Conformationally Rich Catalytic Membranes[1]

Amyloid: Encoding Information Through Conformation

The mechanisms of information storage within DNA are well studied, even to the degree of synthesizing synthetic genomes[1]. The key to our understanding of DNA information storage is rooted in molecular recognition elements within oligonucleotides that are strongly biased for specific base hydrogen pairs (A:T, G:C)[2]. While genomes direct an organisms phenotypes, Nature has exploited amyloid based prions as a secondary or epigenetic "template"[3] to pass on heritable traits. The molecular recognition elements that lead to amyloid conformational polymorphism or prion "strains" remain poorly understood. In this dissertation, Aβ(16-22) was used as a model system to systematically explore the molecular origins of amyloid conformational variation and molecular recognition.

Amyloid Conformational Variation in β-sheet strand registry

β-Sheet registry can change from parallel[4] to anti-parallel[5] to a wide range of out of registry configurations[6]. In Chapter 2, I examined the effect pH had on the self-assembled conformation of KLVFFAE[7]. Under neutral conditions, E22 is deprotonated and molecular interactions between a positively charged lysine and a negatively charged glutamic acid direct the peptide to form anti-parallel in-register assemblies. Protonation of E22 glutamic acid under acidic conditions resulted in a β-sheet registry shift that was dictated by the bulky β-branched valine (V18) packing against the least bulky residue alanine (A21)[7]. Indeed, further systematic structural changes of V18 indicated that β-branching (valine, isoleucine) directed the registry to

[1] Concepts published as Childers, W. S., R. Ni, et al. (2009). Peptide membranes in chemical evolution. Current Opinion in Chemical Biology **13**(5-6): 652-659.

be anti-parallel and out-of-registry, with non-branched amino acids forming anti-parallel in-register assemblies[8]. Therefore, a single proton directs charge neutralization and molecular recognition within KLVFFAE assemblies. Other studies have shown replacement of the C-terminal glutamate with a glutamine directs the peptide to form parallel assemblies[9]. Glutamine's impact on β-sheet registry is the result of side-chain hydrogen bonding that directs the assembly to form parallel assemblies[9]. Using the 20 natural amino acids, a diversity of molecular recognitions ranging from salt bridges[7] to hydrogen bonding[9] to sterics[8] impact the final assembled β-sheet registry. Using this knowledge, the β-sheet registry of KLVFFAED can now be understood. Future extensions of these studies will be needed to fully understand the delicate cross-strand pairings of each of the 20 amino acids in directing conformational variations in longer peptides (e.g. Aβ(1-40) D23N which forms anti-parallel β-sheets[10] relative to parallel β-sheets for Aβ(1-40)[11])

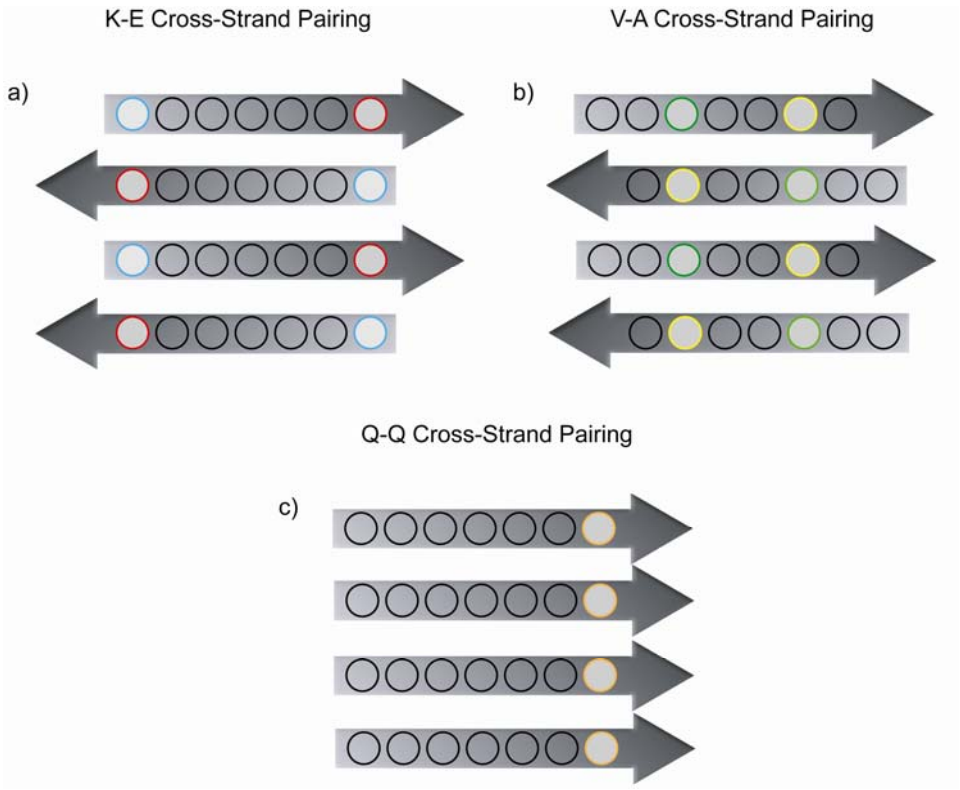

Figure 8-1: Molecular Interactions across strand (i.e. cross-strand pairing) directs β-sheet registry. (a) K-E cross-strand pairing between positively charged (K,H,R) and negatively charged (E,D) results in anti-parallel assemblies. (b) V-A cross-strand pairing between β-branched (V, I) and alanine directs anti-parallel out-of-register β-sheet configuration. (c) Q-Q side-chain hydrogen bonding directs β-strands to be parallel and in-register.

Amyloid Conformational Variation in β-sheet pleat registry

In Chapter 6, structural analysis of KLVFFAL and KLVFFAV peptide assemblies revealed that side-chain interactions across-sheets directs pleat alignment. In the simplest examples of peptides composed of a single amino acid, side-chain lengths and volumes control the distance between laminated β-sheets, as laminates of poly-glycine are separated by 3.7Å[12] and laminates of calcium salts of poly-glutamic acid are separated by 14Å[7,13]. The lamination of β-sheets of mixed peptide sequences becomes more complicated and must optimize side-chain packing to maximally desolvate the entire laminate in a hole-and-peg manner. Characterization of KLVFFAL and KLVFFAV peptide assemblies indicate that decreasing the leucine side-chain by a single methylene caused the laminates to shift the pleat registry to optimize side-chain packing. A systematic study of E22 mutants with varying lengths indicated longer side-chains (leucine, isoleucine, and glutamic acid) packed with pleats in-register, while shorter side-chains (valine, alanine, and glycine) packed with pleats out-of-register. Therefore, distances between laminated β-sheets and pleat registry is a function of maximizing side-chain molecular interaction across β-sheets. In a parallel study, it was shown that parallel assemblies with positively charged lysines at the N-terminus and glutamic acids and the C-terminus pack with pleats in an anti-parallel arrangement to form cross-sheet salt bridges[9]. These two examples highlight the capacity of cross-sheet sheet side-chain interactions to direct pleat arrangement.

Indeed it now appears side-chains play a complex role in directing amyloid internal architecture through both cross-strand and cross-sheet pairing. Subtle amino acid rearrangments can even simultaneously direct β-sheet registry and pleat registry to form an assortment of amyloid conformations providing the molecular source of cross-β strains. This is consistent with the observation of single amino acid substitutions forming yeast species barriers[14], hetkaryon incompatibility[3], and inhibition of amyloid formation in mixed assemblies[15]. Using knowledge gained from Aβ(16-22) we have begun to accurately predict the amyloid conformations of similar peptides, demonstrating Aβ(16-22) provides a powerful platform to dissect the rules of cross-strand and cross-sheet pairings for combinations of all the 20 natural amino acids. Further studies using Aβ(16-22) as a model system will provide the necessary information to predict the amyloid conformation of nearly any amyloid forming peptide. With this foundational knowledge in hand, it is now possible to systematically design molecular recognition elements that specifically recognize unique amyloid conformations for the purpose of developing a recognition strategy and even directing phenotypes.

Amyloid: As a Peptide Bilayer Membrane

In Nature, amyloid assemblies have been exploited for construction of biomaterials ranging from protective barriers for embryos[3,16] to the key element for bacterial biofilm assembly[17,18]. Initial morphological studies of KLVFFAE amyloid nanotubes revealed a membrane-like wall with a wall thickness of 4 nm[19,20]. With an extended peptide length of ~2nm, a bilayer membrane model was proposed with charged lysines exposed to the surface and the C-terminus buried at the bilayer interface[19,21]. However, in Chapter 2 NMR characterization of the KLVFFAE assembly indicated an anti-parallel out-of-register peptide arrangement. This arrangement placed half the charged lysines buried within a bilayer interface and the remaining half exposed to the surface. In Chapter 3, NMR labeling schemes were

designed to directly probe a bilayer interface by placing isotope labels at the N- and C-terminus ends of the peptide and we were able to use these peptides to provide direct support for a peptide bilayer[22]. Further NMR experiments indicated that the positively charged lysines were passivated by TFA ions[22]. The experimental data then established that short amyloid peptides can self-assemble into bilayer membranes morphologically similar to lipids, but with a local order quite distinct from lipid membranes. Typical lipid membranes are organized in a parallel arrangement placing charged head groups at the exposed surface and hydrophobic alkyl chains at the buried interface. In contrast, amyloid peptides can spontaneously form membrane-like bilayer in a rich assortment of configurations based on rules of cross-strand and cross-sheet pairings derived from protein folding.

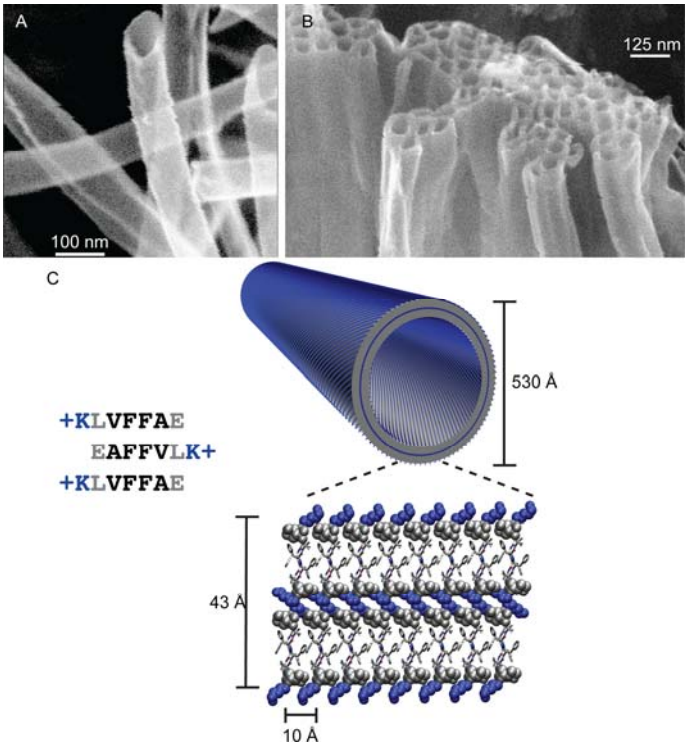

Figure 8-2: Cryo-etch SEM image of 1.3 mM KLVFFAE nanotubes assembled in 40% acetonitrile with 0.1% TFA[7]. (b) bundling of positively charged nanotubes upon addition of sodium sulfate[23]. (c) Proposed bilayer model indicating hydrophilic lysines (blue) are

localized at the buried bilayer interface and the solvent exposed surface. The remaining peptides are drawn as sticks.

To further examine the phase transitions for amyloid assembly, I found that temperature could modulate the peptide from a more fluid oligomer phase at high temperatures to a more crystalline phase at lower temperatures. As well, assemblies undergo a phase change from a twisted state to a helical state based upon a critical number of β-sheets that laminating together. pH conditions modulate the crystalline phase, switching assemblies from a fibrous state to a hollow nanotube state[7], and addition of salts further drive nanotubes into a lamellar-like phase[23]. Clearly I have shown that amyloid peptide assemblies can achieve a wide array long-range ordered phases, in some cases similar to those accessible to lipid membranes[24].

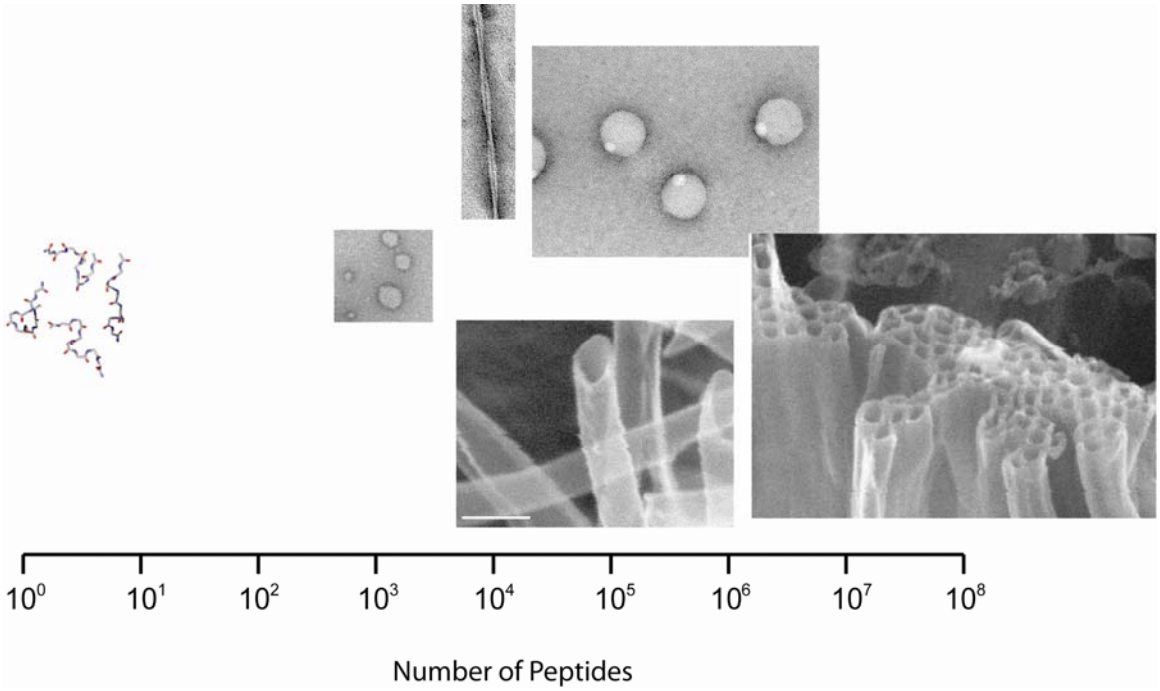

Figure 8-3: Observed amyloid peptide phases as a function of number of peptides.

Amyloid as a Catalyst

Unlike the passive lipid membrane assemblies, amyloid assemblies are composed of polypeptides and have the potential for protein-like functions. Amyloid assemblies have the capacity to bind and interact with small molecules much like an enzyme. To understand the relationship between the cross-β structure and commonly used histochemical dyes, binding of Congo red to KLVFFAL amyloid nanotubes was studied in Chapter 5[25]. As shown in Figure **8-4**, amyloid structures can bind small molecules in high density with individual small molecule binding sites organized side-by-side in a grid arrangement[25].

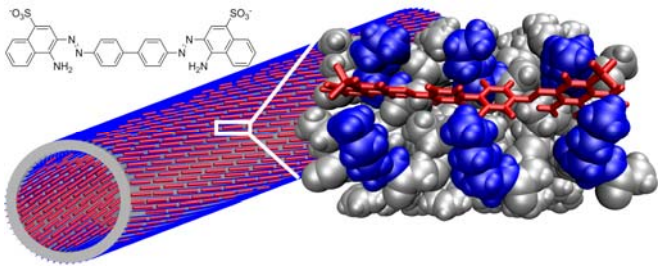

Figure 8-4: Binding of congo red arrays along the KLVFFAL nanotube surface. The nanotube surface is composed of individual small molecule binding sites in close proximity[25].

Indeed, it appears amyloid assemblies share many common structural features of well folded enzymes including buried ions[22], metal binding sites[4,26,27,28], and substrate binding sites[25,29]. Our initial catalysis studies even reveal assemblies contain enzyme-like active site capable of retro-aldolase activity. The catalytic strategy employed by amyloid structures appears to exploit the repetitive cross-β structure by placing numerous catalytic sites in close proximity, increasing the probability of catalysis. While having low activity and poor specificity by natural enzymatic standards, such residual non-specific catalytic activity could be detrimental within a cellular environment. Perhaps more intriguing, such a catalytic strategy could have provided the necessary catalyst to build up a diverse prebiotic chemical inventory[30].

Amyloid: A Platform for Emergence of Chemical Systems

In summary, studies within this thesis have revealed the physical properties and molecular origins of cross-β polymorphism. These long-range ordered morphologies can access a wide range of phases including fibers, ribbons, nanotubes, oligomers, and lamellar bundles. Using rules of cross-strand and cross-sheet pairing, intricate cross-β conformations can be designed to not only build relative peptide arrangements, but also construct entire morphologies from the bottom up. A critical finding observed in Chapters 2 and 6, was that unique cross-β conformations resulted in distinct solvent exposed surfaces. These surfaces present small molecule binding sites for histochemical dyes[31,32] and emerging Alzheimer's diagnostic molecules[33,34]. More intriguing however, the side-chain composition of the surface localized small molecule binding sites can masquerade as catalytic active sites (e.g. retro-aldolase activity of KLVFFAL). This preliminary example opens the door to exploring the catalytic capabilities of amyloid by modulating the side-chain composition of the surface. Given the array of active sites situated side-by-side it presents the possibility of using the surface in template-like polymerizations. Overall, with amyloid merging the properties of information storage similar to DNA, membrane-like architecture similar to lipids, and catalytic capacity similar to proteins, amyloid presents a functionally diverse and robust platform for the construction of complex chemical systems for nanotechnology and investigations into the chemical origins of life.

References

1. Lartigue C, Vashee S, Algire MA, Chuang RY, Benders GA, et al. (2009) Creating Bacterial Strains from Genomes That Have Been Cloned and Engineered in Yeast. Science 325: 1693-1696.
2. Watson JD CF (1953) The Structure of DNA. Cold Spring Harbor Symposia on Quantitative Biology 18: 123-131.

3. Inge-Vechtomov SG, Zhouravleva GA, Chernoff YO (2007) Biological Roles of Prion Domains. Prion 1: 228-235.

4. Dong J, Canfield JM, Mehta AK, Shokes JE, Tian B, et al. (2007) Engineering metal ion coordination to regulate amyloid fibril assembly and toxicity. Proc Natl Acad Sci 104: 13313-13318.

5. Balbach JJ, Ishii Y, Antzutkin ON, Leapman RD, Rizzo NW, et al. (2000) Amyloid Fibril Formation by Ab16-22, a Seven-Residue Fragment of the Alzheimer's b-Amyloid Peptide, and Structural Characterization by Solid State NMR. Biochemistry 39: 13748-13759.

6. Petkova AT, Buntkowsky G, Dyda F, Leapman RD, Yau WM, et al. (2004) Solid state NMR reveals a pH-dependent antiparallel b-sheet registry in fibrils formed by a b-amyloid peptide. J Mol Biol 335: 247-260.

7. Mehta AK, Lu K, Childers WS, Liang Y, Dublin SN, et al. (2008) Facial Symmetry in Protein Self-Assembly. J Am Chem Soc 130: 9829-9835.

8. Liang Y, Pingali SV, Jogalekar AS, Snyder JP, Thiyagarajan P, et al. (2008) Cross-strand pairing and amyloid assembly. Biochemistry 47: 10018-10026.

9. Ni R (2010): Emory.

10. Tycko R, Sciarretta KL, Orgel JPRO, Meredith SC (2009) Evidence for Novel -Sheet Structures in Iowa-mutant -Amyloid Fibrils. Biochemistry 48: 6072-6084.

11. Petkova AT, Yau WM, Tycko R (2006) Experimental Constraints on Quaternary Structure in Alzheimer's Beta-Amyloid Fibrils. Biochemistry 45: 498-512.

12. Fraser RDB, Gillespie JM, Macrae TP (1973) Tyrosine-rich proteins in keratins. Comp Biochem Physiol B 44: 943-947.

13. Keith HD, Padden FJ, Jr., Giannoni G (1969) Crystal Structures of b-Poly-L-glutamic Acid and its Alkaline Earth Salts. J Mol Biol 43: 423-438.

14. Chen BX, Newnam GP, Chernoff YO (2007) Prion species barrier between the closely related yeast proteins is detected despite coaggregation. Proceedings of the National Academy of Sciences of the United States of America 104: 2791-2796.

15. Di Fede G, Catania M, Morbin M, Rossi G, Suardi S, et al. (2009) A Recessive Mutation in the APP Gene with Dominant-Negative Effect on Amyloidogenesis. Science 323: 1473-1477.

16. Fowler DM, Koulov AV, Balch WE, Kelly JW (2007) Functional amyloid - from bacteria to humans. Trends in Biochemical Sciences 32: 217-224.

17. Hammer ND, Schmidt JC, Chapman MR (2007) The curli nucleator protein, CsgB, contains an amyloidogenic domain that directs CsgA polymerization. Proc Natl Acad Sci U S A 104: 12494-12499.

18. Romero D, Aguilar C, Losick R, Kolter R (2010) Amyloid fibers provide structural integrity to Bacillus subtilis biofilms. Proceedings of the National Academy of Sciences of the United States of America 107: 2230-2234.

19. Lu K, Jacob J, Thiyagarajan P, Conticello VP, Lynn DG (2003) Exploiting amyloid fibril lamination for nanotube self-assembly. J Am Chem Soc 125: 6391-6393.

20. Lu K (2005) Discovery of Diverse Peptide Nanotube Architecture from the Self-assembly of Designed Amyloid-β Cassettes. Atlanta: Emory University. 257 p.

21. Lu K, Conticello VP, Lynn DG (2004) In: Conticello VP, Chilkoti A, Atkins E, Lynn DG, editors. Mater Res Soc Synp Proc 826E. Warrendale, PA. pp. V1.6.

22. Childers WS, Mehta AK, Ni R, Taylor JV, Lynn DG (2010) Peptides Organized as Bilayer Membranes. Angewandte Chemie International Edition 49: 4104-4107.

23. Lu K, Guo L, Mehta AK, Childers WS, Dublin SN, et al. (2007) Macroscale assembly of peptide nanotubes. Chem Commun (Camb) 2729-2731.

24. Hianik T (2006) Structure and physical properties of biomembranes and model membranes. Acta Physica Slovaca 56: 687-806.

25. Childers WS, Mehta AK, Lu K, Lynn DG (2009) Templating Molecular Arrays in Amyloid's Cross-Beta Grooves. Journal of American Chemical Society 131: 10165-10172.

26. Dong J, Shokes JE, Scott RA, Lynn DG (2006) Modulating amyloid self-assembly and fibril morphology with Zn(II). J Am Chem Soc 128: 3540-3542.

27. Dong JJ (2006) Metal Ions: a Probe of Amyloid Fibril Formation. Atlanta: Emory University. 288 p.

28. Morgan DM, Dong JJ, Jacob J, Lu K, Apkarian RP, et al. (2002) Metal switch for amyloid formation: Insight into the structure of the nucleus. Journal of the American Chemical Society 124: 12644-12645.

29. Biancalana M, Makabe K, Koide A, Koide S (2009) Molecular Mechanism of Thioflavin-T Binding to the Surface of beta-Rich Peptide Self-Assemblies. Journal of Molecular Biology 385: 1052-1063.

30. Childers WS, Ni R, Mehta AK, Lynn DG (2009) Peptide membranes in chemical evolution. Current Opinion in Chemical Biology 13: 652-659.

31. Divry P FM (1927) The optic properties of amyloid. Omptes rendus des seances de la societie de biologie et de ses filiales 97: 1808-1810.

32. Levine IIIH (2005) Multiple ligand binding sites on Aβ(1-40) fibrils. Amyloid 12: 5-14.

33. Rosen RF, Ciliax BJ, Wingo TS, Gearing M, Dooyema J, et al. (2010) Deficient high-affinity binding of Pittsburgh compound B in a case of Alzheimer's disease. Acta Neuropathologica 119: 221-233.

34. Rosen RF, Walker LC, LeVine Iii H PIB binding in aged primate brain: Enrichment of high-affinity sites in humans with Alzheimer's disease. Neurobiology of aging In Press, Corrected Proof.